Pulsed laser sources utilising liquid crystals as intracavity modulators

By

Christoph Wieschendorf

A thesis submitted to Macquarie University

for the degree of Doctor of Philosophy

Department of Physics

January 2018

MACQUARIE
University
SYDNEY·AUSTRALIA

Typeset in LaTeX 2_ε.

Contents

List of Figures

List of Tables

Statement of candidate

This project evolved from a collaboration between Zedelef Pty Ltd and Macquarie University, combining Zedelef's expertise in liquid crystal cell technology with Macquarie's expertise in integrated waveguide lasers. It was my responsibility in this project to design and develop a concept for the integration of Zedelef's liquid crystal cells into different laser cavities. This included the experimental realisation and characterisation of various laser cavities. Each chapter also contains the outcomes of a numerical model that was developed to match the experimentally recorded data to theory. Those models were programmed using Mathematica and/or MatLab by myself. All the experimental data presented within this work is my original data and contribution. In Chapter 3, relevant material parameters of liquid crystal cells provided by Zedelef and their modulation performance for fast switching are characterised. Based on my feedback, Zedelef improved the liquid crystal cell design to provide better modulation performance for the specific needs of this project. Additionally, within the scope of this work I fabricated depressed-cladding waveguides with the in-house femtosecond direct-write facilities at Macquarie University. The fabrication included polishing/grinding and characterising the waveguide chips. Depressed-cladding waveguide chips, fabricated in ZBLAN by Dr Simon Gross[1] and by myself, and stressed waveguides chips, fabricated in YAG and SRA by Dr Thomas Calmano[2], were used by me for building various pulsed-laser sources incorporating different liquid crystal cells. The outcomes, i.e. actively Q-switched waveguide laser sources, are presented in Chapter 4. Chapter 5 presents the results of a fibre laser cavity that incorporates a liquid crystal cell for active mode-locking. I designed and built the fibre laser cavity; the fibre Bragg grating used was femtosecond laser-inscribed with the

[1] Dr Simon Gross – Macquarie University, Australia

[2] Dr Thomas Calmano – University of Hamburg, Germany

assistance of Dr Sergei Antipov[3]. Lastly, as reported in Chapter 6, the actively Q-switched Tm:ZBLAN waveguide laser was used for nonlinear spectral broadening. I designed the experimental setup, identified a suitable nonlinear fibre, and analysed the results.

This thesis is submitted in fulfilment of the requirements of the degree of Doctor of Philosophy at Macquarie University and has not been submitted for a higher degree to any other university or institution. I certify that to the best of my knowledge, all sources used and assistance received in the preparation of this thesis have been acknowledged. This thesis does not contain any material which is defamatory of any person or corporation and is not in breach of copyright or breach of other rights which shall give rise to any action at Common Law or under Statute.

Christoph Wieschendorf

[3]Dr Sergei Antipov – Macquarie University, Australia

Abstract

A range of techniques for fabricating optical waveguides in actively doped media has previously been developed. Macquarie University has specialised in the femtosecond laser direct-write technique, a flexible method that enables the inscription of three-dimensional structures into transparent media. By inscribing depressed-cladding waveguides into doped fluoride glass chips, continuous-wave (CW) lasers with extraordinarily large fundamental mode-field diameters have been realised. However, in order to generate optical pulses with high peak-power levels, an actively controlled intracavity loss modulator would be required. While the use of bulk acousto-optic modulators has been demonstrated, the waveguide chip laser architecture is best utilised with a modulator that is compatible with a monolithic and integrated design.

In the present work, a novel type of a liquid-crystal based transducer was utilised as an intracavity loss modulator that can be integrated onto the laser chip, opening up the possibility of realising monolithic miniaturised actively Q-switched high peak-power laser sources. This liquid crystal cell was initially developed by our collaborator in the context of distributed sensor networks and therefore its switching behaviour on a microsecond to sub-microsecond timescale had to be studied first. Next, the cell was employed as an active Q-switch in an ytterbium glass waveguide laser, resulting in peak power levels approaching 100 W. Further, the use of this technology in laser chips based on polarisation-maintaining waveguides in crystalline materials was investigated in the visible spectral region, and this approach was also extended towards the mid-infrared spectral region with the aim of utilising nonlinear optical effects in chalcogenide fibres to generate broadband radiation in the important mid-infrared fingerprint region of the optical spectrum.

Finally, the feasibility of using the liquid-crystal modulator as a mode-locking device in fibre lasers was investigated and a fibre laser that can be switched between mode-locked, Q-switched and CW operation was demonstrated.

Acknowledgements

I would like to express my sincere gratitude to the people, who provided me with support and friendship throughout the time of my candidature. In particular, I would like to thank my supervisors Alex Fuerbach, Simon Gross and David J Spence. Your guidance and mentorship has been a continuous inspiration. Thank you for providing me with useful insights, advice, critical feedback and fruitful discussions during my PhD. A special thanks goes to Michael Withford who always had the door open to provide feedback and advice.

To all the people at Macquarie University that shared this journey with me, it was a great time working with you, Glen Douglas, Blake Entwisle, Michelle Withford, Thomas Gretzinger, Sergei Antipov, Saheed Oladipupo Fashola, Zach Chaboyer, Matt Collins, Robert Woodward, Darren Hudson, Gayathri Bharathan, Alex Arriola, Peter Decker, Ben Johnston, Alex Stokes, Robert Williams and Aaron McKay. I am indebted to the administrative staff Anita, Carol, Lisa, Laura and Liz for their support and dealing with my paper work.

Most importantly I am thankful to my lovely girlfriend Hella Fassauer for her devotion, patience and love which has been truly inspiring. She has been always there for me, building me up after long and frustrating hours in the lab.

Finally, I would like to thank my parents Irin, Peter and my sister Christin for their endless support, love, and the education I received. It is to them I dedicate this thesis.

Cheers,
Christoph

1

Motivation

After the first report in 1996 of a femtosecond laser-inscribed waveguide [1], the field of femtosecond laser-inscribed photonic devices rapidly expanded. In the following years, the fabrication of passive and active waveguides, as well as more complicated 3D photonic circuits, was reported [1–9]. In contrast to classical bulk lasers, the potentially detrimental effects of beam divergence can be avoided in lasers that utilise a laser-inscribed optical waveguide as the active medium. In such a guided-wave laser, high optical intensities can be maintained over long distances, resulting in a high optical gain and a high efficiency. Moreover, these lasers feature a monolithic laser resonator and thus offer a more stable and compact setup than a bulk laser. In many applications, fibre lasers have now almost completely replaced their bulk laser counterparts. However, for low- to medium-power applications, switching to a fully integrated and monolithic waveguide laser geometry can provide significant additional advantages. While still offering all the benefits of fibre lasers, embedded waveguide lasers are inherently protected from air and moisture exposure and are thus insensitive to environmental influences. Moreover, those lasers can be further reduced

in size and the development of fully miniaturised laser sources becomes feasible. Most of the previous work in this space was aimed at developing compact and narrow linewidth continuous-wave (CW) lasers [10–14].

In 2012, the principle of large mode area (LMA) waveguides, which had long been used within the fibre laser community, was adopted for femtosecond laser-inscribed waveguides. Lancaster *et al.* demonstrated quasi–single-mode waveguides with LMAs, thus opening up the possibility of developing pulsed waveguide laser sources with ultrahigh peak intensities [15]. LMA fibres proved to be an enabling step for generating high intracavity peak power levels in fibre lasers, as the increased mode-field diameter drastically reduces unwanted nonlinear effects and increases the damage threshold. So far, pulsed operation of waveguide lasers has been demonstrated in both actively and passively modulated setups. Passive switching can be achieved by utilising semiconductor saturable absorber mirrors (SESAMs) or thin layers of materials that exhibit saturable absorption, such as graphene or carbon nanotubes, that can be deposited on a high reflecting end mirror which is subsequently butt-coupled onto the waveguide chip. Using this approach, mode-locked and Q-switched operation of waveguide lasers was demonstrated, with pulse durations ranging from a few ps up to several hundred ns [16–18]. Due to their inherently small size, the use of passive saturable absorbers is appealing for monolithic pulsed waveguide lasers. In passively Q-switched lasers, however, the repetition rate is determined by the properties of the gain medium and the saturable absorber. Consequently, the repetition rate cannot be controlled externally. To achieve active Q-switching, commercially available acousto-optical modulators (AOMs) and electro-optical modulators (EOMs) are typically used. With those actively controlled devices, the repetition rate of the laser can be selected on demand. The trade-off is that the laser setup becomes bulky and the advantage of a monolithic and miniaturised design is lost. In addition, the modulators need to be controlled by either radio frequency (RF) or high voltage (HV) drivers, and water-cooling is often required.

To date, several key elements required for the development of a truly compact and actively Q-switched integrated waveguide lasers have been demonstrated utilising femtosecond laser inscription. These include waveguide couplers that can act as pump combiners. Gross *et al.* demonstrated depressed cladding directional couplers in ZBLAN for an astronomical nulling interferometer [19]. Ams *et al.* demonstrated tuneable waveguide couplers and proposed

that the same method could be used for fabricating a Mach-Zehnder interferometer [20]. Furthermore, Dekker *et al.* utilised the femtosecond laser inscription method to inscribe Bragg gratings into a glass chip (Schott AF45) [21]. The Bragg grating was then used as a narrow linewidth high-reflecting mirror in conjunction with a Yb:YAG waveguide chip laser. In principle, a Bragg grating could also be written directly into the active gain material along with the active waveguide, in one fabrication process. Due to the flexibility of femtosecond laser inscription, the Bragg grating could either be used as a high-reflecting mirror or an output-coupling mirror, depending on the reflectivity. All these methods can be seen as steps towards the development of a truly monolithic (pulsed) waveguide laser source.

Compact pulsed laser sources are in high demand and hold promise for many future applications. For example, small compact laser sources could be used for selective remote sensing of different materials [22–24]. Douglas *et al.* have utilised a dual-wavelength LiDAR source for mapping forest structures at high spatial resolution while differentiating between trunks and leaves [25]. Depending on the availability of suitable gain materials, arrayed laser sources with distinct wavelengths could be used for similar applications, while sensing different materials. Another example would be the use of several compact narrow linewidth pulsed laser sources for greenhouse gas monitoring. Their distinct absorption lines lie within the range 1562–1640 nm [26], which is accessible by commonly available gain materials. Other applications include wind sensing by using the Doppler shift of a back-reflected probing beam [27]. The recent development of labs on a chip could also benefit from a small integrated pulsed laser source. For example, Merklein *et al.* recently demonstrated a photonic-phononic memory chip [28]. Although the memory chip is compact, the driving laser source consists of an oscillator and two fibre amplification stages to achieve nanosecond pulses with several watts of peak power. In addition, the described optical memory writing mechanism relies on a intensity modulator which would become avoidable with an actively pulsed laser source.

In this work, the ultimate aim was to identify a compact cavity internal loss modulator that can be integrated within a waveguide laser cavity and enables a monolithic setup. The long-term goal is to build an actively Q-switched and miniaturised laser source as illustrated in Fig. 1.1. The loss modulator should be controlled by a low voltage signal and should not require active cooling. For this, the switching capabilities of a smectic liquid crystal transducer as a cavity internal loss modulator were studied. Unlike previously demonstrated

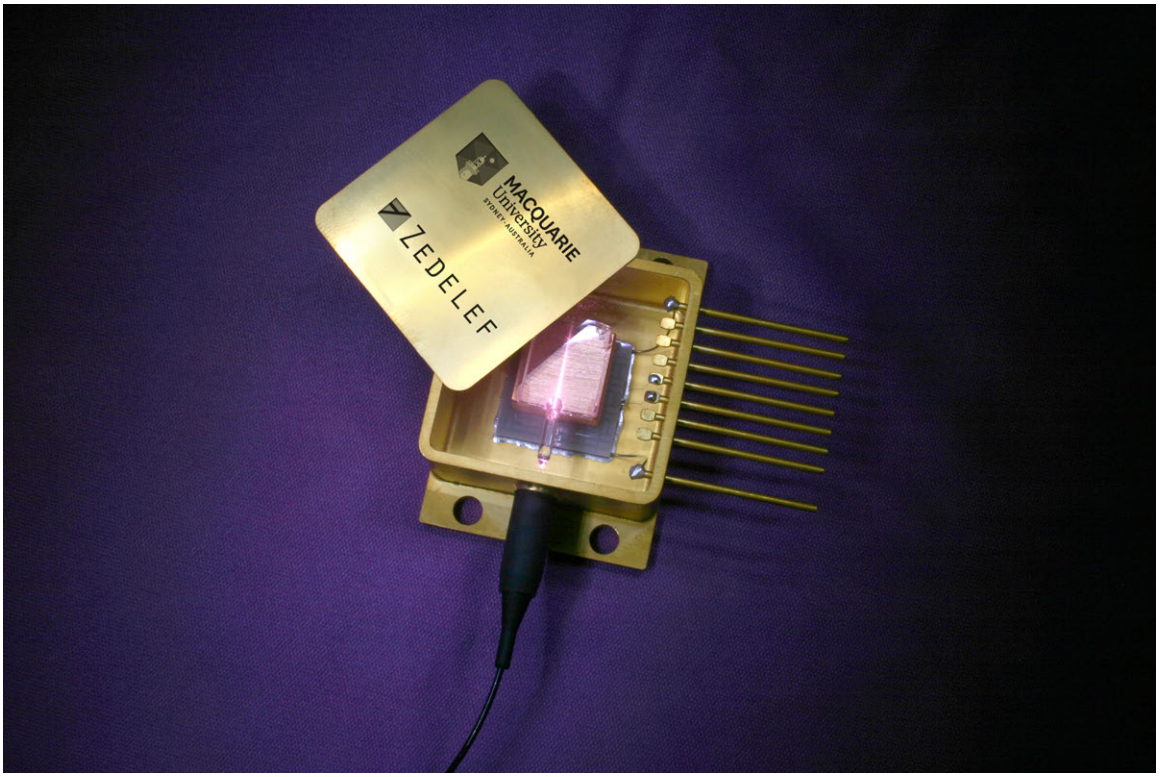

Figure 1.1: Illustration of an actively Q-switched waveguide laser that gives the user full control over repetition rate and other laser parameters (such as the pulse peak power). This vision includes the logos of the collaborators Zedelef Pty Ltd and Macquarie University. Zedelef designed and fabricated the liquid crystal transducers. Image courtesy of Dr Martin Ams.

methods using nematic liquid crystals [29–33], the device investigated here can be directly integrated onto the waveguide chip and can be controlled by low-power, low-voltage drivers. Furthermore, the capabilities of this liquid crystal transducer were explored for active mode-locking. An actively pulsed laser source, based on a liquid crystal transducer, is promising as it also opens up possible nonlinear applications, such as nonlinear spectral broadening without the need for post-amplification.

This work is organised as follows. Chapter 2 provides a brief background to the basic principles of femtosecond laser-inscribed waveguides and describes the in-house facilities used to fabricate femtosecond laser-inscribed waveguides. The Mueller matrix formalism – which will be used throughout the work to describe polarisation-related phenomena – is also introduced. In Chapter 3, the active loss modulator is introduced and characterised, with the main goal being to maximise the switching capabilities when used as a cavity internal loss modulator. Chapter 4 explores the use of this loss modulator in various waveguide laser cavities. Each of these cavities uses a distinct active laser ion doped to the host material and

oscillation at several different wavelengths is thus achieved. In Chapter 5, the loss modulator is employed as an active mode-locking device in a fibre laser cavity. Chapter 6 presents experimental results achieved using a liquid crystal-based actively Q-switched laser source for nonlinear spectral broadening within a chalcogenide fibre. In Chapter 7, the conclusions of this work and a future outlook are presented.

2

Background – theory and experimental methods

2.1 Laser interaction with transparent dielectrics

To induce material modification in transparent dielectrics utilising a laser beam, energy transfer from the laser field to the material is necessary. Therefore, to cause linear absorption the photon energy of the laser beam must be at least as high as the characteristic band-gap energy (E_g) of the material. The band-gap energy E_g is determined by the energy needed to promote an outer bound valence band electron to the conduction band. Once in the conduction band, the initial bound electron is ionised and can be regarded as a free carrier. For example, in fluorozirconate glass the energy needed to create a free carrier is approximately $E_g = 5$ eV [34]. To overcome E_g, by means of linear absorption, an ultraviolet laser source with a wavelength of $\lambda \leq 248$ nm is required. However, linear absorption takes place at the surface of a material. In order to deposit energy inside a material, nonlinear absorption is required.

2.1.1 Nonlinear excitation mechanisms

Nonlinear excitation mechanisms enable material modifications even though the photon energy of the laser beam is smaller than E_g. However, high field intensities are necessary; these can be attained by tight focusing a high-power continuous-wave laser beam on a small spot and/or by the interaction with high peak intensities emitted by a pulsed laser source. The driving mechanisms behind nonlinear photon excitation are based on either a one-step process, strong electric field ionisation, or a two-step process, avalanche photonionisation. A detailed description can be found in [35] or [36].

Strong electric field ionisation

Femtosecond lasers deliver high peak intensities and, when focused onto or inside transparent materials, can result in multiple laser photons being absorbed simultaneously by a single bound electron. This process is called multiphoton absorption, a nonlinear absorption process that can lead to the ionisation of an electron. In Fig. 2.1a, the process of multiphoton ionisation (MPI) is depicted. Multiple photons are absorbed at once by a single (outer band) electron, thus causing the atom to become ionised. When the laser intensity is even higher, another process becomes dominant, causing deformation of the atomic potential barrier. As a result, the Coulomb force that binds the electron to the positively charged atomic core weakens, enabling a valence band electron to tunnel through the atomic potential barrier to become ionised. The mechanism of tunnelling ionisation is depicted in Fig. 2.1c. It is also possible to have a combination of multiphoton ionisation and tunnelling ionisation, where a high-energy photon deforms the atomic potential and multiple photons are absorbed by a single electron. The combination of the two processes is depicted in Fig. 2.1b.

In 1965, Keldysh *et al.* established an expression to obtain the probability of ionisation of atoms in the field of a strong electromagnetic wave [38]. The Keldysh parameter, γ, is defined as follows:

$$\gamma = \frac{\omega}{e}\sqrt{\frac{m_e c n \epsilon_0 E_g}{I}} \tag{2.1}$$

where I is the intensity in the area of interest (e.g. in the laser focus), ω is the laser frequency, m_e and e are the mass and charge of an electron, c is the speed of light and n is the refractive index of the material. The band-gap energy of the material is E_g and ϵ_0 is the vacuum permittivity. When $\gamma \gg 1.5$, the dominant process is multiphoton ionisation; for $\gamma \ll 1.5$,

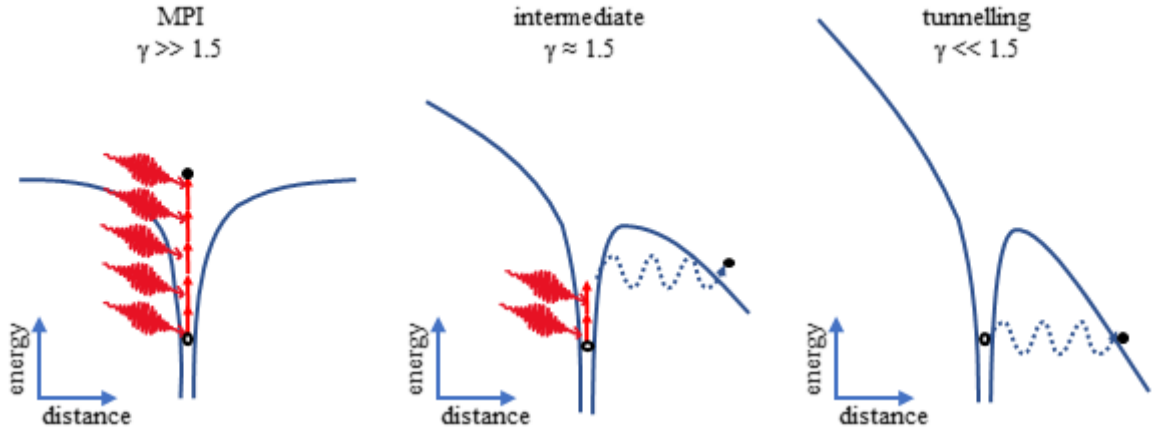

(a) Multiphoton ionisation. (b) Intermediate regime. (c) Tunnelling ionisation.

Figure 2.1: Nonlinear strong electric field ionisation mechanisms and their corresponding Keldysh parameter, γ [37].

tunnelling ionisation is dominant. In the intermediate regime, a mix of both processes takes place. The multiphoton ionisation rate strongly depends on the intensity in the area of interest and can be estimated by $dN/dt = \sigma_k \times I^k$. The ionisation cross-section σ_k is a material-specific characteristic and describes the probability of the ionisation process taking place when absorbing a number of photons (k). Note that σ_k depends on the polarisation state of the incident radiation [39–41]. The minimum number of photons required to overcome the band-gap energy for ionisation is $k \times E_{ph} \geq E_g$ in the case for $(k-1) \times E_{ph} < E_g$ and k being an integer.

Avalanche photonionisation

In order to seed avalanche photonionisation, an initial free seed electron – that is, an electron in the conduction band (free carrier) – must be available. It can be generated by multiphoton ionisation, by thermal energy deposited into the material or by impurities/defects in the host lattice. Once generated, two effects can follow, as illustrated in Fig. 2.2. First, the free carrier gains energy by absorbing multiple photons (see Fig. 2.2a). By the time this energy reaches E_g, the free carrier can initiate the second step: a valence band electron gets promoted to the conduction band by impact ionisation, which results in the existence of two free carriers in the valence band, as shown in Fig. 2.2b. Those two carriers can absorb further laser photons which then eventually produce more free carriers through impact ionisation. This process can be best described by an avalanche effect with exponential growth. Schaffer *et al.* [37]

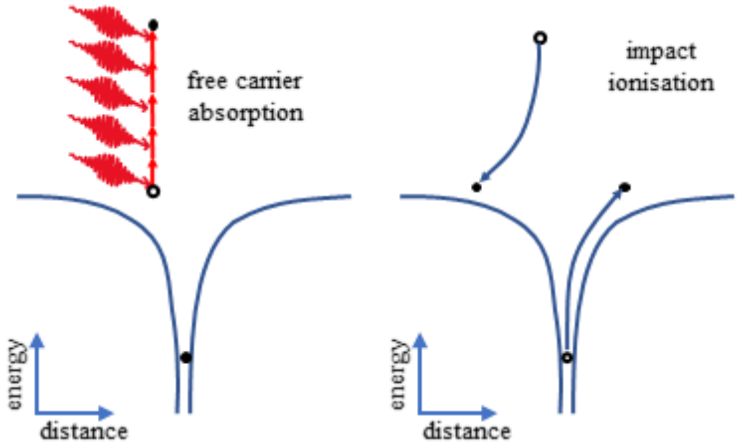

(a) Free carrier absorption. (b) Impact ionisation.

Figure 2.2: Mechanism of avalanche ionisation: free carrier gains energy until it has sufficient energy to generate another free carrier by impact ionisation [37].

demonstrated that the growth in free carriers (N) can be described by:

$$\frac{dN}{dt} = \eta(E)N. \tag{2.2}$$

Here, $\eta(E)$ is the avalanche ionisation rate, which depends on the incident electrical field strength, E. Note that several models have been proposed to estimate the avalanche ionisation rate [42–45].

2.1.2 Refractive index change

Once free carriers are generated, the deposited energy is transferred to the lattice by electron-phonon coupling. The resulting local heating causes structural modifications. In addition, when utilising ultrashort pulses, e.g. from a femtosecond laser, shockwaves and micro-explosions can also result in structural modifications. Depending on the material, three different kinds of modifications can be identified – firstly, a positive or negative smooth refractive index change; secondly, at higher peak powers, a birefringent refractive index change; and, finally, void formation for even higher peak powers.

Isotropic refractive index change

A homogeneous positive or negative refractive index change can be attributed to localised heating (due to electron-phonon collisions), that causes melting and fast resolidification (after

a few picoseconds) of the host material within the focal spot. It is because of the strongly confined thermal gradient within a tiny region of the lattice that the material cools rapidly. The fast cooling freezes-in the material properties of the higher temperature state [46] and results in either local densification or rarefication. This thermal model is backed up by several findings [47–49]. For example, Chan *et al.* proposed that in fused silica an increase in the refractive index was caused by densification of the material [49]. They analysed the Raman spectra of the femtosecond laser-beam exposed region and found an increase in 3- and 4-member ring structures. In the unexposed region, 5- and 6-member ring structures were dominant. The increase of 3- and 4-member ring structures indicates a densification, as these can be packed more densely than 5- and 6-member ring structures. In the zirconium fluoride glass (ZBLAN) used in this thesis, quenching causes single bridging fluorine bonds to form, instead of double bridging bonds [35]. Single bridging bonds in the glass network occupy more volume compared to the same amount of double bridging bonds. Thus, in ZBLAN glass the refractive index change is negative.

However, the thermal model does not fully describe the underlying mechanism of a homogeneous refractive index change. Streltsov and Borrelli showed that, utilising different pulse energies, it was possible to achieve the same amount of refractive index change [6], even though theory indicates that different pulse energies result in different temperatures within the focal spot. As a result, an additional model was suggested that makes colour centres responsible for a refractive index change [50–54]. In sufficient numbers, colour centres can cause a refractive index change through a Kramers-Kronig mechanism [55]. A high density of free carriers can result in trapped species (colour centres) which are responsible for changes in the molecular structure. Several research groups were able to reveal modifications attributable to colour centres by utilising confocal fluorescence spectroscopy [50, 51, 54, 56]. The amount of refractive index change through colour centre formation depends on the laser parameters, e.g., the repetition rate, and on the material itself [57].

Birefringent refractive index change

Under similar conditions but a slightly higher pulse energies, in fused silica it has been shown that the irradiated region contains nanoporous structures that have a strong dependency on the polarisation orientation of the laser beam [58–61].These nanostructures are perpendicular to

the electric field vector of the irradiating linear polarised laser beam. They are self-ordered and periodic, with a size as small as 20 nm and a periodicity typically in the order of 140 nm. It was shown that the period structure contained alternating regions which exhibited a dense part and a slightly less dense part. Within the irradiated material volume, the varying material composition results in a birefringent refractive index change [62, 63]. To date, this kind of induced birefringence has only been observed in limited types of silica-based glasses – for example, in alkali-free aluminoborosilicate glass [64] – and thus is not relevant to the work presented here.

Voids

At very high intensities, nonlinear absorption gives rise to a localised plasma [65][66]. The plasma causes an intense pressure within the focal region, which results in microexplosions (Couloumb explosion) sending out shock waves [66–68]. Those shock waves carry matter and energy away from the focal region. As a result, a less dense focal volume and a densified surrounding shell are left behind, resulting in a refractive index change. This theory was confirmed by sensing the pressure shock waves originating from the focal spot [69–71].

2.2 Femtosecond direct-writing method

To inscribe optical waveguides into bulk material, several steps are required. This section outlines each of these steps. First, the raw glass block needs to be cut into smaller chips, and those need to be polished to enable the inscription laser to be focused inside the glass (sample pre-processing). Next, the actual writing of the waveguide, utilising a femtosecond laser, takes place (sample waveguide inscription). After that, grinding and polishing of the end-facets is required to reveal the waveguides and to remove unwanted defects. There are two reasons for this: first, due to aberrations of the writing beam it is not possible to write across the edge unless adaptive optics are used [72], and second, asymmetric conditions near the end-facets cause stress and unwanted reflections that can result in cracks or tapers.

2.2.1 Sample pre-processing

Since most glass samples used for femtosecond laser inscription come directly from the manufacturer in bulk pieces (ingot or slab), several pre-processing steps must be carried

out. These usually begin with dicing the bulk material into samples of the desired size. As an active gain medium, the chip dimensions must be chosen to guarantee a net gain; thus, when choosing the chip length the available pump power, doping concentration, internal losses (e.g. propagation losses in the waveguide) and incoupling losses must be considered. Once diced, the samples are ground and polished parallel to the intended direction of the waveguide. This ensures that the focused inscription laser beam is not disturbed or scattered at the sample surface. Note that the samples that were used throughout this work were already pre-processed; a more detailed description of this stage can be found elsewhere [35].

2.2.2 Sample waveguide inscription

This subsection briefly covers the in-house setup used for the waveguide inscription, as depicted in Fig. 2.3. Each element is described below: (i) the laser system, (ii) the beam delivery system (which manipulates the beam before it is focused into the sample) and (iii) the translation stage, which moves the sample across the focused laser beam. The subsection concludes with the inscribed waveguide geometry utilised throughout this work.

Laser

The nonlinear absorption-based inscription method requires a laser source that delivers ultrashort pulses, high pulse energy and, as a result, a high pulse peak power. One way to achieve these specifications is to amplify low-energy pulses external to the cavity. This involves a complicated setup; the pulse first needs to be stretched in time and, after amplification, must be recompressed (chirped pulse amplification (CPA)). Another approach is to have an oscillator with an intracavity dispersion design to stretch the pulses internally. Once the pulse leaves the cavity, it can be recompressed. To enable working without any further amplification, the cavity must be as long as possible to reduce the repetition rate and thus increase the pulse energy at constant average output power. In the presented work, a laser oscillator (FEMTOSOURCE XL500 from Spectra-Physics) with intracavity stretching and enhanced cavity length was used. The cavity length is enhanced with a Herriott multipass cell (MPC) to 30 m in total, corresponding to a repetition rate of 5.1 MHz. The pulse duration is approximately 50 fs at full width half maximum (FWHM) and its corresponding autocorrelation trace is depicted in Fig. 2.4a. The corresponding spectrum measures 43 nm (FWHM) (see Fig. 2.4b).

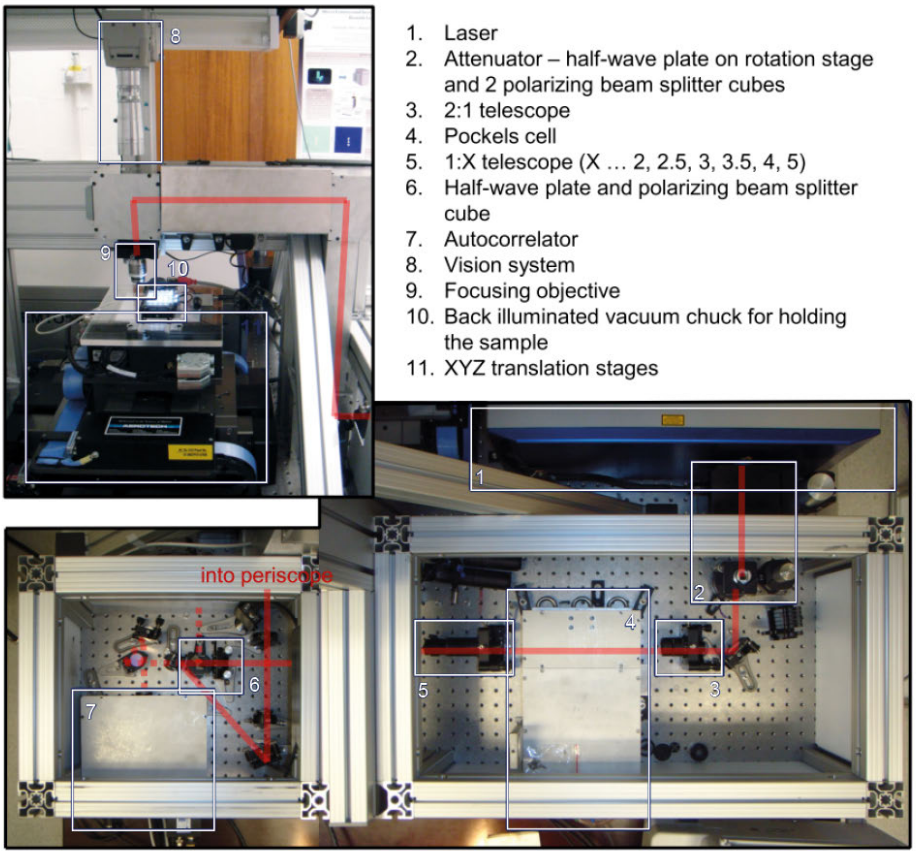

Figure 2.3: Photos of the fabrication setup used for the waveguide inscription. The beam path is indicated by the red line. Images are courtesy of Dr Simon Gross.

Beam delivery system

The output beam of the femtosecond laser has a diameter of two millimetres. It is directed towards an attenuator, which also acts as a periscope to lower the beam height. A reduced beam height enhances the overall stability of the setup. The attenuator consists of a zero order half waveplate (mounted on an Aerotech ADR75 rotation stage) and two polarising beam splitters (PBS). Changing the angle of the wave plate changes the transmittance of the attenuator. In addition, the two PBS enhance the polarisation extinction ratio of the transmitted light. The beam is then directed onto a fixed 2:1 telescope, to reduce the beam diameter from 2 mm to 1 mm, which is necessary to prevent the beam being clipped from the clear aperture of the subsequent Pockels cell. The Pockels cell acts as a pulse picker, which means that it scales down the repetition rate of the laser oscillator by a user-defined integer factor X. The new repetition rate is given by $f_{new} = f_{oscillator}/X$. Variation of the pulse

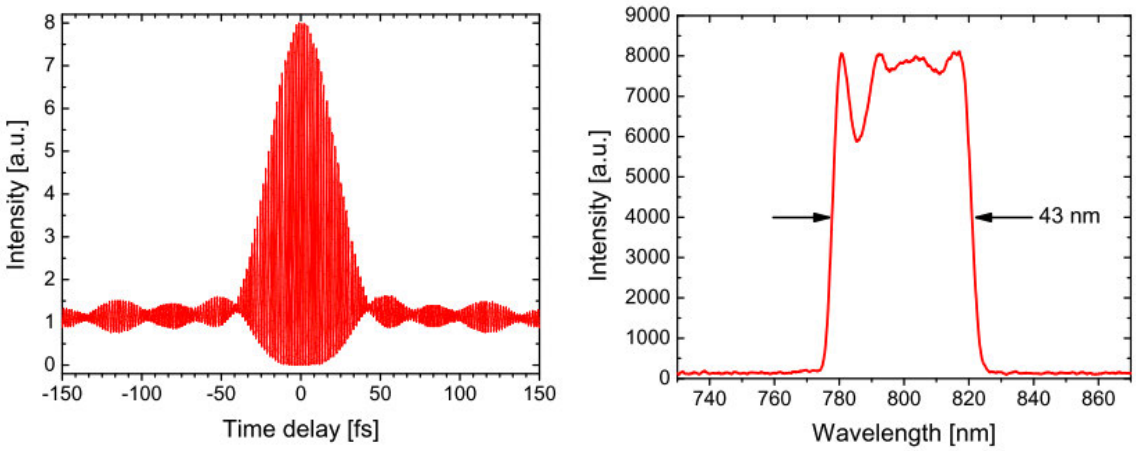

(a) Intensity autocorrelation trace.

(b) Output spectrum.

Figure 2.4: Characteristics of the femtosecond laser source.

repetition rate greatly influences the waveguide writing process [73]. Once the beam passes the Pockels cell, the diameter is increased by another telescope. The magnification factor of this second telescope can be varied to match the NA of the focusing objective used. Depending on the magnification, the beam size can vary between 2 mm and 5 mm. Behind the telescope is an iris, a half waveplate and a PBS. The iris is for alignment purposes, ensuring the beam path is parallel to the optical table. The half waveplate and the PBS can be used to further attenuate the beam. The rotation angle of the half waveplate determines the percentage of the beam that is reflected at the PBS towards a beam dump and the percentage that is transmitted through the PBS. In addition, a detachable mirror behind the PBS can be used to redirect the beam to an autocorrelator to determine the pulse duration. To ensure reproducible results, the pulse duration must be checked each time before waveguide inscription. Without the mirror, the beam is steered through a second iris and a quarter waveplate before entering a periscope. The iris allows the user to align the beam path when misaligned, and the quarter waveplate converts the linear polarised beam to a circular polarised beam. The latter is important, as it results in a higher photonionisation rate and helps avoid nanogratings (at low repetition rates) [74]. It also facilitates homogeneous beam absorption when writing curved waveguides. To bring the beam height to the height of the sample, it is directed through a periscope. A removable power meter is located behind the periscope to measure the average power of the laser. The beam is then reflected via a dielectric mirror through a focusing objective and onto the sample. The objective can be varied depending on the required power density and beam spot size. For alignment purposes, the objective is mounted on a 4-axis translation

stage that allows for tip/tilt and X/Y translation. Above the dielectric mirror, which is highly reflective for the laser wavelength (at 800±25 nm) but transmissive for the visible wavelength region, sits a CCD camera permitting visual alignment of the beam position relative to the sample. The camera is a low-light colour CCD CCTV camera from Sony. A 15 cm f4.5 lens from Wollensak images the focus plane on to the CCD chip. The sample is mounted on a back-illuminated vacuum chuck, which is itself mounted on a mirror mount to allow alignment perpendicular to the beam. An additional camera next to the vacuum chuck is used for adjusting the on-axis alignment of the microscope objective.

Translation stages

The sample is held in position by a vacuum chuck, which is placed on top of an XYZ Aerotech high-precision linear translation stage. The translation stages are crucial for realising uniform and good quality waveguides. In detail, the stage itself consists of two stacked linear motor air bearing stages, an Aerotech ABL-series linear stage for controlling the X and Y axes (100 mm travel range) and an Aerotech WaferMax Z lift stage for controlling the Z axis (5 mm travel range). For precision with sub-micrometre resolution, a servo feedback to the motion controller is used. The stages are fully remote controlled by the Aerotech A3200 software motion controller. They are programmed with a Computer Numerical Control (CNC) code, which enables velocity profiling to generate smooth 3-dimensional trajectories.

Waveguide geometry

The host material defines which driving mechanism can be used to modify the refractive index. Those three mechanisms, which have been introduced earlier in this chapter, are (i) isotropic refractive index change, (ii) birefringent refractive index change, and (iii) refractive index change by void formation. In this work, different host materials were utilised and thus the waveguide geometry was chosen depending on the achievable refractive index change mechanism. The in-house inscribed waveguides were written into zirconium fluoride glass (in particular heavy metal fluoride glass (ZBLAN - ZrF_4, BaF_4, LaF_4, AlF_3, NaF_3). In ZBLAN, the driving mechanism for modifications is an isotropic refractive index change, which is commonly referred to as Type I modification [75]. In yttrium aluminum garnet $Y_3Al_5O_{12}$ (YAG) and strontium hexaluminate $SrAl_{12}O_{19}$ (SRA), the refractive index modifications are driven by voids, which in the literature is referred to as a Type II modification [75].

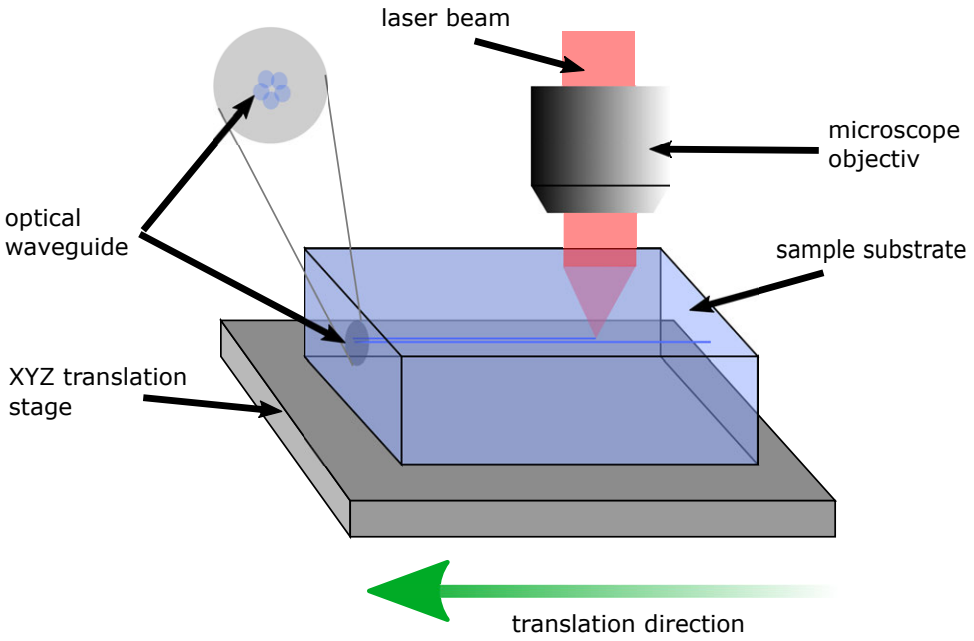

Figure 2.5: Illustration of waveguide inscription by moving the sample across the focused laser beam. The translation speed and repetition rate of the laser determine the pulse-to-pulse overlap.

The waveguides in YAG and SRA were inscribed by another research group (Institut fuer Laserphysik, University of Hamburg, Germany) using a very similar setup.

In ZBLAN, the refractive index change is negative and thus depressed cladding waveguides were inscribed by modifying the area surrounding the core. This was done by moving the sample relative to the stationary laser beam, as illustrated in Fig. 2.5. In Figure 2.6a, a schematic of the modification geometry is depicted from the viewpoint looking at the end face of the sample. In the illustrated example, the depressed cladding is formed by six separate modifications surrounding the core. Each modification is written separately as a line across the length of the entire sample. The modifications (which form the cladding) exhibit a lower refractive index compared to the unmodified core and thus the refractive index profile is very similar to that of an optical fibre. The microscopic image of the optical waveguide is shown in Fig. 2.6b.

In the YAG and SRA, Type I modifications cannot be inscribed due to the crystalline structure of the materials, and the waveguides were therefore written as Type II modifications. Those modifications typically exhibit a decrease in refractive index within the central region and an increase in refractive index in the area surrounding the voids. As shown by Okhrimchuk *et al.* it is possible to inscribe depressed cladding waveguides utilising Type II modifications

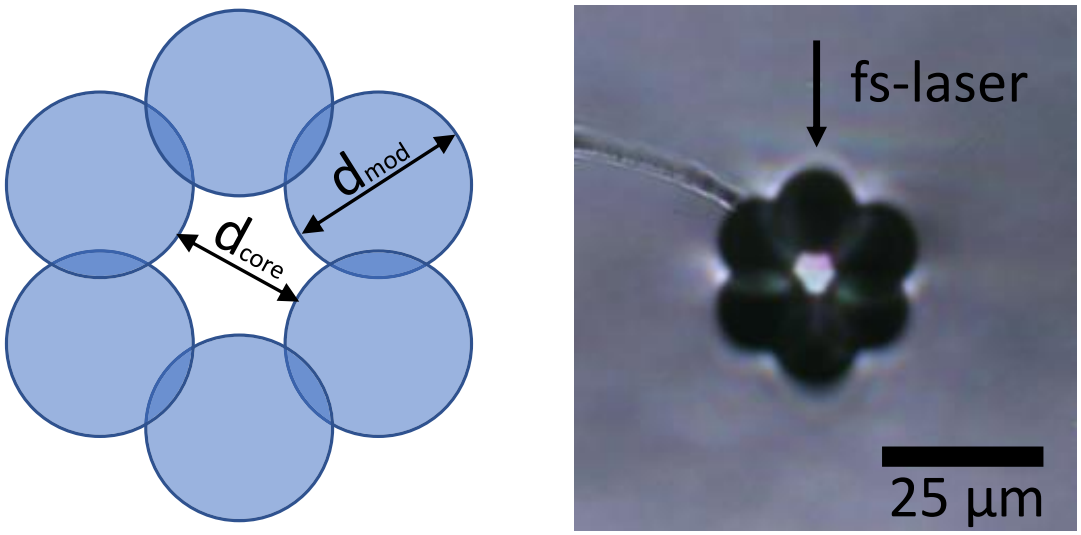

(a) Map of the modifications around the core.

(b) Photo of the resulting modifications.

Figure 2.6: (a) Schematic of a depressed cladding waveguide, which is composed of refractive index modifications surrounding an unmodified core. In (b) a microscope image of the resulting depressed cladding waveguide is shown.

[11]. However, in most publications waveguides are formed by two adjacent damage tracks that form a stress-induced waveguide [76–80]. For that, the sample is translated through a stationary laser beam, as shown in Fig. 2.7a. The cross-section of the fabricated structure is shown in Fig. 2.7b. The laser beam is focused into the material and causes an elliptical damage area. The shape of the damaged area is caused by astigmatism [81, 82] and the shape of the beam waist. Note that the damage threshold for void formation is reached not only within the focus but also above because the intensity is still sufficient. The resulting transverse profile clearly shows the elliptical shape of that area, depicted in Fig. 2.7b. The pressure were induced by void formation leads to a stress field surrounding the void. Depending on the distance between the two damage tracks, a waveguide can be therefore formed between them. The stress induces an increase of the refractive index in the middle area, as shown in Fig. 2.7b (red lines). The stress induced waveguide is highly asymmetric which results in polarisation selective guiding properties.

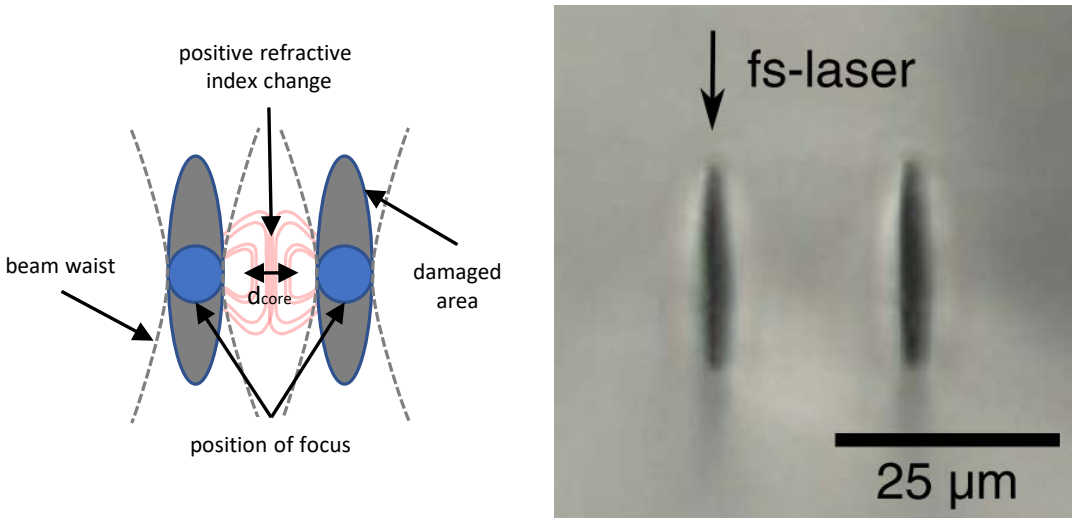

(a) (b)

Figure 2.7: In (a) a schematic of the cross-section of a stress-induced waveguide is shown. The stress induced waveguides are produced by inscribing two adjacent damage tracks. The laser beam is focused into the material and results in an elliptical damage shape. The damaged area causes stress surrounding it, which increases the refractive index (red lines). The core size can be tailored by the separation distance between the two damage tracks. In (b) a microscopic image of the two adjacent elliptical damage profiles is shown [83].

2.2.3 Sample post-processing

Once the waveguide inscription is finished, the next step is grinding and polishing of the end faces. The sample must be placed upright in a jig (PP5 from Logitech – see Fig. 2.8b), which can be realised by using a 'star mount', shown in Fig. 2.8a. On each star mount, six samples can be glued at the same time to one of its precisely right-angled corners. Norland Blocking adhesive, a UV curing glue, was used because it can be readily dissolved using acetone. The thickness of the star is chosen depending on the sample length. A major advantage of employing a star mount is that once one facet of the chip is processed, it can be turned up side down to allow processing of the other facet. First, both surfaces are ground successively using 25 µm grit Al_2O_3 powder (Micro Abrasives Corporation, MA). Then both surfaces are ground using 5 µm grit (Al_2O_3 powder). Finally, the polishing takes place on both surfaces. There is no need to detach the sample during this process, so misalignment errors due to re-gluing are avoided. However, before the sample is attached to the star mount it is sandwiched between slightly larger microscope glass slides to protect the sample from uneven stress. Six additional glass slides are glued onto the outer arms of the star mount (see Fig. 2.8a). Therefore, before grinding/polishing, the end faces of the protective glass slides

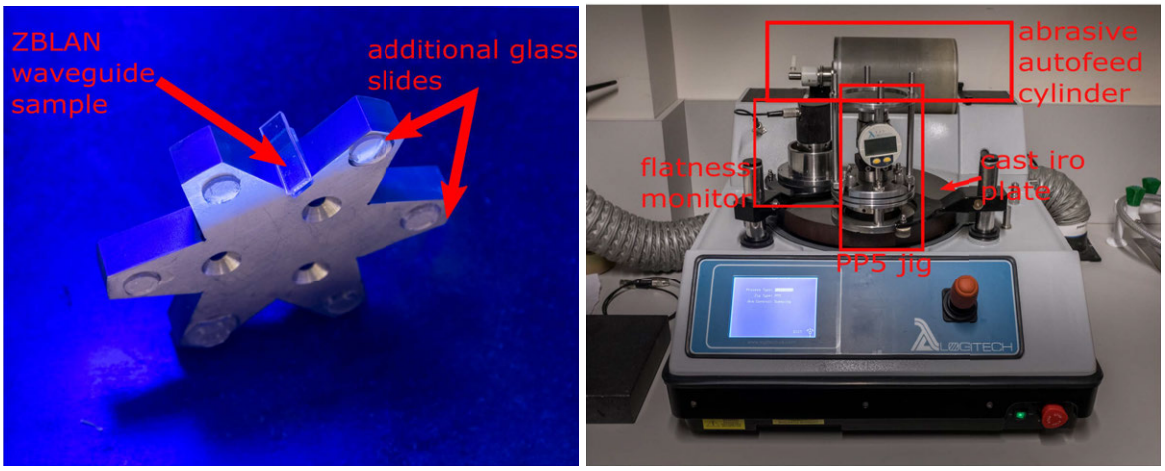

(a) ZBLAN sample glued to the star mount. (b) Logitech PP5 grinding/polishing machine.

Figure 2.8: Photos of tools utilised for grinding/polishing. In (a) a ZBLAN sample is glued to the star mount ready for grinding/polishing. Additional glass slides in the corners of the star need to be ground down before the sample surface touches the grinding plate. This ensures smooth spinning of the jig and evenly distributed stress. In (b) the grinding/polishing machine is shown (Logitech PP5). The jig positions the star mount on the grinding/polishing plate. A flatness monitor ensures even grinding/polishing. In the background a cylinder containing the grinding/polishing solution is mounted.

must be worn down. Once the star mount is attached to the jig, a HeNe laser is used to align the star tilt angle relative to a flat surface. In particular, an interferometric setup was used with the beam reflected back from an unused spot on the puck. The jig allows the user to mount the puck at a particular angle (resolution about one arcmin) and to define the pressure needed for grinding/polishing. Again, the pressure must be chosen carefully to reduce stress that could otherwise result in chipping of the sample. The trade-off, when using low pressure, is an increased processing time.

As a next step, the jig is mounted on a Logitech PM5 grinding/polishing machine (Fig. 2.8b), with auto lapping and automated flatness control. The machine is equipped with 30 cm cast iron plates. Grinding was achieved in two steps, coarse and fine grinding. For coarse grinding a 25 µm grit, dissolved in filtered tap water, was employed. The solution was mounted next to the grinding plates. From there the mixture is dripping onto the plates. The grinding process starts with the rotating plates. After a few tens of micrometres were removed from the chip, the jig was removed to clean the plates and to change to a fine-grained solution, 5 µm grit. The second grinding process is accomplished after another few tens of micrometres, and is followed by a polishing process. For polishing, the original

grinding plate was removed and a dense, non-woven, low-nap porous polyurethane cloth was mounted (Allied High Tech Products Inc., CA). As a polishing solution, an aqueous colloidal silica slurry was used (Ultra-Sol 500S, Eminess Technologies Inc., AZ). It consists of silica particles (80 nm) dissolved in an alkaline solution of pH 9.9 to prevent aggregation.

2.3 Characterisation of laser-inscribed waveguides

The following section covers the methods used to characterise the femtosecond laser-inscribed waveguides. The characterisation is subdivided into three sections: (i) measuring the physical size of the waveguides using a microscope, (ii) quantifying the refractive index profile with a refractive index profilometer, and (iii) characterising the waveguides by measuring their mode-field profile and loss parameters (e.g. propagation losses).

2.3.1 Visual inspection

Femtosecond laser-inscribed modifications can be of the size of a few microns and, depending on the inscription method, are typically pure phase objects. With conventional microscopic methods it is not possible to reveal phase objects, and thus an advanced optical inspection technique is necessary. For that purpose, the method of 'transmission differential interference contrast microscopy' (T-DIC – Olympus IX81) was used to reveal and characterise the waveguides. The idea behind T-DIC is that a phase difference is converted into a change in intensity. For that, a specific optical setup is needed, as depicted in Fig. 2.9. A polariser and a Wollaston prism are positioned in the beam path between the condenser and the light source. The polariser is introduced at a polarisation axis angle of 45° relative to the shear axis of the Wollaston prism. The latter is placed in the front focal plane of the condenser. Once the linear polarised beam passes through the Wollaston prism, the prism introduces a shear (a lateral offset) between the two orthogonal polarised components. In other words, it separates the beam spatially into a sample beam and a reference beam. The condenser focuses those two beams into the sample with the focal points positioned side by side as a result of the introduced shear. In the presence of a material modification (e.g. a waveguide), the sample beam experiences a slightly different refractive index as the reference beam and thus a phase difference between those two beams is introduced. The two beams are collected in the following objective and recombined behind a second Wollaston prism. Note that the second Wollaston prism is exactly the same as the first but reversed. Once recombined, the initial linear polarised beam is elliptically polarised in the presence of a waveguide. The analyser transfers the polarisation state to a intensity state which is then observed by the viewer.

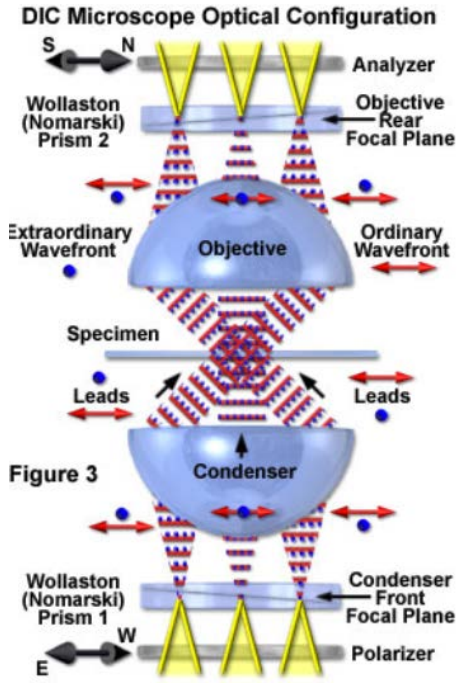

Figure 2.9: Beam path of the microscope (Olympus IX81) utilising a transmission differential interference contrast microscopy setup. Image courtesy of Olympus America Inc.

2.3.2 Refractive index profilometer

The refractive index profilometer (RINCK Elektronik, Germany) is based on the refracted near-field (RNF) method. It is adopted for the purpose of measuring the transverse refractive index profile of optical waveguides [84]. There are several variations of this technique available for the purpose of characterising planar or buried waveguides [85–87]. A schematic of a RINCK device is shown in Fig. 2.10. The probing laser source (1) is positioned behind a sector stop (2) that partially blocks the incoming laser beam. The beam is focused via a microscopic objective onto the end face (6) of the device under test (DUT). The DUT is positioned by a carrier cover slip (4) and a reference glass block (9). Note that all air gaps are filled with a refractive index oil (5) to prevent Fresnel reflections. The focused beam is refracted by the DUT and the angle of the refracted beam changes depending on the refractive index. The amount of light that reaches the detector (8) depends on the refractive index change and the resulting refraction angle. The larger the refractive index change, the more light reaches the detector. Absolute numbers for the refractive index change can be retrieved by knowing the refractive indeces of the bulk sample (without an optical waveguide) and of the reference glass.

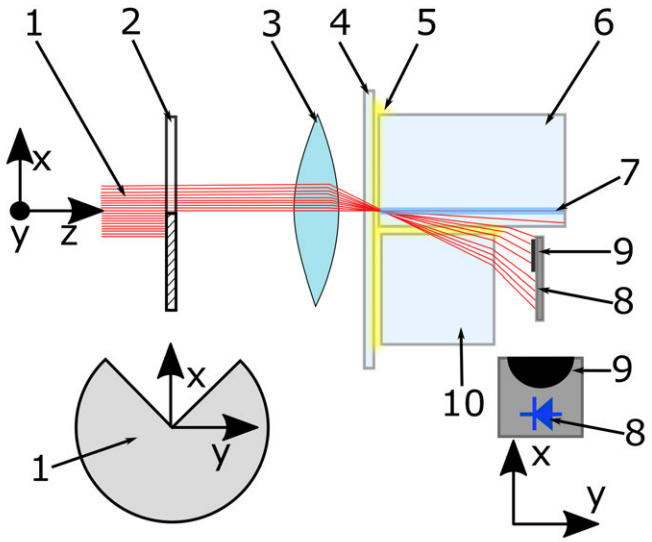

Figure 2.10: Schematic of a refracted near-field profilometer. The probing light beam enters through the left side (1) and is partly blocked by a sector stop (2). The beam is than focused by a microscopic objective (3) through a carrier cover slip (4) and refractive index oil (5) onto the surface of the sample (6). The focused beam transmits through the sample that includes the inscribed waveguides (7) and is collected by the detector (8) which is partially obstructed (9). Note that the sample under test is positioned by being butted against the cover slip (4) and the reference glass block (9).

2.3.3 Mode-field measurement

The setup shown in Fig. 2.11 was used to characterise the laser-inscribed waveguides. It is built around a 6-axis stage (Thorlabs NanoMax 600), which positions an optical fibre, and a 3-axis stage that positions the waveguide sample relative to the fibre. A fibre-coupled amplified spontaneous emission (ASE) light source was employed to characterise the waveguide for different wavelengths inbetween 400 nm and 2000 nm. Depending on which wavelength the waveguides are probed at, the camera in Fig. 2.11 can be modified. To measure the mode-field diameter (MFD), a laser beam is launched via a fibre into one end of the waveguide under test. The opposite end is then imaged to a camera utilising a microscope objective. A 12-bit PCI frame grabber and Wincam software are used to capture and analyse the mode field profiles. To calculate the MFD, the commonly used fitting methods of the $1/e^2$ Gaussian curve or the 4-sigma method based on the second intensity moment were employed. Depending on the expected MFD, an oil immersion objective, either an NPL Fluotar 50x 1.00 NA or a Zeiss Achromat 100x 1.25 NA, was used. Due to different probing wavelengths, each objective had to be calibrated before the actual measurement. For that, a single-mode fibre with known MFD was imaged to the camera and then used for calibration.

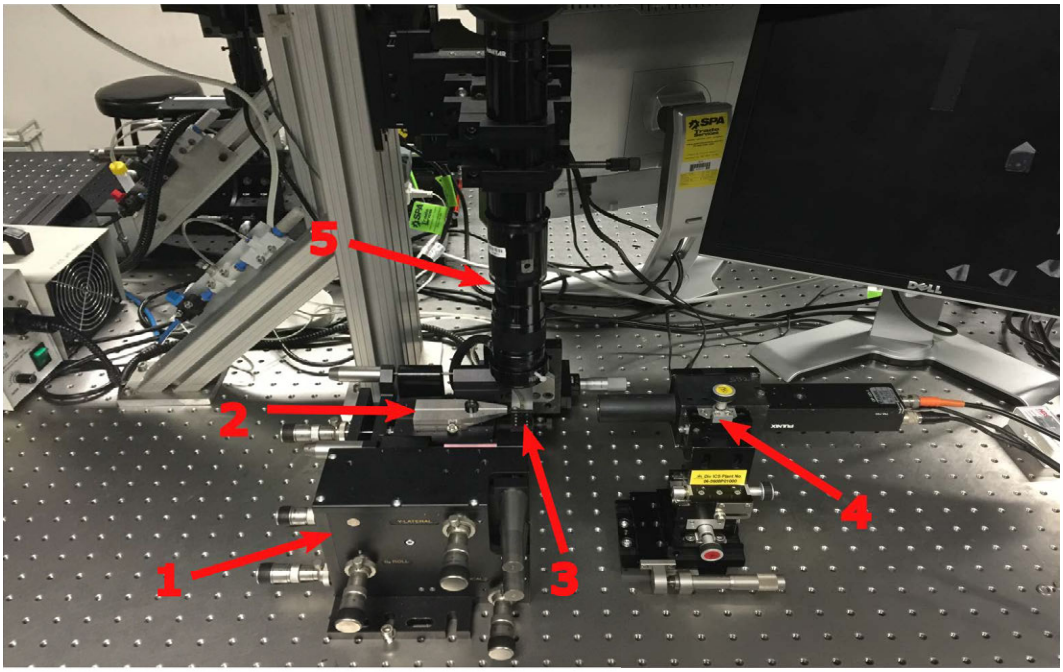

mode-field measurement:

1. fibre alignment stage
2. fibre mount
3. vacuum chuck holding the waveguide chip
4. camera to measure the modefield
5. camera system for alignment of the setup

Figure 2.11: Image of the waveguide characterisation facility for the mode field measurement. A fibre-coupled amplified spontaneous emission source is aligned to couple its optical power (2) into the waveguide under test (3). For alignment purposes a camera (5) is employed above the waveguide sample. The mode field is measured by imaging the end facet of the waveguide sample to a camera (4).

2.3.4 Propagation loss measurement

In general, it is desirable to reduce the losses within the cavity as much as possible when building an efficient laser. For a waveguide laser, one of the loss mechanisms introduced into the cavity is the propagation loss within the guiding structure itself. When inscribing waveguides, it is desirable to keep the propagation loss as small as possible. To measure the propagation losses of the waveguide, two methods are usually employed. One is a fibre-based method that enables measurement of the insertion losses and the coupling losses. The propagation losses can be derived by subtracting the coupling losses from the insertion losses. The second method enables measurement of the propagation losses through a Findley-Clay analysis.

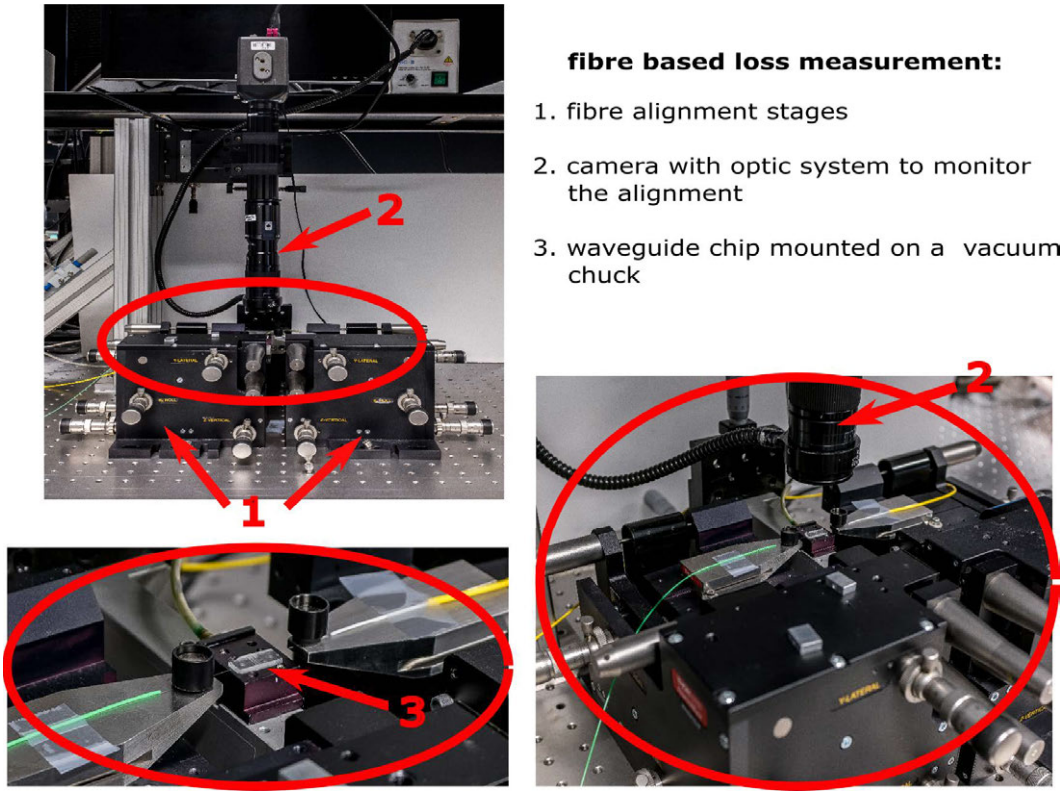

Figure 2.12: Images of the waveguide characterisation facilities for the fibre-based loss measurement. In the top left the whole setup is depicted. The photographs in the bottom left and right show a close up of the circled area. The waveguide chip is mounted on a vacuum chuck (3) and two fibres are coupled to it on each side of the chip. The camera (2) allows for precise alignment via monitor.

Fibre-based loss measurement

The insertion loss (IL_{dB}) can be derived by butt-coupling two fibres to the waveguide chip and measuring the total throughput. It can be summarised by three different loss mechanisms within the waveguide.

$$IL_{dB} = MM_{dB} + FL_{dB} + PL_{dB} \tag{2.3}$$

MM_{dB} refers to the mode mismatch losses between the fibre mode and the waveguide mode at the input and output surface, FL_{dB} resembles the Fresnel losses at each material interface and PL_{dB} equals the propagation loss. The insertion losses can also be calculated by measuring the total transmitted power P_{tr} and the total injected power P_{inj}. Both values are connected to the following formula:

$$IL_{dB} = 10\log_{10}(\frac{P_{tr}}{P_{inj}}) \tag{2.4}$$

The total transmitted power is recorded by measuring the power through the chip when butt-coupling two single-mode fibres to the ends of the waveguide. The injected power is

measured by coupling the same single-mode fibres directly together and filling the air gap in between with an index matching oil to avoid Fresnel reflection. In the absence of index matching oil, Fresnel reflections would take place at each glass-air interface. In general, these are summarised in FL_{dB} and can be calculated for each interface by the following equation:

$$FL_{dB} = -10\log_{10}(\frac{(n_{glass} - n_{air})^2}{(n_{glass} + n_{air})^2}) \tag{2.5}$$

where n_{glass} is the refractive index of the chip under test at the measured wavelength and n_{air} is the refractive index of air. To calculate the mode mismatch losses, it is necessary to evaluate the mode overlap integral as follows:

$$MM_{dB} = -10\log_{10}(\frac{|\int\int_A E_1 E_2^* dxdy|^2}{\int\int_A |E_1|^2 dxdy * \int\int_A |E_2|^2 dxdy}) \tag{2.6}$$

with E_1 and E_2 representing the transverse electric field profiles of the waveguide and fibre respectively. The overlap integral describes the mismatch between the transverse mode profiles when coupling from one mode to another. Special precautions must be taken when measuring the transverse intensity profiles using the camera; one must use an objective with a magnification high enough to fill the available camera pixels sufficiently to reduce statistical error. Furthermore, the background noise within the captured image must be subtracted.

Findley-Clay analysis

Loss mechanisms within a waveguide laser cavity include propagation losses within the waveguide, coupling losses, Fresnel reflection losses and cavity losses at the output coupling mirror. To obtain the overall cavity loss, which summarises all loss mechanisms in a single term (excluding the output coupling losses), the Findley-Clay analysis can be applied [88]. This method is based upon the relationship between cavity losses and threshold gain. At the lasing threshold, the cavity losses equal the gain and the following relationship is true:

$$e^{gl}\sqrt{R}V_R = 1. \tag{2.7}$$

Here, gl_{active} is the small signal gain, R is the reflectivity of the output coupler and V_R is the loss term $V_R = 1 - losses$. Measuring the threshold pump power for different output couplers (different R) and plotting it against $-\ln\sqrt{R}$ results in the characteristic Findlay-Clay

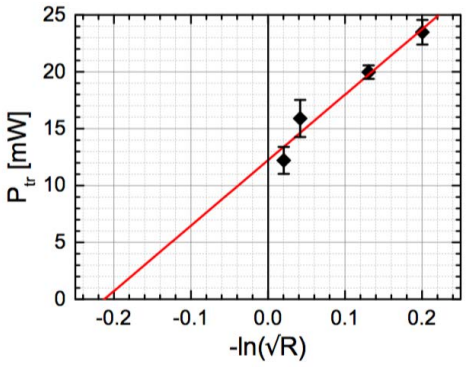

Figure 2.13: Example of a typical Findlay-Clay diagram [35].

diagram. When applying a linear fit to the diagram the intersection with the x-axis results in the loss term $-\ln(V_R)$.

2.4 Mueller matrices for describing optical switching

Throughout this work, the Mueller matrix formalism is utilised to simulate and estimate material parameters of various liquid crystal cells; a brief description is thus given here. Fresnel's wave theory describes diffraction, interference and polarisation of light. Fresnel was able to prove that a propagating optical field consists of two oscillating components, which are commonly known as the two polarisation states. Those two states are defined in a plane transverse to the propagation direction. To present the polarisation states, Fresnel's wave theory was simplified and represented in elliptical coordinates. The equation of an ellipse:

$$\frac{E_x(z,t)^2}{E_{0x}^2} + \frac{E_x(z,t)^2}{E_{0x}^2} - \frac{2E_x(z,t)E_y(z,t)}{E_{0x}E_{0y}}\cos(\delta) = \sin^2(\delta) \tag{2.8}$$

can be visualised and interpreted in form of a polarisation ellipse, as shown in Fig. 2.14a. In Eq. (2.8), E_x and E_y describe the time-dependent field amplitude while the maximum amplitudes in the x and y plane are represented by E_{0x} and E_{0y}. The relative phase is $\delta = \delta_x + \delta_y$, with δ_x and δ_y symbolising the arbitrary phases of each oscillating field within each direction. In Fig. 2.14a, all essential variables to describe the overall polarisation state are shown. Note that the coordinate system is rotated by ψ to represent the electrical field in terms of the maximum and minimum field amplitude. The most crucial polarisation states are the so-called degenerated states: (1) linear horizontal/vertical, (2) linear ±45 deg, (3) right/left circular polarised. With these three states, one can retrieve any possible polarisation

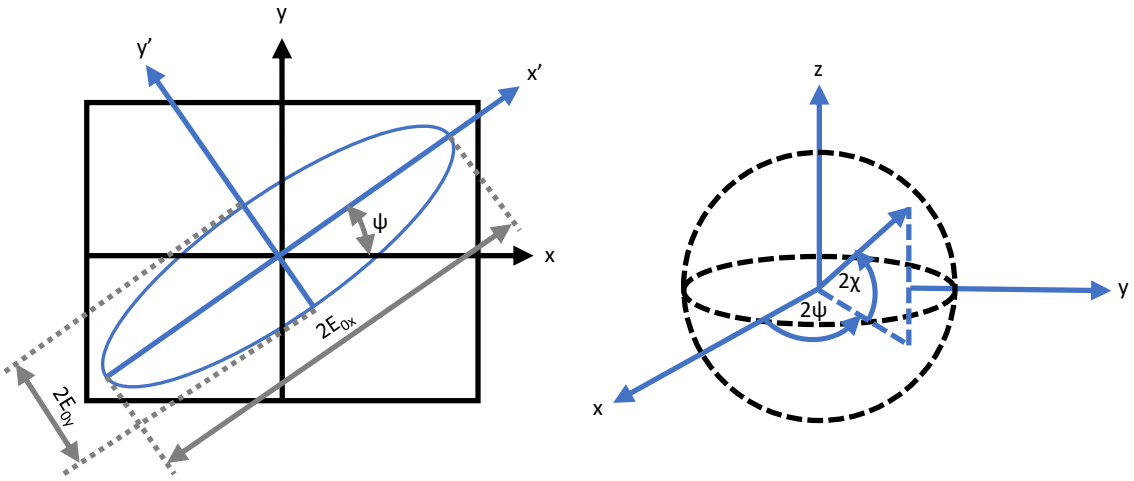

(a) (b)

Figure 2.14: Different illustrations of the polarisation state. In (a) the polarisation ellipse is presented in a rotated coordinate system. Note that this view fails to illustrate the ellipticity angle χ. In (b) the polarisation state is represented within a Poincaré sphere. [89]

state. The polarisation ellipse can adequately be described by the orientation angle ψ and the ellipticity angle χ:

$$\tan(2\psi) = \frac{2E_{0x}E_{0y}}{E_{0x}^2 - E_{0y}^2}\cos(\delta), \qquad 0 \leq \psi \leq \pi \tag{2.9}$$

$$\sin(2\chi) = \frac{2E_{0x}E_{0y}}{E_{0x}^2 - E_{0y}^2}\sin(\delta). \qquad -\pi/4 \leq \chi \leq \pi/4 \tag{2.10}$$

The above equations can be rewritten in trigonometric terms and a new angle, the auxiliary angle α, can be introduced:

$$\tan(\alpha) = \frac{E_{0y}}{E_{0x}}. \qquad 0 \leq \alpha \leq \pi/2 \tag{2.11}$$

A further visualisation technique describes the polarisation state on the surface of a sphere. In Fig. 2.14b, the orientation and ellipticity angle describe the position of the Poynting vector within the sphere. The plane defined by the equator line describes various linear polarisation states. The poles indicate right/left circular polarised light and everything between the poles and equator characterises an arbitrary elliptical polarisation state.

Both methods can be used to visualise the polarisation state for a given moment in time,

but measuring its characteristic values is difficult. Taking the time average of Eq. (2.8) leads to the following equation:

$$\langle E_i(z,t)E_j(z,t)\rangle = \lim_{x\to\infty}\frac{1}{T}\int_0^T E_i(z,t)E_j(z,t)dt, \quad i,j = x,y \tag{2.12}$$

which allows to extract four measurable definitions (Stokes parameters) to describe the polarisation state:

$$S_0^2 = S_1^2 + S_2^2 + S_3^2, \tag{2.13}$$

with

$$S_0 = E_{0x}^2 + E_{0y}^2$$

$$S_1 = E_{0x}^2 - E_{0y}^2$$

$$S_2 = 2E_{0x}E_{0y}\cos(\delta)$$

$$S_3 = 2E_{0x}E_{0y}\sin(\delta).$$

As introduced earlier, $\delta = \delta_y - \delta_x$ describes the relative phase. The first parameter, S_0, is equal to the total intensity of the beam. S_1 characterises the prevalence of horizontal over vertically polarised light. Further, S_2 is a measure of the dominance of linear polarised light at an angle of +45 deg over −45 deg, while S_3 characterises the rotational direction and the degree of circular polarised light. The Stokes parameters can be arranged as a column vector as follows:

$$S = \begin{pmatrix} S_0 \\ S_1 \\ S_2 \\ S_3 \end{pmatrix} = \begin{pmatrix} E_{0x}^2 + E_{0y}^2 \\ E_{0x}^2 - E_{0y}^2 \\ 2E_{0x}E_{0y}\cos(\delta) \\ 2E_{0x}E_{0y}\sin(\delta) \end{pmatrix}. \tag{2.14}$$

The degenerated polarisation states can than be written in the same form, as follows:

$$S_{LHP} = I_0 \begin{pmatrix} 1 \\ 1 \\ 0 \\ 0 \end{pmatrix}, \quad S_{LVP} = I_0 \begin{pmatrix} 1 \\ -1 \\ 0 \\ 0 \end{pmatrix}, \quad S_{L+45P} = I_0 \begin{pmatrix} 1 \\ 0 \\ 1 \\ 0 \end{pmatrix},$$

$$S_{L-45P} = I_0 \begin{pmatrix} 1 \\ 0 \\ -1 \\ 0 \end{pmatrix}, \quad S_{RCP} = I_0 \begin{pmatrix} 1 \\ 0 \\ 0 \\ 1 \end{pmatrix}, \quad S_{LCP} = I_0 \begin{pmatrix} 1 \\ 0 \\ 0 \\ -1 \end{pmatrix}.$$

In this work, a laser cavity is built by making use of a cross-polarised setup. Thus, linear polarised light is propagating through the setup through a polariser in combination with a half and quarter waveplate before being reflected back into itself after passing through a variable waveplate (the liquid crystal). By making use of the Mueller matrices, the polarisation state can be calculated and later used for optimisation using the following matrix equation:

$$S' = M \times S. \tag{2.15}$$

Here, S resembles the initially launched polarisation state and S' is the final polarisation state. The Mueller matrix M is a 4×4 matrix with 16 coefficients, $m11$ to $m44$. For the optical components used throughout this work, there are Mueller matrices available in the literature; these are briefly presented here:

A linear polariser can be described by the matrix M_{POL}:

$$M_{POL}(p_x, p_y) = \frac{1}{2} \begin{pmatrix} p_x^2 + p_y^2 & p_x^2 - p_y^2 & 0 & 0 \\ p_x^2 - p_y^2 & p_x^2 + p_y^2 & 0 & 0 \\ 0 & 0 & 2p_x p_y & 0 \\ 0 & 0 & 0 & 2p_x p_y \end{pmatrix}. \tag{2.16}$$

Where the p_x and p_y values are determined by the orientation of its axis. For example, for a polariser with its transmission axes in x direction, p_x equals 1 and p_y equals 0.

A variable waveplate is described by the matrix $M_{WP}(\alpha, \beta)$:

$$M_{WP}(\alpha, \beta) = \begin{pmatrix} 1 & 0 & 0 & 0 \\ 0 & \cos(2\beta)^2 + cos(\alpha)\sin(2\beta)^2 & \sin(4\beta)\sin(\frac{\alpha}{2})^2 & \sin(2\beta)\sin(\alpha) \\ 0 & \sin(4\beta)\sin(\frac{\alpha}{2})^2 & \cos(2\beta)^2 cos(\alpha) + \sin(2\beta)^2 & -\cos(2\beta)\sin(\alpha) \\ 0 & \sin(2\beta)\sin(\alpha) & \cos(2\beta)\sin(\alpha) & \cos\alpha \end{pmatrix}, \quad (2.17)$$

where the introduced phase delay between the two orthogonal polarisation axes is given by α. For a quarter waveplate, α equals $\pi/2$ and for a half waveplate, α is π. The rotation angle of the waveplate is β. The liquid crystal is treated as a variable waveplate, and thus α depends on the applied voltage.

Finally, the matrix for an ideal 100 % mirror $MMirror$ is as follows:

$$MMirror = \begin{pmatrix} 1 & 0 & 0 & 0 \\ 0 & 1 & 0 & 0 \\ 0 & 0 & -1 & 0 \\ 0 & 0 & 0 & -1 \end{pmatrix}, \quad (2.18)$$

3

Liquid crystal cell

3.1 History

In the late 1880s, Friedrich Reinitzer and Otto Lehmann reported the first observation of what is today referred to as a liquid crystal [90, 91]. They observed a state between a disordered state, common to liquids, and a solid ordered state. It was a finding made when Reinitzer was investigating the purity of a cholesterol-based material by determining the melting points with high precision. During that measurement, Reinitzer discovered that between the solid and the liquid state the material transformed into a cloudy liquid before it assuming a clear crystal state. He also investigated the reversibility of this process, as the material cooled down. The findings were unusual and Reinitzer formed a collaboration with Lehmann, who was an expert in crystal optics at that time.

Nowadays, liquid crystals can be found everywhere in our daily lives. Many commercial electronics rely on them [92–96]; liquid crystal displays in mobile phones and liquid crystals in overhead projectors are just two of their ubiquitous applications [96]. The main characteristic

of liquid crystals is that they undergo an additional phase transition at specific temperatures [97], whereas common materials only exhibit two phase transitions (i.e., from gas to liquid and from liquid to solid). The additional state, called a nematic state, is an anisotropic liquid state [98]. For some substances, there is even a supplementary state in which a lamellar structure is formed, like sheets of paper in a book [98]. The sheets are loosely bound to each other with a degree of freedom to move relative to each other – the so-called Smectic-A phase. In addition, some liquid crystals can have slightly tilted molecules within a lamellar structure, the Smectic-C phase. In fact, there are many more permutations giving rise to distinctive features in various liquid crystals [99].

In this chapter, the fundamental properties of liquid crystal phases are introduced. This knowledge is required to understand the distinct features of the ferroelectric liquid crystal that was used for Q-switching and mode-locking in this work.

3.2 Liquid crystal phases

In general, liquid crystal phases can be divided into nematic and smectic phases. There is a third form, the cholesteric phase [100], but this can be partly described as a nematic phase, and this section therefore concentrates on nematic and smectic phases. Liquid crystalline phases exhibit some degree of orientational and positional order, which are characteristics of a crystalline state. They also show, to some degree, a disordered state, which is a characteristic of liquids. For different sub-phases of the liquid crystal, the nature of the ordering is a primary indicator of the apparent phase.

The ordering is further divided into orientational and positional order. Liquid crystals can have any degree of mixture of those two particular orders but, in general, the ordering lies between the order of solid matter and the disorder of liquids. One can think of liquid crystals consisting of rod-shaped molecules best described by an elliptical cylinder, with the long axis being used to characterise the different phases. Some examples of those characteristics are depicted in Fig. 3.1. In Fig. 3.1a, the molecules show a strong positional order. The degree of a positional order can be described by the tendency of the molecules to sit near their expected position. In the best case, the molecules are constrained to a specific location within a lattice. In Fig. 3.1b the molecules show a positional disorder. Positional and directional

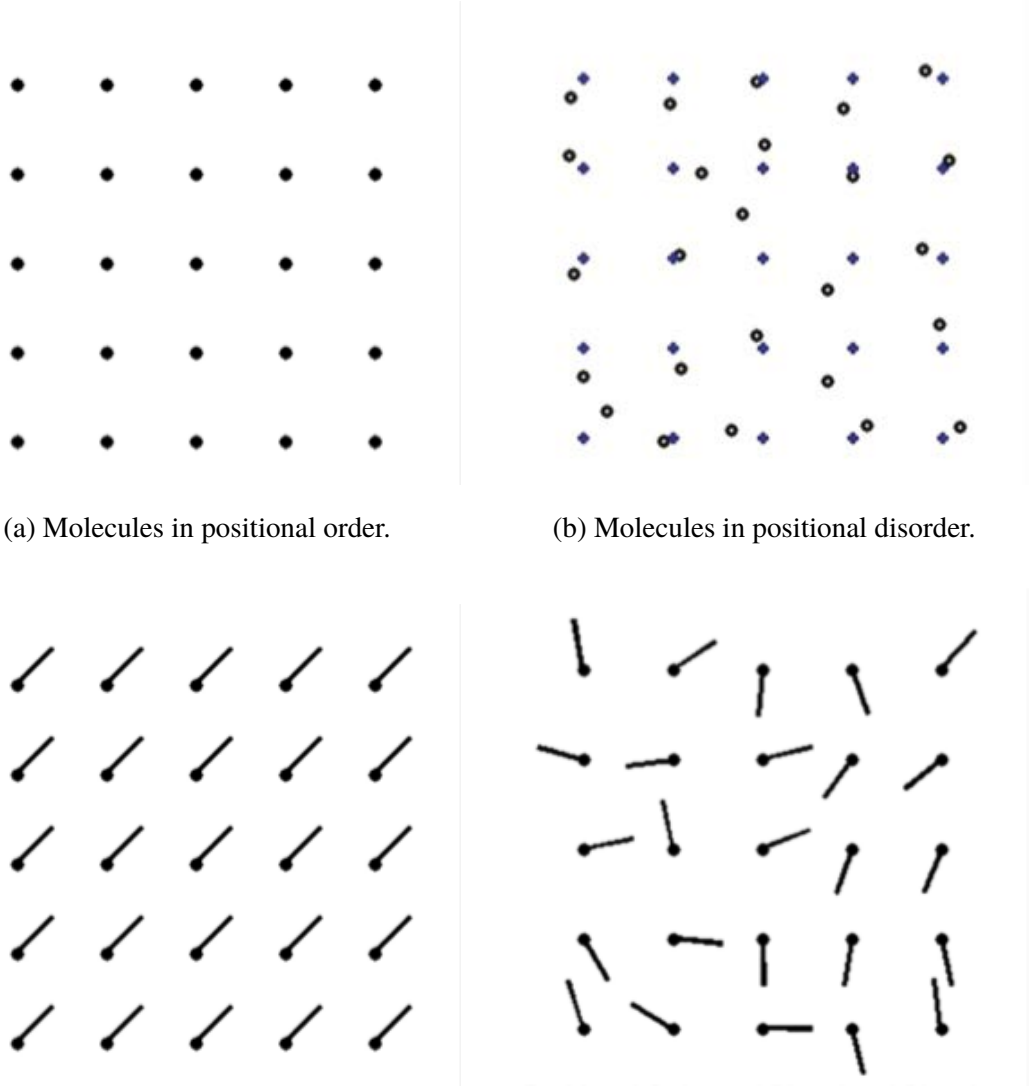

(a) Molecules in positional order.

(b) Molecules in positional disorder.

(c) Rod-shaped molecules in positional and directional order.

(d) Rod-shaped molecules in positional order and directional disorder.

Figure 3.1: The schematic shows a plane across a liquid crystal. Characteristics can be determined by looking at the position pattern, which describes the positional order of the molecules relative to each other. In case of rod-shaped molecules, the characteristics include a directional order of the molecular axis [101].

order is depicted in Fig. 3.1c. The tips of the molecules have a defined position along a grid. Additionally, the long axes of the molecules all point in the same direction. The tendency of the molecules to point in one direction is described as the degree of orientational order. In Fig. 3.1d, an example of positional order and directional disorder is shown. The long axes of the molecules do not show any tendency to line up with their neighbors.

Generally, in the nematic phase molecules show directional order to some extent but not necessarily positional order. That means that the long axes of the molecules tend to line up

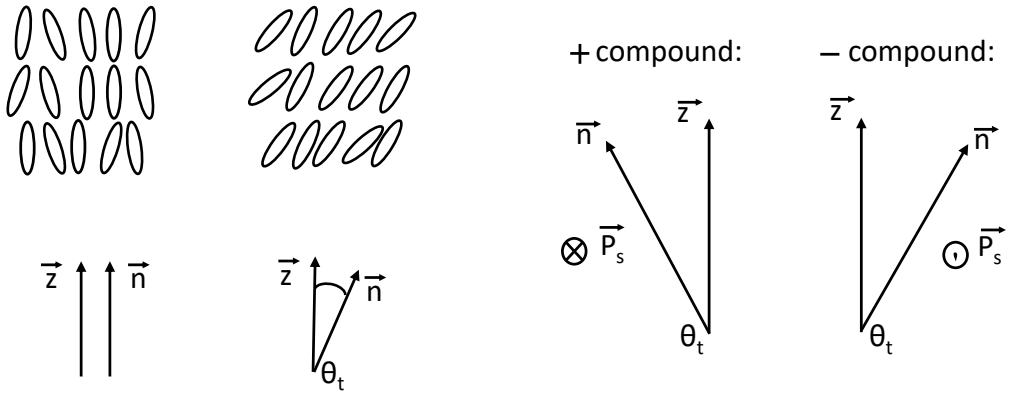

Figure 3.2: Smectic liquid crystals can be divided into several subcategories. In the smectic-A phase, the director $\vec{n}$ is aligned along the molecular axis and its layer normal $\vec{z}$ (left sketch in (a)). The smectic-C phase introduces an angle θ_t to the director $\vec{n}$ relative to the layer normal $\vec{z}$ (right sketch in (a)). In the smectic-C phase the layer normal $\vec{z}$ and the director $\vec{n}$ define the spontaneous polarisation $\vec{P}_s$ of each layer within the liquid crystal. Shown in (b) is an example of switching the applied voltage amplitude from a positive to a negative value. As a result the vector $\vec{P}_s$ flips by 180° [102].

parallel to each other whereas the molecules themselves are scattered within the liquid. On the other hand, the smectic phase exhibits both directional and positional order. The smectic phase can be subdivided into its two most common phases, the smectic-A and smectic-C phase. There are many more phases, with the most recently discovered being the smectic-L phase. A characteristic feature of the smectic phase is that the molecules line up to a lamellar structure consisting of several 1D structures like a stack of paper sheets. The molecules within the layers show a directional and positional order, as shown in Fig. 3.1c. In the smectic-A phase the director $\vec{n}$, pointing along the long molecular axis, is parallel to the layer normal $\vec{z}$ (left sketch in Fig. 3.2a). The smectic-C phase is similar, but in addition introduces an angle, θ_t, between the director $\vec{n}$ and $\vec{z}$ (right sketch in Fig. 3.2a). Furthermore, the smectic phases can consist of or contain non-chiral or chiral compounds, adding different features to the liquid crystal. In the latter, a helical (chiral) structure is mapped out by the director $\vec{n}$. The helix is formed by the director $\vec{n}$ spiralling around the surface normal $\vec{z}$ on a cone shape (Fig. 3.3). In fact, $\vec{n}$ experiences a small relative angle change $\Delta\phi$ from layer to layer. The helical structure is characterised by the periodicity of the helix around the layer normal $\vec{z}$. Thus, a helical pitch p can be introduced. The pitch p is the liquid crystal layer thickness needed for the director $\vec{n}$ winding around the layer normal $\vec{z}$ by 360°. Typical values for p

Figure 3.3: In the helical smectic-C phase of the liquid crystal, the director $\vec{n}$ changes its angle ϕ slightly from layer to layer. The director $\vec{n}$ circulates in a cone shape around the layer normal $\vec{z}$ [102].

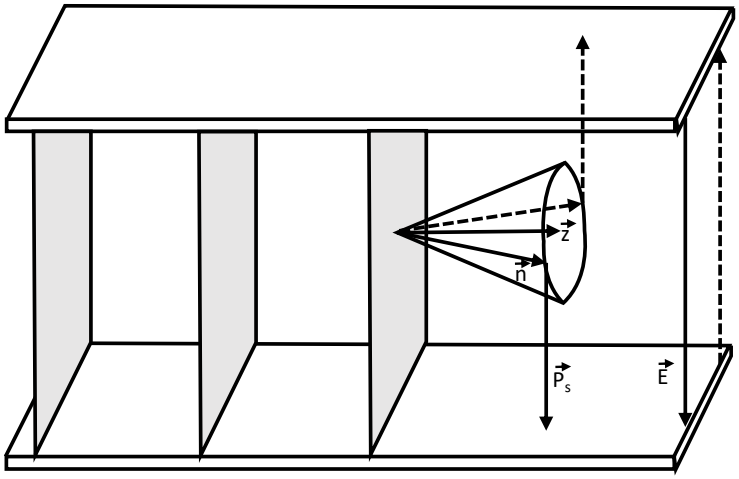

Figure 3.4: Schematic of a liquid crystal sandwiched between two electrodes. Within each layer the director $\vec{n}$ can rotate on a cone shape around the layer normal. The layer normal $\vec{z}$ and the director $\vec{n}$ define the spontaneous polarisation $\vec{P}_s$ [102].

can be as small as 100 nm or up to several micrometres. Another important result of a liquid crystal phase with a chiral component is that it exhibits ferroelectric properties. This gives rise to a spontaneous electrical polarisation, $\vec{P}_s$, as illustrated in Fig. 3.4. The direction of the spontaneous electrical polarisation $\vec{P}_s$ is defined as the cross-product of the director $\vec{n}$ and the surface normal $\vec{z}$. Thus, the electrical polarisation rotates around the surface normal $\vec{z}$. From layer to layer $\vec{P}_s$ experiences a small relative change of the azimuthal angle ϕ, similar to the angular position of the director $\vec{n}$. On a macroscopic scale, this leads to a vanishing average spontaneous electrical polarisation. On a microscopic level, taking into account only a few layers, it results in a small polarisation. Note that the angle θ_t and the spontaneous electrical polarisation are temperature dependent. The Landau theories give a more detailed description of this behaviour. When an external electric field $\vec{E}$ perpendicular to $\vec{z}$ is applied, it causes a torque to the spontaneous polarisation vectors $\vec{P}_s$. As a result, the helical structure within the smectic-C layers distorts and the spontaneous polarisation vectors $\vec{P}_s$ tend to align with the external field vector $\vec{E}$. For small electric fields, $E \ll E_{crit}$, this deformation produces a gradual change in the optical properties and in particular a rotation of

the crystal axes proportional to the strength of the external field. Note that, E_{crit}, is a material specific constant which will be discussed in greater detail later in this chapter. This mode of operation is called Deformed Helix Ferroelectric (DHF) [103–105]. For strong external fields, $E \geq E_{crit}$, the director $\vec{n}$ is free to move on a cone shape around the layer normal $\vec{z}$, there are only two possible positions on the outer cone ring for $\vec{n}$. Those two positions are defined by the angle θ_t, as illustrated in Fig. 3.2b. Generally, θ_t defines the liquid crystal axis when a voltage is applied. When switching the applied voltage between a positive and negative value, the liquid crystal axis changes by $2\theta_t$. Changing the axis between those two states is a feature used commonly in surface-stabilised ferroelectric liquid crystal cells. A helical unwinding is desired and can be generated without an external field applied. This can be achieved by introducing a regular surface structure between the liquid crystal layer and the electrode. Therefore, a thin polymer layer – commonly referred to as an alignment layer – is added and the polymer chains are partially aligned by evaporative, chemical or rubbing techniques [101]. The outer layers of the liquid crystal line up with the directional order given by the alignment layer; thus, it is possible to reliably control the overall alignment of the liquid crystal. In general, that means that a surface alignment layer unwinds the outer molecules by redirecting them in the plane of the alignment layer. As a result, the spontaneous polarisation vector is favoured only in the direction perpendicular to the alignment layer. An external field will force all the local polarisation vectors towards one direction in a steady state. Once the external field is removed, the polarisation vector direction will remain. In this way it is possible to switch between two steady states with the polarisation vector pointing upwards or downwards. However, when the liquid crystal layer is thicker than a few micrometres, the alignment layer only defines the boundary conditions of the liquid crystal cell. Throughout this work, the liquid crystal layer thickness ranges from 3.3 µm to 9.0 µm. The purpose of the alignment layer is thus to set the boundary conditions of the outermost region of the liquid crystal layer.

3.3 Liquid crystals for optical switching

An essential characteristic of liquid crystals is their voltage-controllable birefringence. Liquid crystals can be described in optical terms as anisotropic media. That means their refractive index strongly depends on the propagation direction and the incident polarisation of light. An

incoming ray of light is split into its two orthogonal polarisation states when travelling through a birefringent medium. Each part sees a different refractive index and, thus, the two rays travel on different paths when incident at an angle relative to the liquid crystal axes. A double image forms after the propagation through the medium, a phenomenon commonly known as double refraction, which is caused by birefringence. Birefringent media are subdivided into uniaxial materials and biaxial materials. Uniaxial materials are characterised by one crystal axis. A polarised beam with its polarisation axis perpendicular to this axis sees a refractive index n_o (o for ordinary). Light with its polarisation axis in the direction of the crystal axis is governed by a different refractive index n_e (e for extraordinary). Those two refractive indices describe the principal axis of the crystal. More complex are biaxial materials, which are characterised by three refractive indices n_a, n_b and n_g.

Liquid crystals can be described as uniaxial materials and thus are characterised by an ordinary and an extraordinary refractive index, n_o and n_e respectively. Applying an electric field across a liquid crystal results in a refractive index change Δn. As described earlier, an incident ray of light will see two different refractive indices depending on its initial polarisation state with respect to the liquid crystal axis. The two orthogonal polarisation components will pass the material with different phase velocities. This results in a phase retardation (α) depending on the thickness of the liquid crystal layer (d) and the applied electrical field (E) across the liquid crystal layer:

$$\alpha = \frac{2\pi\Delta n(E)d}{\lambda}. \tag{3.1}$$

Here λ is the wavelength of the beam travelling through the liquid crystal layer and Δn is the difference between the ordinary and extraordinary refractive index, $\Delta n = n_o - n_e$. Its dependence on E will be discussed later in greater detail. The overall introduced phase retardation in Eq. 3.1 is similar to the one introduced by common waveplates. Waveplates make use of birefringent media and, depending on the relative angle of the optical axis to the polarisation axis of the incoming beam, modify the beam's polarisation state. For example, a quarter waveplate introduces a phase retardation of $\lambda/4$ to transform an incoming linear polarisation into a circular or elliptical polarisation. In the case of liquid crystals, it is possible to change the phase retardation by adjusting the thickness (d) or the applied electric field (E), thus acting as a voltage-controlled retardation plate. In nearly all commercial

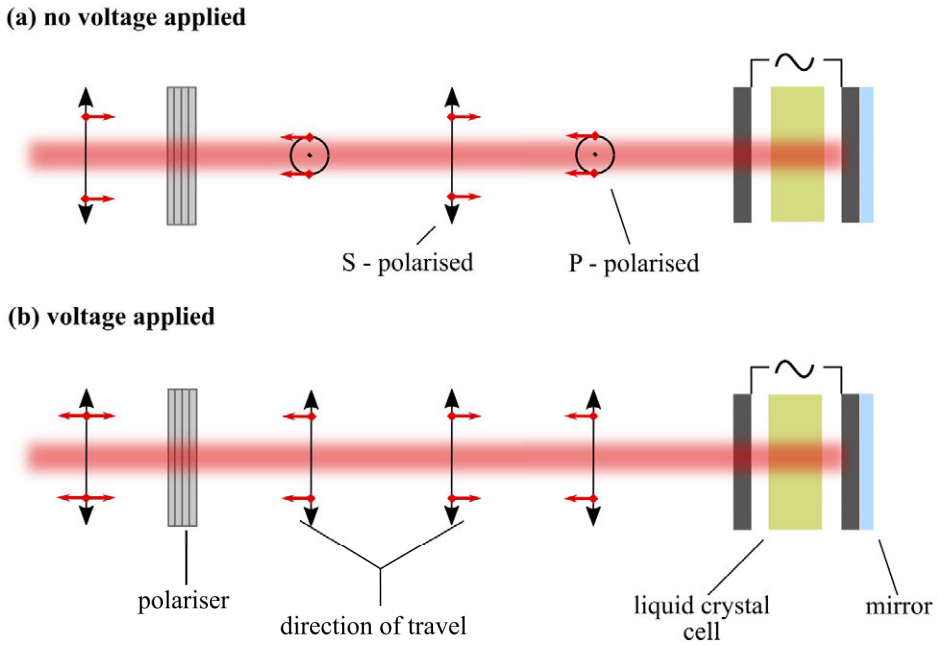

Figure 3.5: Schematic setup of the liquid crystal cell used as an optical switch. Reflective cross-polarised setup: the liquid crystal is placed between a polariser and a mirror. If there is no voltage applied (a) the polarised beam will be blocked by the polariser on its way back. When a voltage is applied (b) the beam is transmitted through the polariser on its way back. Note that the liquid crystal thickness must be optimised in order to introduce a phase retardation of $\lambda/2$ when no voltage is applied.

applications that utilise liquid crystals by switching them between two states, they are placed in a cross-polarised setup. The most common configuration is to place a polariser before and behind a liquid crystal cell; whereas in a double-pass reflective setup, a single polariser and a mirror are used. The reflective setup is the most suitable for utilising the liquid crystal as an intracavity loss modulator, as shown in Fig. 3.5. The liquid crystal is aligned to introduce a phase retardation of $m \cdot \lambda/2$ with $m = 0, 1, 2, 3, \ldots$. The initial alignment can be done either by changing the thickness of the liquid crystal layer or the relative angle between the incoming polarisation axis and the axis of the liquid crystal. That way, the reflected beam is blocked by the polariser on its way back (see the top schematic in Fig. 3.5). For the second state, a voltage is applied across the liquid crystal cell, introducing a different phase retardation. Ideally the applied voltage is chosen to introduce a phase retardation of $m \cdot \lambda$ (on a double pass) with $m = 1, 2, 3, \ldots$. As a result, the beam is fully transmitted on its way back through the polariser, as illustrated in the bottom schematic in Fig. 3.5. In general, two effects account for the switching process within a cross-polarised setup: (i) the phase retardation due to birefringence and (ii) the polarisation axis rotation.

Utilising the Mueller Matrices formalism, one can derive the overall performance of a variable waveplate, such as the liquid crystal cell, in a cross-polarised setup. For the mathematical approach shown here, one must multiply the transformation matrices for each element in the order in which that element is encountered when a beam enters from the left (in Fig. 3.5). The following transfer matrix describes the fraction of the beam that is absorbed at the polariser in Fig. 3.5 and would be transmitted in the later setup shown in Fig. 3.7. Note that the various transformation matrices for each element, e.g. polariser, are summarised in Chapter 2.4. Following the beam path, the overall transformation matrix can be expressed by successively multiplying the individual matrices:

$$M = \mathrm{MPol}_{\mathrm{horizontal}} \times \mathrm{MWP}(\alpha, -\beta) \times \mathrm{MMirror} \times \mathrm{MWP}(\alpha, \beta) \times \mathrm{MPol}_{\mathrm{vertical}} \tag{3.2}$$

As a result, the overall transfer matrix is:

$$M = \begin{pmatrix} \frac{1}{2}\sin(\alpha)^2\sin^2(2\beta) & \frac{1}{2}\sin(\alpha)^2\sin^2(2\beta) & 0 & 0 \\ -\frac{1}{2}\sin(\alpha)^2\sin^2(2\beta) & -\frac{1}{2}\sin(\alpha)^2\sin^2(2\beta) & 0 & 0 \\ 0 & 0 & 0 & 0 \\ 0 & 0 & 0 & 0 \end{pmatrix}. \tag{3.3}$$

Here, α is the phase retardation introduced by the birefringence (see Eq. (3.1)), and β is the rotation angle of the liquid crystal. The rotation angle is measured relative to the polarisation state of the incoming beam. If the beam entering the setup is horizontally polarised then the resulting optical power measured after the cross-polarised setup can be calculated by multiplying the transfer matrix with the scalar of the horizontally polarised beam (S_{LHP}):

$$M \times S_{LHP} = \begin{pmatrix} \sin^2(\alpha)\sin^2(2\beta) \\ -\sin^2(\alpha)\sin^2(2\beta) \\ 0 \\ 0 \end{pmatrix}. \tag{3.4}$$

Thus, the throughput of the cross-polarised setup becomes:

$$R_{\perp} = \sin^2(\alpha)\sin^2(2\beta). \tag{3.5}$$

with $\alpha = 2d\Delta n/\lambda$ and β the angle between the incident linear polarised light and the axis of the liquid crystal cell. This equation describes the general case with no voltage applied to the liquid crystal cell. When applying a voltage, the first term describing the influence of birefringence will change, as well as the second term, describing the relative angular position of the liquid crystal axis with respect to the polarisation axis. Following the approach from Brodzeli *et al.* [106] it follows for Δn:

$$\Delta n \approx \Delta n_m \Big[1 - \frac{3}{2}\sin^2\theta_t + \frac{2+\tan^2\theta_t}{8} \frac{\sin^2(2\theta_t)}{1-\frac{3}{2}\sin^2\theta_t} \frac{\alpha_E^2}{4} \Big]. \tag{3.6}$$

As mentioned by Brodzeli *et al.*, this approximation is valid for low applied fields $\alpha_E << 1$ and a small overall change in birefringence Δn compared to the average refractive index $n_m = (n_o + n_e)/2$. Here, θ_t is the characteristic tilt angle defined by the liquid crystal material composition, while Δn_m is the birefringence introduced by the liquid crystal itself ($\Delta n_m = n_e - n_o$). The material property α_E depends on the applied electric field and can be expressed in terms of the Goldstone susceptibility of the helical structure [106]:

$$\alpha_E = 2\epsilon_0 \frac{\chi_G}{P_s} E = \frac{\pi^2}{16} \frac{E}{E_{crit}}. \tag{3.7}$$

Here, ϵ_0 is the vacuum permittivity and χ_G is the Goldstone susceptibility of the helical structure. The spontaneous polarisation of the liquid crystal is described by P_s. The electric field E_{crit} needed to fully unwind the helix across the liquid crystal cell is a characteristic of the specific liquid crystal composition and its layer thickness. Additionally, the second term in Eq. (3.5) β changes by a small angle Ω, which is a function of the applied electric field. The angle β thus changes to a modified angle $\beta' = \beta - \Omega$ when an external field is present. By using the same approximations for Ω as mentioned above, it follows [106]:

$$\Omega(\alpha_E) \approx \frac{\sin(2\theta_t)}{1-\frac{3}{2}\sin^2\theta_t} \frac{\alpha_E}{4}. \tag{3.8}$$

Putting Eqs. (3.6), (3.7) and (3.8) into Eq. (3.5) leads to a modified version of the latter that describes the overall behaviour of the liquid crystal cell in a cross-polarised setup with an applied electric field [106]:

$$L(E) = R_\perp(E) = \sin^2\left[\frac{2\pi}{\lambda} d\Delta n(E)\right] \sin^2[2\beta'(E)]. \tag{3.9}$$

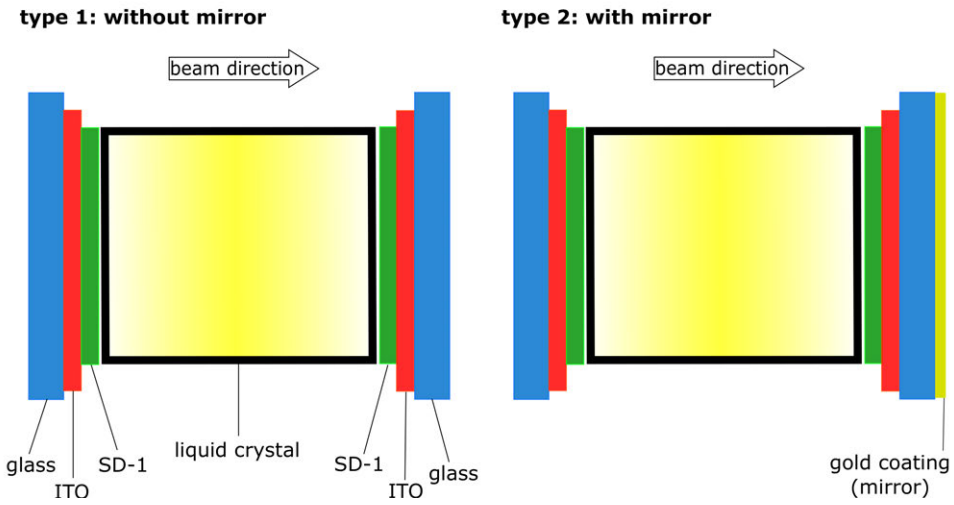

Figure 3.6: Schematic of the liquid crystal cell (sideview). The liquid crystal layer is sandwiched between two ITO electrodes, each with a deposited SD-1 alignment layer on it. The ITO layers are deposited on ordinary microscope glass slides (soda-lime-silica glass). There are two types of liquid crystal cells throughout this work: type 1 has a mirror coated to the back, type 2 has a gold layer that acts as a mirror coated to the back.

This formula represents the losses L introduced into the cavity by the liquid crystal. Note that, as mentioned by Kiselev *et al.* [107], the Goldstone susceptibility strongly depends on the shape and frequency of the applied voltage, as well as the design parameters such as the thickness and operating temperature of the cell.

3.4 Characterisation

Throughout this work the liquid crystal composition used was FLC 576 [107], provided by the P. N. Lebedev Physical Institute of Russian Academy of Sciences. The liquid crystal composition (FLC 576) exhibits a helical pitch of P = 200 nm [108] and the phase transition from the smectic-C to the smectic-A phase is around 65 °C and the smectic-A to the isotropic transition is around 75 °C. The liquid crystal cell was build by Zedelef Pty Ltd. A schematic of the liquid crystal cell is shown in Fig. 3.6. From left to right, the liquid crystal cell consists of: glass substrate (soda-lime-silica glass), ITO layer, SD-1 layer (the alignment layer), liquid crystal (FLC 576), SD-1, ITO layer and a second glass substrate. Two types of cell were utilised during this study, one with a deposited gold mirror coated to the back of the cell (on the back of the glass slide) and another without a mirror coated to the back. For both cell types, three different liquid crystal layer thicknesses were used: (i) 3.3 µm, (ii) 5.0 µm and (iii)

9.0 µm. In the first part of this section, the material parameters of the liquid crystal cell were characterised (Δn, θ_t, E_{crit}) using a Yb:YAG laser source (λ = 1030 nm). In the second part, the intracavity switching capabilities were investigated at several probing wavelengths. The reflectivity and transmission were determined, in addition to the modulation depth for different liquid crystal layer thicknesses, applied voltage amplitudes and modulation frequencies.

A general comment: It has been shown that liquid crystals can exhibit very high optical nonlinearities and director axis reorientation which can initiate self-optical switching as described in [109]. However, such a laser induced optical switching effect, commonly reported in the nematic phase (in a cross polarised setup), as discussed in [110–115] was not observed within this work and thus the optical modulation was best described by Eq. (3.9).

3.4.1 Experimental determination of Δn

The birefringence Δn was measured in a cross-polarised setup, as shown in Fig. 3.7a. Note that in Fig. 3.7a a polarising beam splitter was utilised, instead of a thin film polariser as shown in Fig. 3.5. This modified setup allows measurement of the fraction of the beam that would be absorbed within a thin film polariser, and is thus preferable for characterisation purposes. To maintain the position of the beam on the liquid crystal cell, a half waveplate was added to the setup. Instead of rotating the liquid crystal cell itself, the half waveplate was rotated. Rotating the half waveplate by an angle β_1 is the same as changing the rotation angle of the liquid crystal cell by $2\beta_1 = \beta_2$. In the absence of an external electric field ($E = 0$), Eq. (3.9) simplifies to:

$$L = R_{\perp} = \sin^2\left[\frac{2\pi}{\lambda} d\Delta n\right] \sin^2[2\beta]. \tag{3.10}$$

Note that when no external field is applied, Eq. (3.6) simplifies to:

$$\Delta n \approx \Delta n_m \left[1 - \frac{3}{2}\sin^2\theta_t\right]. \tag{3.11}$$

Measuring the transmission of the cross-polarised setup for variable rotation angles ($\beta = \beta_1$) of the half waveplate results in a sine function that exhibits a specific amplitude that is characteristic of the liquid crystal layer thickness. The sine function can be fitted utilising Eq. (3.10). The half waveplate rotation angle β is changed from 0 to 180° (which is equivalent to changing the rotation angle of the liquid crystal cell from 0 to 360°), while Δn is kept variable. Only specific values for Δn result in a good fit as illustrated in Fig. 3.8. In Fig. 3.8,

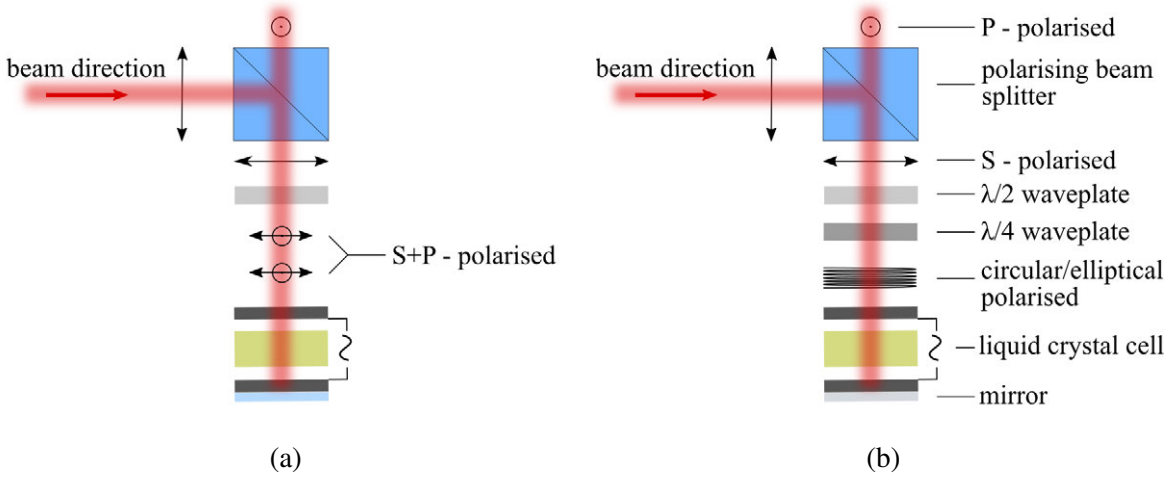

Figure 3.7: Schematic drawing of the cross-polarised setup used. The additional wave plates help to align the setup for maximum performance without varying the beam position on top of the liquid crystal cell. (a) An additional $\lambda/2$ wave plate is introduced in order to prevent the beam from changing the position on the liquid crystal when aligning it for the right angle. (b) An additional $\lambda/4$ wave plate to account for a mismatched cell thickness. With the two wave plates the setup is aligned for maximum through-put when no voltage is applied.

the experimentally measured functions (crosses) for a 3.3 µm and 9.0 µm cell are depicted respectively. Note that the transmitted power (y-axis) describes the power that is transmitted through a cross-polarized setup which is thus proportional to the cavity losses. The state at which the gain medium is pumped and the Q-switch prohibits the pulse build-up is indicated by high a transmission through the cross polarised setup. In Fig. 3.8a it can be seen that this is almost 100 %, i.e. the crystal does have an excellent hold-off. The minimum transmission through the cross polarised setup indicates the low resonator loss state, which is directly related to how much energy is coupled to the Q-switch pulse. The best fits (solid curve) using different values for Δn resulted in three possible values: for (a) $\Delta n_1 = 0.063$, $\Delta n_2 = 0.098$ and $\Delta n_3 = 0.225$, and for (b) $\Delta n_1 = 0.074$, $\Delta n_2 = 0.104$ and $\Delta n_3 = 0.132$. Those results were compared with published work (using the same liquid crystal composition FLC 576): in Ref. [108] $\Delta n = 0.111$ with $\theta_t = 35°$ and in Ref. [106] $\Delta n = 0.127$ with $\theta_t = 32°$. The closest value that was retrieved experimentally here is $\Delta n_2 = 0.098$ for the 3.3 µm and $\Delta n_2 = 0.104$ for the 9.0 µm thick liquid crystal layer. Ambiguity in the results between several possible values for Δn can be avoided by introducing an additional quarter waveplate to the cross-polarised setup. The mathematical description is retrieved by using the Mueller Matrix formalism in the same manner as described above. Each optical element in Fig. 3.7b is added in the order

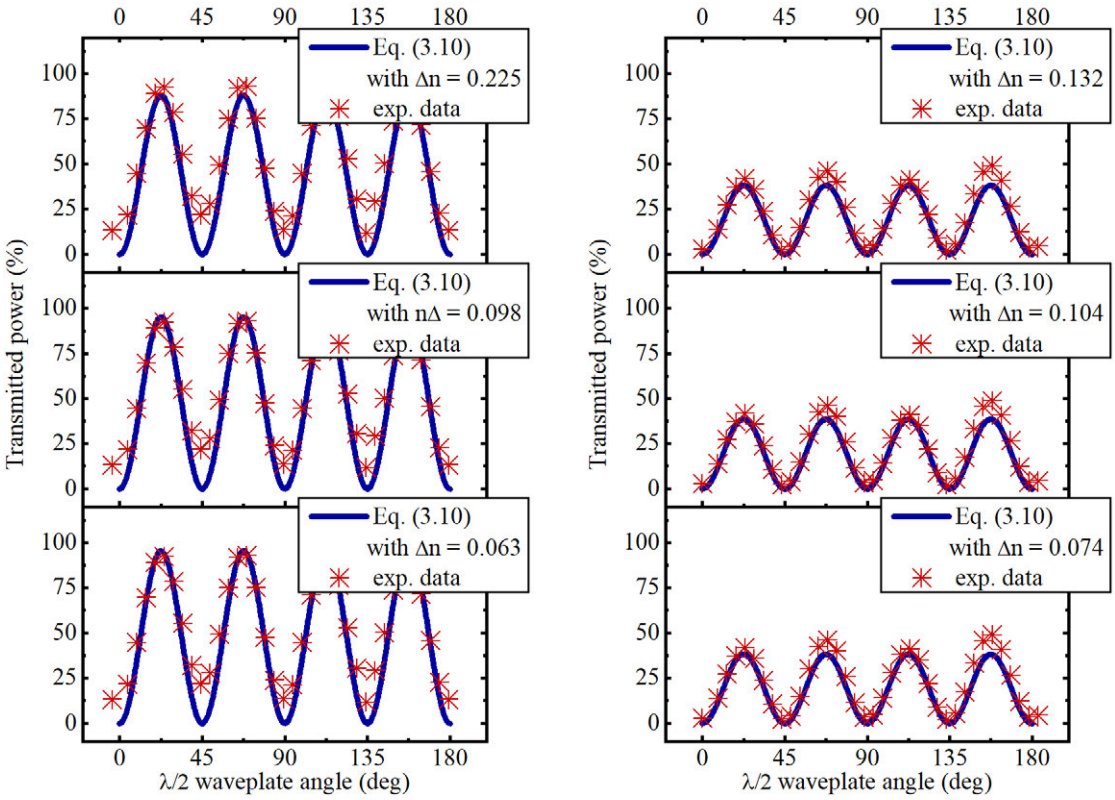

(a) Layer thickness: 3.3 µm.

(b) Layer thickness: 9.0 µm.

Figure 3.8: Experimental results measured using different layer thickness for the liquid crystal in a cross-polarised setup. The transmitted power was recorded as a function of β (rotation angle of $\lambda/2$ wave plate). The dotted lines indicate the best fit using Eq. (3.5) with different values for Δn.

it is encountered. As a result, the equation for the transfer matrix is:

$$L = R_{\perp} = \left(\cos\left[\frac{2\pi\Delta n d}{\lambda}\right] - \cos\left[2\beta\right]\sin\left[\frac{2\pi\Delta n d}{\lambda}\right]\right)^2 \sin\left[2\beta\right]^2. \tag{3.12}$$

Note that this equation presents a special case, where the quarter waveplate is introduced at an angle of 45°. According to the Mueller transfer matrix, when using the quarter waveplate at 45° and rotating the half waveplate by $\beta = 360°$, the resulting function for each prior experimentally retrieved Δn should be different. In Fig. 3.9 the result of the measurement utilising a half and a quarter waveplate within the cross-polarised setup is shown. While the quarter waveplate rotation angle was kept at 45°, the half waveplate was rotated from 0 to 360°. The measurements were taken for the cells utilising a 3.3 µm and a 9.0 µm thick liquid crystal layer. In Fig. 3.9, the experimentally retrieved data is fitted by using the prior retrieved data for Δn_1, Δn_2 and Δn_3 in Eq. (3.12). As illustrated in Fig. 3.9, only $\Delta n_2 = 0.098$ for the 3.3 µm and $\Delta n_2 = 0.104$ for the 9.0 µm thick liquid crystal layer result in a good fit; thus,

these values will be used throughout this work.

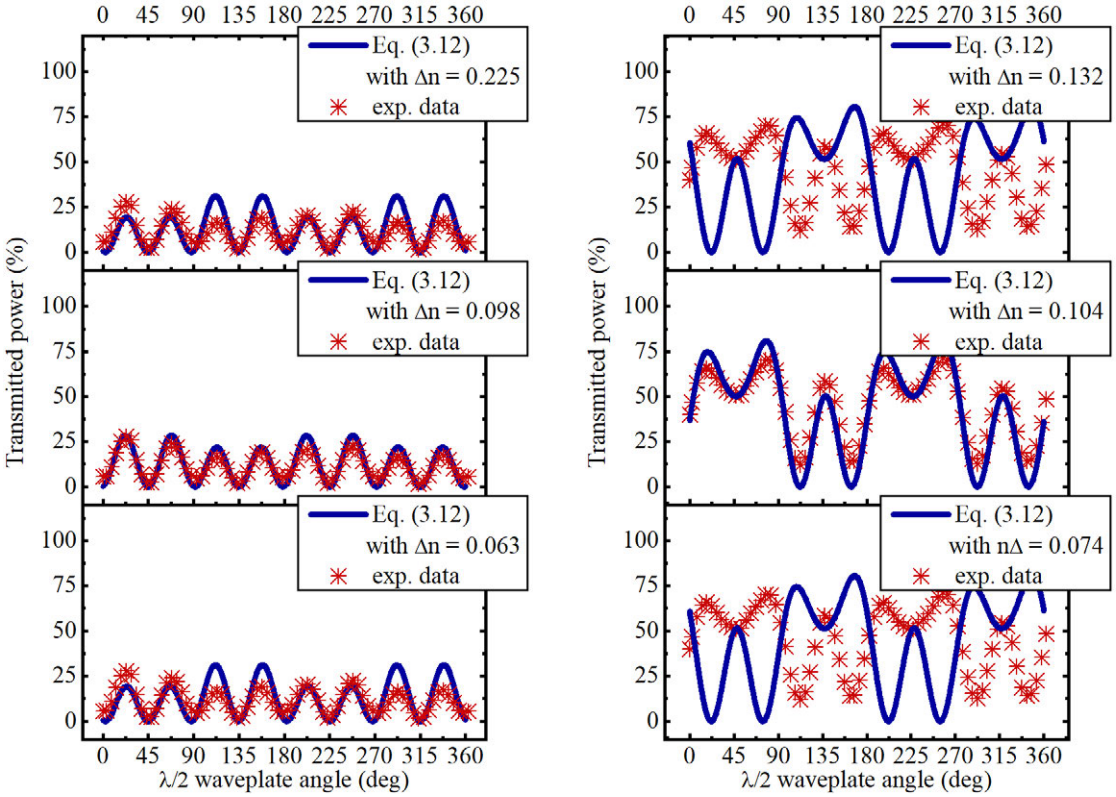

(a) Layer thickness: 3.3 μm.

(b) Layer thickness: 9.0 μm.

Figure 3.9: Graph of the transmitted power as a function of the half waveplate rotation angle. The liquid crystal is located within a cross-polarised setup together with a half and quarter waveplate (see Fig. 3.7b). The quarter waveplate angle is kept fixed at 45° while the half waveplate angle is rotated from 0° to 360°. In the graph, the data points indicate the experimental measured data while the solid curve shows the outcome of Eq. (3.5) for different values of Δn. Note that the values for Δn were determined in a previous setup (see Fig. 3.8). Only $\Delta n \approx 0.11$ resulted in a good fit for both cells and this was therefore used throughout this work.

3.4.2 Experimental determination of E_{crit} and θ_t

The experimental method used to retrieve the tilt angle θ_t was adapted from references [116, 117]. Instead of a linear setup, as used in those publications, a cross-polarised setup in reflection and an additional half waveplate were used. The critical electric field (E_{crit}) is defined as the field strength needed to separate the director $\vec{n}$ by $2\theta_t$. Once E_{crit} is reached, the tilt angle θ_t can be measured simultaneously. Measuring E_{crit} requires monitoring the angle β'. The angle β' is directly connected to the angular position of the director $\vec{n}$ to the layer normal $\vec{z}$ (see Fig. 3.2). The tilt angle θ_t is defined by the liquid crystal composition itself. As mentioned earlier, the liquid crystal can be treated as a uniaxial birefringent material that has a liquid crystal axis with its position defined by the director $\vec{n}$ and the angle θ_t. The angle θ_t can lean to either side of the layer normal $\vec{z}$ depending on the sign of the applied voltage, resulting in two possible directions for the crystal axis. If the polarisation of an incident linear polarised beam is oriented orthogonal to or in the direction of this axis, it will not encounter a phase retardation. Thus, for each position of the axis (corresponding to $\beta'(\pm U)$) there is a polarisation configuration at which minimum transmission through the cross-polarised setup occurs. By rotating the half waveplate – and thus the polarisation axis relative to the axis of the liquid crystal – a state of minimum transmission can be reached. The angular change of the polarisation axis relative to the liquid crystal axis required to achieve minimum transmission determines the angle $\Delta\beta' = \beta' \pm \beta_0$. Here, β_0 is the angular position retrieved in the zero measurement. The zero measurement refers to the case in which no voltage is applied while the half waveplate is rotated to achieve minimum transmission through the cross-polarised setup.

The measurement of E_{crit} is undertaken in iterative steps by applying a square voltage waveform across the liquid crystal cell. Note that it is important that the applied voltage waveform has no DC offset; otherwise, permanent damage to the cell would occur. Thus, a square voltage waveform with a voltage amplitude of $\pm U$ is applied. In each iterative step, the applied voltage amplitude ($\pm U$) is increased and with it the elecrical field ($E = \pm U/d$) across the liquid crystal cell. While increasing $\pm U$, the transmitted signal through the cross-polarised setup is monitored and $\Delta\beta'$ is recorded. Therefore, each time U is increased, the half waveplate must be rotated in order to achieve minimum transmission for $+U$ and $-U$ respectively. Once E_{crit} is reached, $\Delta\beta'$ does not grow any further. In Figure 3.10, the angle $\Delta\beta'$ corresponding to $+U$ was monitored while increasing the applied voltage amplitude from

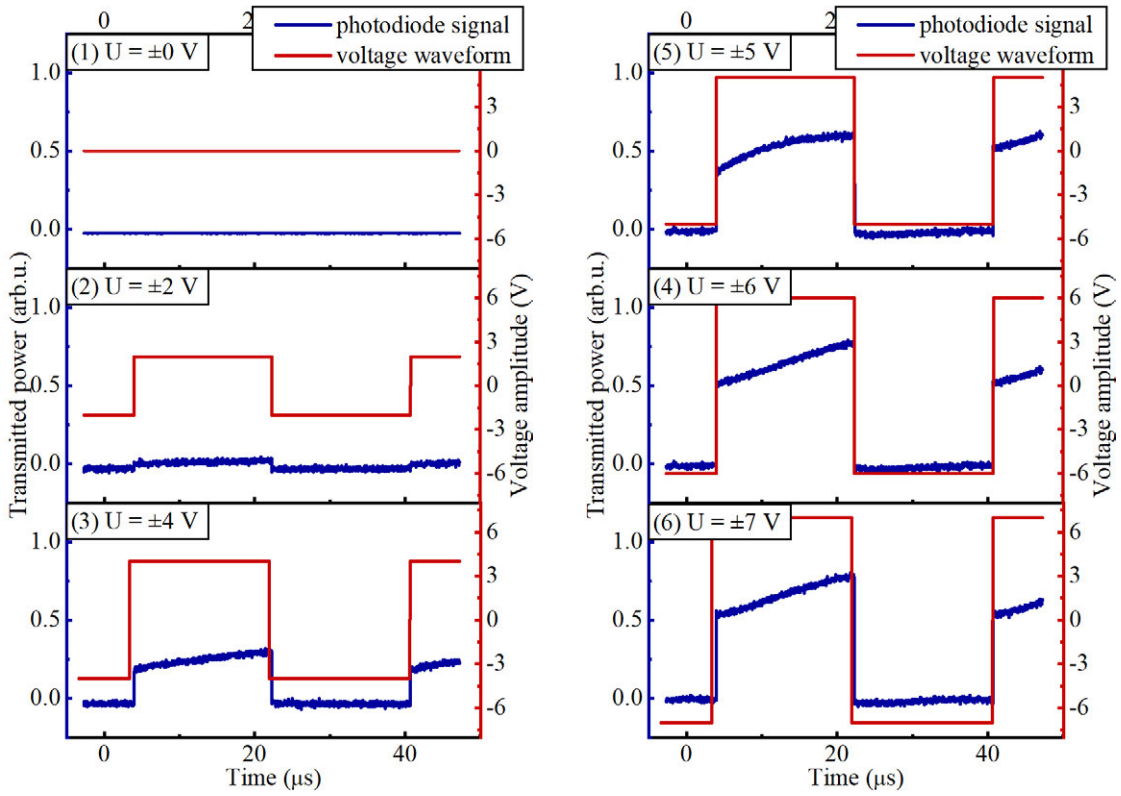

Figure 3.10: Measurement of the critical electric field (E_{crit}) needed to separate the director $\vec{n}$ by $2\theta_t$. The electric field across the liquid crystal cell (3.3 µm) was increased stepwise and the transmitted signal through a cross-polarised setup was recorded utilising a photodiode. Each time the electric field was increased a half waveplate was rotated in order to maximise the difference in maximum to minimum photodiode signal. Once the director $\vec{n}$ is separated by $2\theta_t$, the critical electric field is reached and the ratio of the maximum to minimum signal does not change when further increasing the electric field across the cell. In the case shown here the critical electric field is $E_{crit} \approx 15.15\,\mathrm{kV\,cm^{-1}}$.

$U = 0\,\mathrm{V}$ to $U = 7\,\mathrm{V}$. While the voltage amplitude was increased, the angle $\Delta\beta'$ increases as well. However, starting at an applied voltage amplitude of $U = 5\,\mathrm{V}$, the angle $\Delta\beta'$ no longer changes, and thus E_{crit} is reached. In Fig. 3.11, the measured angle $\Delta\beta'$ is plotted against the applied voltage amplitude $+U$. Above a value of 5 V, the slope changes to zero.

Once E_{crit} is reached, the tilt angle θ_t can be retrieved. Therefore, the applied voltage amplitude must be at least as high as the corresponding value for E_{crit}. The maximum angle $\Delta\beta'$ corresponding to $+U$ and $-U$ must be measured. The tilt angle equals:

$$\theta_t = \frac{|\Delta\beta'(+U)| + |\Delta\beta'(-U)|}{2}. \tag{3.13}$$

In Fig. 3.12, the applied voltage amplitude is $U = 6\,\mathrm{V}$. Starting from the position of the zero measurement (3), the half waveplate is rotated anti-clockwise through (2) until the maximum

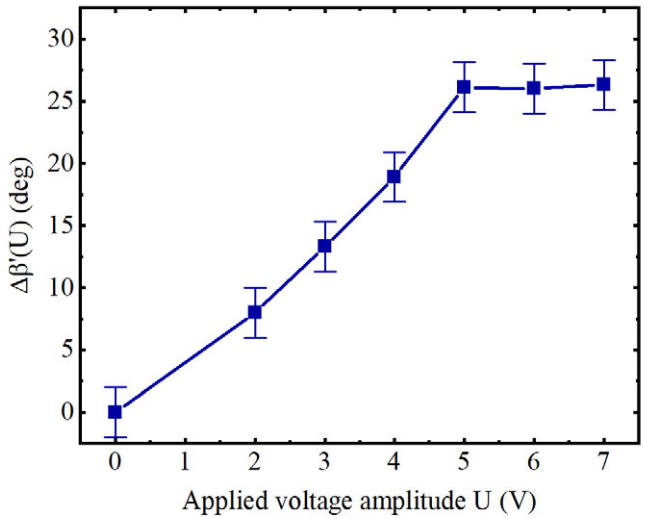

Figure 3.11: The angle $\Delta\beta'$ as a function of the applied voltage amplitude U to determine the critical electric field E_{crit}. Here the measurement is shown for a 3.3 µm thick liquid crystal cell. The critical field E_{crit} is reached once the angle $\Delta\beta'$ saturates. The error bars depend on the precision given by the rotation mount for the half waveplate (Thorlabs: continuous rotation mount RSP1).

transmission is reached at an angle $\Delta\beta'(+U) = 26°$. The same steps are undertaken to measure the maximum angle $\Delta\beta'(-U)$. Starting at (3), the half waveplate is rotated clockwise through (4) until the maximum angle at minimum transmission is reached in (5), $\Delta\beta'(-U) = -24°$. Note that if rotating the half waveplate further, the transmission increases again, as shown in (6). The resulting tilt angle is $\theta_t = 25°$ according to Eq. (3.13).

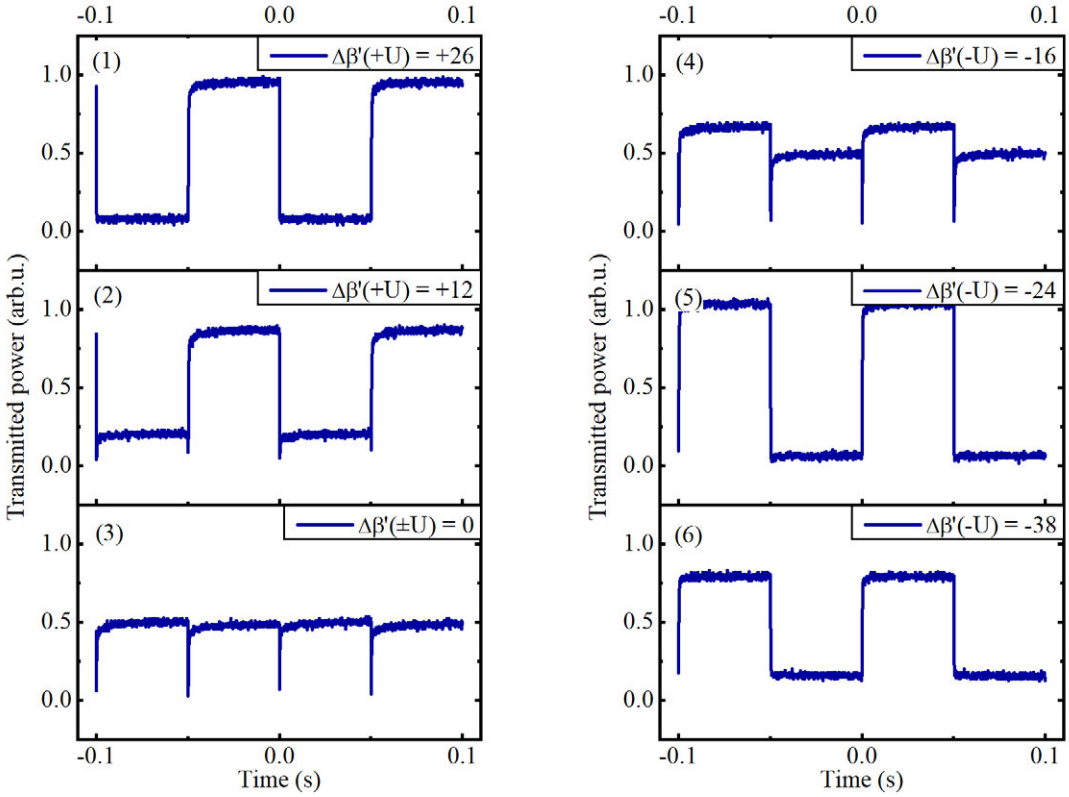

Figure 3.12: Graph indicating the process of determining the tilt angle θ_t by rotating a half waveplate in front of the liquid crystal cell. For the measurement, a square waveform with $U = \pm 6\,\mathrm{V}$ was applied. The transmitted power goes through a minimum when the incoming polarisation orientation coincides with the optical axis of the cell. The maximum angle $\Delta\beta'$ is reached at $\Delta\beta'(+U) = 26°$ and $\Delta\beta'(-U) = -24°$. Those two values are used to estimate the characteristic tilt angle θ_t according to Eq. (3.13).

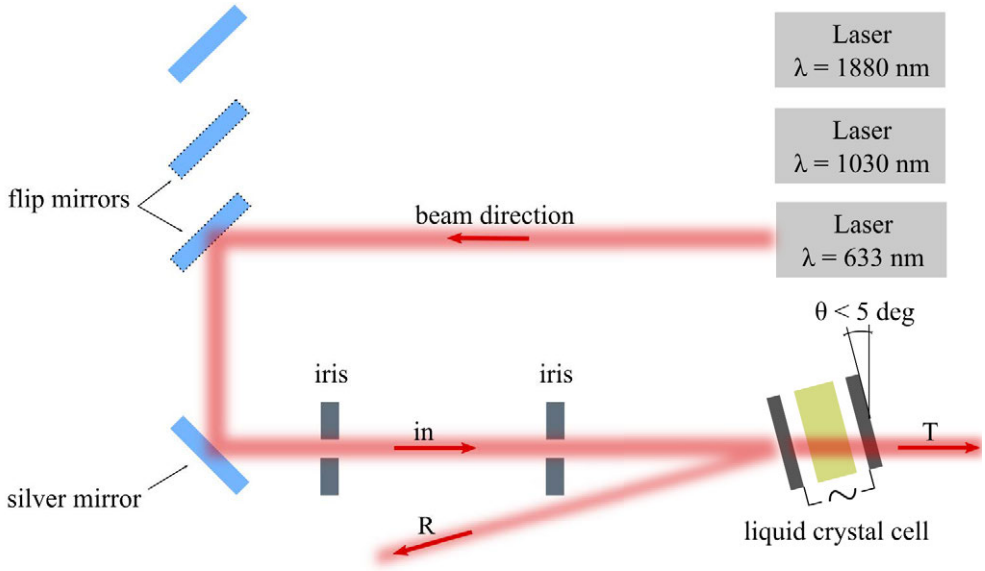

Figure 3.13: Schematic of the setup used for characterising the spectral properties of the liquid crystal cell at three different wavelengths. The optical power is measured at three positions, that are marked by the arrows labelled 'in', 'T' and 'R'. For each wavelength a distinct laser was used. Each was aligned through two irises to minimise positional errors on the liquid crystal surface. Moving the beam on the cell surface by even 2 mm can result in ±2 % transmission. Note that the 1030 nm and 632 nm laser were linear polarised the polarisation axis parallel to each other. The 1880 nm laser source was unpolarised.

3.4.3 Reflectivity and transmission

The liquid crystal cell is composed of different layers (see Fig. 3.6), each with different optical properties. It is of particular interest to identify the layer with the highest losses for further improvement of the overall performance. Note that, to measure the reflectivity and transmission of the liquid crystal cell, no mirror was attached to the back. A cell with a 3.3 µm thick liquid crystal layer and an empty cell were characterised simultaneously. The empty cell still includes the alignment and ITO layers, as shown earlier in Fig. 3.6, but lacks the liquid crystal layer. A schematic drawing of the setup used for characterisation is shown in Fig. 3.13. Due to the limited availability of laser sources, the optical properties have been tested for three different wavelengths, 633 nm, 1030 nm and 1880 nm, as shown in Fig. 3.13, and two apertures were introduced to ensure that all laser beams are collinear and thus hit the same spot on the liquid crystal cell. To separate the back-reflected beam from the incoming beam, the liquid crystal cell was tilted. The angle was kept small ($\alpha < 5°$) to minimise any unwanted effects (e.g. increased path length of the beam within the liquid crystal cell). The measurement points that were recorded are indicated within the schematic drawing by

Table 3.1: This table summarises the transmission (T), reflectivity (R) and scattering/absorption (L) losses, see also Fig. 3.13, in a single pass and compares them to the estimated transmission in a double pass.

Wavelength		Single pass R (%)	L (%)	T (%)	Double pass T^2 (%)
633 nm	with LC	6.4	37.6	63.4	40.2
	without LC	30.2	0.7	69.1	47.7
1030 nm	with LC	8.2	25.6	66.2	43.8
	without LC	24.9	0.9	74.2	55.1
1880 nm	with LC	17.5	35.0	47.5	22.6
	without LC	25.0	25.9	49.1	24.1

arrows with the inset 'in' for the total power entering the setup, 'T' the optical power that leaves the setup in transmission and 'R' the optical power that reflects from the setup. Each measurement point represents the average value that results from recording the optical power over thirty seconds. That way it was possible to decrease the measurement errors that arise as a result of power fluctuations of the probing laser source. The scattering/absorption losses are estimated to be $L = in - T - R$. Note that all results are presented in relative terms with respect to the incoming beam, which is symbolised as 'in'. The results are summarised in Fig. 3.14 and in Table 3.1.

For 633 nm, the transmission decreased by 5.7 % with the liquid crystal present. The reflectivity decreased by 23.8 %. This can be attributed partly to reduced Fresnel reflections (instead of four air glass/transitions, there are only two when the liquid crystal layer is inserted) and partly to scattering/absorption losses due to the liquid crystal. The latter increased by 36.9 % with the liquid crystal layer. At 1030 nm, the single-pass transmission decreased by 8 %. The measured value for the reflectance decreased by 16 % and the scattering/absorption losses increased by 24.7 % with the liquid crystal layer. At 1880 nm, the transmitted signal, with and without the liquid crystal, decreased by 1.6 %. The reflectivity accordingly decreased by 7.5 % and the scattering/absorption losses increased by 9.1 % with the liquid crystal layer. From the single-pass measurements, the transmission in a double-pass setup can be estimated. The transmission in a double-pass setup at a probing wavelength of 633 nm is T^2 = 47.7 % without, and T^2 = 40.2 % with, a liquid crystal layer present. At a probing wavelength of 1030 nm, the double-pass transmission is estimated to be T^2 = 55.1 % without, and T^2 = 43.8 % with, the liquid crystal layer. At 1880 nm, the double-pass transmission is approximately T^2 = 24.1 % without, and T^2 = 22.6 % with, the liquid crystal layer. Note

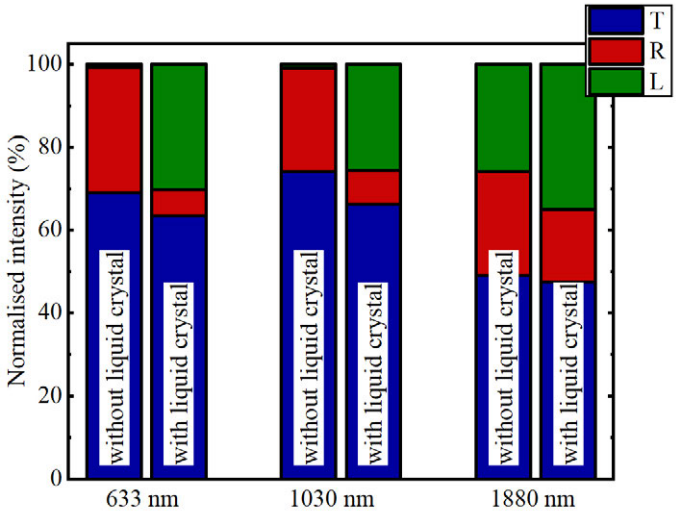

Figure 3.14: Loss, reflectivity and transmission of the liquid crystal cell at different wavelengths measured in setup shown in Fig. 3.13. The cell was tested with and without a liquid crystal layer. The input was measured and compared to the measured transmission (T) and reflection (R). The losses were estimated to be $L = in - T - R$. From this graph, one can see that the losses increase when the liquid crystal was present. However, for a intracavity setup only the measured transmission matters (compare blue bars). The absolute values can be calculated from the total optical power that was measured at the position 'in': $in_{633} = 3.3\,\text{mW}$, $in_{1030} = 367.5\,\text{mW}$, $in_{1880} = 5.6\,\text{mW}$.

that the above values are estimated for the case that the back-reflecting mirror is not coated directly to the cell. If the back-reflecting mirror is coated directly to the cell then the estimated transmission is increased due to the lack of the Fresnel reflection on the back surface.

From the above values, and from Fig. 3.14, it seems clear that at wavelengths of 633 nm and 1030 nm, the absorption and transmission losses are significantly increased once the liquid crystal layer is present. However, at a wavelength of 1880 nm the result is different. It seems the scattering/absorption losses are initially already high and the presence of the liquid crystal cell does not significantly decrease the overall transmission. This finding suggests that at 1880 nm the ITO and/or the SD-1 layers cause the majority of losses. Note that, the empty cells were provided with an ITO and SD-1 layer already coated to it and thus it was not possible at times to investigate each layer on its own. Furthermore, a similar cell incorporating a 3.3 µm liquid crystal layer was also characterised utilising a spectrophotometer. The result is shown in Fig. 3.15.

For future designs it might be of interest test different liquid crystal compositions to improve the overall performance (e.g. transmission). That is especially true for wavelengths of 633 nm and 1030 nm. At a wavelength of 1880 nm, it may be possible to improve the

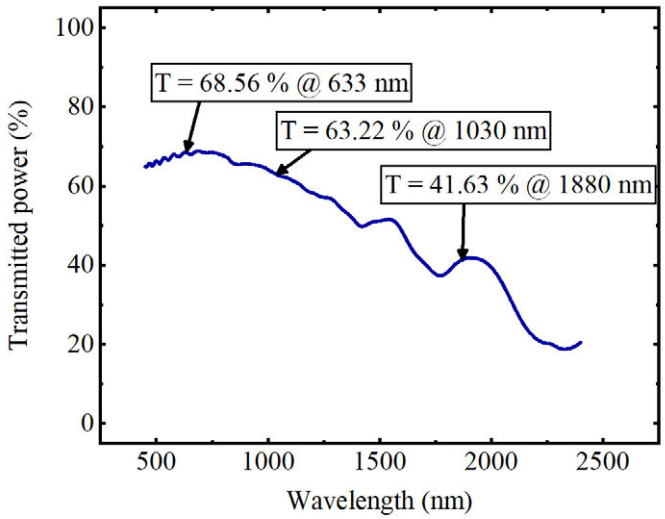

Figure 3.15: The single pass transmission measured as a function of the wavelength. The data was recorded utilising a spectrophotometer (Cary 5000 UV-Vis-NIR from Agilent).

transmission by replacing one ITO layer with a back-mirror (e.g. gold) that can also be used as an electrode. It may also be possible to improve the quality of the ITO and SD-1 layer or change their composition. It must be mentioned that when testing different cells with the same liquid crystal composition and layer thickness, slightly different results in the overall measured transmission were observed. In a double-pass setup, it was found that the transmission could vary by up to ±10% at a single wavelength. Changing the beam position on the cell surface accounted for a maximum of ±2% variance in transmission, and thus could not be held responsible for the variance of ±10 %. The liquid crystal layer thickness and its influence on losses was also investigated. Cells of different thicknesses, ranging from 3.3 µm to 19.0 µm, were characterised. On average, at a probing wavelength of 1030 nm the double-pass transmission was 40 ±10% regardless of the layer thicknesses. It was found that a cell with a 3.3 µm thick layer could even introduce higher losses than a cell incorporating a 9.0 µm layer. The thickness of the liquid crystal cell was found to have a negligible influence on the overall transmission within the repeatability of the cell fabrication processes. Thus, the variability in double-pass transmission can be attributed to repeatability issues during the fabrication of the cells.

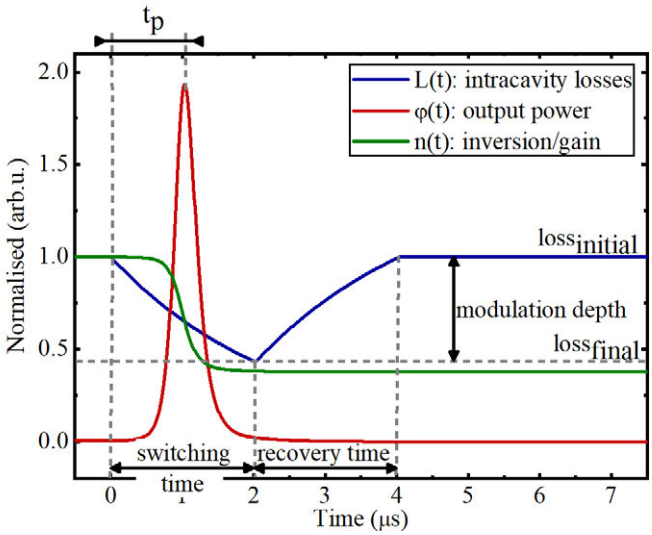

Figure 3.16: Laser dynamics of a Q-switched laser: The intracavity Q-switched loss (black line) is switched from a high to a low loss state which defines the modulation depth. A pulse builds up (black line) and depletes the inversion (blue line).

3.4.4 Modulation depth

To use the liquid crystal cell within a laser cavity as an optical switch, the most important property is its modulation depth per unit time. Throughout this work, the modulation depth is defined as the difference between two states (see Fig. 3.16). Note that the final loss state normally represents the overall cavity losses ϵ. For example, when the overall cavity losses are ϵ = 20 % (e.g. due to output coupling and scattering in the cavity) the final cavity losses can not reach a value lower than 20 %. However, throughout this work ϵ is regarded separately, and the final loss state ($loss_{final}$) can therefore reach any value between 0 % and 100 % depending on the modulation depth. Thus, the modulation depth is determined by:

$$modulation\ depth\ =\ loss_{initial} - loss_{final}. \tag{3.14}$$

For example, in Fig. 3.16 the modulation depth is approximately 55 %. Throughout this work the diagrams are represented in terms of the modulated cavity losses, L, which can take any value between 0 % and 100 %:

$$L = 100 - modulation\ depth. \tag{3.15}$$

Another important characteristic is the switching time, which is defined as the time it takes to obtain a maximum in modulation depth. For example, in Fig. 3.16 the switching time is set

to 2.0 µs. The switching time will vary throughout this work because it strongly depends on parameters of the laser setup (e.g. the gain material, doping concentration, resonator losses and the pump rate). Those parameters define the time a pulse needs to build up within the cavity, and therefore determine the switching time. In fact, the switching time is set by the user to prevent multiple pulses (a more detailed description is provided in Section 4.2.2). Dividing the modulation depth by the switching time gives the modulation depth per unit time, which is defined here as the switching speed. In the following sections the switching time of 2 µs was chosen for calculating the switching speed. Generally, switching speed (m_s) is defined as:

$$m_s = \frac{loss_{initial} - loss_{final}}{switching\ time} \left[\frac{\%}{\mu s}\right]. \tag{3.16}$$

To build an efficient short-pulsed laser, the primary requirement for the optical switch is that it switches from a high-loss state to a low-loss state in a short enough time. Conventionally available intracavity optical switches, such as acoustic optical modulators (AOM), typically switch from a high- to a low-loss state within a few nanoseconds. It is essential to switch fast enough to guarantee that the gain that has been built up is transferred into one single pulse. Slow switching speeds will result in inefficient coupling of the stored gain into one pulse, and in fact can result in the gain being coupled into multiple pulses, as discussed in Section 4.2.2.

To summarise, there are two requirements for building an efficient intracavity switch. First, the initial loss state has to be maximised. The rule is: the higher the initial loss state, the more energy can be pumped into the gain material without parasitic oscillation. Second, the switching speed must be increased, as it directly relates to the energy that is coupled into the first pulse. The following study is organised in three sections. In the first section, the effect of the liquid crystal layer thickness on the initial loss state is discussed (no voltage is applied). In the second part, the switching speed for different liquid crystal layer thicknesses and applied voltage amplitudes is characterised. Finally, the switching performance at high frequencies is characterised.

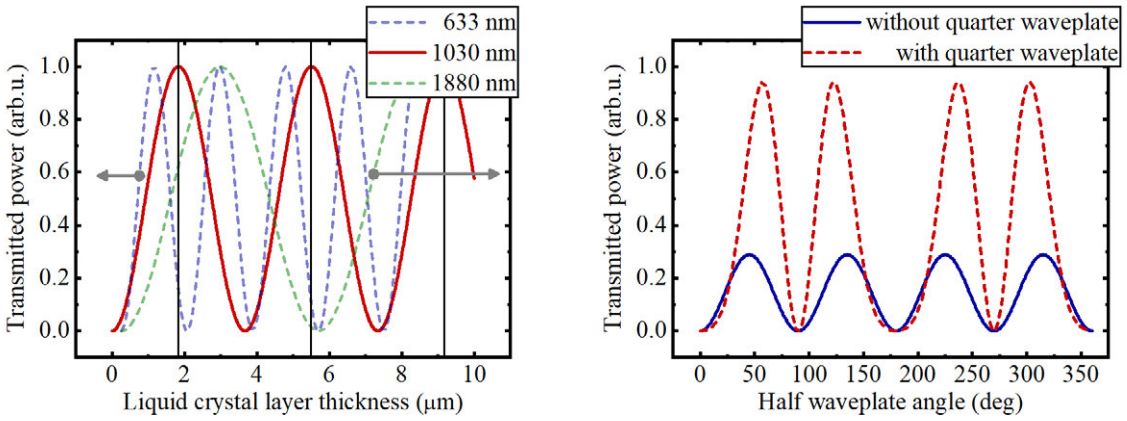

(a) (b)

Figure 3.17: The transmitted power through a cross-polarised setup as a function of liquid crystal cell thickness and its rotation angle. Simulated results using Eq. (3.10) in (a) and Eq. (3.12) in (b). In (a) the layer thickness was increased from 0 to 20 µm at 633 nm (blue line), 1030 nm (red line) and 1880 nm (green line). The optimal layer thickness for a wavelength of 1030 nm is marked (vertical black lines). In (b) at a wavelength of 1030 nm a cell thickness of 3.3 µm results in a maximum transmission of 30 % (blue line). Adding a quarter waveplate to the setup increases the maximum transmission to almost 100 %.

Effect of cell thickness

The liquid crystal layer thickness has a significant impact on the switching speed (m_s) and is thus one of the most critical parameters when optimising the cell. However, it cannot be chosen arbitrarily, as the thickness defines the initial loss state. The latter must be maximised because it defines how much energy can be stored into the gain material while pumping without continuous wave breakthrough. Equation (3.10) can be used to model the influence of the liquid crystal layer thickness on the initial loss state. In Eq. (3.10), the wavelength was set to 1030 nm and the angle β was set to 45°. Note that, according to Eq. (3.10), at an angle of 45° the transmission is maximised. The angle β describes the angle of the polarisation orientation of the laser beam relative to the axis orientation of the liquid crystal. In Fig. 3.17a, the outcome of Eq. (3.10) as a function of the liquid crystal layer thickness is plotted (red trace). The favourable liquid crystal layer thicknesses that result in a maximum transmission are marked (black vertical lines – for a wavelength of 1030 nm). Additionally, the outcome of Eq. (3.10) for different wavelengths is shown in Fig. 3.17a. For longer wavelengths, the liquid crystal layer thickness must be increased to achieve maximum transmission. This makes sense when thinking about the phase retardation introduced by the liquid crystal cell. Ideally, the phase retardation should be $\lambda/2$ or an odd integer multiple thereof to result

in maximum transmission in Eq. (3.10). At a given liquid crystal layer thickness, shorter wavelengths experience higher phase retardations compared to longer wavelengths when no voltage is applied. Note that this is only true for a zero-order phase retardation. In the case of a multi-order phase retardation, the cell thickness can be increased or decreased to optimise the initial cavity loss state. In general, when used in a cavity configuration, it is preferred that the LC cell introduces a $\lambda/2$ phase retardation without any voltage applied. That way, the initial intracavity losses are maximised (at $U = 0$ V). This sets stringent requirements for the cell thickness. The shorter the wavelength, the higher the requirement to match the exact layer thickness during the fabrication process of the cell. This is illustrated in Fig. 3.17a (blue dashed line); for short wavelengths, even half a micrometre deviation from the ideal layer thickness already causes a substantial decrease in transmitted power. According to Fig. 3.17a, for a wavelength of 633 nm increasing the layer thickness from 1.0 µm to 1.5 µm decreases the transmission by 50 %. For longer wavelengths the thickness has a smaller impact on the initial loss state.

Throughout this project, liquid crystal cells of specific layer thicknesses were provided. Thus, it was not possible to tailor each cell to our needs. From Fig. 3.17a it is evident that maximum transmission in a cross-polarised setup can only be reached for specific dimensions. To optimise the initial state, i.e. to maximise the cavity losses when no voltage is applied, a quarter waveplate was added to the cross-polarised setup. In Fig. 3.17b, equation (3.12) (dashed red trace) was used to model the influence of an additional quarter waveplate. The modelling utilised a 3.3 µm thick liquid crystal layer at a wavelength of 1030 nm. By comparing the solid to the dashed curve in Fig. 3.17b, it can be seen that by adding a quarter waveplate it is possible to optimise the phase retardation when no voltage is applied. For a liquid crystal layer thickness of 3.3 µm, the outcome of Eq. (3.10) (solid blue trace) cannot reach values higher than 30 %. According to Eq. (3.12), when adding a quarter waveplate (at 45° relative angle to the LC axis) in addition to the half waveplate, the transmission can be increased to almost 100 %.

In Figure 3.18, the outcome of Eq. (3.12) is plotted for any possible half/quarter waveplate configuration. For this simulation, the liquid crystal layer thickness is set to 3.3 µm and the wavelength is set to 1030 nm. Areas of interest are those which exhibit a rapid change from a low to a high transmission state. Corresponding waveplate configurations will result in a fast switching speed m_s, as those areas are sensitive to small changes in phase retardation.

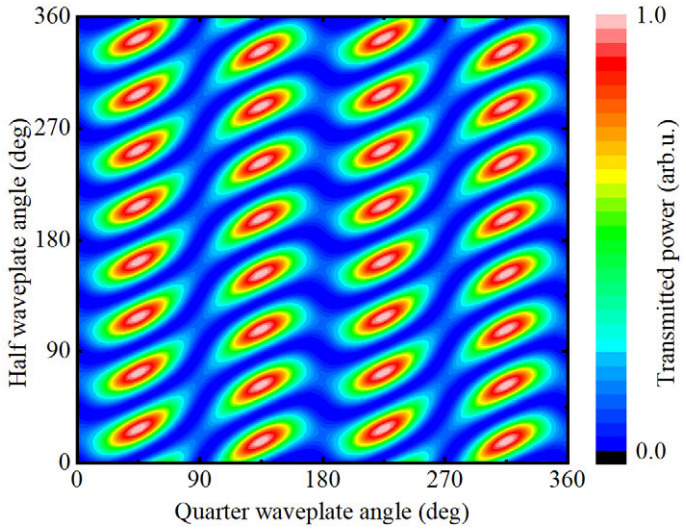

Figure 3.18: The outcome of Eq. (3.11) is plotted for different waveplate rotation angles. The result of this simulation predicts the transmitted power through a cross-polarised setup utilising the liquid crystal cell in sequence with a half and quarter waveplate. It was illustrated in Fig. 3.7b that utilising a half and quarter waveplate can maximise the initial loss state when no electric field is applied across the liquid crystal cell. This density plot reveals waveplate configurations that result in areas of high contrast. Areas of high contrast will result in a fast switching speed (m_s).

Effect of applied voltage

Another important aspect is how a varying liquid crystal layer thickness impacts the switching speed when an external electric field is applied. To compare the results, the electric field strength ($E = U/d$) is kept constant across all liquid crystal cells. That means that for a thicker liquid crystal layer the voltage must be increased by the ratio of the thick to the thin layer size (d_1/d_2). The modulation depth per unit time will be used as a figure of merit. The following study requires application of high voltage amplitudes. However, when an electric field above 30.3 kV cm^{-1} is applied for durations longer than a few 10 µs, damage to the liquid crystal cell is possible; thus, steady-state analyses at high voltages were not possible. This threshold value was determined experimentally and may vary from cell to cell. It marks the lowest value at which permanent damage was observed and is independent of the applied voltage waveform. In addition, as mentioned earlier, liquid crystals in the smectic-C phase (as used throughout this work) are likely to be damaged if the applied voltage waveform has a DC offset. To avoid a DC offset, the voltage waveform was modified to include a small negative offset so that the integral over time was zero.

A typical applied voltage waveform is illustrated in Figure 3.19. Throughout this work, the applied voltage amplitude is always referred to as U_+. Depending on the period T and

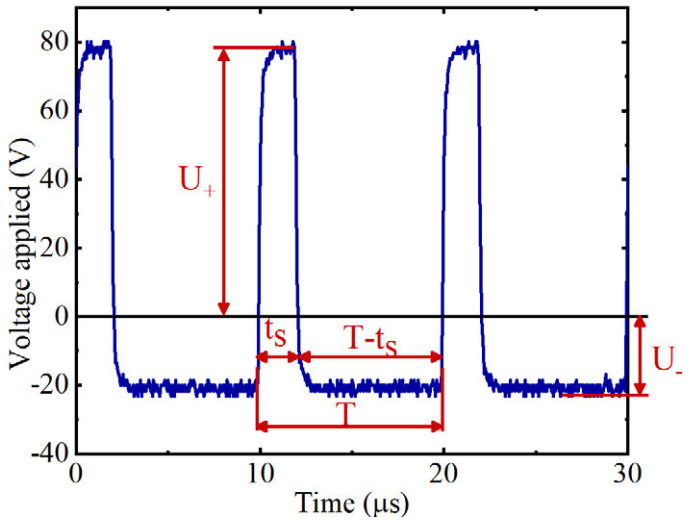

Figure 3.19: Schematic of the applied voltage waveform. Throughout this work the voltage waveform applied across the cell is as illustrated here. In each experiment, the value for U_+, the frequency $f = 1/T$ and the switching time t_s is provided. The missing values can be calculated utilising Eq. (3.17).

the switching time t_s of the applied voltage waveform, the value for U_- can be calculated as follows:

$$U_- = U_+ \frac{T - t_s}{t_s}. \tag{3.17}$$

The setup used for characterising the modulation depth is shown in Fig. 3.20. A half and quarter waveplate were used to maximise the initial cavity losses and the switching speed. The signal in transmission through the cross-polarised setup was recorded using a photodiode. Before the measurement, the photodiode was calibrated with a power meter to express the overall result in terms of cavity losses. The calibration was performed by first measuring the power at position P5 with a power meter before it was replaced by a photodiode. The photodiode was fixed in place to prevent introduction of errors from movement. The measured value of the power meter was divided by the voltage recorded with the photodiode. This provides a calibration factor k in units of mW mV^{-1}, which was then used to calculate the overall transmitted power through the cross-polarised setup. The total optical power entering the setup was calculated by subtracting the measurement of P2 from the measurement of P1. Additionally, the reflected beam coming from the liquid crystal cell was measured before the photodiode alignment under a slight angle at P4. The cavity losses were calculated by the ratio P5/P4 for each trace, i.e. each applied voltage amplitude. The normalised applied waveform is depicted by the black trace in Fig. 3.21, for an applied voltage of 2 µs. The

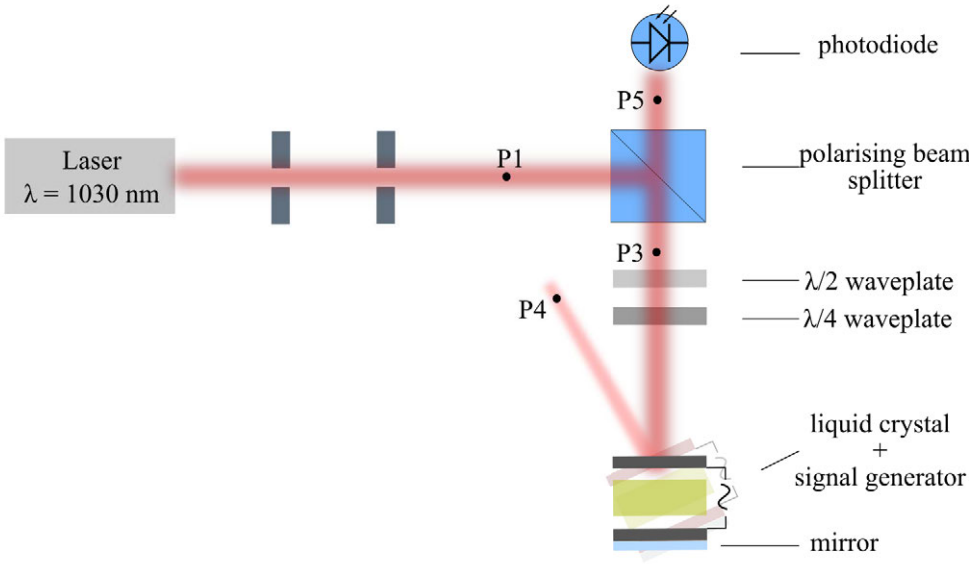

Figure 3.20: Schematic drawing of the setup for characterising the switching speed and modulation depth of the liquid crystal cells. The liquid crystal is located in a cross-polarised setup. Two waveplates allow alignment of the setup in such a way that maximum transmission is achieved when no voltage is applied to the liquid crystal cell. The measurements were recorded at the indicated positions P1 to P5. Note that position P4 was measured during the calibration process. For that, the liquid crystal cell was slightly tilted.

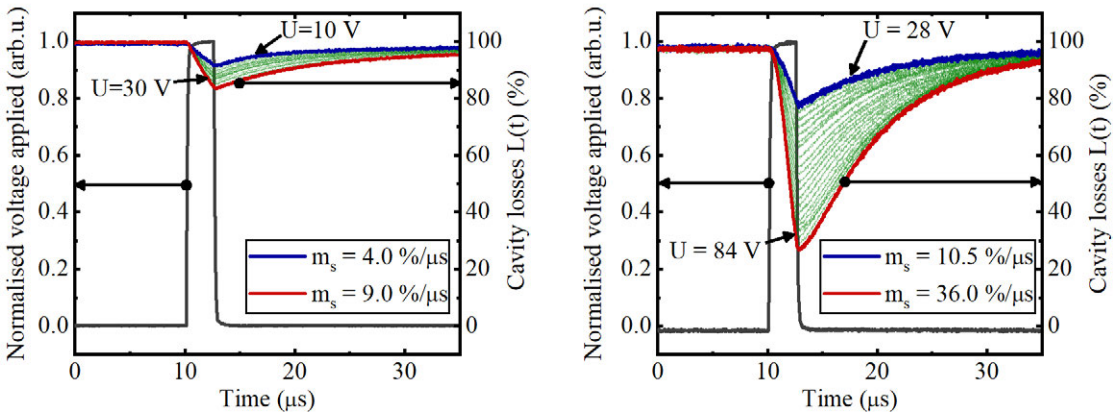

(a) 3.3 µm cell

(b) 9.0 µm cell

Figure 3.21: Normalised cavity losses as a function of time (blue, green and red lines) for different amplitudes of the applied voltage at a frequency of 5 kHz. In green, the transition between the miniumum and maximum applied voltage is shown. As shown in the graph, the transition between a high and a low loss state is linear. The 3.3 µm thick cell (a) exhibits in a switching speed of 4.0 % μs^{-1} at 10 V and 9.0 % μs^{-1} at 30 V. The highest switching speed was achieved with a layer thickness of 9.0 µm (b), which resulted in a switching speed of 10.5 % μs^{-1} at 30 V and 36.0 % μs^{-1} at 84 V.

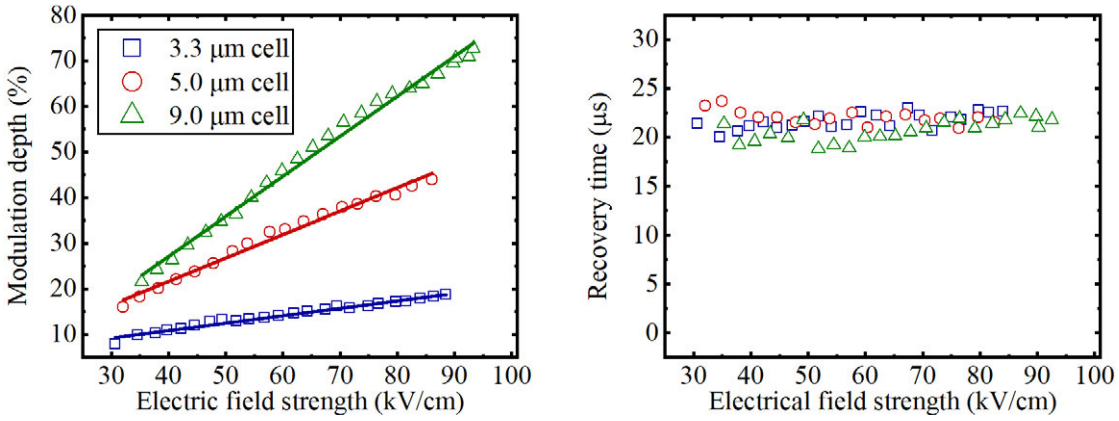

(a) (b)

Figure 3.22: Three cells of different liquid crystal layer thickness were characterised. The modulation depth was measured after 2 µs of switching time in (a). The thicker the liquid crystal layer the higher the modulation depth. In (b) the corresponding recovery time is depicted for different electrical field strengths.

resulting photodiode signals for different applied voltages are also shown in Fig. 3.21. The blue trace indicates the response to the minimum applied voltage amplitude. The response of the maximum applied voltage amplitude is depicted by the red plot. All the values in between are shown in green. Using the thinner cell (3.3 µm) in Fig. 3.21a, the switching speed increased from 4.0 % μs^{-1} to 9.0 % μs^{-1} when tripling the applied voltage from 10 V to 30 V, corresponding to an applied electric field of 30.3 kV cm^{-1} and 90.9 kV cm^{-1} respectively. However, above 30 V the modulation depth started to saturate and the voltage was not further increased to avoid any damage to the cell. In Fig. 3.21b the modulation depth increased from 10.5 % μs^{-1} to 36.0 % μs^{-1} for the 9.0 µm thick cell when increasing the applied electric field from 31.1 kV cm^{-1} to 93.3 kV cm^{-1} (corresponding to 28 V and 84 V). As with the thinner cell, the modulation depth started to saturate for electric fields above 93.3 V cm^{-1}. Increasing the cell thickness from 3.3 µm to 9.0 µm increased the switching speed for similar electric field strengths. Figure 3.21 illustrates that, for the thicker cell (3.3 µm compared to 9.0 µm), the switching speed was increased by a factor of 2.6 at 31.1 kV cm^{-1} and by a factor of 4.0 at around 93.3 kV cm^{-1}. In Fig. 3.22a the graph shows the modulation depth as a function of electric field strength for 3.3 µm, 5.0 µm and 9.0 µm thick liquid crystal cells. It can be seen that the modulation depth increases with the liquid crystal layer thickness. In Figure 3.22b, the corresponding recovery time is plotted as a function of the electrical field strength. The recovery time was measured by determining the time it takes for the liquid crystal to recover from 90% to 10% of the *modulation depth*, as shown in Fig. 3.23. Note that it was not

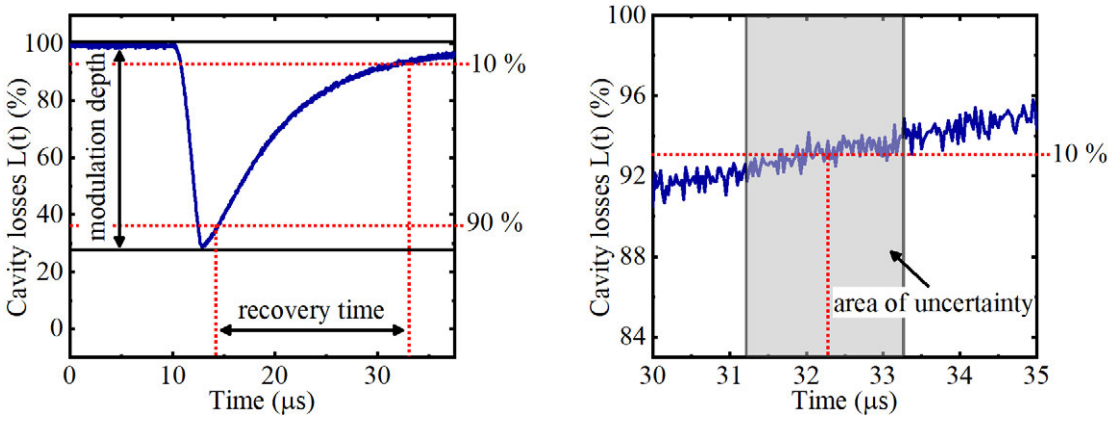

Figure 3.23: (a) Illustration of the upper ($modulation\ depth \cdot 0.1$) and lower values ($modulation\ depth \cdot 0.9$) that define the recovery time. (b) Shows the source of uncertainty for the fluctuations, shown in Fig. 3.22b when measuring the recovery time.

possible to apply an exponential fit, as the loss function depicted in Fig. 3.23a is a double exponential function. The fluctuations in the plotted graph resulted from the noise of the photodiode signal, as shown in Fig. 3.23b.

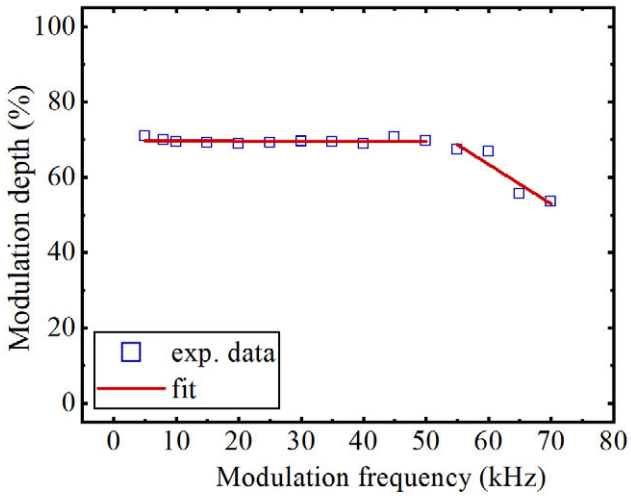

Figure 3.24: Modulation depth for a fixed voltage amplitude of 84.0 V as a function of the applied voltage waveform frequency for the 9.0 µm cell. Note that the pulse repetition rate is determined by the frequency of the applied voltage waveform. The solid line (red) is a fit that emphasises the decline of modulation depth starting at frequencies above 50 kHz.

Frequency response

From the results shown in Fig. 3.21, it is evident that, for constant modulation depth, the switching frequency is limited by the recovery time of the liquid crystal cell. The recovery time (see Fig. 3.16) is the time the liquid crystal molecules require to return to their initial state before a new cycle of applied voltage waveform can be applied. This sets an upper bound on the possible repetition rate of the laser. Figure 3.24 illustrates the modulation depth as a function the modulation frequency. The recorded data is for a 9.0 µm thick liquid crystal cell, which reached the highest modulation depth. When applying a voltage of 84.0 V across the 9.0 µm thick cell the recovery time was approximately 20 µs, which also marks the maximum frequency ($f = 1/20\,\mu s = 50$ kHz) of the applied waveform before it effects the modulation depth. Once a frequency of 50 kHz is reached, the modulation depth drops. However, this roll-off frequency can be partially overcome by applying a modified waveform. The idea is that a voltage signal with opposite polarity must be applied in order to help recover the initial molecule position faster. A similar behaviour was previously reported for nematic liquid crystal cells [118]. In Fig. 3.25, a comparison between the original and the modified waveform is plotted. With the modified waveform, it is possible to maintain a modulation depth of 60 % up to 100 kHz. Note that the unsymmetrical waveform results in a higher modulation depth compared to a symmetrical waveform; the reason for this is that, during the whole time interval ($T - t_s$), a negative voltage is applied, which helps to recover the

high-loss state. For even higher modulation frequencies, a symmetrical waveform becomes more practical as the modulation depth is maximised when switching from U_- to U_+.

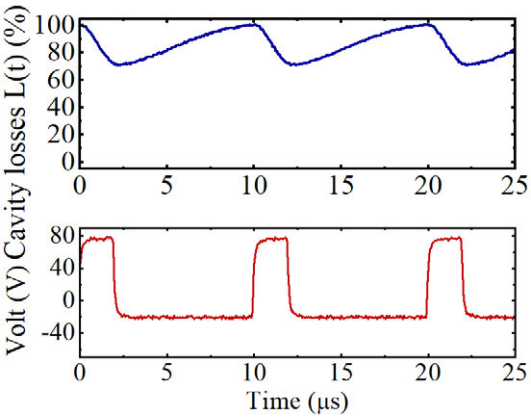

(a) 100 kHz applied waveform

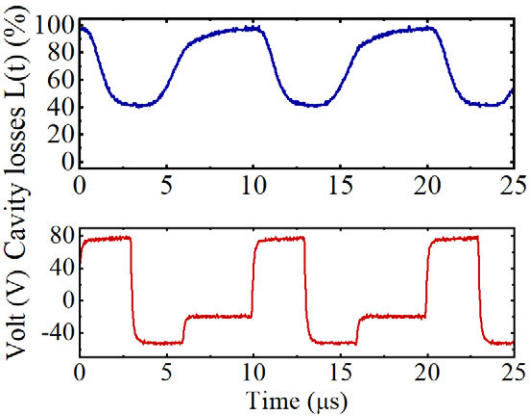

(b) modified 100 kHz applied waveform

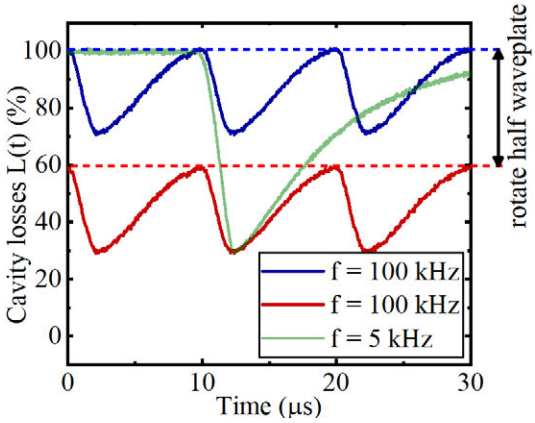

(c) 100 kHz applied waveform

Figure 3.25: The graphs show the applied voltage waveform and the response of the liquid crystal cell in terms of cavity losses. Utilising the 9.0 µm thick liquid crystal cell, there is a roll-off frequency at which the modulation performance will degrade, as shown in Fig. 3.24. However, applying a modified waveform it is possible to overcome this roll-off frequency. As shown in (a), with a pulsed waveform it is possible to achieve a modulation depth of 30 %. Applying a modified waveform in (b), it is possible to attain a modulation depth of 60 %. In (c), the loss function for different applied voltage waveform frequencies is depicted. The maximum modulation depth that can be reached can be measured at low frequencies (green trace). Once the frequencies reach a critical value, the modulation depth decreases as the initial loss state decreases (red trace). This can be compensated by rotating the half waveplate (blue trace).

It must be mentioned that a modified waveform cannot increase the overall modulation depth. The overall modulation depth depends on the maximum applied voltage amplitude, U_+. Thus, at high frequencies the modulation depth cannot exceed the values reached at low frequencies (e.g. in Fig. 3.21b at 5 kHz). Once the frequency of the applied voltage waveform reaches a critical value, the modulation depth decreases because the initial loss state cannot

be recovered in a timeframe shorter than the recovery time. The decrease in the initial loss state can be compensated by rotating the half waveplate; this process is shown in Fig. 3.25c. The maximum modulation depth that can be reached for low frequencies is indicated by the green trace. While increasing the frequency, the green trace transforms into the red curve. Note that the red curve still decreases the cavity losses to 30 %; however, the initial loss state reaches only 60 % rather than returning to 100 %. To increase the initial loss state again, the half waveplate must be rotated. While configuring the half waveplate angle, the red curve transfers into the blue curve.

In Chapter 5, the liquid crystal will be employed in a fibre laser cavity for active mode-locking. This requires modulation of the cavity with the axial mode spacing $\nu_{ax} = c/(2nl_{cavity})$ and high modulation frequencies are thus needed. In Figure 3.26, the modulation depth for modulation frequencies ranging from ν_{mod} = 198.08 kHz to 913.8 kHz are characterised for a cell using a 5.0 µm thick liquid crystal layer. The 5.0 µm cell was used because the 9.0 µm cell without a mirror coated to the back was of insufficient quality. As illustrated, the corresponding modulation depths range from 5.9 % to 29.3 %.

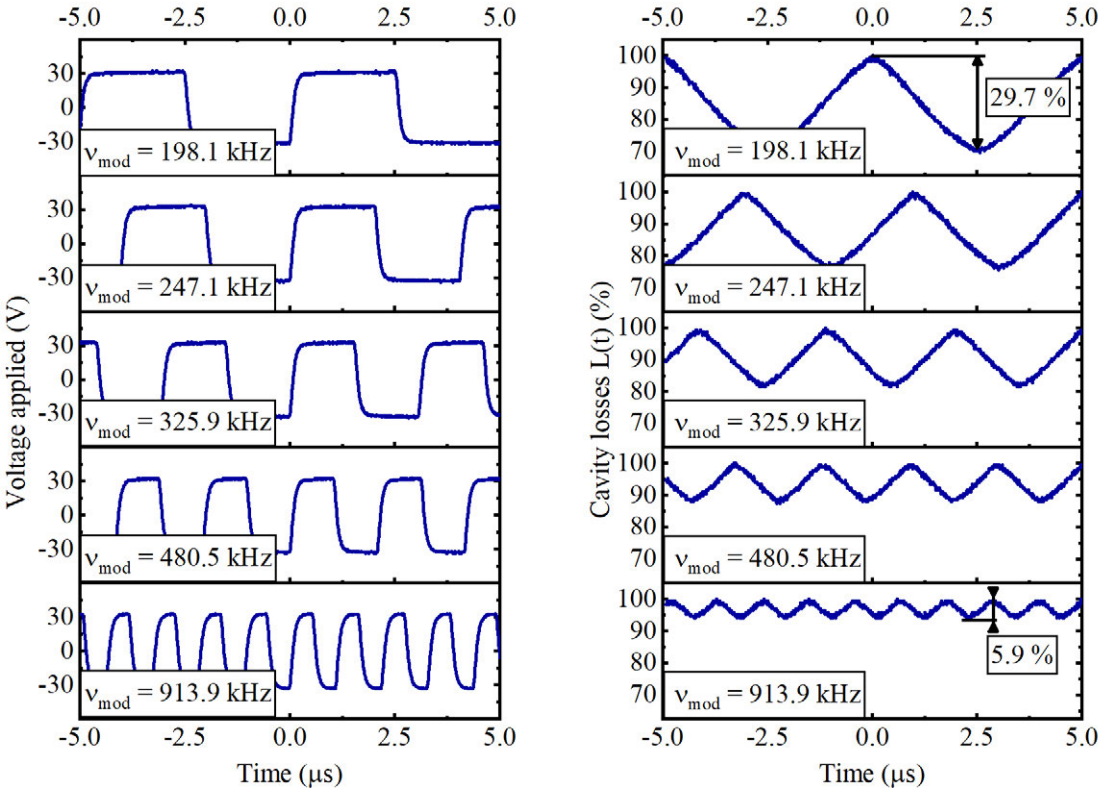

(a) (b)

Figure 3.26: Applied voltage waveform for amplitude-modulated mode-locking in (a) and the corresponding loss function L(t) in (b) respectively. At high modulation frequencies ν_{mod} =198.08 kHz, 247.08 kHz, 325.87 kHz, 480.45 kHz and 913.9 kHz the corresponding modulation depths are 29.7 %, 22.7 %, 17.9 %, 11.4 % and 5.9 %.

3.5 Conclusion

In this chapter, liquid crystal cells of different thickness were characterised with respect to their use as an intracavity loss modulator. The key finding of this study is that thicker cells show the same recovery time but have a higher modulation depth at constant switching times, and thus are preferable as intracavity loss modulators. A switching speed as high as 36 % μs^{-1} was reached when an electric field of 93.3 kV cm^{-1} was applied across a cell that incorporates a 9.0 µm thick liquid crystal layer. The key enabling method was to apply high electric field strengths for short durations (e.g. below 3 µs). Other comparable compact optical modulators consist of either nematic or smectic liquid crystals. Typically, nematic liquid crystals have a lower viscosity than smectic liquid crystals and thus, in theory, they switch faster [119], although ferroelectric smectic-C liquid crystals (similar to the one used in this study) are known for a high switching speed at low voltages. For example, Clark *et al.* demonstrated microsecond switching speed for electric fields of 266 kV cm^{-1}, corresponding to a voltage amplitude of 40 V across a 1.5 µm thick liquid crystal layer [120]. For even lower electric field strengths of approximately 7.7 kV cm^{-1}, sub-millisecond switching times were reported [121]. However, the switching speed for ferroelectric smectic-C liquid crystals scales with $1/E$ [122], whereas the switching speed of nematic liquid crystals scales with $1/E^2$ [123]. Nanosecond switching times were reported when using (twisted) nematic liquid crystal cells [124–128]. Geis *et al.* used a twisted nematic liquid crystal to modulate an optical signal from 90 % to 10 % in 30 ns, which corresponds to a switching speed of approximately 2667 % μs^{-1} [125]. However, the applied electric field strength measured 900 kV cm^{-1} and the probing wavelength was 633 nm. Thus, comparing this value to the value achieved in this study, the switching speed decreases by a factor of approximately λ_2/λ_1 = 633 nm/1030 nm = 0.61. For an applied electric field of 100 kV cm^{-1} V, Geis *et al.* reported a switching time of 30 µs. The resulting switching speed is approximately 2.7 % μs^{-1} (estimated for a wavelength of 1030 nm). Furthermore, those results were recorded at a temperature of 33.1 °C and decrease at lower temperatures [125]. An alternative approach was presented by Li *et al.*, who used a nematic liquid crystal cell in a multi-pass setup [128]. The minimum switching time of 30 ns was achieved at an electric field strength of 1696 kV cm^{-1} with a probing wavelength of 633 nm. Thus, the switching speed estimated for a wavelength of 1030 nm is 2110 % μs^{-1}. Further, due to multiple transmission through the ITO layer and scattering/absorption in the liquid crystal, the reported losses are as high as 85 % in a single pass and thus substantially

higher than those reported in this study. Table 3.2 provides a summary that includes the fastest switching speeds reported for optical modulators based on liquid crystals. It shows that utilising a ferroelectric smectic-C phase liquid crystal offers the highest switching speed for electric field strengths $<100\,\mathrm{kV\,cm^{-1}}$, while nematic liquid crystals are faster for higher voltages. Low voltages are preferable, as they are easier to provide (particularly for a miniaturised laser that can potentially used as a mobile device) and generate less electronic RF radio frequency noise.

Alternatively, there are several reports on integrated waveguide modulation schemes based on electro-optical crystals. In recent years, (femtosecond laser-inscribed) single-mode waveguides in electro-optical crystals have been demonstrated [129–134]. Thus, in principle, optical modulators based on electro-optical crystals are fully compatible with single-mode waveguide lasers. Intensity modulation is usually achieved by varying the refractive index in the arms of an interferometric waveguide setup [129, 135–138]. Modulation depths >90 % were demonstrated for driving voltages of a few millivolts [136]. However, such modulator schemes require complex fabrication methods and cannot be built as cost effectively, or made as compact, as liquid crystal modulators.

Additionally, in the course of this study it has been shown that the liquid crystal cells are well suited to modulate losses up to 50 kHz, as this marks the roll-off frequency at which the switching speed starts to decrease. This roll-off frequency can partly be overcome by applying a modified voltage waveform. The layer thickness of the liquid crystal does not noticeably increase the overall losses, at least within the tested range of layer thicknesses between 3.3 µm and 9.0 µm. However, the reproducibility of the cells is still an issue and must be addressed in future work. In the present study, cells were tested that had a 3.3 µm liquid crystal layer yet the transmission losses were, in some cases, higher than for a cell with a 9.0 µm layer thickness. Furthermore, it has been demonstrated that the same liquid crystal cell can be used throughout a broad range of wavelengths, ranging from the visible (633 nm) to the mid-infrared (1880 nm). According to the simulations shown here, the switching speed should increase for shorter wavelengths and decrease for longer wavelengths as a result of the optical path lengths and the resulting phase retardation within the liquid crystal layer.

Table 3.2: Fast optical modulators based on liquid crystal cells. The fastest switching speeds (from top to bottom) were demonstrated with liquid crystals in the (twisted) nematic phase; however, the electric field across the cell is substantially higher than was demonstrated in the scope of this work (marked yellow).

LC phase	layer thickness (μm)	voltage amplitude (V)	switching speed (%/μs)	electric field strength (kV/cm)	temperature (C)	Ref.
nematic	5.6	950	2110.0[1]	1696.0	23.0	[128]
nematic	10.0	900	1627.0[1]	900.0	33.1	[125]
smectic	9.0	84	36.0	93.3	23.0	
nematic	10.0	100	1.6[1]	100.0	33.1	[125]
smectic	1.5	40	1.0[2]	266.7	69.0	[122]
smectic	2.6	2	<0.1[2]	7.7	23.0	[121]

In conclusion, the characterised cells proved to be promising for use as a fast optical intracavity switch. In future work, different liquid crystal compositions within the smectic-C and nematic phases need to be tested. In addition, the switching performance should be tested in various temperature environments. Lastly, the mechanisms that result in reproducibility issues during the fabrication process should be identified and addressed.

[1]Based on estimation, data was published for a wavelength of 633 nm.

[2]Wavelength was not specified.

4

Liquid crystal Q-switched waveguide chip lasers

Q-switching is a widely used method for generating high energy and high-peak power pulses directly from a laser oscillator. Using this technique, pulse widths ranging from picoseconds to several microseconds, at repetition rates ranging from a few hertz to megahertz, can be achieved. The parameter Q refers to the optical quality factor, which is strongly related to the finesse of an optical resonator. High Q means that low intracavity losses are present, whereas low Q refers to high losses. As an analogy, a pendulum in air (high Q) will oscillate freely, whereas a pendulum in water (low Q) will be strongly damped. In a Q-switched laser, the idea is to rapidly change the Q-factor from high losses – where oscillation is prevented – to low losses, where oscillation is permitted. This modulation can be provided by any intracavity device that is able to alter the losses on a short timescale. Q-switching can be divided into active and passive methods. In active Q-switching, which is the subject of this study, the loss modulation is controlled by an externally applied electric signal. The

theoretical approach presented here follows that presented in Koechner's *Solid-State Laser Engineering* and Siegman's *Lasers* [139, 140].

In the first section of this chapter, the theoretical background of Q-switching is introduced, with a detailed explanation of the underlying dynamics of fast and slow Q-switching. A theoretical model is established to provide guidance for subsequent optimisation of the Q-switched laser performance. Experimental results are presented in the last part of the chapter. Liquid crystal cells with different thicknesses were employed as intracavity active Q-switches in laser cavities incorporating different active waveguides. Using various rare-earth ions as the active laser medium, it was possible to demonstrate Q-switching at 644 nm, 1016 nm, 1030 nm and 1879 nm.

4.1 History of Q-switching

Continuous wave lasers were first patented in 1960. The first quasi-CW laser was built by T. H. Maiman *et al.* and was a ruby laser pumped by flash lamps [141]. In 1961, R. W. Hellwarth *et al.* presented theoretical work on optimising a ruby laser [142]. They also described the mechanism underlying the process of Q-switching. Their model recommended rapid switching of the reflectivity of the end mirrors from a state where laser oscillation is prevented to a state where it is permitted (i.e. from low Q to high Q). In 1962, Hellwarth *et al.* proved his theory and demonstrated the first Q-switched ruby laser, with a pulse peak power more than 100 times that of a conventional ruby laser [143]. Those high peak powers enabled the first applications for processing metals. One year later, the first mode-locked laser was demonstrated, using an acousto-optical modulator [144].

Since 1963, the ever-increasing peak powers and pulse energies generated by Q-switched lasers have resulted in their use in a wide range of applications, from optical measurement and processing techniques to optical telecommunications. Laser sources for those applications can range in size from chip-sized to those that would fill a concert hall, and are mainly characterised by their pulse duration, peak power and pulse energy. Table 4.1 provides an overview of state-of-the-art available femtosecond laser-inscribed–waveguide-based Q-switched laser sources and their parameters. This table includes passive and active Q-switched lasers. The latter requires an extended cavity, as the beam must be imaged onto the bulk loss

modulator. To date, this class of laser cannot be build in a monolithic setup (i.e. a setup without free space components).

Table 4.1: List of published Q-switched waveguide lasers, from lowest to highest peak power. (*Type: Refers to active (a) or passive (p) Q-switching)

Peak power (W)	**Output power (mW)**	**Pulse duration (ns)**	**Pulse energy (nJ)**	**wave-length (nm)**	**Type***	**Ref.**	**Published**
0.03	57	85	2.5	1064	p	[145]	2014
0.04	10	9800	370	1064	p	[146]	2014
0.09	48	52	4.5	1064	p	[147]	2014
0.13	12.8	98	12.3	1031	p	[148]	2014
0.14	1.2	1200	120	1845	p	[149]	2010
0.17	7.8	125	21.7	1024	p	[150]	2017
0.19	24	57	11	1064	p	[151]	2014
0.24	330	75	19	1064	p	[152]	2014
0.25	26	802	200	607	p	[153]	2017
0.27	33	170	44	1040	p	[154]	2009
0.29	110	90	26.5	1064	p	[155]	2014
0.29	45	52	19	1064	p	[155]	2016
0.30	30	433	124	1030	p	[156]	2013
0.32	129	25	8.1	1064	p	[157]	2015
0.32	129	25	8.1	1064	p	[157]	2015
0.38	84	203	89	1064	p	[158]	2016
0.38	85.2	203	89	1064	p	[158]	2016
0.43	60	88	39.2	1029	p	[159]	2015
0.43	115	80	36	1064	p	[160]	2016
0.61	47	21	14	1064	p	[161]	2013
0.66	173	90	63	1064	p	[162]	2015
0.81	85	79	64	1029	p	[163]	2016
1.00	442	1000	1000	2090	p	[164]	2017
1.59	265	179	221	1064	p	[165]	2015
1.96	456	158	310	1064	p	[166]	2015
2.40	0.36	75	180	1562	a	[167]	1998
2.50	0.004	1.5	3.8	1085	a	[168]	1992
2.98	0.75	12		1030	p	[169]	2015
3.04		25	76	1054	p	[170]	1994
27.0	27	100	2700	1535	a	[171]	2000
59.0	11.8	200	11800	1535	a	[171]	2000
67.2	7.8	200	13400	1536	a	[172]	1997
350	0.01	0.3	105	1085	a	[173]	1993
650	104	32	20800	1900	a	[174]	2012
1000	300	1	1000	1064	p	[175]	2012
1440	6.2	4.3	6192	1562	a	[176]	1998
1809	78.1	21	38000	1900	a	[174]	2012
2500	5.25	2.1	5250	1562	a	[177]	2000
7060	680	2.8	19700	1064	p	[178]	2016
18668	2300	1.6	30000	1030	p	[179]	2002
33750	8100	3	90000	1064	p	[180]	2001
300000	22500	15	4500000	1030	a	[181]	2007

4.2 Theory of Q-switching

The dynamic behaviour of a Q-switched laser can be derived from the well known rate equations [139, 140]. From the rate equations of a three-level gain medium, one can obtain an equation to describe the rate of change of the photon flux φ within the resonator:

$$\frac{d\varphi}{dt} = c\varphi\sigma n + S - \frac{\varphi}{\tau_c}. \tag{4.1}$$

The first term on the right of the equation describes the increase of photon flux due to stimulated emission, where c is the speed of light, σ is the material constant for the emission cross-section and n is the inversion density of the upper-state laser level. The second term, S, refers to spontaneous emission, which initiates the oscillation. However, this variable is usually very small and can be neglected when analysing the Q-switching behaviour. The third term describes the losses and the output coupling within the resonator; it can be represented by the average photon lifetime τ_c:

$$\tau_c = \frac{t_r}{\epsilon} = \frac{2l_{cavity}}{c(2\alpha l_{active} - \ln(R_1 R_2))}. \tag{4.2}$$

Where $t_r = 2l_{cavity}/c$ is the round-trip time depending on l_{cavity}, the resonator length, and ϵ is the loss term. The length of the active medium is denoted by l_{active}, c is the speed of light, α is the small signal gain of the active gain medium, R_1 is the reflectivity of the output coupling mirror and R_2 is the reflectivity of the high-reflectance end mirror. All other length-independent losses can be seen as leakage through the high-reflecting mirror $R_2 = 1-\delta_m$. Here, δ_m represents Fresnel losses as well as scattering losses on optical surfaces. For Q-switching, the loss term ϵ must be modified to include a time-varying function:

$$\epsilon = 2\alpha l_{active} - \ln(R_1 R_2) - L(t). \tag{4.3}$$

Here, $L(t)$ represents the cavity losses, that is, the transmission through the cross-polarised setup. Typically, the Q-switch alternates between a low-loss and a high-loss state. In an ideal case, the loss function can be described by a step function, i.e. $L(t < 0) = L_{max}$ and $L(t \geq 0) = L_{min}$. This case will be referred to as fast Q-switching. However, when the pulse round-trip time becomes much shorter than the transition time of the loss function, the model for fast Q-switching is no longer applicable. In that case, the loss function must be modified

from an ideal step-function – for example, to an exponential function to account for the finite switching speed from the high- to low-loss state of the Q-switch. This is referred to as slow Q-switching.

As mentioned earlier, the rate Eg. (4.1) for the photon flux can be simplified in the case of Q-switching. The spontaneous emission term can be neglected because, once the stimulated emission builds up, the photon flux is much greater than the spontaneous emission. In Eq. (4.1) it is assumed that the resonator is filled with the active gain medium. However, when that is not the case the term for stimulated emission must be reduced by the ratio of the active gain medium length (l_{active}) to the resonator length (l_{cavity}). The rate equation for Q-switching can then be rewritten as:

$$\frac{d\varphi}{dt} = \varphi\left(c\sigma n\frac{l_{active}}{l_{cavity}} - \frac{\epsilon}{t_r}\right). \tag{4.4}$$

The photon flux φ is a direct result of the change in inversion density n, which can mathematically be described by:

$$\frac{dn}{dt} = -\gamma n\varphi\sigma c. \tag{4.5}$$

Degenerated states within the active laser ion are accounted for by $\gamma = 1 + g_2/g_1$. The degree of degeneracy is defined by the ratio of the degenerated states g_2/g_1. For example, when the ground state is not degenerated but the upper laser level is split into two states, then $\gamma = 1 + 2/1 = 3$.

The above formulas are sufficiently accurate to describe the laser dynamics within a three-level system. In a four-level system, the degeneration factor γ equals one, and γ can thus be interpreted as an 'inversion reduction factor' as it relates to the required pump power. For example, in a three-level system with no degeneracy, $\gamma = 2$, which means that one must pump twice as hard as in a four-level system to achieve the same inversion.

4.2.1 Fast Q-switching

Q-switches are usually designed to enable switching times in the order of a few nanoseconds or even less. Acousto-optical modulators (AOMs) typically feature switching times of a few nanoseconds, whereas saturable absorbers can achieve switching times down to a few picoseconds. This section is focused on the laser dynamics when fast Q-switches with

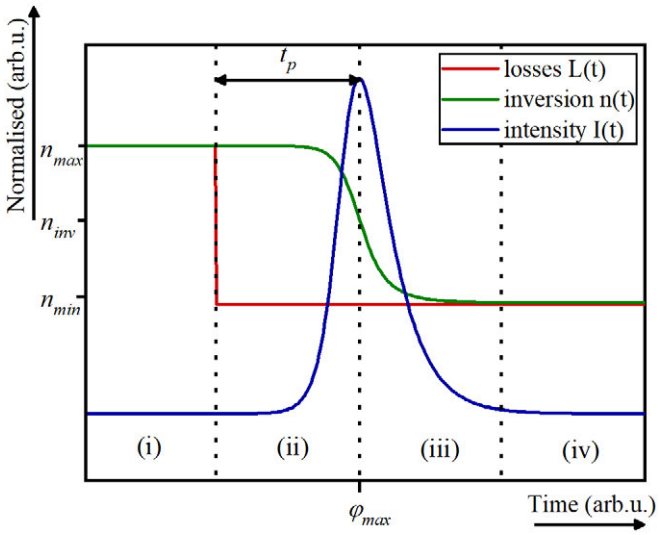

Figure 4.1: Schematic of the cavity dynamics of a Q-switched laser. An initial inversion is depleted when the loss function is switched from a high state to a low state. The pulse grows in intensity and reaches its peak when the inversion is exhausted.

switching times of a few nanoseconds are used. Even though the overall focus of the study is on slow Q-switching, the underlying laser dynamics are very similar. In this section, guidelines for optimising a pulsed laser utilising a fast Q-switch are developed. Those rules also apply to slow Q-switches.

The laser dynamics resulting from Eq. (4.4) and (4.5) are depicted in Fig. 4.1. To understand the dynamics, the process is subdivided into four stages:

(i) The active gain medium is pumped and an inversion builds up, until its final state is reached (n_{max}). This means that, for each laser ion that is pumped to the upper state, one decays to the ground state through spontaneous emission.

(ii) Once the losses are switched from a high- to a low-loss state, the gain greatly exceeds the cavity losses and a pulse builds up from spontaneous emission. The time between the sudden change in losses and the maximum flux is called the pulse build-up time, t_p. This time defines the initial build-up of the photon flux within the cavity, which initiates from a few spontaneously emitted photon(s) as stated in Eq. (4.1). It can be thought of as an avalanche getting started.

(iii) Due to the rapid pulse build-up, the initial inversion (n_{max}) is depleted and drops below the point where gain equals losses. The latter point marks the position of maximum pulse peak power (φ_{max}).

(iv) With net loss in the cavity there is no further growth, and thus the pulse dies out.

Simulations

It is crucial to be able to interpret the results of the rate equations shown above in order to optimise a Q-switched laser. In the present work the aim is to use a liquid crystal cell to realise a monolithic laser setup that has a cavity length as small as the active gain medium itself. In addition, the pulse peak power must be maximised. Therefore, the purpose of the following simulations is to identify the key parameters for optimisation, which are the resonator length and the modulation depth of the Q-switch. In particular, the aim is to find the parameter that has the greatest impact in further improving the laser performance. For the following simulations, the loss function used in Eq. (4.3) is defined as follows:

$$L(t) = e^{-\frac{t}{\tau}} \tag{4.6}$$

From the outcome of the simulations shown in Fig. 4.2, the following points can be extracted.

From Fig. 4.2a: The pulse width strongly depends on the resonator length and the modulation depth. Note that the modulation depth equals the initial loss minus the final loss state, as described in Section 3.4.4. In addition, a ratio $l_{cavity}/l_{active} = 1$ corresponds to a cavity being exactly as long as the gain medium (l_{active}), while a cavity length of 2 corresponds to a cavity being twice as long as the gain medium ($l_{cavity}/l_{active} = 2$). The shorter the resonator, the smaller the round-trip time and thus the pulse experiences more gain within the same time. A higher gain results in higher peak power as well as shorter pulse durations. In the case of a small modulation depth in combination with a long resonator, the pulse width asymptotically approaches a maximum value. Higher modulation depths will result in a higher net gain per unit time and thus result in a faster depletion of the inversion. A high gain favors self-pulse shortening by constantly suppressing the wings of the pulse while further amplifying the central part of the pulse.

From Fig. 4.2b: The higher the modulation depth, the greater the depletion of the stored energy. Thus the modulation depth defines how much energy can be extracted by the pulse. On the other hand, the resonator length does not influence the available energy within the resonator; therefore, the pulse energy does not depend on the resonator length.

From Fig. 4.2d: The pulse peak power decreases with the inverse exponential of the resonator length. Moreover, the peak power increases with the square of the modulation depth.

From these simulations the following conclusions can be drawn:

- The resonator should be as short as possible, ideally as short as the active gain medium.
- The modulation depth should be as high as possible.

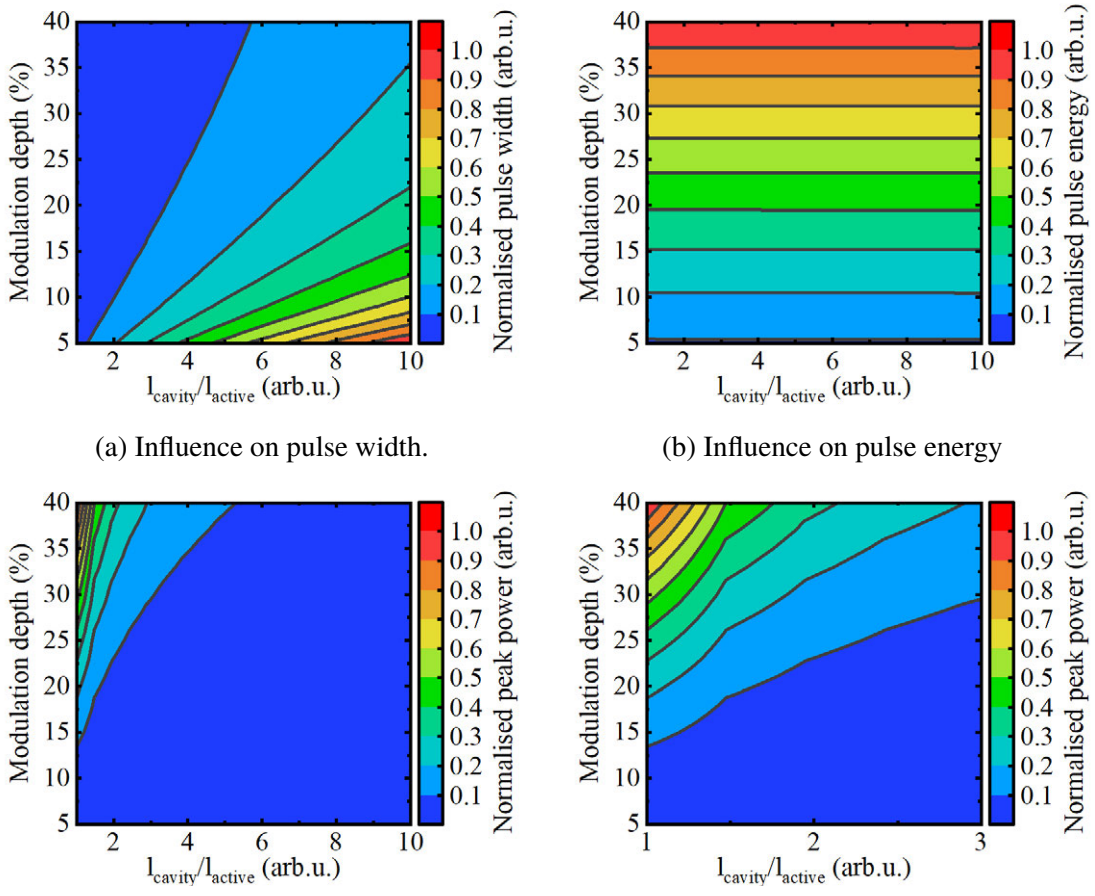

(a) Influence on pulse width.

(b) Influence on pulse energy

(c) Influence on repetition rate.

(d) Influence on Peak-power.

Figure 4.2: Laser dynamics of a fast Q-switched laser. The graphs show the influence of the modulation depth of the Q-switch and the ratio of the total cavity length (l_{cavity}) to the length of the gain medium (l_{active}) on the pulse width, the pulse energy and peak power. A ratio l_{cavity}/l_{active} = 1 corresponds to the cavity being exactly the length of the gain medium, while l_{cavity}/l_{active} = 2 corresponds to a cavity being twice as long as the gain medium.

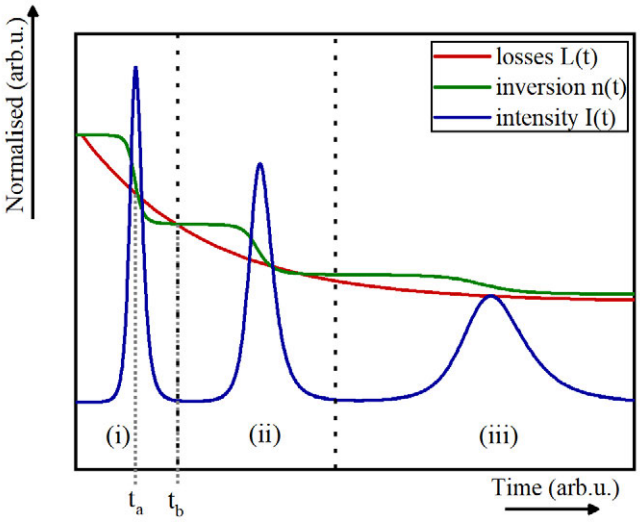

Figure 4.3: Graph of the laser dynamics of a slow Q-switch. Once the round-trip gain overcomes the cavity losses, a pulse will build up (i). The pulse will suppress the gain up to the point where the cavity losses are higher than the gain (t_a). As a result, the pulse sees no gain and will die out. However, the modulation function is still decreasing the cavity losses; at a certain time (t_b) the gain overcomes the losses again and initiates a second laser pulse (ii). This process will repeat until the final loss state (iii) is reached or the inversion is completely depleted.

4.2.2 Slow Q-switching

As discussed in Section 4.2, it is not always feasible to utilise a loss modulator that can switch on a timescale shorter than the pulse build-up time. When the switching speed is slower than the pulse build-up time t_p, this must be accounted for in the cavity loss function (see Eq. (4.3)). Note that, in general, slow Q-switching is not desirable because it results in decreased laser efficiency. As a general rule, the slower the switching the less efficient the laser.

The underlying dynamics of the pulse build-up when utilising a slow Q-switch are presented in Fig. 4.3. The build-up process can be subdivided into three sections.

(i) The internal cavity losses slowly change from high to low losses, ideally from 100 % to 0 %. A pulse starts to build up as soon as the gain overcomes the internal losses. At that point in time, the loss function $L(t)$ is still decreasing and has not yet reached its final state (0 %). The generated pulse reduces the inversion $n(t)$ and with that the gain. The pulse therefore only grows until the gain drops below a value equivalent to the cavity losses (t_a). From that point in time there is insufficient gain and the pulse cannot grow any further.

(ii) The cavity losses are still decreasing, which means that the remaining optical gain can overcome the losses again at $t = t_b$. As a result, a second pulse builds up that depletes the gain again. Due to the decreased slope of the loss function $L(t)$, the pulse has an increased pulse duration compared to the previous one, resulting in a lower pulse peak power. Note that, depending on the shape of the loss function $L(t)$, it is also possible that the second pulse has a higher pulse energy than the first one.

(iii) Once the loss function $L(t)$ is close to its final state, all the remaining stored energy is coupled into a last pulse. This last pulse can still carry substantial energy but has relatively low pulse peak power.

Simulations

The primary goal of the following simulations is to identify the key parameters necessary to optimise a slow Q-switched laser. Therefore, the effect of shortening the resonator length and increasing the switching speed is investigated. The simulations present a guideline for achieving shorter pulse durations and higher pulse peak powers. For slow Q-switching, the same rules apply as for fast Q-switching (Section 4.2.1), namely, the modulation depth should be increased and the resonator length decreased.

The difference from the simulations presented for fast Q-switching is that now the switching speed is varied in contrast to the modulation depth. To make it easier to compare the results, the modulation depth was kept constant at 100 %. The results of the simulations are presented in Fig. 4.4. The Q-switch was approximated by a linear loss function changing from high to low loss. It was found that this is sufficiently accurate since the loss function $L(t)$ in Section 3.4.4 (Fig. 3.21) can be considered as linear for electric field strengths above $30\,\mathrm{kV\,cm^{-1}}$. The loss function used in Eq. (4.3) becomes:

$$L(t) = 1 - m_s t \tag{4.7}$$

The benefit of a linear function is that it allows for direct comparisons regarding the switching speed. For example, increasing the switching speed by a factor of two changes the gradient by a factor of two (e.g. from $m_s = 1$ to $m_s = 0.5$).

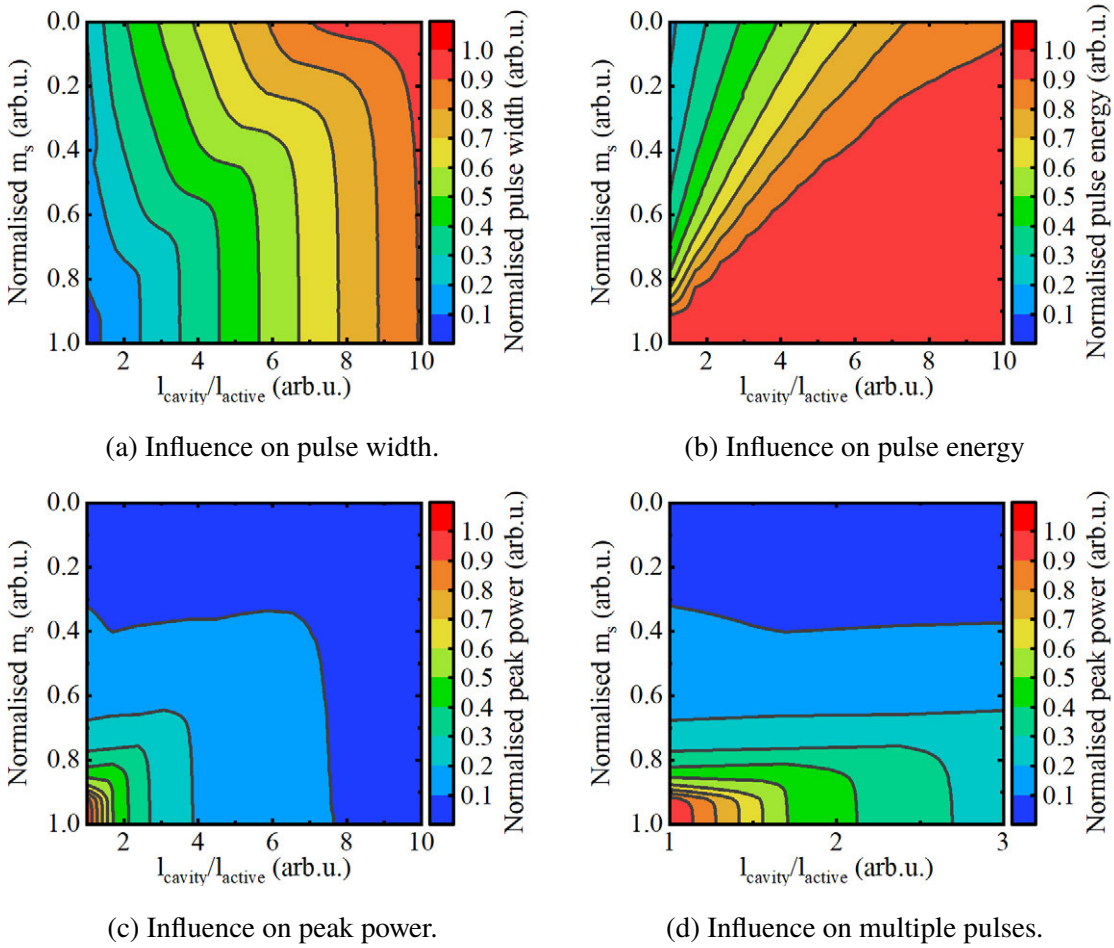

(a) Influence on pulse width.

(b) Influence on pulse energy

(c) Influence on peak power.

(d) Influence on multiple pulses.

Figure 4.4: Laser dynamics when employing a slow Q-switch. The presented graphs here show the influence of the ratio of total cavity length (l_{cavity}) to gain medium length (l_{active}) and switching speed (m_s is defined in Eq. (3.16) units are in % μs^{-1}) on laser performance. A ratio of $l_{cavity}/l_{active} = 1$ marks that the resonator is as short as the active gain medium itself. A ratio of $l_{cavity}/l_{active} = 2$ stands for a cavity twice the size of the active gain medium. In (a) a point is marked at which increasing the switching speed does not further decrease the pulse duration or the peak power.

From Fig. 4.4, the following points can be extracted:

From Fig. 4.4a: It is evident from the graph that at some point the switching speed does not further affect the pulse width. For example, at $l_{cavity}/l_{active} = 6$ and $m_s = 0.6$ further increasing the switching speed does not decrease the pulse duration nor does it increase the peak power or pulse energy. Reaching this point is the primary goal when optimising the laser setup. This point strongly depends on the pulse build-up time within the cavity, which is determined by the resonator length and the intracavity losses. Higher intracavity losses result in a larger pulse build-up time. Even though it is not practical when the primary goal is to achieve a short pulse width with a slow Q-switch, the key is to increase the intracavity

losses or the output coupling ratio. However, the downside is that the laser becomes less efficient (e.g. lower slope efficiency, smaller pulse peak power).

From Fig. 4.4b: The longer the resonator length, the higher the pulse energy at constant switching speed. Decreasing the switching speed (that means higher values for m_s) while keeping the resonator length constant results in lower pulse energy. This is a direct result of the available net gain and the time a pulse needs to build up. At a lower switching speed, the available net gain is less; however, the pulse build-up time is almost constant and, thus, the circulating pulse sees less gain within the pulse build-up timeframe. In general, the combination of resonator length and switching speed determines the pulse energy. Increasing the resonator length decreases the pulse build-up time and allows for a slower Q-switch while maintaining the pulse energy. Similarly, it is possible to reach the same pulse energy achieved with a fast Q-switch by increasing the intracavity losses or the output coupling ratio (both results in larger pulse build-up times).

From Fig. 4.4c: Shortening the resonator length exponentially increases the pulse peak power. This directly correlates to the gain per unit time; shortening the round-trip time increases the gain per unit time. Consequently, in the same timeframe the pulse traverses the gain medium more often and thus experiences more gain. The same is true for the switching speed; increasing the switching speed exponentially increases the pulse peak power. This is a result of available gain per round-trip as the modulation depth increases with the switching speed at a given instant in time. The comparison is illustrated Fig. 4.5a (slow switching speed) and Fig. 4.5c (fast switching speed). To summarise, both the resonator length and the switching speed greatly influence the peak power and must be optimised to achieve best performance.

To further understand the dynamics, the direct effects of decreasing the resonator length and increasing the switching speed are illustrated in Fig. 4.5. In order to obtain a more universal impression of the laser dynamics, an exponential loss function for $L(t)$ was used instead of the linear one previously shown. While a linear loss function $L(t)$ is sufficient for simulating the leading pulse, it fails to accurately describe the following pulses in shape and peak power. From Fig. 4.5a to Fig. 4.5b, the resonator length was decreased. As discussed in the previous section and shown in Fig. 4.4, a direct consequence is a reduction in pulse width.

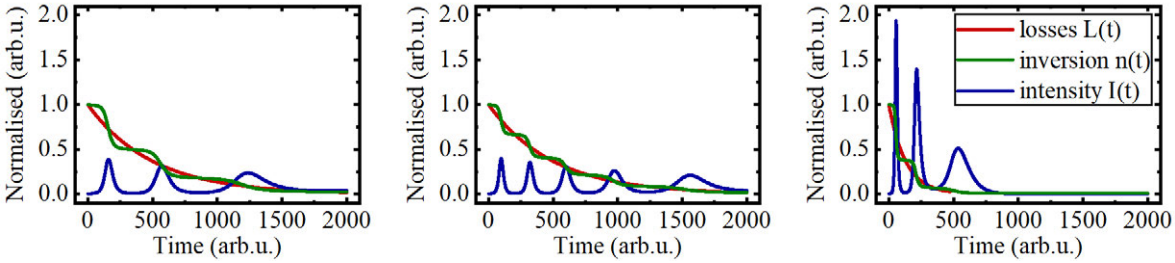

(a) (b) (c)

Figure 4.5: Dynamics of a Q-switched laser when decreasing the cavity length by a factor of two (from (a) to (b)) and decreasing the switching speed by a factor of two (from (b) to (c)).

In addition, the pulse energy decreases while the pulse peak power is constant. Shortening the cavity will shorten the round-trip time and, due to a slow switching speed, even more pulses will be emitted. From Fig. 4.5b to Fig. 4.5c, the switching speed was increased. As a result, fewer pulses will be emitted, as predicted in Fig. 4.4d. Consequently, each pulse carries more energy. The pulse peak power also increased as a result of the shorter pulse duration. From Fig. 4.5 it is evident that, to decrease the pulse width and increase the pulse peak power, the most effective approach is to increase the switching speed and to decrease the resonator length.

In summary, when optimising a slow Q-switched laser several parameters must be taken into account. Interpreting the simulation results shown in Fig. 4.4 and 4.5, one can draw the following key conclusions for optimisation.

- Increasing the switching speed is the primary goal when decreasing the pulse width and increasing the pulse peak power.
- A slow switching speed can be compensated for by choosing an appropriate resonator length (increasing the round-trip time).
- A decrease in resonator length in combination with slow switching speed will result in multiple pulses. Furthermore, it will reduce the overall laser efficiency.

4.3 Experimental Q-switching results

Throughout this section, the liquid crystal cell will be introduced into different cavity setups utilising different laser gain materials. The focus lies on femtosecond laser-written waveguides inscribed into different host glasses/crystals. Utilising those different hosts, it was possible to demonstrate Q-switching using a liquid crystal cell for different laser wavelengths ranging from the visible to the mid-infrared wavelength region. The main goal was to maximise the pulse peak power and to minimise the pulse duration for a given pump power. Throughout this work, the peak power is calculated on the base of a Gaussian fit. The latter performed well in fitting the experimental retrieved pulse shape and thus was appropriate in estimating the pulse peak power. Further, the slope efficiency and the onset of CW-breakthrough is investigated.

4.3.1 Yb: ZBLAN

The active gain medium, used in the setup shown in Fig. 4.6 was a heavy-metal fluoride glass (ZBLAN - ZrF_4, BaF_4, LaF_4, AlF_3, NaF_3) doped with 2.5 mol% ytterbium (Yb). The length of the Yb: ZBLAN chip and the embedded waveguides measured 10 mm. The fluorescence lifetime of Yb doped into ZBLAN is τ_{sp} = 1.81 ms and the emission cross-section is $\sigma_{em} = 0.46\times10^{-20}$ cm^2 [182]. The longer the fluorescence lifetime and the smaller the emission cross-section, the longer the pulse build-up time, which is favourable for a slow

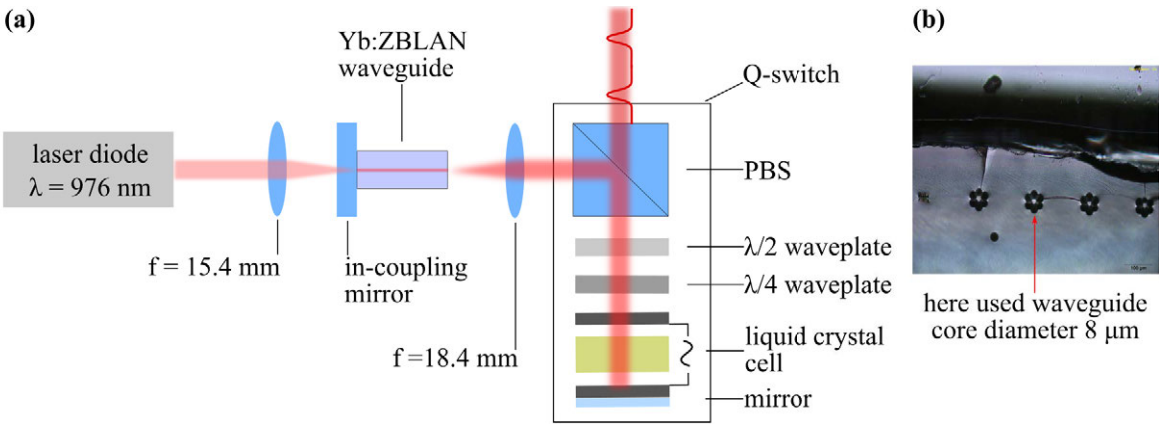

Figure 4.6: (a) Schematic of the laser setup. The resonator was formed by a dichroic in-coupling mirror butt-coupled to the waveguide and a short extended cavity including the liquid crystal cell. In this setup, the polarising beam splitter, in combination with the liquid crystal cell, acts as a actively-controlled variable output-coupling mirror. (b) Cross-section of the depressed-cladding waveguides.

Q-switch. Depressed cladding waveguides were inscribed using a femtosecond Ti:sapphire extended-cavity oscillator (FEMTOSOURCE XL 500 - Femolasers GmbH). In ZBLAN, femtosecond-laser inscription introduces a negative refractive index change and, thus, a cladding structure is inscribed that surrounds a unaltered core region (see Chapter 2.2.2). The laser source utilised for inscription has a centre wavelength of 790 nm, a repetition rate of 5.1 MHz and a pulse duration of 50 fs. The inscription beam was focused utilising a 100 × immersion oil objective with a NA of 1.25. The pulse energy on the target was 80 nJ and resulted in a refractive index change of $\Delta n \approx -1.2\times10^{-3}$. The sample was translated at a speed of 1000 mm/min. The waveguide core diameters ranged from 6 µm to 14 µm [183]. In the following experiments, the 8 µm diameter waveguide was used as it delivered the highest output power. The waveguide was pumped by a fibre-coupled laser diode (976 nm) that delivered a maximum pump power of 460 mW. It was focused into the waveguide through the coupling mirror via an aspheric focusing lens (f = 15.4 mm). The input-coupling mirror was highly transmitting (> 99.8 %) at 976 nm and high reflective (> 99.99 %) in the wavelength range 1010 nm to 1200 nm. Inside the laser cavity, the beam was collimated using an aspheric lens (f = 18.4 mm, anti-reflection coating 650 nm to 1050 nm). The collimated beam diameter measured approximately 3 mm. Inside the cavity, the beam was directed onto a polarising beam splitter and reflected through a half and a quarter waveplate onto the liquid crystal cell. The half and quarter waveplate were introduced into the setup for two reasons: (i) instead of rotating the liquid crystal cell itself, the half waveplate was rotated, which was more convenient as the liquid crystal was connected by two wires; (ii) the waveplates were used to maximise the modulation depth of the cells (see Section 3.4.4). The resonator length shown in Fig. 4.6 measured 250 mm and was limited in length by the size of the optical mounts used. The overall round-trip loss is defined by the losses of each component and can be calculated as follows:

$$L_{min} = 1 - (1 - L_{LC})(1 - L_{PBS})(1 - FL)(1 - PL). \tag{4.8}$$

As noted in Chapter 2, the waveguide propagation losses are represented by PL, the Fresnel losses are accounted for by FL, the loss introduced by the polarising beam splitter is L_{PBS} and the liquid crystal cell losses equals L_{LC}. Note that all losses represented in Eq. (4.8) are double-pass losses. The loss parameters for this particular setup are summarised in Table 4.2.

Table 4.2: Cavity losses of the setup shown in Fig. 4.6.

Component	Description	Variable	Single-pass loss x	Double-pass loss $1-(1-x)^2$
waveguide chip	propagation losses	PL	6.8 %	13.1 %
waveguide chip	Fresnel losses	FL	4.0 %	7.8 %
PBS	reflection losses	L_{PBS}	1.0 %	2.0 %
LC cell (3.3 μm)	transmission losses	L_{LC}		62.0 %
LC cell (9.0 μm)	transmission losses	L_{LC}		65.0 %

The overall cavity losses were estimated to be 70.1 % with the 3.3 µm thick liquid crystal layer and 72.5 % with the cell incorporating a 9.0 µm thick layer. It has to be mentioned that the losses introduced by the liquid crystal cell could be further reduced by an AR-coating. However, as the long-term goal was to directly glue the liquid crystal to the waveguide chip an AR-coating would be of no further use.

The liquid crystal cell in Fig. 4.6 required an AC signal in order to prevent it from being damaged. Applying a step function across a 3.3 µm thick liquid crystal layer with a frequency of 500 Hz and a maximum voltage amplitude of 4 V resulted in relaxation oscillation followed by a CW background, as depicted in the oscilloscope trace in Fig. 4.7a. In the bottom of each graph, the applied voltage waveform is depicted. In Figure 4.7a, the duty cycle was 50 % and the period was set to 2 ms. The maximum voltage amplitude was chosen to prevent the cell from being damaged. Reducing the duty cycle to 10 % diminishes the CW background, as shown by comparing Fig. 4.7a to Fig. 4.7b. The corresponding applied voltage waveform is shown in the bottom part of Fig. 4.7a and Fig. 4.7b respectively. Further shortening the duty cycle to approximately 1 % resulted in a single pulse (see Fig. 4.7d). Besides enabling single pulse operation, such short duty cycles allowed for an increase in the maximum applied voltage amplitude beyond the previously found damage threshold (30.3 kV cm^{-1} – see Section 3.4.4). Additionally, increasing the applied voltage amplitude improves the switching speed and thus maximises the peak power.

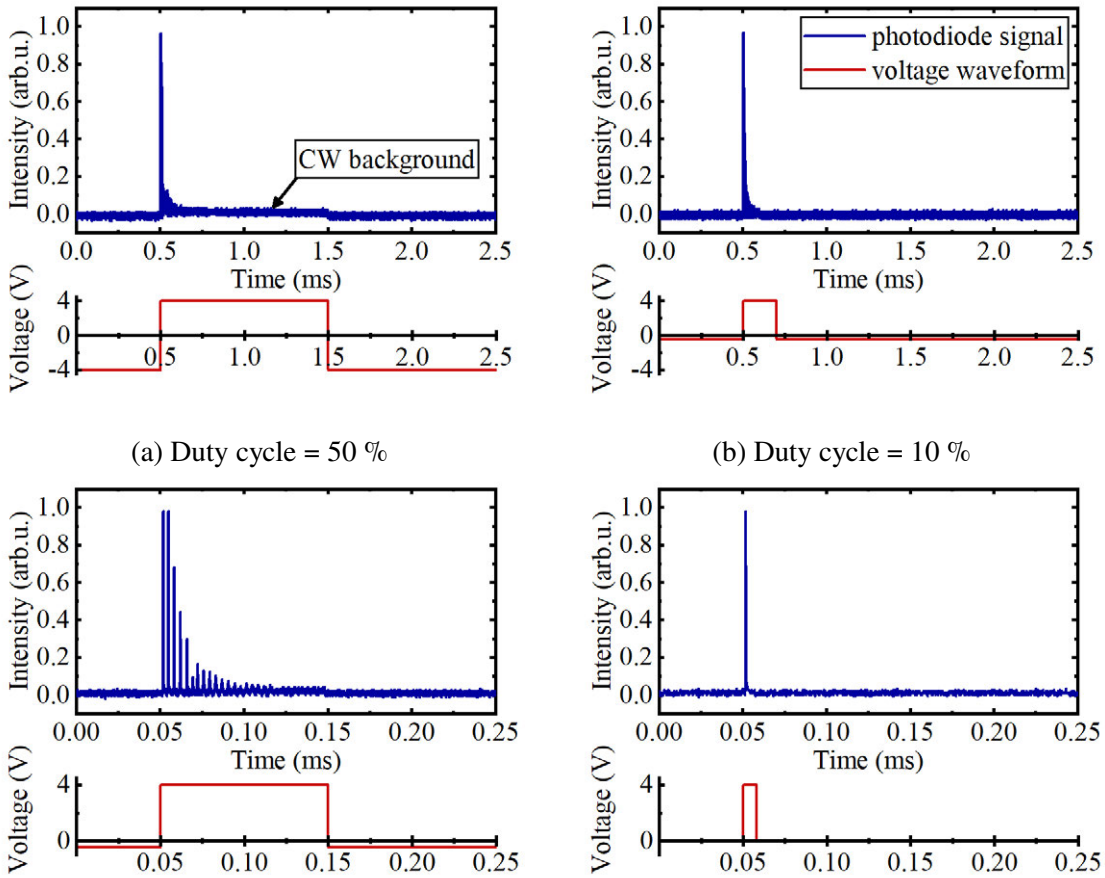

(a) Duty cycle = 50 %

(b) Duty cycle = 10 %

(c) Duty cycle = 10 %

(d) Duty cycle < 1 %

Figure 4.7: Oscilloscope trace of the emitted laser beam behind the cavity and the applied voltage waveform. Note that the voltage amplitude was 4 V for each measurement; however, to keep the time average zero a small negative voltage was applied when the waveform was not on a high state. Decreasing the duty cycle of the applied voltage waveform from 50 % in (a) to 10 % in (b) results in a reduction of almost all the continuous wave background. When zoomed in (c) it is possible to resolve multiple pulses that are apparent at a duty cycle of 10 %. Further decreasing the duty cycle to below 1 % in (d) results in a single Q-switched pulse.

Before characterising the setup, the relative angular position of the half and quarter waveplate required alignment to guarantee the highest possible peak power. This task was done empirically by changing the relative angles in sequence. The half waveplate angle was changed in 5° steps from 0° to 180°. Each time the angle of the half waveplate was changed, the quarter waveplate angle was altered from 0° to 360°. In Figure 4.8, the outcome of this iterative process is partially depicted. The highest peak power was recorded for each 5° angular step of the half waveplate while rotating the quarter waveplate through a full 360° cycle. As shown, the relative angle drifts towards smaller angles when increasing the applied voltage amplitude. Thus, when changing the applied voltage amplitude the half waveplate

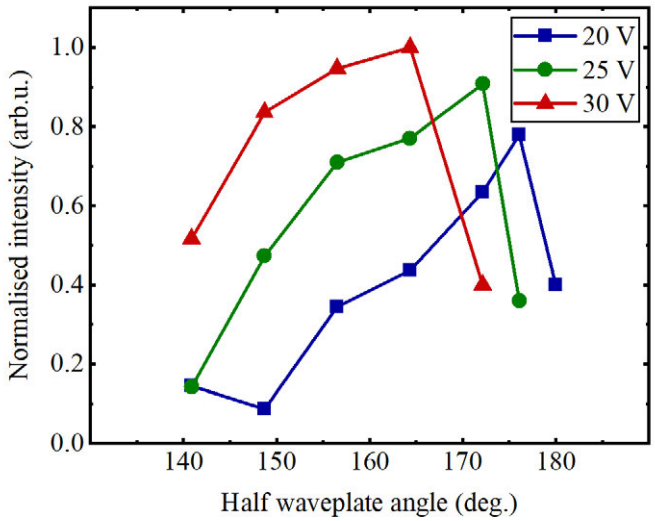

Figure 4.8: Peak height of the photodiode signal measured behind the output coupler of the laser as a function of half/quarter waveplate angle. The half waveplate angle was increased in 5° steps from 0° to 180°. Each time the half waveplate angle was increased, the quarter waveplate was rotated by 360° while the output signal was monitored by a photodiode. The purpose of this measurement was to record the highest possible peak power for each angular configuration. At a maximum applied voltage amplitude of 30 V, the highest peak was measured at a half waveplate angle of 160° and a corresponding quarter waveplate angle of 237°.

angle had to be readjusted slightly. For each laser setup utilising different active gain media, this process was repeated to determine the angular configuration that led to the highest peak power.

Two different liquid crystal cells were employed, one with a layer thickness of 3.3 µm and another one with a 9.0 µm thick layer. Both had a gold mirror directly coated to the back of the cell. Those two cells were similar in terms of reflection losses and thus suitable for direct comparison (see Table 4.2). To compare the laser performance using the two different cells, the same electric field strength was applied across the cells. Note that the voltage applied, U_+, refers to the amplitude that is measured from 0 V to the maximum voltage amplitude (see Fig. 3.19 in Section 3.4.4). To keep the electric field strength across the different cells constant, the voltage was increased by a factor of 9.0/3.3 when using the 9.0 µm cell instead of the 3.3 µm cell. Applying a voltage of $U_+ = 10$ V across the thinner liquid crystal cell resulted in a slope efficiency of $\eta = 1.4$ % at 5 kHz. The slope efficiency increased to $\eta = 2.1$ % when using a higher voltage of $U_+ = 30$ V (see Fig. 4.9a). Utilising the 9.0 µm thick cell, a slope efficiency of $\eta = 4.2$ % at 5 kHz was measured at an applied voltage of $U_+ = 30$ V. After increasing the voltage to $U_+ = 84$ V, the slope efficiency increased to $\eta = 7.9$ % for the same

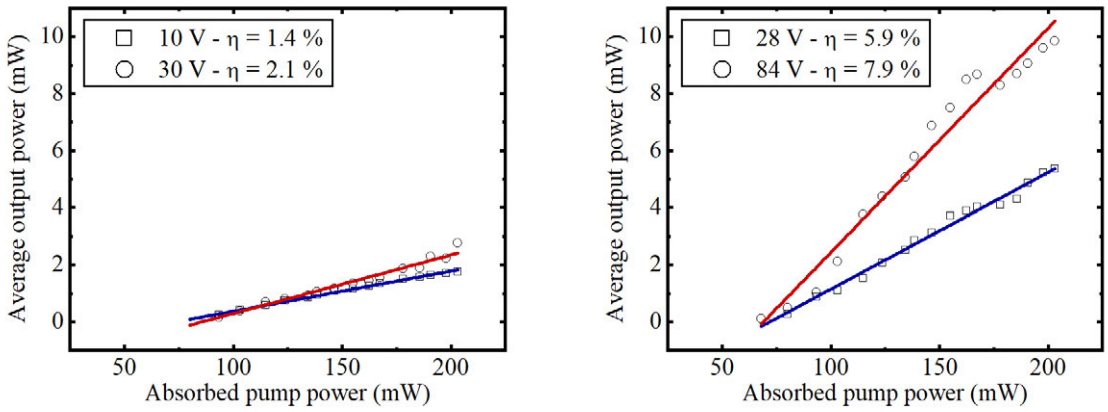

(a) (b)

Figure 4.9: Average output power at 5 kHz as a function of absorbed pump power for the (a) 3.3 µm and (b) 9.0 µm thick cell. The total birefringence introduced by the thicker liquid crystal cell increases at high applied voltages, resulting in a faster Q-switch and thus an increased slope efficiency.

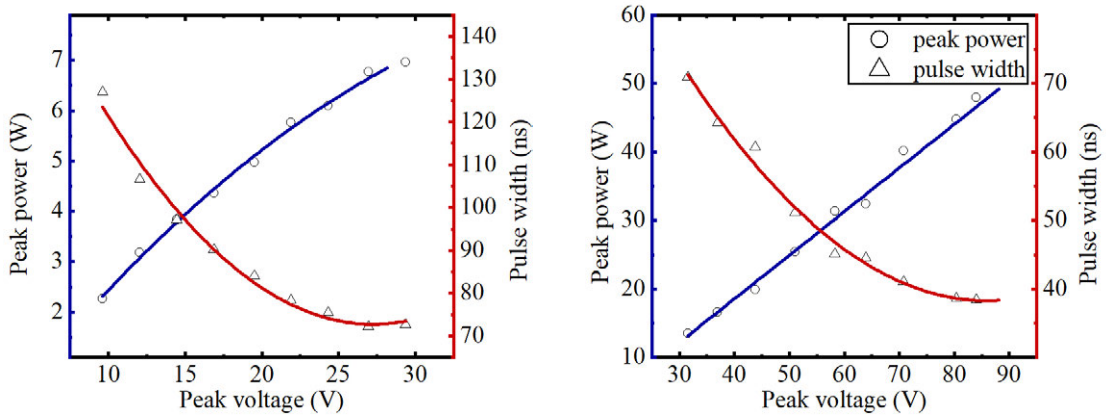

(a) (b)

Figure 4.10: Pulse width (red trace) and pulse peak power (blue trace) as a function of the applied voltage for the (a) 3.3 µm thick cell and the (b) 9.0 µm thick cell.

repetition rate (see Fig. 4.9b). The improvement in overall performance is consistent with the guidelines established in the beginning of this chapter. The switching speed m_s increases when the thickness of the liquid crystal layer and/or the amplitude of the applied voltage are increased (see Fig. 3.21). Another important quantity to analyse is the dependence of the pulse duration and pulse peak power on the applied voltage amplitude, U_+, for a given liquid crystal cell, as shown in Fig. 4.10. For the 3.3 µm thick cell, the pulse width at FWHM decreased from 127.1 ns down to 72.6 ns for voltages ranging from U_+ = 10 V – 30 V (corresponding to m_s = 4.0 % µs^{-1} to m_s = 9.0 % µs^{-1}). The pulse peak power increased linearly from 2.3 W to 7.0 W (estimation based on a Gaussian pulse). Using the 9.0 µm thick cell, the pulse width

decreased from 71 ns down to 38 ns, as shown in Fig. 4.10b. The peak power increased from 13.5 W to 49.0 W for voltages from U_+ = 30 V – 84 V, (corresponding to m_s = 10.5 % µs^{-1} to m_s = 36.0 % µs^{-1}). The oscilloscope trace of the output signal associated with the shortest pulse duration is shown in Fig. 4.11a. The spectral width was approximately 50 pm FWHM centred at 1016.02 nm and was independent of the applied voltage waveform (see Fig. 4.11b).

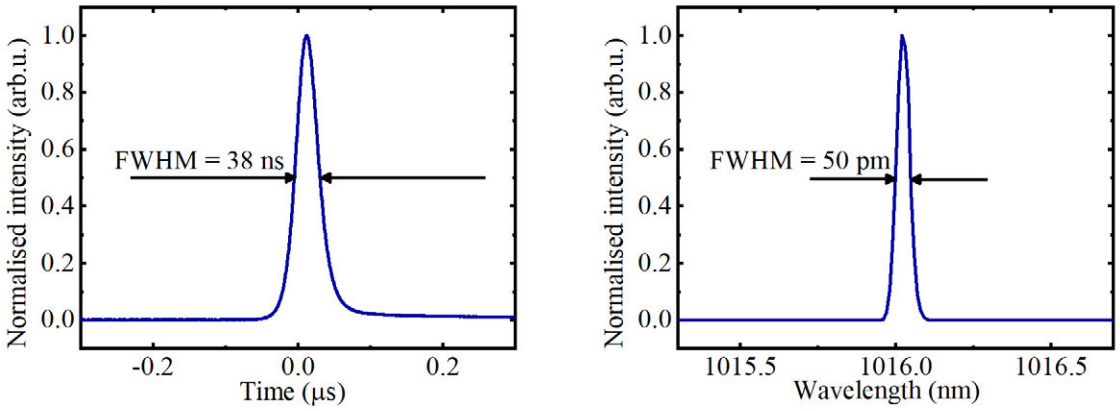

Figure 4.11: Laser characteristics at a repetition rate of 5 kHz utilising the cell with a 9.0 µm thick liquid crystal layer: (a) oscilloscope trace of pulse form; (b) emission spectrum of the laser output.

The average output power of the laser as a function of the repetition rate, using the 9.0 µm thick cell, is shown in Fig. 4.12. The output power increases linearly up to a repetition rate of 10 kHz (corresponding to a constant energy per pulse) after which it starts to saturate. Thus, the slope efficiency increases at higher frequencies, reaching as high as 22 % at 20 kHz with a (frequency-independent) laser threshold of 80 mW of absorbed pump power.

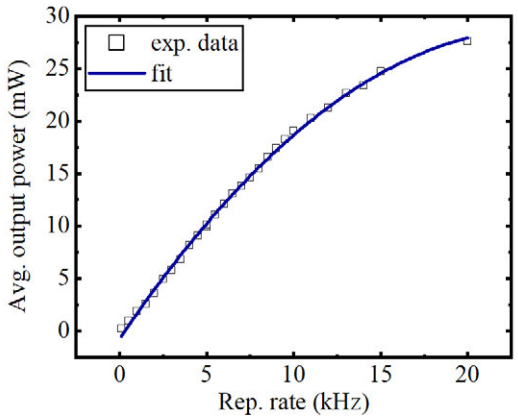

Figure 4.12: Average output power as a function of repetition rate for the 9.0 µm thick cell. The solid line (blue trace) shows a quadratic fit to the experimental data.

The model for slow Q-switching, presented earlier, was used to compare these results with the outcomes that could potentially have been achieved utilising a similar setup but with a commercially available Q-switch. The influence of the switching speed on the pulse width was the focus of this model. At constant round-trip losses, the pulse width is here presented as a quality factor of the laser source. The shorter the pulse width the better the laser performance, i.e. the higher the pulse peak power. The switching speed depends on the modulation depth (i) and the switching time (ii). In the following simulations, the consequence of changing each of those parameters is modelled separately.

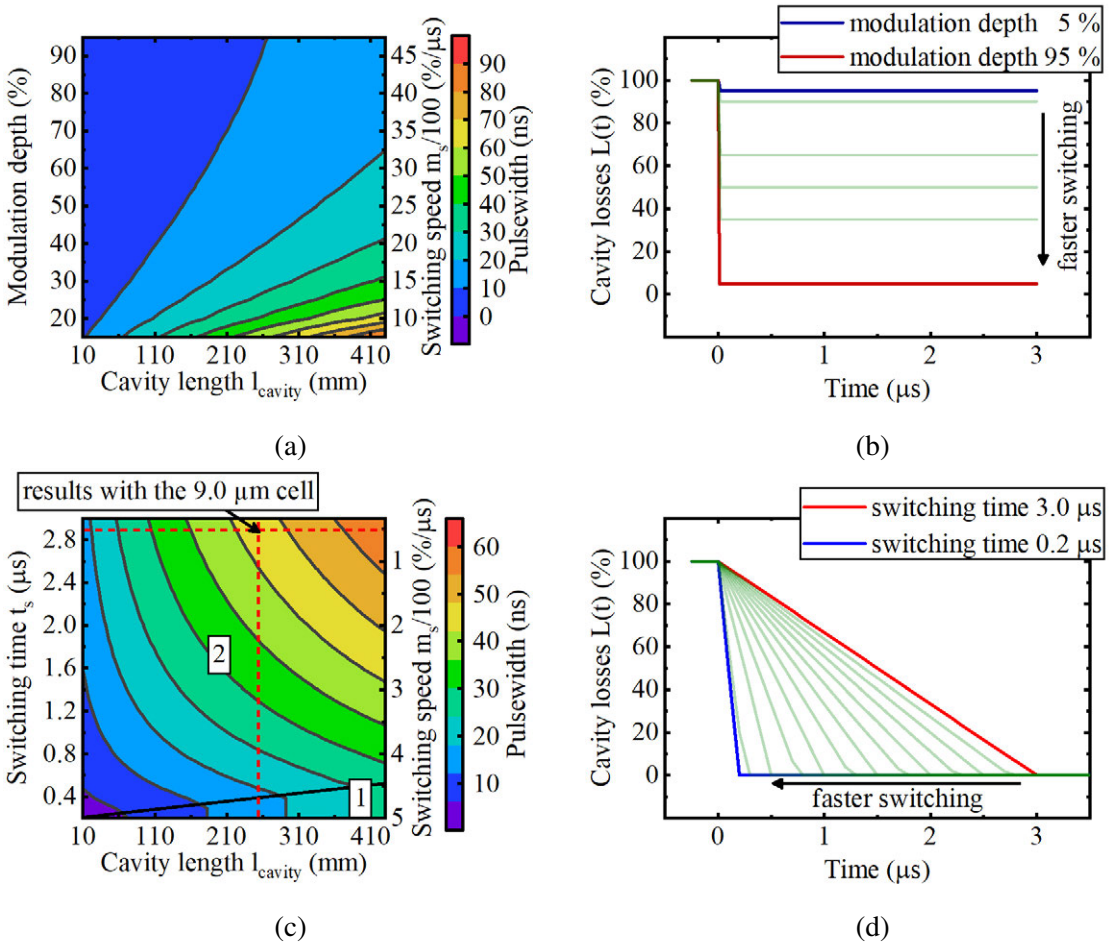

Figure 4.13: Simulated pulse width as a function of cavity length, modulation depth and switching time. (a) The smallest possible pulse duration (dark blue contour) is reached by maximising the modulation depth and minimising the cavity length. (b) The corresponding loss function ($L(t)$) for the simulations shown in (a). (c) Minimising the switching time (corresponding to a faster switch) and minimising the cavity length results in the shortest possible pulse duration; Region 1: switching time does not affect the pulse width; Region 2: pulse width depends on switching time. (d) The corresponding loss function ($L(t)$) for the simulations shown in (c).

For (i): the modulation depth was varied between 15–95 % and the switching time was kept constant at 20 ns. Note that a switching time of 20 ns was used because it also represents the typical switching time of commercially available active Q-switches (which is typically in the range of a few hundreds of picoseconds to hundreds of nanoseconds). Thus, as mentioned earlier the simulated data using a switching time of 20 ns, can be used to directly compare the slow Q-switch performance against a much faster commercially available active Q-switch. In Figure 4.13a, the results are depicted as a function of the modulation depth. The corresponding loss function $L(t)$ is depicted in Fig. 4.13b. The total resonator length (l_{cavity}) consists of two parts; the length of the active gain medium (l_{active}) and a short free space part ($l = l_{cavity} - l_{active}$). In the simulations, as well as in our experimental setup, the active medium had a length of $l_{active} = 10$ mm, which therefore represents the shortest possible cavity length. Figure 4.13a shows that the highest modulation depth and the smallest resonator length (ideal for an integrated waveguide laser geometry) result in the shortest pulse width, as expected.

For (ii): the switching time was varied from 0.2–3 µs in Fig. 4.13c while the modulation depth was kept constant at 100 %. Figure 4.13c shows that while a faster switching time initially decreases the pulse width, there is a point at which further reducing in switching time does not affect the pulse width (Region 1). Thus, a liquid crystal cell with a switching time at least close to this value (typically hundreds of ns) can be considered sufficiently fast. While the exact location of that point depends on design parameters such as the resonator length and the intracavity losses, it is evident that the liquid crystal does not have to switch as fast as commercially available AO or EO modulators in order to achieve a similar Q-switching performance. Note that, in the presented case the Q-switching performance refers to the pulse duration. The experimental results achieved earlier with the cell incorporating a 9.0 µm thick liquid crystal layer are marked in Fig. 4.13c. To reach Region 1, the switching speed should be increased by a factor of approximately 14.

According to the simulations in Fig. 4.13c, there is still potential for further optimising the laser by employing a faster switch. By increasing the liquid crystal layer thickness, the overall birefringence of the cell is increased, as is the relative change in birefringence when a voltage is applied. This results in an increased modulation depth and an effective decrease in switching time, which improves the overall laser performance (i.e. the pulse duration

becomes shorter and the peak power increases). The disadvantage of using thicker liquid crystal cells is that a higher voltage must be applied to keep the electric field strength (E) constant.

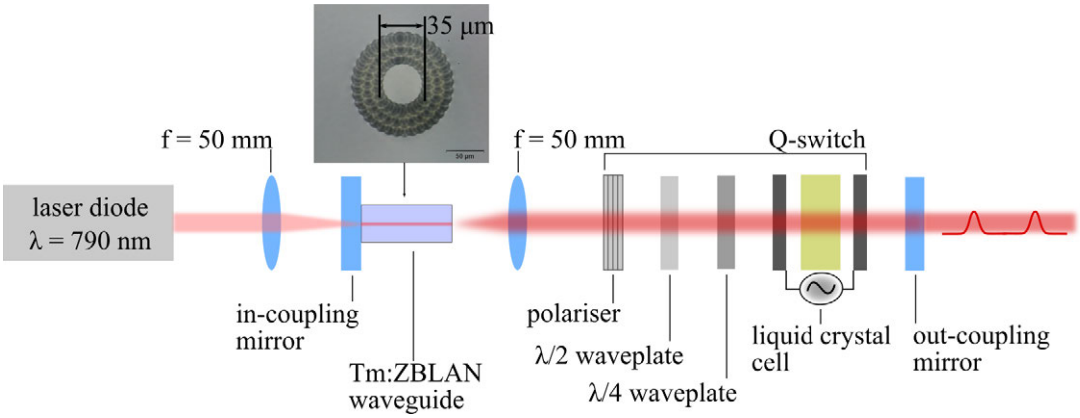

Figure 4.14: Schematic of the laser setup utilising a Thulium-doped ZBLAN chip as active gain medium. The depressed-cladding waveguide had a core diameter of approximately 35 µm. Two laser diodes (each emitting 350 mW, and selected to emit at a center wavelength of 790 nm) were multiplexed and focused (f = 50 mm) into the waveguide through an input-coupling mirror. Inside the cavity the beam is collimated (f = 50 mm) before it is coupled out through a 6 % output coupler. The Q-switch is comprised of a thin film polariser in combination with two waveplates and the liquid crystal cell itself.

4.3.2 Tm: ZBLAN

As an active gain medium, a heavy-metal fluoride host glass (ZBLAN - ZrF_4, BaF_4, LaF_4, AlF_3, NaF_3) was doped with 2.0 mol.% thulium fluoride (TmF_3) [184]. The dimension of the Tm: ZBLAN chip measured 9 × 8 × 2 mm ($l_{active} \times w \times h$). The Tm^{3+} ion allowed for efficient two-for-one cross-relaxation when pumped at 790 nm. The ${}^3F_4 \rightarrow {}^3H_6$ transition, which is responsible for the wavelength of approximately 1.9 µm, has a fluorescent lifetime of τ_{sp} = 13.7 ms and an emission cross section of σ_{em} = 0.24×10^{-20}cm^2 [185, 186]. The long fluorescence lifetime and low emission cross-section (compared to the other setups: Yb: ZBLAN, Yb: YAG, Pr: SRA) result in a long pulse build-up time; thus, the Tm: ZBLAN is perfectly suitable for Q-switching utilising a slow Q-switch. The depressed cladding waveguides were inscribed using the inscription method and parameters previously used to inscribe the waveguides into Yb:ZBLAN. A translation speed of 1000 mm min^{-1} resulted in smooth waveguides. Waveguides of different diameters, ranging from 15 to 45 µm, were inscribed. For the following results the 35 µm waveguide was used, as it resulted in the highest output power. The laser setup is schematically shown in Fig. 4.14. The overall round-trip losses within the cavity are estimated to be 82.5 % for the cell with a 3.3 µm thick liquid crystal layer and 84.3 % for the 5.0 µm thick layer. Note that the losses were calculated on the base of Table 4.3 and Eq. (4.8). It has to be mentioned that when comparing Table 4.2 to 4.3 it is evident that the polariser used in this section introduces much higher losses. To clarify,

Table 4.3: Cavity losses of the setup shown in Fig. 4.14.

Component	Description	Variable	Single-pass loss x	Double-pass loss $1-(1-x)^2$
waveguide chip	propagation losses	PL	3.5 %	6.9 %
waveguide chip	Fresnel losses	FL	4.0 %	7.8 %
polariser	reflection losses	L_{PBS}	15 %	27.8 %
output mirror	output coupling	L_{LC}		6.0 %
LC cell (3.3 μm)	transmission losses	L_{LC}		70.0 %
LC cell (5.0 μm)	transmission losses	L_{LC}		73.0 %

two different kind of polarisers were used: for the setup Yb:ZBLAN a polarising beamsplitter with an AR-coating tailored for the specific wavelength was used as shown in Fig. 4.6. In the setup presented within this section (Tm:ZBLAN), as shown in Fig. 4.14, a thin film polariser is used that is not tailored for the specific wavelength and has no AR-coating.

The setup was pumped using two commercially available laser diodes (Thorlabs - LD785) with an output power of up to 350 mW, emitting at a wavelength of 790 nm. The two laser diodes were polarised and hence could be multiplexed via a polarising beam splitter to achieve double the pump power. The pump beam was then focused into the waveguide through an input-coupling mirror using a plano-convex lens $f = 50$ mm (AR coated from 650 to 1050 nm). The input-coupling mirror was highly reflective for the wavelength at 1880 nm and highly transmissive for the pump wavelength at 790 nm. The beam was collimated within the cavity by a plano-convex lens $f = 50$ mm (AR coated from 1.65 to 3.0 µm). The collimated beam diameter within the cavity measured approximately 1 mm. The collimated beam was then passed through a thin film polariser and a half and quarter waveplate before it was transmitted through the liquid crystal cell onto the output-coupling mirror. The dielectric polariser was designed for a wavelength of 1550 nm, however used at 1880 nm the transmission measured 85 % and the extinction ratio (1:20) was sufficient for the study purpose. Three different output-coupling mirrors (4 %, 6 %, 21 %) were tested, with the 6 % resulting in the highest output power at maximum pump power.

The liquid crystal cells employed, which all came without a gold layer coated to the back (in contrast to the ones used in the Yb: ZBLAN setup), had a 3.3 µm, 5.0 µm and a 9.0 µm thick liquid crystal layer. The double-pass losses of those cells were measured at 70 % for the cell with a 3.3 µm thick layer, 73 % for the 5.0 µm thick layer and 79 % for the 9.0 µm thick layer. Unfortunately, the cell with a 9.0 µm thick layer was of insufficient quality and could

not be used for comparison. As mentioned in Chapter 3, due to reproducibility issues in the fabrication of the cells there is variation in the double-pass transmission losses of ±10 %. Thus, only the cells with a 3.3 µm and a 5.0 µm thick liquid crystal layer were used. For comparison, the same electric field strength was applied across both cells. For the 5.0 µm cell the voltage was thus increased by a factor of 5.0/3.3 compared to the 3.3 µm cell.

Applying a voltage of $U_+ = 40$ V for up to 2.5 µs across the 3.3 µm thick cell resulted in a slope efficiency of 1.0 % (see Fig. 4.15). Using the 5.0 µm cell, a slope efficiency of 0.92 % was achieved (see Fig. 4.15). Note that the 5.0 µm cell would be expected to be faster than the 3.3 µm cell, but also introduces higher losses. In the present case the 5.0 µm cell introduced 3.0 % higher losses, which is also reflected in an increased laser threshold for the 5.0 µm thick cell (336 mW of incident pump power compared to 300 mW for the thinner 3.3 µm cell).

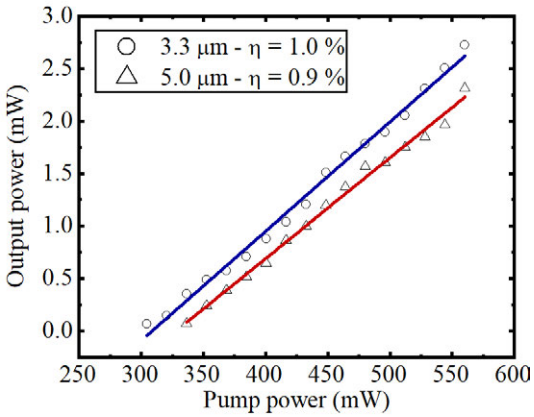

Figure 4.15: Average output power as a function of pump power for the 3.3 µm and the 5.0 µm thick liquid crystal layer. The total birefringence introduced by the liquid crystal cell increases for a higher applied voltage and a thicker layer, resulting in a faster Q-switch and thus an increased slope efficiency. However, for the case presented here the cell with the 5.0 µm thick layer introduced higher transmission losses.

In Fig. 4.16, the relationship between voltage, peak power and pulse duration is recorded at a repetition rate of 5 kHz. When increasing the voltage, the modulation depth and the switching speed increase. According to the model presented in Section 4.2.2, the pulse duration should decrease and the peak power increase under these conditions. This can be seen for both the 3.3 µm and the 5.0 µm cell. For the 3.3 µm cell, the pulse duration decreases from 512 ns (FWHM) to just above 256 ns (see Fig. 4.16a). The peak power increases from 1 W to 2 W. Using the 5.0 µm cell, the pulse duration decreases from 330 ns to just below 250 ns when increasing the applied voltage from $U_+ = 40$ V to $U_+ = 90$ V (see Fig. 4.16b). Accordingly, the peak power increased from 1.2 W to above 2.3 W (Gaussian

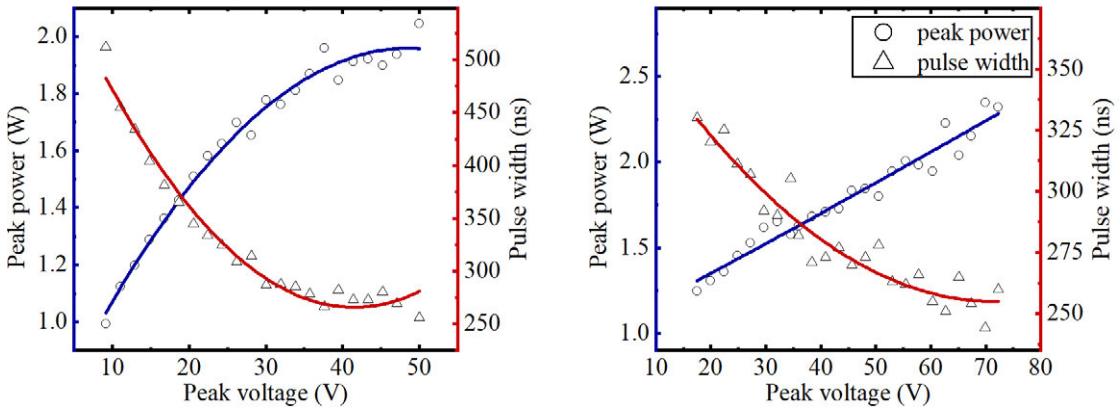

Figure 4.16: Peak-power (circles) and pulse width (triangles) as a function of the applied voltage for the (a) 3.3 µm thick and the (b) 5.0 µm thick liquid crystal layer. The blue and red curves represent polynomial fits to the experimental data.

pulse approximation).

In order to use the laser as a seed source to drive nonlinear optical processes, it is desirable to increase the peak power to the highest possible value. Therefore, both setups were characterised for low repetition rates with the aim of maximising the peak power. In Fig. 4.17 the repetition rate was decreased from 15 kHz down to 0.9 kHz for the 3.3 µm cell and to 0.8 kHz for the 5.0 µm cell. At lower repetition rates the laser became unstable, due to the onset of relaxation oscillations in the low-Q state. The applied voltage (see Fig. 4.17a) across the 3.3 µm cell measured $U_+ = 40$ V and $U_+ = 60$ V for the 5.0 µm cell. For the 3.3 µm cell, the pulse duration decreased from 748.5 ns at 15 kHz to 88.0 ns below 1 kHz. At 0.9 kHz, the highest pulse peak power recorded was 21.0 W before unwanted lasing occurred at a repetition rate around 0.8 kHz. Note that increasing the cavity losses, e.g. with a higher output coupling ratio, would shift the threshold for CW breakthrough to even lower repetition rates. When decreasing the repetition rate from 15 kHz to 0.8 kHz using the 5.0 µm cell, the pulse duration decreased from 780.0 ns to 64.0 ns (see Fig. 4.17b and Fig. 4.18a). The peak power reached a maximum of 27.4 W before parasitic lasing occurred below 0.8 kHz. As mentioned earlier, the collimated beam diameter within the cavity was approximately 1 mm. A peak power of 27.4 W behind the output coupler (6 % output coupling) corresponds to an intracavity peak power of 456.7 W. The peak intensity on the liquid crystal cell was as high as 58.1 kW/cm^2 without any signs of damage. The spectral width measured approximately 11.61 nm and was centred around 1877.7 nm, as shown in Fig. 4.18b.

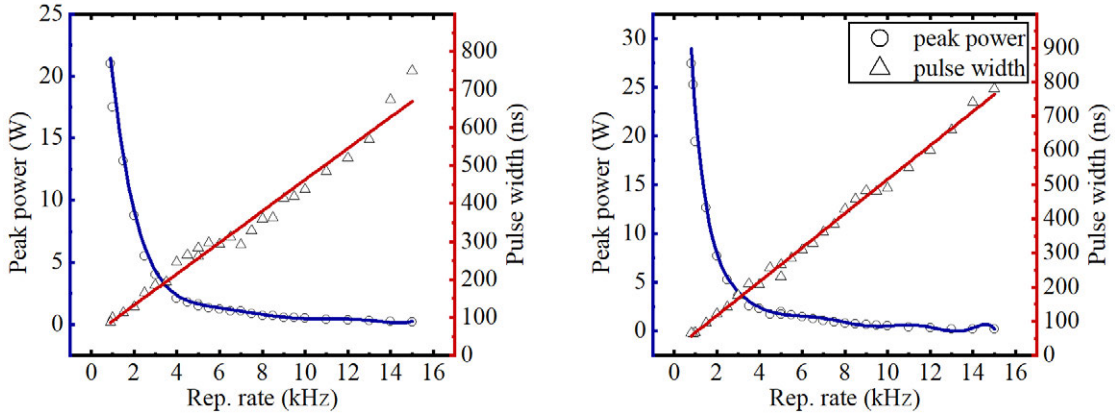

(a) (b)

Figure 4.17: When reducing the repetition rate the peak power increases and the pulse width decreases. In (a) the liquid crystal cell with a 3.3 µm thick layer was employed and a total peak power of 21 W was reached. In (b) the cell with a 5.0 µm thick layer was introduced into the cavity. Due to faster switching speed compared to the 3.3 µm thick layer, the peak power reached values of up to 27.4 W.

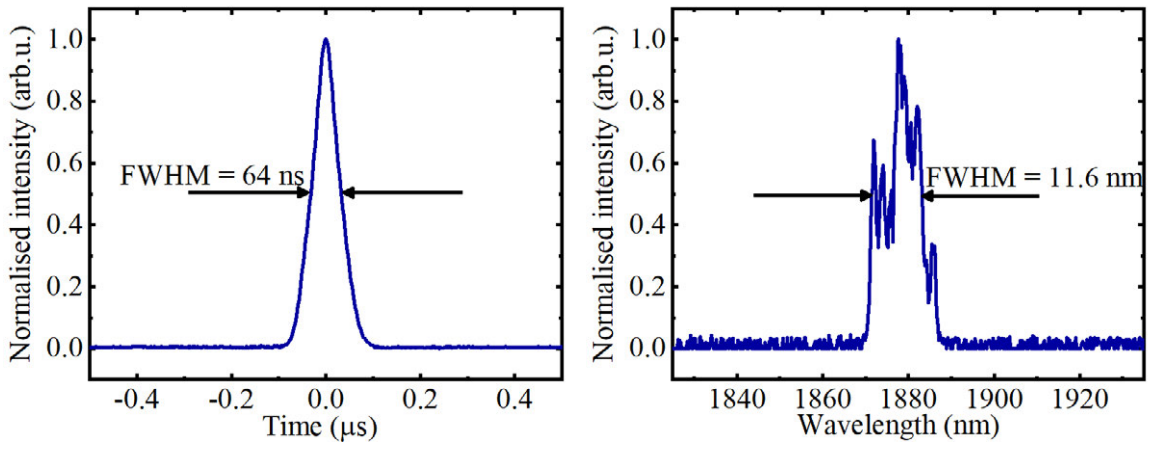

(a) (b)

Figure 4.18: Laser characteristics at a repetition rate of 0.8 kHz utilising the cell with a 5.0 µm thick liquid crystal layer: (a) oscilloscope trace of pulse form; (b) emission spectrum of the laser output.

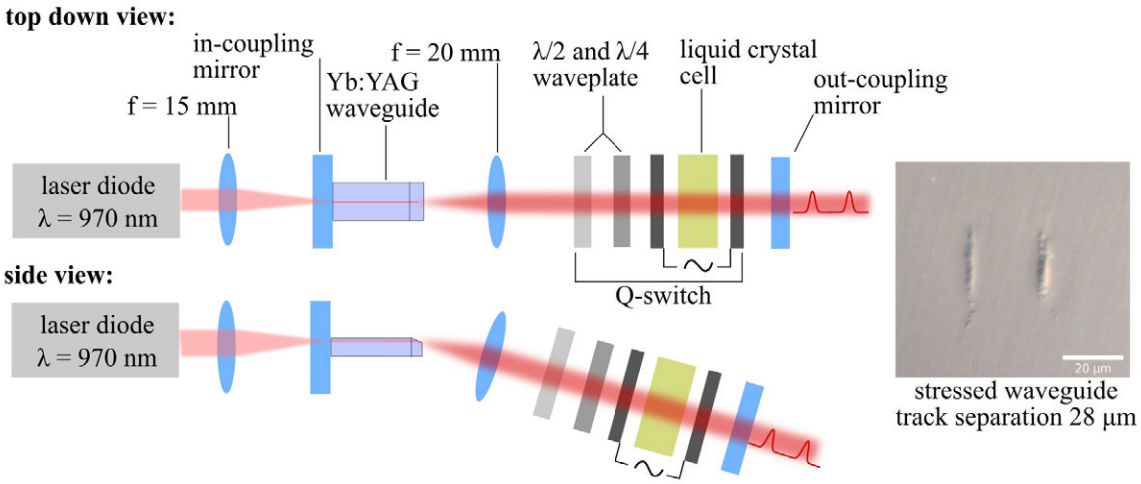

Figure 4.19: Schematic setup used with the Yb:YAG waveguide. A high-brightness distributed Bragg reflector tapered-diode laser was used for pumping the active gain medium. The pump beam was focused (f = 15 mm) through an input coupler onto the end of the waveguide. The chip end-facet facing the liquid crystal was polished at Brewster's angle to reduce cavity internal reflection losses. Within the resonator, the beam was collimated (f = 20 mm) before being transmitted through a waveplate configuration towards the liquid crystal cell (9.0 µm thick layer). A 20 % output coupler formed the end of the resonator.

4.3.3 Yb:YAG

Ytterbium (Yb)-doped yttrium aluminum garnet $Y_3Al_5O_{12}$ (YAG) active gain medium is a crystalline material; thus, inscribing depressed-cladding waveguides was not possible (see Section 2.2.2). Instead, two parallel damage tracks were inscribed to induce a stress field between them to act as a waveguide. The benefit of such waveguides is that they establish a strong polarisation dependency [21, 79, 187–189] and thus greatly simplify the laser setup. The waveguides were inscribed into the crystalline active gain medium utilising a Ti: sapphire chirped-pulse amplification laser system (Clark-MXR CPA-2010). The writing laser system emitted at a wavelength of 775 nm with a pulse duration of 150 fs and a repetition rate of 1 kHz [79]. The tracks were inscribed with a pulse energy of 1.5 µJ. Two adjacent damage tracks, with a separation of 28 µm, were each written with a translation speed of 25 µm s^{-1}. The waveguides were located 345 µm below the chip surface. The length of each waveguide within the active gain medium measured approximately 9.3 mm. The end facet of the chip facing the liquid crystal cell was polished at Brewster's angle in order to reduce the reflection losses within the cavity. As a result of the waveguide geometry, only one polarisation direction is guided, which makes it possible to build a laser setup without any additional polariser involved. The simplified setup is shown in Fig. 4.19. The overall round-trip losses

Table 4.4: Cavity losses of the setup shown in Fig. 4.19.

Component	Description	Variable	Single-pass loss x	Double-pass loss $1-(1-x)^2$
waveguide chip	propagation losses	PL	11.4 %	21.5 %
waveguide chip	Fresnel losses	FL	7.3 %	14.1 %
output mirror	output coupling	L_{LC}		20.0 %
LC cell (9.0 μm)	transmission losses	L_{LC}		72.0 %

within the cavity were calculated to be 84.9 % (based on Table 4.4 and Eq. (4.8)).

A high-brightness distributed Bragg reflector tapered-diode laser (DBR-TPL) was used as the pump source [187]. The pump wavelength (at 970.5 nm) was fine-tuned to achieve the highest possible output power when pumping the waveguide. The collimated pump beam passed through a Faraday isolator to suppress any back reflections and was focused by an aspheric lens f = 18.4 mm (AR coated for 970 nm) through a dielectric mirror into the waveguide. The dielectric mirror was highly reflective at 1030 nm and low reflecting for the ≈ 970 nm pump beam. The mirror was glued onto the end facet of the waveguide chip. Within the cavity, the laser beam was collimated by a bi-convex lens with a focal length of f = 11 mm (AR coated for 1030 nm). The beam was then passed through a half and a quarter waveplate before it was transmitted through the liquid crystal cell (9.0 µm layer thickness) and reflected back by an output coupling mirror (R = 80 %). The output coupling mirror was chosen when testing two different output couplers (relative transmission of 10 % and 20 %). At constant pump power, the output coupler with 20 % led to the highest output power and thus was used for the following characterisation.

The active laser ion (Yb) was doped at 7 % into the host material (YAG). Beside the much higher doping concentration compared to the Yb: ZBLAN (2.5 %) setup, the emission cross-section (σ_{em} = 2.2×10^{-20} cm^2) is larger and the upper-state lifetime (τ_{sp} = 0.95 ms) of Yb: YAG [190] is smaller than that for Yb: ZBLAN (σ_{em} = 0.46×10^{-20} cm^2, τ_{sp} = 1.8 ms) [182]. The resulting intrinsic gain of the Yb: YAG chip is higher compared to the Yb: ZBLAN chip. As a result, the pulse build-up time is significantly shorter and, thus, the switching time should be shorter compared to previous setups (Yb: ZBLAN and Tm: ZBLAN) to achieve single pulse operation. The results presented here were achieved by using the 9.0 µm thick liquid crystal layer cell (without a mirror coated to the back-side). As shown in Section 3.4.4, the thicker the liquid crystal layer the faster the switching speed. Note that, in the previous

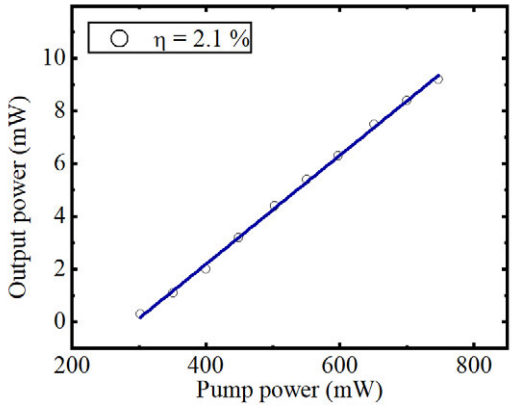

Figure 4.20: Slope efficiency measured for the Ytterbium-doped YAG Q-switched laser source.

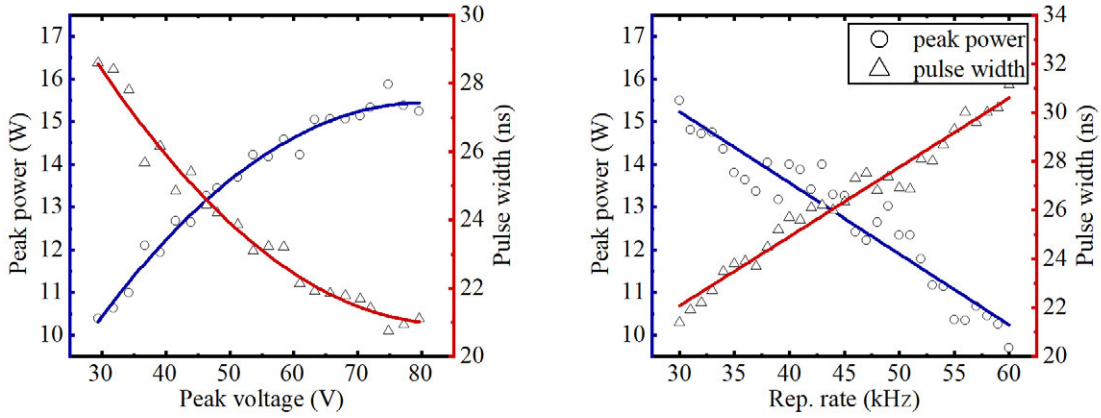

(a) (b)

Figure 4.21: Characteristics of the laser performance utilising Ytterbium-doped YAG as an active gain medium. In (a) peak power (blue trace) and pulse width (red trace) are shown as a function of the applied voltage with a 9.0 µm thick liquid crystal layer. In (b) the repetition rate is altered and both the peak power and pulse width recorded.

setup using the Tm: ZBLAN chip (see Section 4.3.2), it was not possible to utilise that particular cell because the losses were too high to overcome with available pump sources. At an incident pump power of approximately 300 mW, the lasing threshold was reached and Q-switched operation was observed. Above an incident pump power of 800 mW, the laser became unstable and parasitic CW-lasing occurred. To prevent multiple pulses as a result of the short pulse build-up time, the switching time was reduced to 900 ns. When applying a maximum voltage of 80 V it was possible to achieve a slope efficiency of 2.1 % at 30 kHz (see Fig. 4.20).

In Fig. 4.21a, the pulse peak power and pulse duration are plotted versus the amplitude of the applied voltage. At U_+ = 30 V, the peak power measured 10.4 W and towards U_+ = 80 V

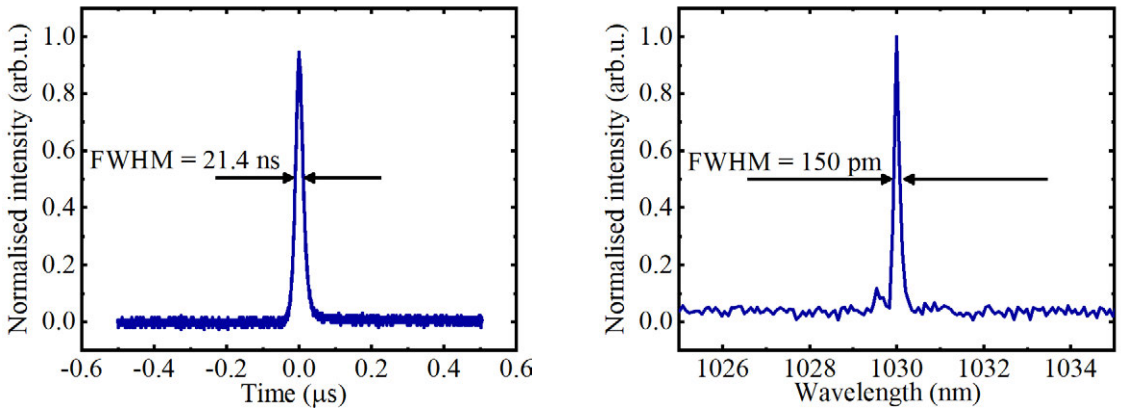

Figure 4.22: Laser characteristics at a repetition rate of 30 kHz utilising the cell with a 9.0 µm thick liquid crystal layer: (a) oscilloscope trace of pulse form; (b) emission spectrum of the laser output.

it increased to a maximum value of 15.2 W. Further, the pulse duration and peak power were measured as a function of repetition rate of the applied voltage waveform. The peak power decreased from 15.5 W to 9.7 W as the repetition was increased from 30 kHz to 60 kHz. At 30 kHz, the pulse duration measured 21.4 ns (FWHM) and the spectral width measured 150 pm (FWHM), centred around 1030.0 nm (see Fig. 4.22). Double pulses occurred at repetition rates below 30 kHz. Note that a saturation of the modulation depth, as previously reported in Section 3.4.4 for repetition rates above 50 kHz, could not be seen in these experiments. It is likely that a decreased duty cycle (due to switching times of 900 ns) resulted in a decreased modulation depth, which made the saturation effect less prominent.

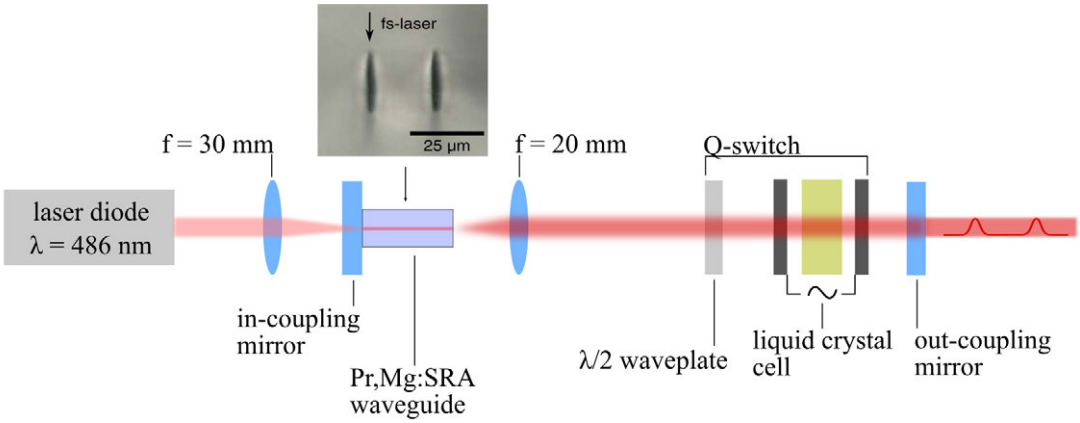

Figure 4.23: Schematic of the laser setup utilising a Praseodymium-doped SAR chip as an active gain medium. A frequency-doubled laser diode with 4 W output power emitting at 486.2 nm is focused (f = 30 mm) into the waveguide through an input-coupling mirror. Inside the cavity, the beam is collimated (f = 20 mm) before it is coupled out through a 30 % output coupler. The Q-switch is assembled by a combination of two waveplates and the liquid crystal cell itself.

4.3.4 Pr,Mg:SRA

The setup is shown in Fig. 4.23. As an active gain medium, trivalent praseodymium ions were doped into strontium hexaluminate $SrAl_{12}O_{19}$ (SRA). The dimensions of the Pr,Mg: SRA crystal was 19 × 6 × 2 mm ($l_{active} \times w \times h$) and the doping concentration of the Pr^{3+} was 3.6 at. % with respect to the Sr^{2+} ions [191]. Because strontium is divalent (two free chemical bonds) and the substituted praseodymium is trivalent (three free chemical bonds), a compensation charge is necessary; thus Al^{3+} is replaced by Mg^{2}+ [192]. The emission cross-section of Pr,Mg: SRA is $\sigma_{em} = 9.8{\times}10^{-20}$ cm^2 for the 644 nm transition and the upper-state lifetime τ_{sp} = 26 µs, which was measured at a dopant concentration of 5 % [193]. Stressed waveguides (two parallel damage tracks) were written into the crystalline material using a chirped-pulse amplification laser system (Clark-MXR CPA-2010) emitting at λ = 775 nm). The pulse duration for inscription measured 150 ns at a repetition rate of 1 kHz with pulse energies between 1.3 and 3.0 µJ [191]. The beam was focused 300 µm below the polished surface using an aspheric lens with a focal length of 4.51 mm and a NA of 0.55. The crystaline chip was moved laterally with a translation speed of 25 µm s^{-1}. The gain medium was pumped using a commercial available quasi–single-mode ($M^2 \geq 1.1$) frequency-doubled optical pumped solid-state laser (Coherent Genesis CX). The maximum output power of the pump setup measured 4 W at a wavelength of 486.2 nm. The pump beam was passed through an isolator before it was coupled through an input-coupling mirror into the waveguide using a

Table 4.5: Cavity losses of the setup shown in Fig. 4.23.

Component	Description	Variable	Single-pass loss x	Double-pass loss $1-(1-x)^2$
waveguide chip	propagation losses	PL	15.7 %	28.9 %
waveguide chip	Fresnel losses	FL	7.4 %	14.3 %
output mirror	output coupling	L_{LC}		30.0 %
LC cell (9.0 μm)	transmission losses	L_{LC}		71.0 %

30 mm focusing lens. The input-coupling mirror was highly transmissive for the pump beam at 486.2 nm and highly reflective from 500 nm to 800 nm. Inside the cavity, the divergent beam emitting from the waveguide was collimated with a 20 mm lens. The collimated beam passed through a half and a quarter waveplate and a 9.0 µm liquid crystal cell. The beam was eventually reflected by the output-coupling mirror, which had a transmission of approximately 30 % at a wavelength of 644.2 nm. The overall intracavity losses (on one round-trip) were calculated to be 87.6 % (based on Table 4.5 and Eq. (4.8)).

The upper-state lifetime of Pr^{3+} in strontium is $\tau_{sp} \approx 26\,\mu s$, which is approximately 20 times smaller compared to the previous setups (Yb: ZBLAN, Yb: YAG, Tm: ZBLAN). In addition, the emission cross-section (σ_{em} = 9.8×10^{-20} cm^2) is the highest out of those four setups. As a result, the pulse build-up time was the shortest and the switching time therefore had to be further decreased. At a maximum voltage amplitude of U_+ = 60 V, the switching time was set to 300 ns. At 20 kHz, the pulse peak power reached its maximum of 2.3 W (assuming a Gaussian pulse)(see Fig. 4.24a). The pulse width measured approximately 45 ns FWHM (see Fig. 4.24b). At repetition rates below 20 kHz, parasitic CW-lasing occurred. When the repetition rate was increased to 60 kHz, the pulse peak power decreased to 1.7 W. At 60 kHz, the pulse width measured 47.0 ns. Throughout the experiments presented here the laser was unstable, a result of jumping between two spectral lines, 644.2 nm and 724.4 nm. Note that the emission cross-section of the 724.4 nm transition is as high as 10×10^{-20} cm^2 and thus must be suppressed significantly over the 644.2 nm transition in order to prevent it from lasing. The output coupler had a transmission of 30 % at 644.2 nm and 40 % at 724.4 nm. Unfortunately, an output coupler that could fully suppress the 724.4 nm transition was not available at the time. As a result, the laser transition alternated between the 644.2 nm and 724.4 nm spectral line. In addition, the phase within the cavity became misaligned over time. In order to prevent phase misalignment, the half waveplate had to be adjusted every

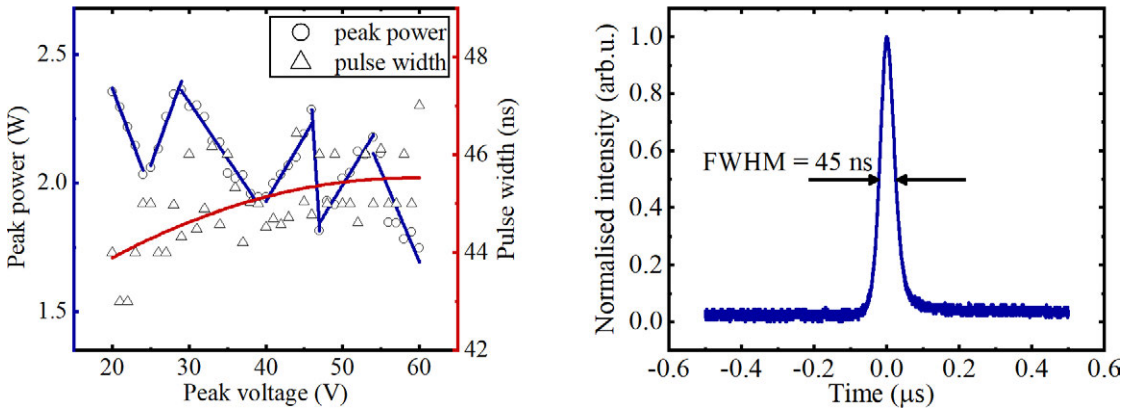

(a) (b)

Figure 4.24: Laser characteristics utilising the cell with a 9.0 µm thick liquid crystal layer. (a) Peak power (orange trace) and pulse width (blue trace) as a function of the applied voltage. Note that the laser was running in a unstable fashion, causing the zig-zag form of the measured peak power. (b) Oscilloscope trace of the pulse shape.

few minutes. In Fig. 4.24a, the fluctuations and misalignment over time is reflected in the varying slopes in the fitted function. Note that while recording the measurement the peak voltage increased at a steady rate. Points where the slope changes from negative to positive mark the point where the laser was realigned using the half waveplate. The sawtooth form of the fitted function and the realignment of the half waveplate indicate that the laser constantly runs out of phase. The misalignment is believed to be a result of temperature fluctuation, which could be solved by active cooling of either (or both) the active laser medium or (and) the liquid crystal cell.

Table 4.6: A summary of laser performance utilising a liquid crystal cell as an active Q-switch for different active gain media.

Wavelength (nm)	**Avg. power (mW)**	**Rep. rate (kHz)**	**Pulse width (ns)**	**Pulse energy (μJ)**	**Peak power (W)**
1878	1.5	0.8 - 14	64	1.9	27.4
1016	10.2	0.1 - 20	38	2.0	49.0
1030	12.0	30 - 80	24	0.4	15.5
644	2.1	20 - 60	45	0.1	2.3

4.4 Conclusion

In this chapter, several different active medium host materials were used in combination with various laser ions to realise active Q-switched waveguide laser sources. The waveguide geometry of the active gain medium is essential, as it offered high gain to overcome the losses introduced by the liquid crystals. In fact, in most waveguide lasers the gain is sufficient to build a laser cavity based solely on Fresnel reflections from the end facets [187]. The liquid crystal cell proved to be a promising addition to commonly available Q-switches. It enables pulsed laser sources of the size of a passively Q-switched laser but with the advantages of a bulky active Q-switched laser. Those benefits include nanosecond pulses accompanied by peak powers in excess of several watts. Furthermore, the repetition rate, unlike with passive Q-switches, is tuneable on demand by changing the applied voltage waveform. The laser sources investigated encompass laser emission ranging from the visible to the mid-infrared wavelength region (see Table 4.6). Laser emission at 1878 nm was achieved by making use of Thulium as an active ion. The repetition rate was tuneable between 0.8 kHz and 14 kHz. The highest peak power of 27.4 W was accomplished with a pulse duration of 64 ns. Furthermore, when employing Ytterbium a wavelength of 1016 nm was attained. It operated over repetition rates ranging from 0.1 Hz up to 20 kHz. The maximum peak power of 49 W was reached with a pulse duration of 40 ns at a repetition rate of 5 kHz. Additionally, stressed waveguides in a crystalline host material exhibit strong polarisation-dependent losses. Thus, it was possible to simplify the prior used setup by removing the thin film polariser. The Yb:YAG laser operated at 1030 nm and repetition rates ranged from 30 kHz to 80 kHz. A maximum peak power of 15.5 W with a pulse width of 24.4 ns was validated. Lastly, utilising praseodymium as an active laser ion it was possible to achieve a pulsed laser source emitting at the wavelength of 644 nm. The repetition rate was tuneable from 20 kHz to 60 kHz. The pulse width demonstrated was as short as 44.7 ns. The pulse peak power reached its

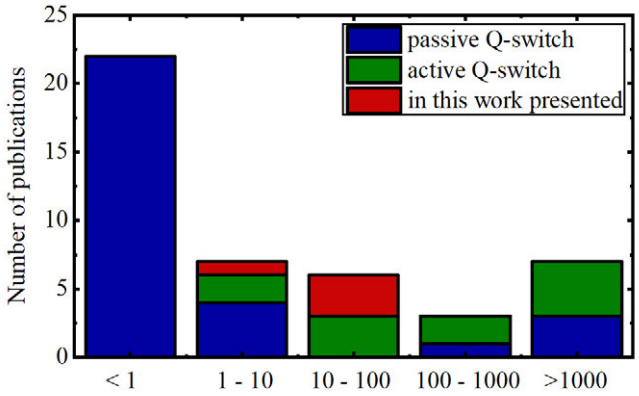

Figure 4.25: Overview of a cross section of reported Q-switched waveguide laser sources. Blue bars indicate demonstrated work using passive Q-switches. The green bars give an indication of published active Q-switched waveguide lasers. It can be seen (red bars – not published) that active Q-switched laser sources investigated in this thesis are well positioned on the upper end of the list of similar-sized passive Q-switched lasers. It must be mentioned that the blue bars on the far right reach high peak powers because of pump powers well above 1 W. The underlying data is from Table 4.1.

maximum of 2.3 W at 20 kHz. In this study, the glass-based waveguides proved to be superior to the crystal-based waveguide chips. With the glass chips pulse build-up time is slower as a result of a decreased emission cross-section and an increased upper-state lifetime. Slower pulse build-up times are in preferable for a slow Q-switch and thus it was possible to reach pulse peak powers up to 49 W.

Figure 4.25 provides an overview of published passive and active Q-switched waveguide lasers. The graph originates from Table 4.1 and gives an indication of the context of this work with regard to different laser pulse peak powers, ranging from 1 W to 1000 W. Blue bars represent reported femtosecond laser-inscribed pulsed waveguide laser sources utilising passive Q-switches, whereas green indicates active Q-switched waveguide sources. The current results are shown in red. According to this data, it is clear laser sources demonstrated in this study are at the upper end of the list of passive Q-switches (peak powers between 10 W and 100 W). Furthermore, the peak power achieved here is situated at the lower end of reported active Q-switches (green bars in Fig. 4.25). Note that the published passive Q-switched laser sources with peak powers above 100 W use significantly higher pump powers, well above 1.5 W. The pump power used in this work is three times lower.

5

Versatile fibre laser

Building a versatile waveguide-based laser source that can be operated as continuous wave (CW), Q-switched and mode-locked is the primary goal of this chapter. For that purpose, a liquid crystal cell is utilised as an intracavity loss/frequency-modulator. Active mode-locking requires modulating the intracavity losses with the inverse of the cavity round-trip time of a circulating pulse. The waveguide chips used in the previous chapter exhibit short cavity lengths, and thus require modulation frequencies in the megahertz to gigahertz region. The liquid crystal cells used in this research cannot be modulated with such high frequencies; a fibre laser cavity is therefore used to enable modulation frequencies in the kilohertz region by scaling the cavity length.

In the following sections, frequency- and amplitude-modulated mode-locking is demonstrated. Furthermore, it is shown that just by varying the applied voltage waveform, the same setup can be switched from mode-locking to Q-switching. In the absence of an applied voltage, continuous wave operation is achieved.

5.1 History of mode-locking

Mode-locking is a method of generating ultra-short pulses with pulse durations down to a few femtoseconds. Evidence of mode-locking was first discovered in 1963 [194] and early 1964 [195]; however, reports on the demonstration of mode-locking were first published in 1964 and early 1965 [196–198]. It was shown that, due to optical nonlinearity, a self-locking mechanism led to several longitudinal resonator modes (also called axial modes) being coupled [199]. Following this passive mode-locking approach, active mode-locking was proposed [198, 200] and demonstrated experimentally within a HeNe laser cavity [201]. This technique was later extended to ruby lasers, resulting in the first work published based on a solid-state laser [202–204]. In those experiments it was demonstrated that with solid-state lasers the generated peak power was much higher than previously demonstrated in mode-locked gas lasers. Throughout 1966, mode-locking was applied to Neodynium-doped laser systems via various methods, such as utilising internal modulators [205, 206] and saturable dyes [207]. The main challenge up to this point was that the pulse duration was too short to be measured with conventional detectors. Theory indicated that the pulse duration could be as small as the reciprocal of the spectral bandwidth, which led to an estimation of pulse durations as short as a few picoseconds. The first success in detecting such short signals was achieved by using the laser pulses to produce a second harmonic signal, which was found to be highly dependent on pulse parameters [206, 208]. An advanced method was developed in late 1966 by splitting the beam into two parts before recombining them inside a nonlinear crystal with a relative temporal delay [209–211]. The second harmonic signal was only generated when the relative delay was short enough to allow a pulse overlap within the nonlinear crystal. Using this method, pulses down to a few picoseconds were measured [210]. Ever since, mode-locking techniques have been improved and refined for shorter pulse durations and higher peak powers.

Mode-locked laser systems have widespread scientific and industrial applications. Although liquid crystals were used to initiate mode-locking [212], mode-locking has not so far been demonstrated solely by using an intracavity modulator based on a liquid crystal. In general, mode-locking techniques can be categorised into passive and active methods. This work focuses on active mode-locking.

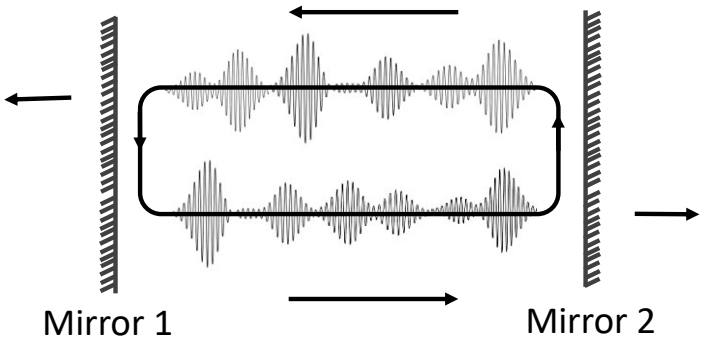

Figure 5.1: Schematic of a laser cavity (formed by two mirrors) and its circulating electric field pattern [140].

5.2 Theory of mode-locking

This section follows the approach of Siegmann for linear resonators [140]. The electric field within a resonator can be thought of as a superposition of a forward- and backward-propagating wave that exhibits a periodic pattern that reproduces itself each round-trip. In a stable state within a cavity, the amplification will not change the field pattern. Minor changes can be introduced by the finite bandwidth of the gain medium, but in a stable state they are negligible. Typically, the superposition of the axial modes defines the field pattern. The axial modes are standing waves within the resonator. After several resonator round-trips, only certain wavelengths interfere constructively and reinforce themselves. As a result, only those wavelengths form standing waves (axial modes) within the resonator; the rest are suppressed by destructive interference. A multimode laser with several axial modes and irregular phases has a field pattern similar to that shown in Fig. 5.1. In a stable state, the field will consist of a periodic repetition given by $T = 2l_{cavity}/c$, depending on the resonator length l_{cavity}. The periodic repetition equals the inverse of the axial mode spacing $T = 1/\nu_{ax}$ and the axial mode spacing frequency is given by:

$$\omega_{ax} = 2\pi\nu_{ax} = \frac{2\pi}{T}. \tag{5.1}$$

In the following sections, the underlying mechanisms required for (active) mode-locking are discussed. First, the influence of multiple resonator modes on the pulse width and spectral shape is reviewed, then the significance of the phase and amplitude relationship is analysed.

In the time domain, after one round-trip in the laser cavity, the temporal signal looks

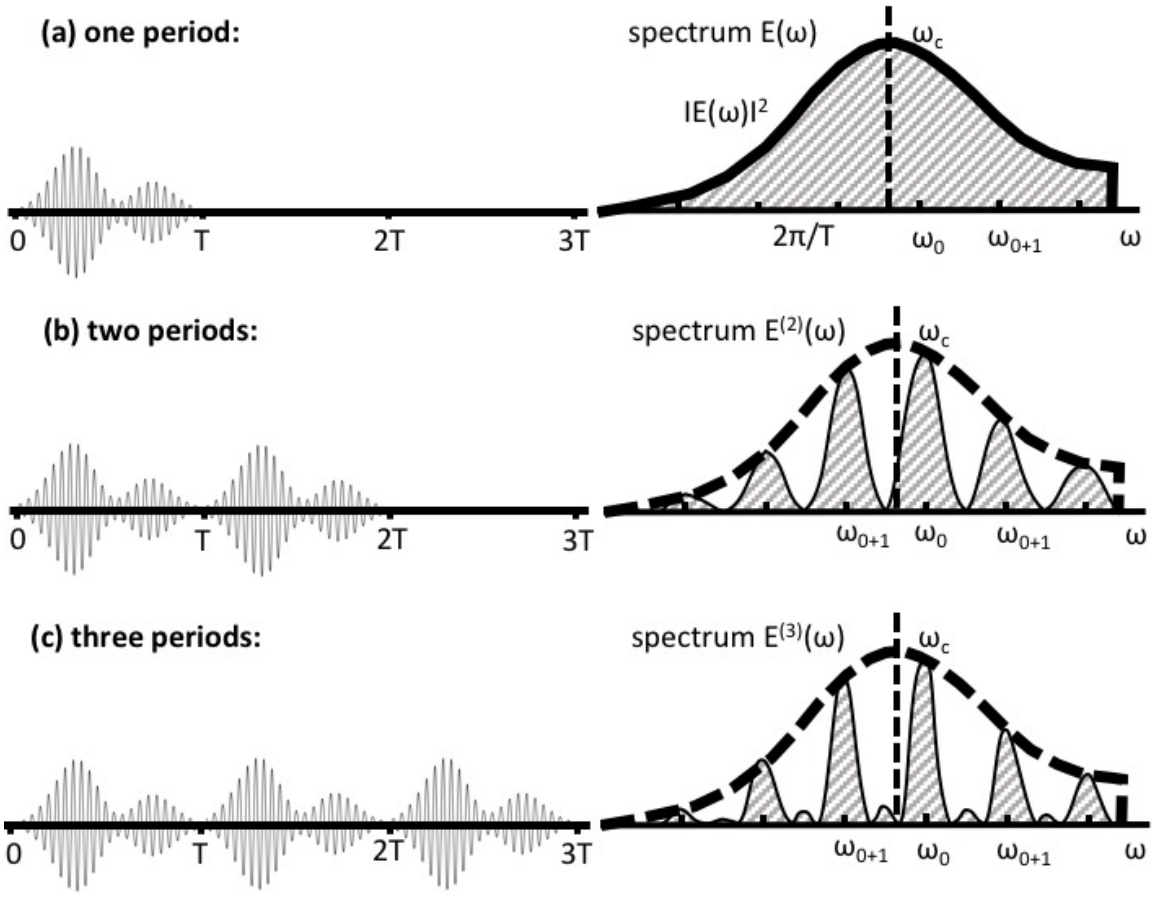

Figure 5.2: The electric field pattern and its Fourier-transformed power spectrum. A highly repetitive signal over several periods results in a discrete spectrum, whereas a nonrepetitive signal shows a continuous spectrum [140].

similar to the one schematically depicted in Fig. 5.2a. The Fourier transformation of this signal is shown on the right-hand side and represents the spectrum of the laser output. In the given example, the carrier frequency ω_c does not coincide with any of the axial modes. Furthermore, the spectrum $E(\omega)$ is wide compared to the axial mode spacing frequency $\omega_{ax} = 2\pi/T$. In Fig. 5.2b the same signal is shown after it has repeated itself after one period. A mathematical description is given by $E_2(t) = E(t) + E(t - T)$. In the time domain, the repetitive case does not show distinctive features over the nonrepetitive case except that the overall signal is now simply $2T$ long. However, when comparing those signals in the frequency domain, the change becomes apparent. The Fourier transformation of a signal that is delayed by an amount T is $\exp(-j\omega T)E(\omega)$. As a result of the second round-trip, the Fourier-transformed signal is now:

$$E^{(2)}(\omega) = (1 + e^{-j\omega T}) \cdot E(\omega) = 2 \cdot E(\omega) \cos\left(\frac{\omega T}{2}\right) e^{\frac{j\omega T}{2}}. \tag{5.2}$$

The intensity or power spectrum thus becomes:

$$I^{(2)}(\omega) = |E^{(2)}(\omega)|^2 = 4 \cdot I(\omega) \cos^2\left(\frac{\omega T}{2}\right). \tag{5.3}$$

It is because of the second repetition that the amplitude ($E(\omega)$) at the axial frequencies in the frequency domain is now twice as high as for a single round-trip. Additionally, the signal drops to zero between the peaks within the spectrum. Consequently, when introducing one more repetition of the electrical field within the cavity, the result is that the power spectrum is even more defined (see Fig. 5.2c). To generalise this theory, one can describe the field after N repetitions mathematically as:

$$E^{(N)}(t) = \sum_{n=0}^{N-1} \mathcal{E}(t - nT). \tag{5.4}$$

The Fourier transform is then:

$$E^{(N)}(\omega) = \sum_{n=0}^{N-1} e^{-jn\omega T} \times E(\omega) = \frac{1 - e^{-jN\omega T}}{1 - e^{-j\omega T}} E(w) \tag{5.5}$$

and its power spectral intensity is given by:

$$I^{(N)}(\omega) = |\mathcal{E}^{(N)}(\omega)|^2 = \frac{1 - \cos(N\omega T)}{1 - \cos(\omega T)} I(\omega). \tag{5.6}$$

From Eq. (5.6) and Fig. 5.2 it is clear that the more successive repetitions (the higher N in Eq. (5.6)), the narrower the peaks within the spectrum. However, it is worth mentioning that the number of round-trips does not determine the total number of axial modes. For a short circulating signal with a width τ_p, or for any circulating signal that has a large amplitude or phase fluctuation with a time constant τ_p, the number of modes can be estimated as $N_{modes} = T/\tau_p$. In other words, the more axial modes involved in the mode-locking process, the shorter the pulse duration and the higher the peak power.

In the frequency domain, the simplest case to describe is a laser running on a single axial mode, because it results (in an ideal situation, i.e. without any phase or amplitude fluctuations) in a constant amplitude-, phase- and frequency-signal. The second simplest

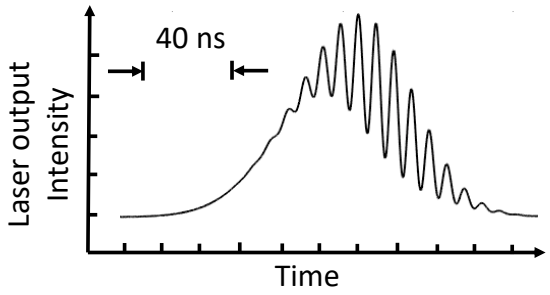

Figure 5.3: A strongly modulated pulse as a result of two axial beating modes. It can be seen as a strong indicator for at least two axial modes within the power spectrum [140].

case involves two axial modes that can be described mathematically by:

$$E^{(2)}(t) = Re\left\{E_1 e^{j(\omega_1 t+\phi_1)} + E_2 e^{j(\omega_2 t+\phi_2)}\right\} \tag{5.7}$$

and

$$I^{(2)}(\omega) = |E^{(2)}(t)|^2 = E_1^2 + E_2^2 + 2E_1E_2\cos[(\omega_2 - \omega_1)t + \phi_2 - \phi_1]. \tag{5.8}$$

The output signal in the time domain of such a bi-axial mode laser is modulated with a beat frequency $\omega_2 - \omega_1$, as shown in Fig. 5.3. The characteristic beating, similar to that shown in Fig. 5.3, can be interpreted as a clear indication of the presence of at least two axial modes within the laser spectrum. The modulation depth is defined by the amplitudes of those modes, e.g., for two axial modes with equal amplitude the modulation depth is 100 %. A laser containing three axial modes with indentical amplitudes results in a similar signal to the one shown in Fig. 5.4a. Each illustrated sine wave is separated by $\Delta\omega = \omega_{ax}$. If the three sine waves are in phase at t = 0 as shown in the figure, the resulting field $E(t)$ is three times as high as the amplitude of an individual mode. The intensity $I(t)$ is thus nine times the individual intensity. It can be seen from this illustration that one can obtain a reasonably short mode-locked pulse even with only three modes locked.

The phasor description further emphasise the phase relationship between different resonator modes. The phasor represents the complex amplitude and phase of each frequency component. In Fig. 5.4b, the central phasor represents the centremost spectral element, which lets the coordinate system rotate with its frequency. However, for convenience the coordinate system is locked to this axial frequency, so that it seems to be still. The sidebands will have a slightly different frequency and thus rotate forward or backward in the coordinate system at a speed relative to the centremost frequency component. The vector sum gives the

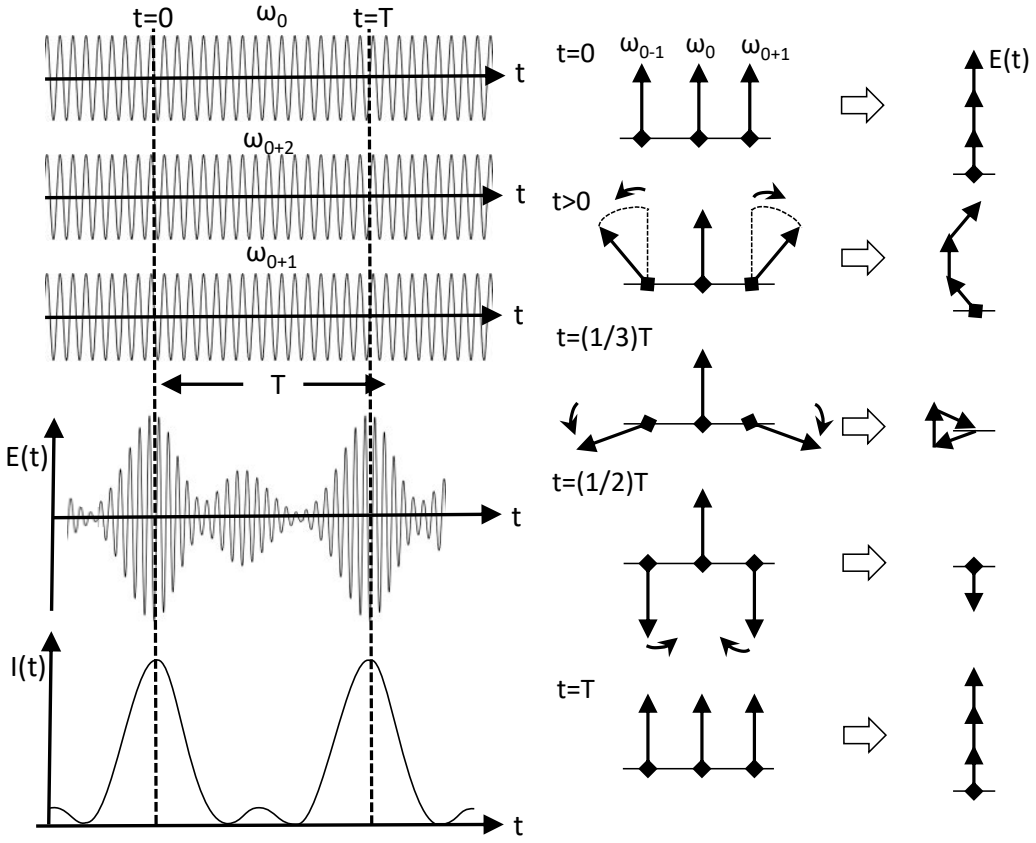

Figure 5.4: In the top part of (a) three different axial modes that are equally spaced in-phase are superimposed. As a result, the electric field strength E(t) is three times as high as the individual one shown in the bottom part of (a). In (b) the underlying mode-locking mechanism is described using a rotating-phasor approach. At $t = 0$ the modes are locked in phase and it is clear that the electrical field is three times that of a single mode. In addition, various phase states between $t = 0$ and $t = \mathrm{T}$ are shown [140].

instantaneous amplitude and phase of the total electric field/optical signal at the instant t. Thus, it represents the temporal pulse shape of the mode-locked pulse. In the example shown in Fig. 5.4b, all the sidebands have the same amplitude. However, for different amplitudes and relative phases the result is still a periodically repeated signal.

For N_{modes} axial modes, assuming that all are in phase and have identical amplitudes, the mathematical description of $E(t)$ is as follows:

$$E(t) = \sum_{n=0}^{N_{modes}-1} e^{-j(\omega_0+n\omega_{ax})t} = \frac{e^{jN_{modes}\omega_{ax}t}-1}{e^{j\omega_{ax}t}-1} e^{j\omega_0 t}, \tag{5.9}$$

and its intensity is given by:

$$I(t) = |\mathcal{E}(t)|^2 = \frac{1 - \cos(N_{modes}\omega_{ax}t)}{1 - \cos(\omega_{ax}t)} = \frac{\sin^2(N_{modes}\omega_{ax}t/2)}{\sin^2(\omega_{ax}t/2)}. \tag{5.10}$$

The pulse width can be estimated by $\tau_p = T/N_{modes}$. In between the peaks (between $t = 0$ and $t = T$) in Fig. 5.4a are $N_{modes} - 2$ weaker subsidiary peaks with a width of T/N_{modes} instead of the $2T/N_{modes}$ for the main peaks.

Using this approach it is possible to simulate the pulse evolution when the axial modes are locked in phase and amplitude (see Fig. 5.5). For instance, with an active mode-locking device the cavity has to be modulated with precisely the same frequency as the centremost axial mode or a multiple thereof (higher harmonics). Tuning the repetition rate of an amplitude modulator (e.g., acousto/electro-optical modulator) towards the frequency of the axial mode will result in an evolution similar to the one shown in Fig. 5.5. Only when the axial modes are locked in phase will a clean temporal output signal be produced. From (a) to (d) increasing the number of axial modes (N_{modes}), assuming all are in phase, results in a reduction in the pulse duration. There are $N_{modes} - 2$ subsidiary peaks between the maxima. As illustrated in (e), a Gaussian spectrum distribution results in a clean pulse train without subsidiary peaks. In (f) and (g) the periodic output signal is shown for eight modes in phase but with random amplitude distributions; depending on the amplitude distribution, the output signal can be totally different. In (h) to (j) the output signal for random phases is shown for a constant amplitude. The signal is periodic, but there are no dominant pulses within the output signal. The output signal looks more like a noise pattern that repeats itself with the round-trip time. Note that increasing the number of axial modes with no phase relationship determines the modulation height within the output signal (comparing (h) and (i) to (j)).

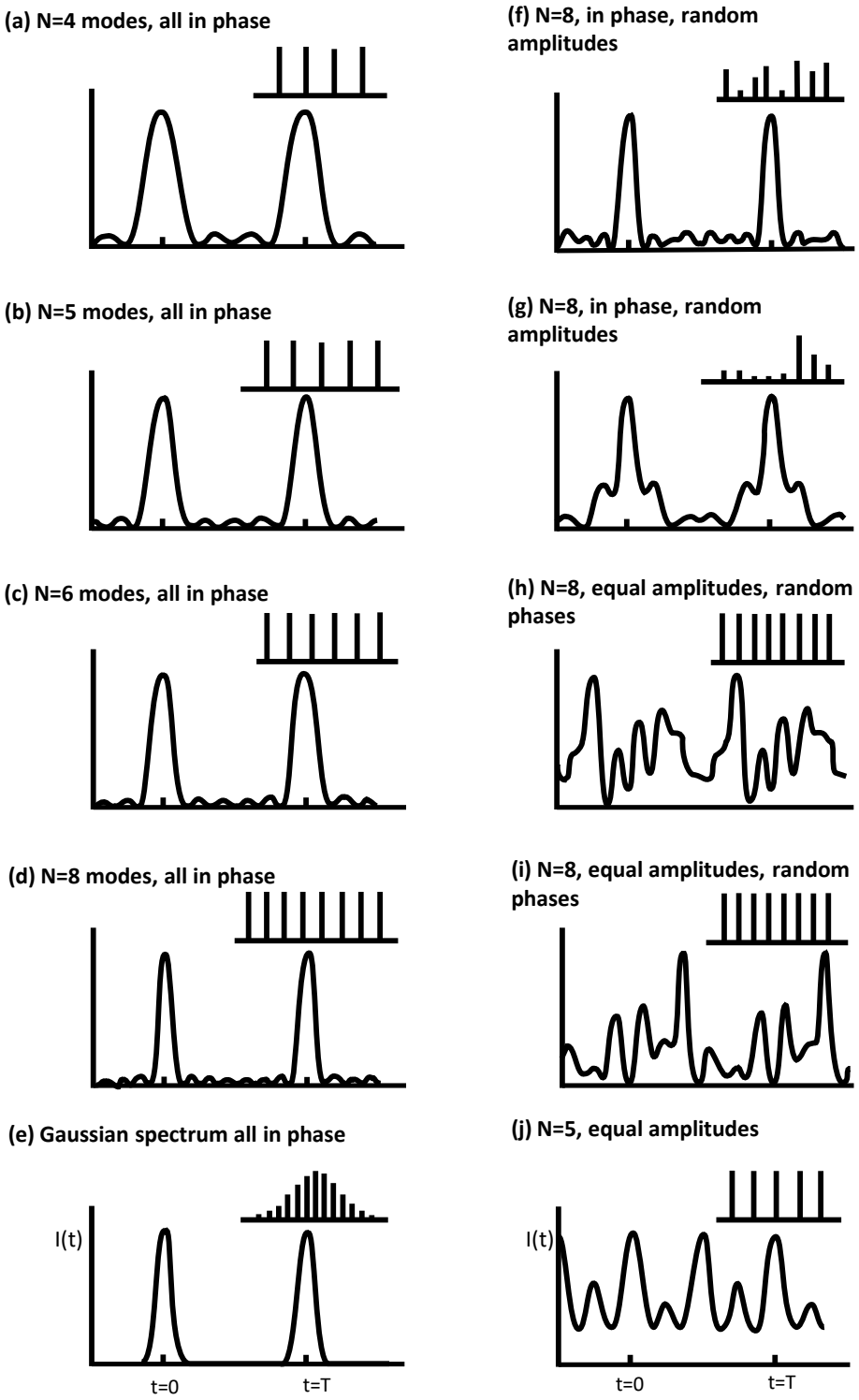

Figure 5.5: Pulse evolution towards locking the relative phase and amplitude. A background-free temporal signal can be achieved when the axial modes are locked in phase and amplitude within a Gaussian spectrum. [140]

5.2.1 Active mode-locking

There are two distinct approaches to mode-locked operation, passive and active. In the present work, an actively controlled liquid crystal cell was used for mode-locking a fibre laser, and thus only the theory behind this particular case is discussed here. For active mode-locking, either an amplitude modulator (AM) or a frequency modulator (FM) can be placed inside the cavity. Driving them with precisely the same frequency as the mode spacing of the axial modes, one can generate a train of mode-locked pulses with a repetition rate that equals the axial mode spacing $\nu_{ax} = c/2l_{cavity}$. In the following section, the different mechanism for amplitude modulation and frequency modulation are described.

Amplitude modulation mode-locking

An amplitude modulator can introduce a periodic and time-varying loss function $L(t)$ into a laser cavity. As a result, sidebands in the frequency domain on each oscillating axial mode are created. For example, for the case of a sine function, the axial mode closest to the gain maximum ν_0 will show sidebands at $\nu_0 + \nu_{mod}$ and $\nu_0 - \nu_{mod}$, with ν_{mod} being the modulation frequency. If the modulation frequency coincides with the axial mode spacing ($\nu_{ax} = c/2l_{cavity}$), those sidebands will couple and synchronise in amplitude as well as in phase with the adjacent axial modes ν_{0+1} and ν_{0-1}. When passing through the gain medium again, those modes will now couple to the ν_{0+2} and ν_{0-2} modes and synchronise them to the ν_0 mode. Each successive axial mode will initiate sidebands in the same way, and thus the sidebands and modes tend to synchronise throughout the supported spectral gain region.

In the time domain, the modulation function will selectively transmit the peak and suppress the outer regions of the pulse circulating in the cavity. On successive round-trips this will result in shortening of the pulse. How much this effect will shorten the pulse width depends on the shape of the modulation function. For example, a square wave modulation function of a duration of 1 ps shortens the pulse to a greater degree than a sinusoidal modulation function. In general, the pulse width is a function of the reciprocal of the gain bandwidth. Longer pulses will experience higher losses in the modulator due to the shortening effect; shorter pulses are limited by the finite gain bandwidth of the active medium. An expression for the dependence of the mode-locked pulse width on the modulation depth, modulation frequency, spectral linewidth and saturated gain can be derived when following a single mode-locked

pulse during one round-trip in the cavity. In a steady state, successive round-trips do not change the shape of the mode-locked pulse. The loss function of an amplitude modulator can be expressed as:

$$L(t) = \exp\left[-\frac{\delta_{AM}(1-\cos\omega_m t)}{2}\right]. \tag{5.11}$$

The angular frequency of the modulation function is ω_m and must be equal to the axial mode spacing frequency $\omega_m = \omega_{ax} = 2\pi\nu_{ax}$. The modulation depth is accounted for by δ_{AM}. The round-trip loss function, Eq. (5.11), can be expanded around the loss minimum where the optical pulse duration is short compared to the modulation period. In that case, it can be rewritten in terms of an exponential function:

$$L(t) \approx \exp\left[-\frac{\delta_{AM} w_{ax}^2 t^2}{4}\right], \quad |t| \ll T. \tag{5.12}$$

As a result, one can derive a relationship that reveals the parameters that influence the pulse duration for amplitude-modulated mode-locking:

$$\tau_{p_{AM}} \propto \left(\frac{2g l_{active}}{\delta_{AM}}\right)^{1/4} \times \left(\frac{1}{\nu_{ax}\Delta\nu}\right)^{1/2}. \tag{5.13}$$

The length of the active gain medium is l_{active} and g is the gain coefficient that accounts for the saturated gain at the line-centre. The laser gain bandwidth is denoted by $\Delta\nu$. For the case of an amplitude-modulated mode-locked laser, it follows from Eq. (5.13) that the pulse duration is inversely dependent on the square root of the modulation frequency and on the fourth root of the modulation depth. As a general rule, the higher the modulation depth and modulation frequency, the shorter the mode-locked pulse.

Frequency modulation mode-locking

Another approach to mode-locking is to introduce a phase modulator into the cavity. By varying the phase with a sinusoidal signal, the modulator introduces a frequency chirp to the circulating pulse as a result of the Doppler shift. The frequency up- or down-chirp is proportional to the slope of the loss function dL/dt. Note that for frequency modulation the loss function does not actually modulate the losses, but instead modulates the cavity length. There is no frequency chirp when the slope is zero. On successive round-trips the Doppler shift eventually pushes some energy out of the spectral width that is supported by the gain

medium (or by the cavity mirrors). For some spectral components, additional losses are introduced, while for the centremost parts there are no additional losses. That scenario leads to a similar effect as in the case of an intracavity amplitude modulator. However, there is a difference because the phase modulator introduces two-phase extrema (positions where the slope of the sine function is zero) and the pulse can occur on either of them and experience low losses [139]. The loss function can be described as in Eq. (5.12) with an additional component to account for the two-phase extrema:

$$L(t) = \exp\left[\pm j\frac{\delta_{FM}\omega_{ax}^2 t^2}{2}\right]. \tag{5.14}$$

Here, δ_{FM} is the maximum phase retardation through the modulator. The ± sign accounts for the two possible positions at which the pulse can pass through the modulator. The pulse duration dependence on the phase retardation, modulation frequency and resonator length can be described by:

$$\tau_{p_{FM}} \propto \left(\frac{2gl_{active}}{\delta_{FM}}\right)^{1/4} \times \left(\frac{1}{\nu_{ax}\Delta\nu}\right)^{1/2}. \tag{5.15}$$

For both the amplitude- and frequency-modulated mode-locking cases, the pulse duration depends on the modulation depth, modulation frequency and the cavity length. In the following study, the liquid crystal is operated to introduce the maximum possible modulation depth and thus the only free parameter to control is the cavity length. The pulse duration is proportional to the cavity length l_{cavity} as follows: $\tau_p \propto 1/\sqrt{c/2l_{cavity}}$.

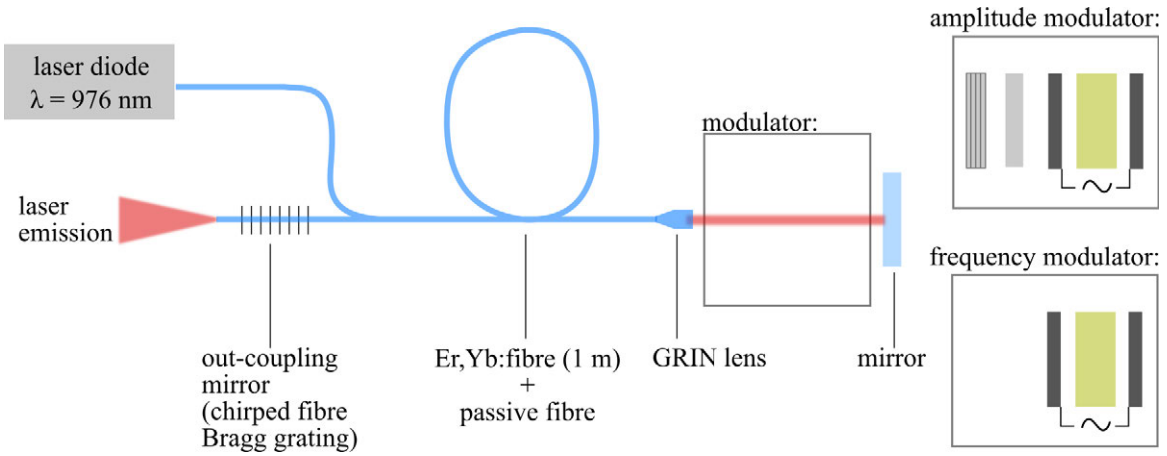

Figure 5.6: Schematic of the actively mode-locked fibre laser. In the case of amplitude-modulated mode-locking, the modulator consists of a liquid crystal cell (layer thickness 5 µm), a half waveplate and a thin film polariser. When utilising the liquid crystal cell for frequency-modulated mode-locking, the half waveplate and the polariser were removed. The passive fibre was varied in length between $l = 518.7 \pm 1$ m and $l = 112.7 \pm 1$ m.

5.3 Experimental mode-locking results

Liquid crystals are significantly slower than other commonly used amplitude or phase modulators such as AOMs or EOMs. Therefore, it is not feasible to mode-lock a short waveguide laser cavity. The round-trip time within one of those cavities is too small to allow a modulation of the liquid crystal cell with the corresponding axial mode spacing. In contrast, the length of a fibre laser cavity can easily be increased by the addition of passive fibre (Thorlabs SMF-28-100: $d_{core} = 8.2\,\mu$m, $d_{cladding} = 125\,\mu$m, $\mathrm{NA}_{core} = 0.14$, $n_{core} = 1.45205$, $\mathrm{MFD}_{core} = 10.4\,\mu$m, dispersion ≤ 18.0 ps (nm km)$^{-1}$, propagation losses ≤ 0.18 dB km^{-1}). The setup used for mode-locking is depicted in Fig. 5.6. A one metre long active Erbium-doped Ytterbium–co-doped fibre (NUFERN SM-EYDF-6/125-HE: $d_{core} = 6.0\,\mu$m, $d_{cladding} = 125\,\mu$m, $\mathrm{NA}_{core} = 0.180$, $\mathrm{MFD}_{core} = 6.8\,\mu$m) was used as a gain medium. It was pumped by a fibre-coupled laser diode with a wavelength of approximately 976 nm, connected via a pump coupler to the gain fibre. The maximum pump power coupled into the active fibre measured 160 mW. The active fibre was spliced on one side to a passive fibre and on the other to a pump coupler (course wavelength division multiplexing - CWDM). The passive fibre was spliced to a gradient index lens (GRIN lens) that collimated the beam within a short free space section of the cavity. The modulator was placed in this free space section, which was terminated by a high-reflecting mirror (Thorlabs: PF10-03-P01, broadband-protected silver mirror). Note that the liquid crystal cell was introduced into the free space section at a small angle to suppress back

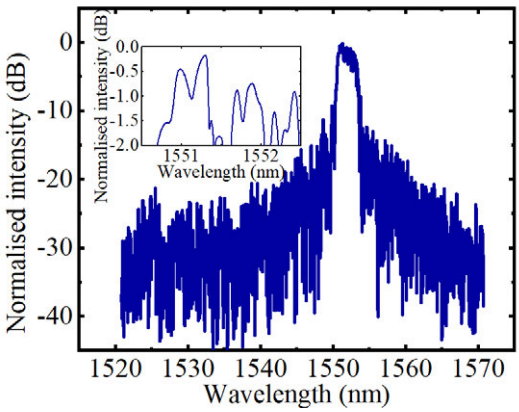

Figure 5.7: Measured reflection of the laser-inscribed chirped-fibre Bragg grating used in this research. Inscription method used was line-by-line [213].

reflections into the gain medium. The pump coupler, on the other side of the active fibre, had three ports. The pump port was spliced to a fibre-coupled laser diode. The port opposite to the active fibre was spliced to a fibre Bragg grating (FBG), which acted as the output coupler. The FBG was femtosecond laser-inscribed using the line-by-line inscription method [213] and had a measured reflection of 95.5 % at 1551.2 nm (see Fig. 5.7). The passive fibre in this setup was used to enhance the cavity length, which was varied from 518.7 m to 112.7 m for the results presented here. Once the cavity was built, the modulation frequency was tuned to achieve mode-locking. By knowing the approximate cavity length (100 m fibre spools were used), the initial modulation frequency could be estimated. In the next step, the modulation frequency was fine-tuned while monitoring the output signal. Once the modulation frequency ν_{mod} that resulted in mode-locking was found, the exact cavity length l_{cavity} was calculated as follows:

$$l_{cavity} = \frac{c}{2n_{core}\nu_{mod}} \cdot \frac{1}{A} \qquad \text{with } A = 1 \text{ or } 2. \tag{5.16}$$

The constant A is introduced to account for the different applied voltage waveforms. As mentioned earlier, frequency-modulated mode-locking requires a sinusoidal waveform, which results in two phase-maximums; thus $A = 2$. For amplitude-modulated mode-locking, a modified pulsed waveform is applied, as shown in Fig 5.8b. The voltage amplitude U_+ accounts for the minimum cavity losses and U_- reverses the molecule rotation in the liquid crystal cell. The maximum cavity losses are defined somewhere between U_- and U_+. However, in the case of amplitude-modulated mode-locking, $A = 1$. In the following sections, the experimental results for frequency- and amplitude-modulating mode-locking are presented.

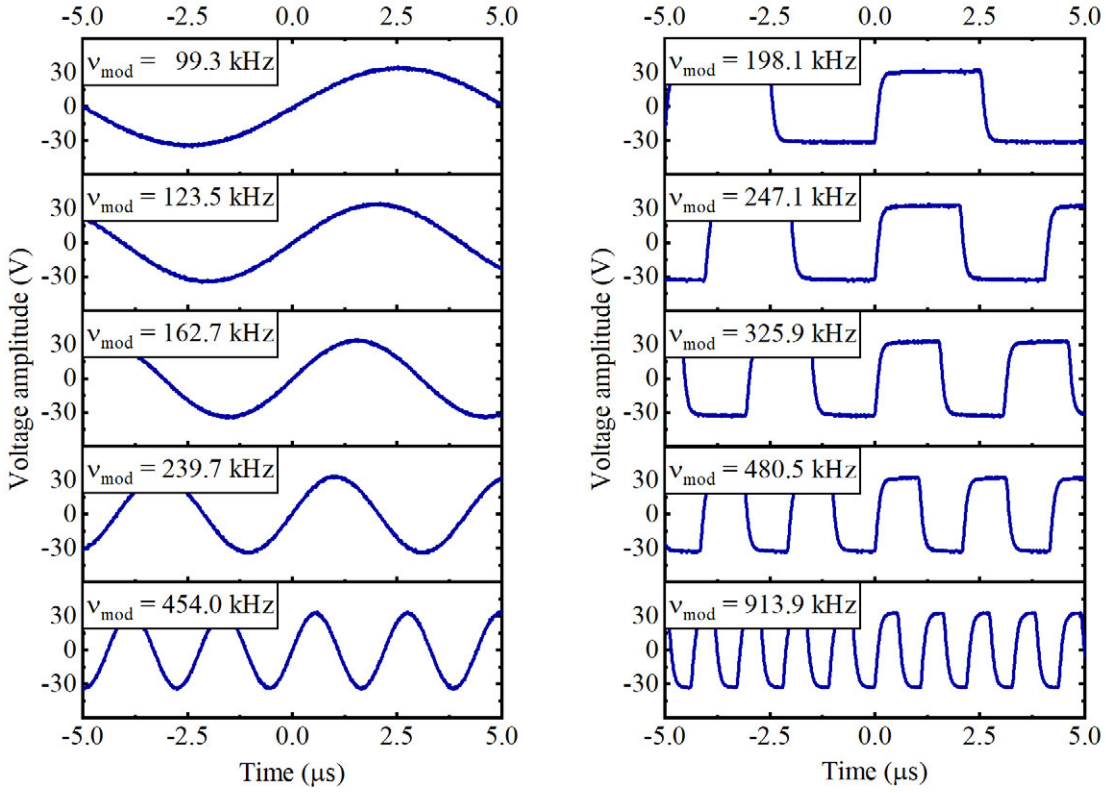

Figure 5.8: Applied voltage waveform for frequency- and amplitude-modulated mode-locking in (a) and (b) respectively. For frequency modulation, the sinusoidal results in two phase-maximums where the slope of the waveform is zero. As a result, the modulation frequency can be half the axial mode spacing ν_{ax}.

5.3.1 Frequency modulation mode-locking

This section is organised in two parts. Part 1 presents the results achieved while building the first setup and focuses on confirming mode-locking. Unfortunately, the achieved pulse duration was rather long (nanoseconds) and thus could not be used to confirm that the modes were locked in phase and amplitude. Thus, in the first part alternative indications to confirm that the modes were locked in phase and amplitude are presented. The second part presents a experimental parameter study, in which the cavity length was altered and laser parameters were recorded.

Part 1

When tuning the modulation frequency, i.e., the voltage waveform applied to the liquid crystal cell, similar states to those presented in Fig. 5.5 could be observed. Mode-locking is established once the modulation frequency is equal to half the axial mode spacing ν_{mod} =

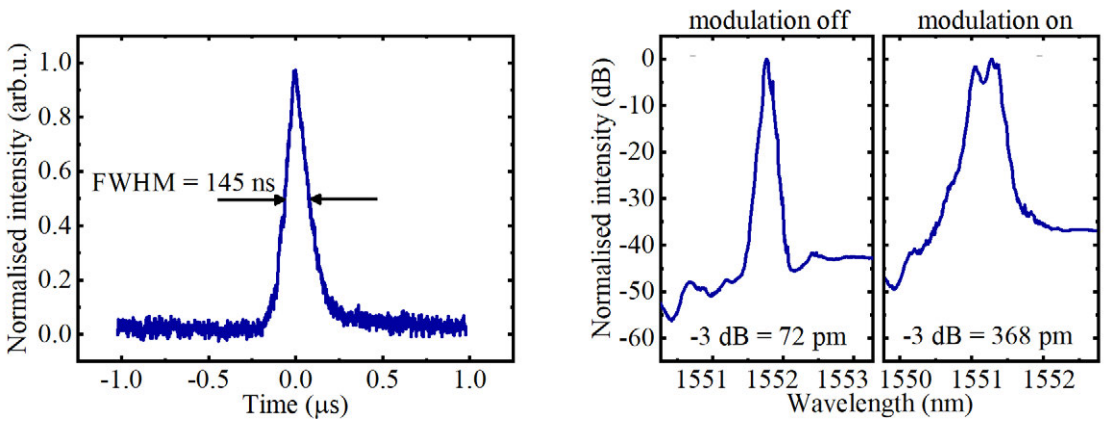

(a) (b)

Figure 5.9: Temporal shape of the laser pulse (a) and the corresponding spectrum (b). In (a) the pulse measured 145 ns at the full width half maximum (FWHM). In (b) the spectrum when the liquid crystal is not modulated (left side) is compared with the frequency-modulated case (right side). The spectrum broadens once the cell is modulated.

$\nu_{ax}/2$. In Fig. 5.9a, the modulation frequency matches this condition and results in a background-free pulse train with pulse durations of 145 ns FWHM. The cavity length was calculated to be 317.3 m and the corresponding modulation frequency measured 324.5 kHz. The pulse duration in Fig. 5.9a is longer than expected from the measured spectrum width of 368 pm (measured at -3 dB), as shown in Fig. 5.9b. Thus it was not possible to judge solely from the pulse duration whether the laser was mode-locked or just weakly coupled. Note that the two peaks and the minimum in the spectrum represent the reflection structure of the fibre Bragg grating. A spectral bandwidth of 368 pm should result in a transform-limited pulse duration of 9.5 ps, assuming a Gaussian fit, or 7.0 ps assuming a Sech^2 fit. However, the fact that the pulse train occurs using only solely the liquid crystal is a strong indicator for mode-locking, as there is no loss modulator within the cavity. To further confirm mode-locking, the radio frequency (RF) spectrum was recorded and analysed. The RF peak located at the axial mode spacing (at 324.5 kHz, corresponding to a cavity length of 317.3 m) was measured to be 1 kHz at FWHM (see Fig. 5.10a). It should be noted that the "hump" that is visible in the background-signal in Fig. 5.10a is unusual for pure mode-locking. This behaviour could be an indication for Q-switched mode-locking, yet in that case the hump should be significantly larger in magnitude. We therefore believe that the cause of this background signal is a small and occasionally appearing Q-switching instability, yet further studies are required. In Fig. 5.10b the fundamental peak and its harmonics were stable between 0 MHz and 2.5 MHz with a minimum of 70 dB above the noise level. The RF spectrum showed a

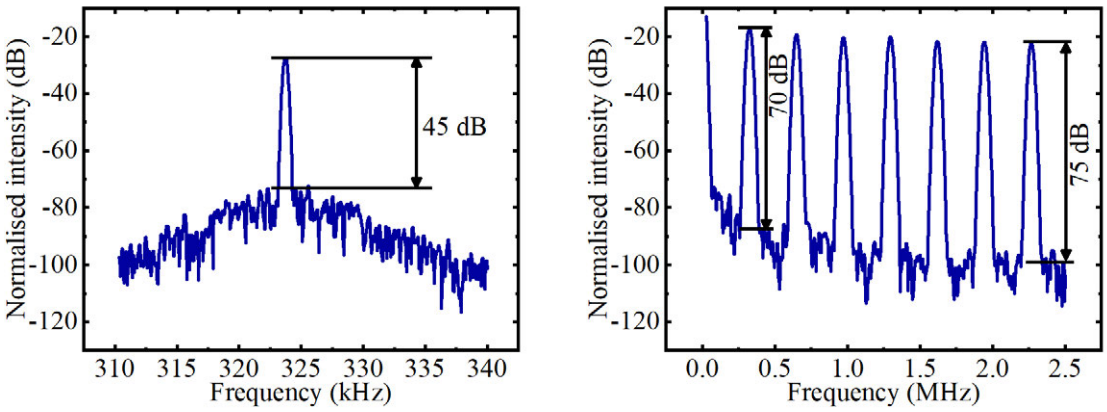

(a) (b)

Figure 5.10: RF spectrum of the laser's output during mode-locked operation. In (a) the axial mode measured a bandwidth of less than 1 kHz at FWHM. In (b) the axial modes are recorded over a bandwidth of 2.5 MHz. An indication of strong mode-locking is the height of the peaks remaining constant over a broad frequency range.

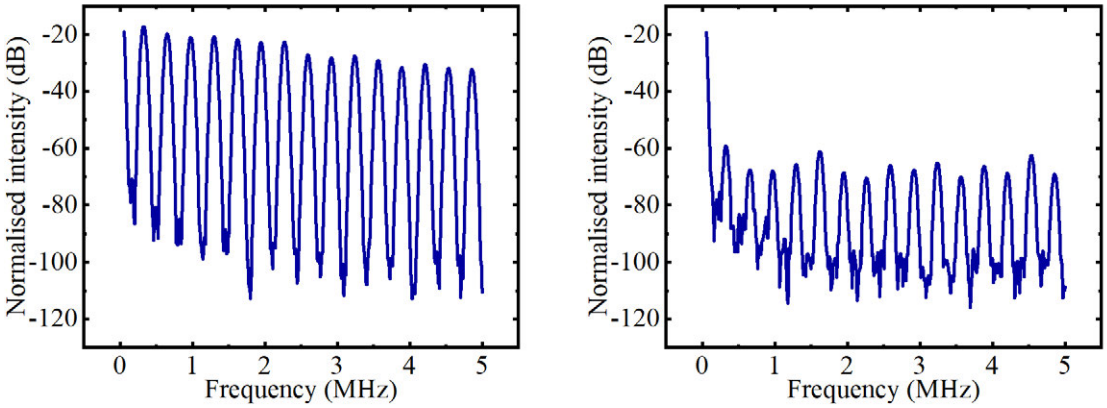

(a) (b)

Figure 5.11: RF spectra of the laser output when (a) modulating the liquid crystal with a sine function (modulation frequency $\nu_{mod} = c/(4n_{core}l_{cavity})$). In (b) no voltage is applied to the cell and the laser is therefore running in continuous wave operation. The output signal looks similar to that shown in the top graph of Fig. 5.12. Mode-locked operation features strong and distinct harmonics of the laser repetition rate compared to the continuous wave laser. Note that, in the unmodulated case, the amplitude of the peaks was unstable and thus indicated noise on the timescale of the round-trip time.

stable comb of peaks over a range of 0–5 MHz. When the laser is running continuous wave by turning off the modulation of the liquid crystal, the peaks drop by 45 dB, as illustrated in Fig. 5.11b. In fact, one would expect the peaks of a noisy CW laser to be small compared to the CW level located in the RF spectrum at zero frequency. The sequence of peaks in Fig. 5.11b spaced at the mode spacing refer to noise on the timescale of the round-trip time, which is typical for a CW laser.

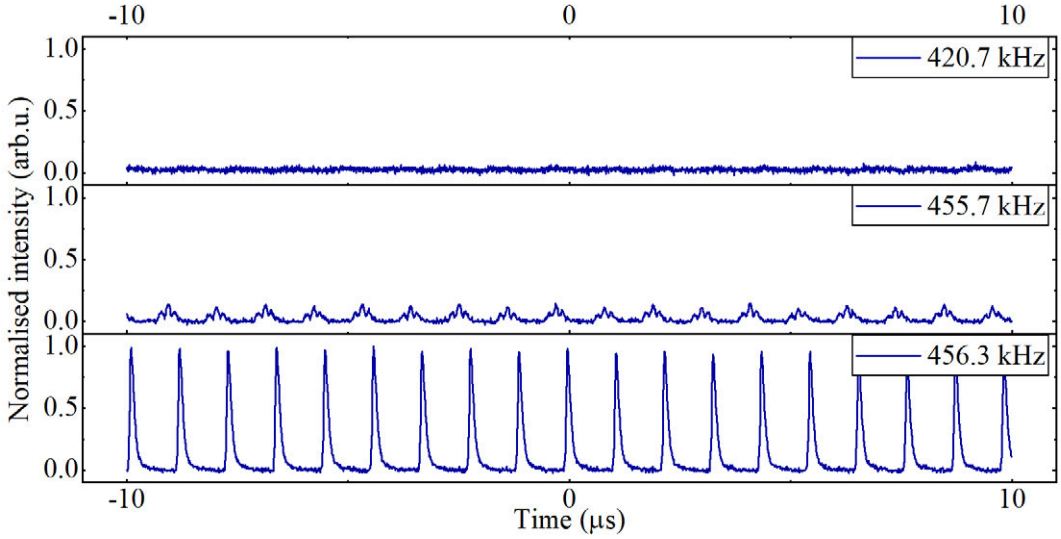

Figure 5.12: Increasing the modulation frequency towards the axial mode spacing frequency of the resonator led to a stable pulse train. A slight detuning of the desired modulation frequency led to a periodic noise-like output signal, as shown in the middle graph. The measurements were taken for a resonator length of 112.8±1 m with a sinusoidal modulation waveform.

Another indication for mode-locking was the fact that a pulse train would only occur when modulating the liquid crystal cell at a frequency consistent with the axial mode spacing or a multiple thereof. In Fig. 5.12, the oscilloscope trace of the output signal is shown for three different modulation frequencies. Note that, in Fig. 5.12, the cavity length was approximately 112.8 m. Only at a corresponding modulation frequency of 456.3 kHz (Eq. (5.16) with $A = 2$) did a stable pulse train evolve. Detuning the modulation frequency by 0.6 kHz results in a periodic signal with a much smaller peak, shown in the middle of Fig. 5.12. Further detuning the modulation frequency results in a CW signal as shown in the top graph of Fig. 5.12.

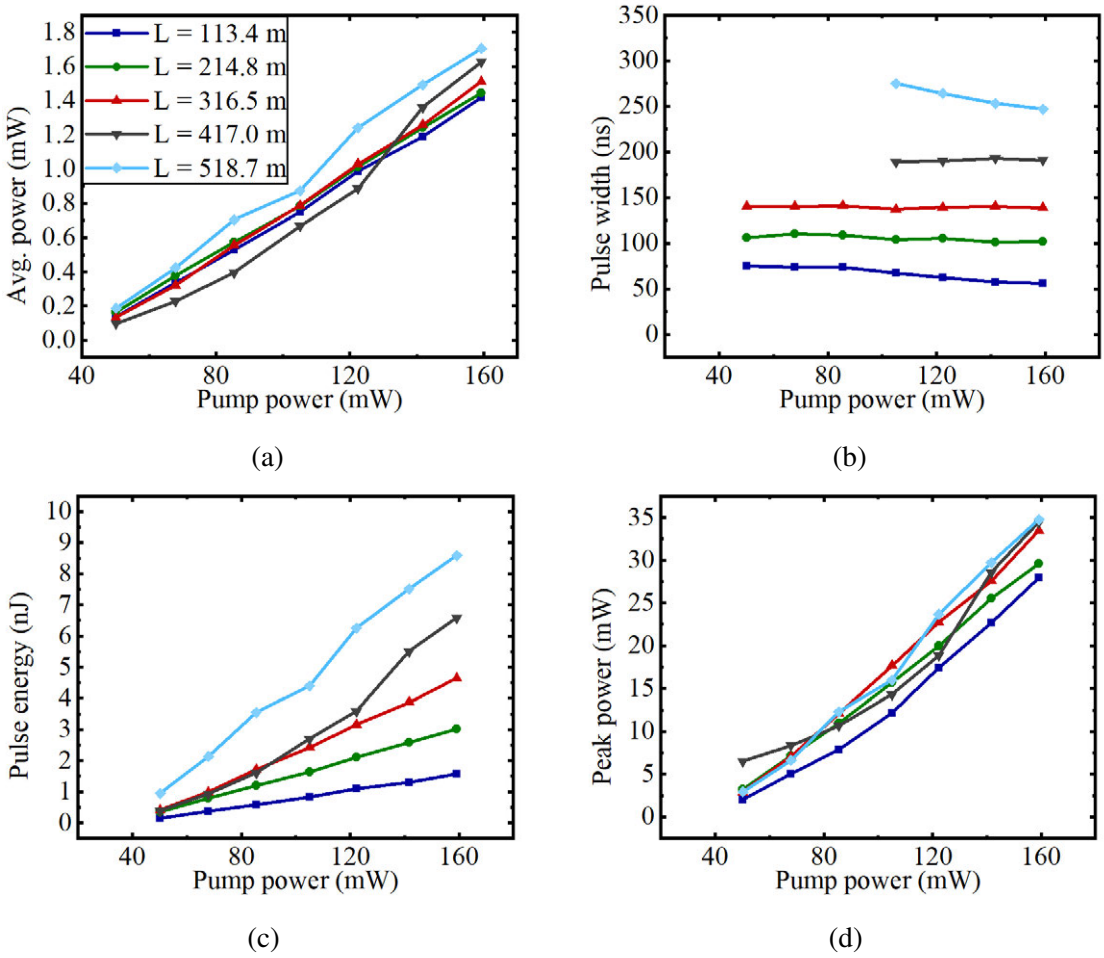

Figure 5.13: Average power (a), pulse width (b), pulse energy (c) and peak power (d) as a function of pump power for the FM mode-locked fibre laser with different cavity lengths l_{cavity}. The corresponding modulation frequency is calculated by $\nu_{mod} = \nu_{ax}/2 = c/(4n_{core}l_{cavity})$ and was ν = 453.95 kHz, 239.65 kHz, 162.65 kHz, 123.45 kHz, 99.25 kHz, starting with the shortest cavity length.

Part 2

The cavity length was reduced in steps from approximately 518.7 m to 113.4 m. As a result, the modulation frequency of the applied sine waveform was increased from 99.25 kHz up to 453.95 kHz. For all cavity lengths the laser was running linearly polarised, even though no polariser was introduced into the cavity. By rotating the liquid crystal cell it was possible to rotate the polarisation axis. Thus, the conclusion was made that the liquid crystal acted as some sort of polariser. However, at this stage it is unclear how the polarisation state was maintained over the lengths of several 100's m of fiber.

The alignment layers of the liquid crystal cells were enough to polarise the laser. By rotating the liquid crystal cell it was possible to rotate the polarisation axis. In Fig. 5.13a, the

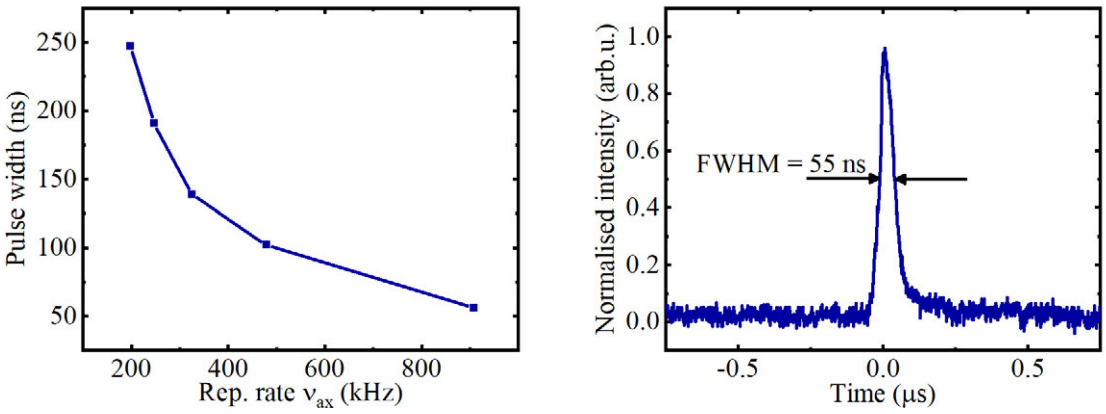

(a) (b)

Figure 5.14: In (a) the cavity length was shortened and thus the repetition rate ν_{ax} increased. As the repetition rate increases, the pulse width decreases. In (b) the oscilloscope trace is depicted. The output signal measured a repetition rate of 907.9 kHz, which corresponds to a cavity length of approximately 113.4 m.

average output power decreased from 1.7 mW to 1.4 mW when shortening the laser cavity from 518.7 m to 113.4 m. In an ideal case, the output power should not change. However, the change in output power could be the result of a decreased modulation depth for increasing driving frequencies. Furthermore, the pulse width decreases from 270 ns to 55 ns, as shown in Fig. 5.13b and Fig. 5.14a. Note that, in Fig. 5.13b the data points for low pump powers and long cavity lengths are not included in the graph because the pulse to pulse stability got unstable (fluctuated by ±50 ns).

From Eq. (5.15) it is clear that the pulse width should decrease when shortening the cavity length as this results in an increase of the axial mode spacing ($tp \propto 1/\delta_{FM}^{1/4} \cdot 1/\nu_{ax}^{1/2}$). However, as shown in Section 3.4.4 (Fig. 3.24), an increase in modulation frequency results in a decrease in modulation depth (and thus in the phase retardation). There is a point where further decreasing the cavity length will not result in a shortening of the pulse duration, as the modulation depth decreases simultaneously. The pulse energy exhibited similar behaviour when shortening the cavity length, as shown in Fig. 5.13c. The pulse peak power, shown in Fig. 5.13d, decreases as the cavity length gets shorter. A shorter cavity length increases the pulse repetition rate and thus results in more pulses per unit time.

5.3.2 Amplitude modulation mode-locking

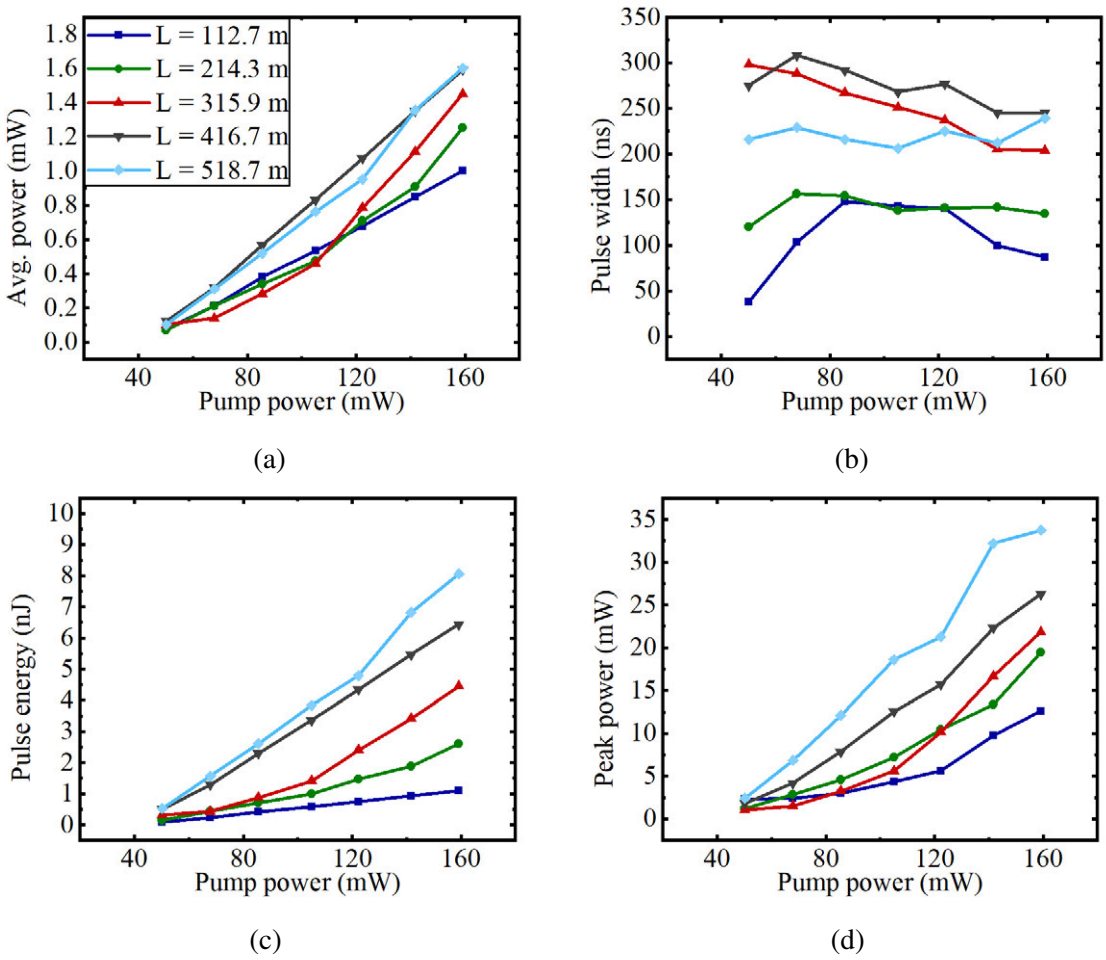

Figure 5.15: Average power (a), pulse width (b), pulse energy (c) and peak power (d) as a function of pump power for the AM mode-locked fibre laser with different cavity lengths l_{cavity}. The corresponding modulation frequency can be calculated from l_{cavity} by $\nu_{mod} = \nu_{ax} = c/(2n_{core}l_{cavity})$ and was ν = 913.9 kHz, 480.5 kHz, 325.9 kHz, 247.1 kHz, 198.5 kHz, starting with the shortest cavity length.

When using the liquid crystal as an amplitude modulator, a polariser must be added to the beam path, as shown in Fig. 5.6. The polariser defined the polarisation state of the whole system. The benefit of using the liquid crystal as an amplitude modulator rather than a phase modulator is that it enables switching between mode-locked, Q-switch and continuous-wave operation. The results are presented in Fig. 5.15. As in the previous frequency-modulated case, the cavity length was shortened from 518.7 m to 112.7 m by cutting the passive fibre back.

The overall behaviour when shortening the fibre was similar to frequency-modulated mode-locking. The difference was that, instead of a sinusoidal modulation function, a pulsed

modulation function was used and thus the modulation frequency equals $\nu_{mod} = \nu_{ax} = c/2n_{core}l_{cavity}$. In order to maximise the modulation depth, a modified pulsed waveform as shown in Fig. 5.15a was applied to the liquid crystal cell. The average output power decreases when shortening the cavity length, as shown in Fig. 5.16a. This is likely to be the result of a combination of two effects. First, each time the cavity was shortened the relative angle of the liquid crystal to the polariser had to be fine-tuned for the best mode-locking performance. Changing the relative angle results in a change of the initial resonator loss state, which alters the laser efficiency. Second, shortening the cavity length required an increase in modulation frequency, which results in a decreased modulation depth. The cavity length shows a stronger influence on the average output power for amplitude-modulated mode-locking than for frequency-modulated mode-locking. This is also likely to be an effect of changing the waveplate angle for the amplitude-modulated case, for frequency-modulation the waveplate did not have to be changed.

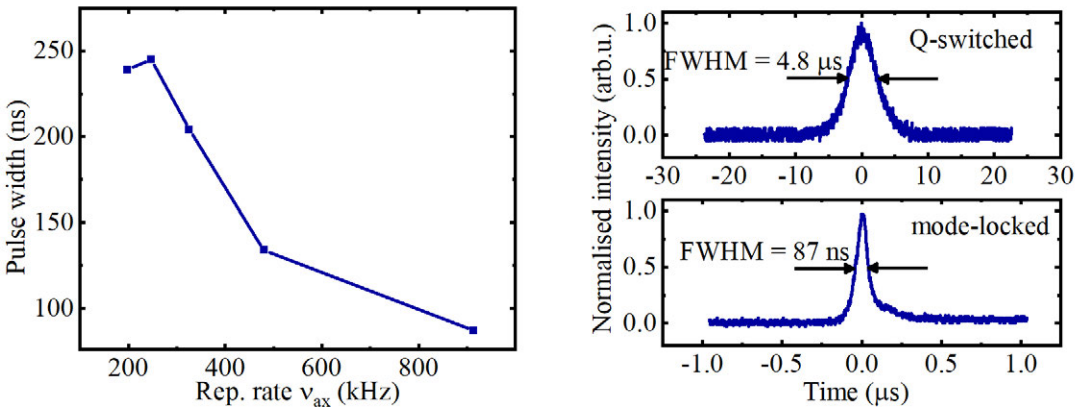

(a) (b)

Figure 5.16: In (a) the pulse width is plotted as a function of the repetition rate of the output signal. The repetition rate is defined by the cavity length. When shortening the cavity length the repetition rate increases. The pulse width decreases, as expected from Eq. (5.13). In (b) the oscilloscope traces are given for Q-switched (top graph) and mode-locked (bottom graph) operation. In both cases the shortest cavity length resulted in the shortest pulse width.

The highest output power of 1.6 mW was demonstrated for a 518.7 m long cavity. When the cavity length was reduced to 112.7 m, the output power measured 1.0 mW. The pulse width decreased from 248 ns to 95 ns when reducing the resonator length from 518.7 m to 112.7 m (see Fig. 5.15b). As implied by Eq. (5.13), the pulse duration should decrease for shorter resonator lengths. The pulse energy showed a similar behaviour, decreasing with the cavity length (see Fig. 5.15c). At a length of 518.7 m, the pulse energy measured 8.07 nJ,

whereas at 112.7 m length it measured 1.1 nJ. This decrease can be explained by an increase in pulse repetition rate and a decrease in output power for shorter cavity lengths. Consequently, the pulse peak power decreased for shorter resonator lengths (see Fig. 5.15d).

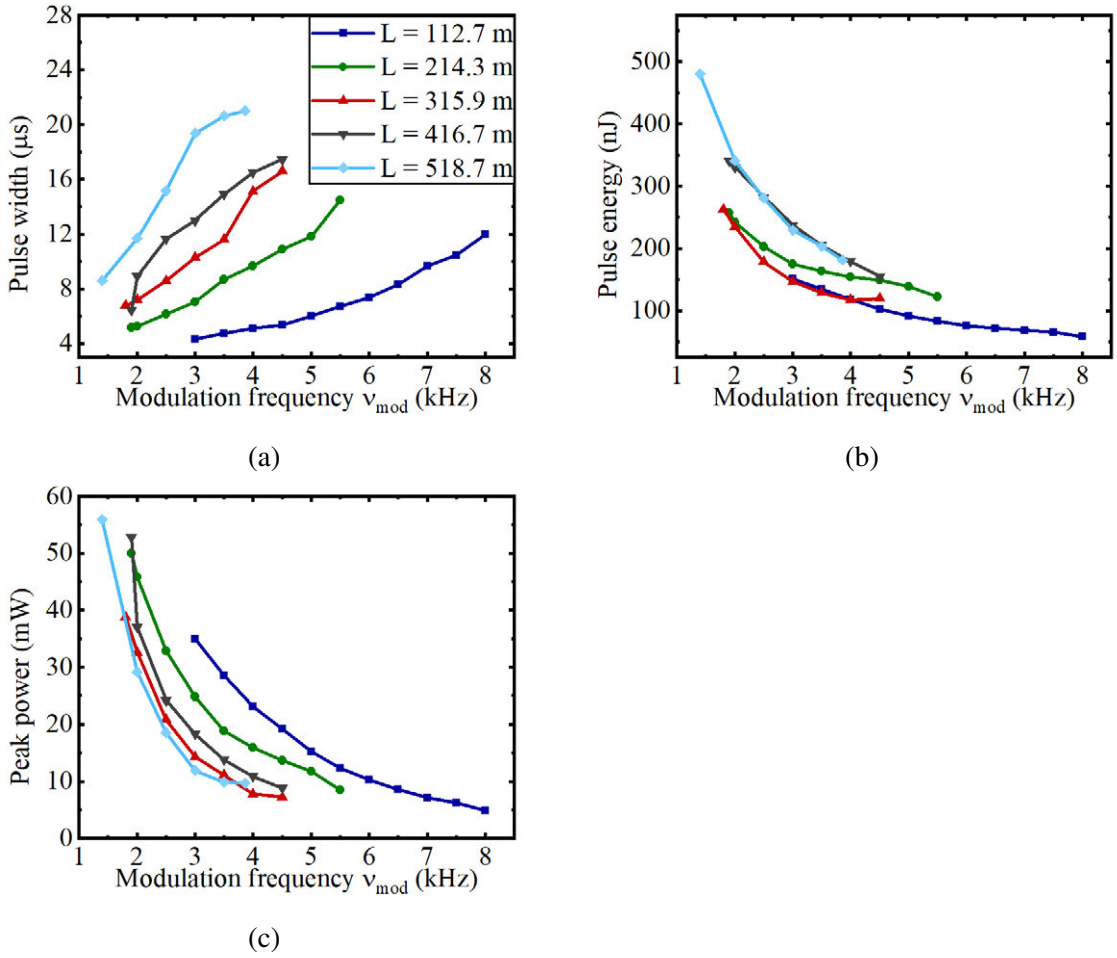

Figure 5.17: Pulse width (a), pulse energy (b) and peak power (c) as a function of the modulation frequency ν_{mod} for active Q-switching at different cavity lengths l_{cavity}. Changing the applied voltage waveform enables the laser to be run in actively Q-switched mode. In (a) the pulse width shortens when going towards shorter modulation frequencies. The pulse energy (c) and pulse peak power (d) increase when decreasing the modulation frequency.

5.3.3 Q-switching and continuous wave operation

For Q-switching, the same setup as for amplitude-modulated mode-locking is used; however, the repetition rate of the applied voltage waveform was reduced. Q-switching was demonstrated for a repetition rate region spanning from 1 kHz to 8 kHz (see Fig. 5.17). Towards the lower end of repetition rates, the laser became unstable and parasitic oscillation occurred. When increasing the cavity length, the threshold for parasitic oscillation shifted towards lower modulation frequencies. For example, at a cavity length of 518.7 m Q-switching was achieved at 1.4 kHz, whereas for l_{cavity} = 112.7 m parasitic oscillation occurred at modulation frequencies below 3 kHz. In general, the greater the cavity length the lower the modulation frequency that could be tuned without the occurrence of parasitic oscillation. The highest

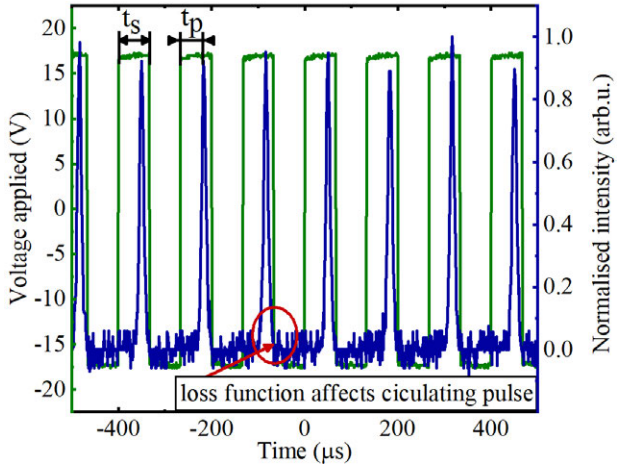

Figure 5.18: The ouput signal (blue line) of the Q-switched laser at a modulation frequency of 8 kHz. The applied voltage waveform (green line) represents the loss modulation within the cavity. Also shown is the boundary at which the loss function affects the circulating pulse. The pulse build up time t_p is almost as long as the switching time t_s.

modulation frequency was defined by the pulse build-up time. For example, using the 112.7 m cavity length at around 8 kHz, the pulse build-up time was approximately 50.0 µs, whereas the switching time t_s measured 62.5 µs, as shown in Fig. 5.18. At modulation frequencies $\nu_{mod} > 8$ kHz, the cavity is switched back to a high-loss state and affects the circulating pulse. Note that the pulse build-up time increased with the cavity length and thus the repetition rate decreased at longer cavity lengths. At low modulation frequencies the pulse duration was decreased from 21 µs (for a cavity length of 518.7 m) to 5.1 µs (for a cavity length of 112.7 m). The pulse energy was higher for the longer cavity lengths, which is a result of smaller modulation frequencies. The smaller the modulation frequency, the fewer pulses are generated per unit time, and therefore the more energy per pulse. At $l_{cavity} = 518.7$ m, the pulse energy measured 480.7 nJ at a repetition rate of 1.4 kHz; this was reduced to 58.6 nJ for a cavity length of 112.7 m at 8 kHz. When comparing the pulse peak power at the same repetition rate for different cavity lengths, the longest cavity length resulted in the highest peak power. At $l_{cavity} = 518.7$ m, the peak power measured 55.8 mW at 1.4 kHz. It decreased to 4.9 mW for $l_{cavity} = 112.7$ m. Furthermore, when the applied voltage waveform was switched off the laser setup ran in continuous wave. The average output power was the same as for AM mode-locking (see Fig. 5.15a).

5.4 Conclusion

In this study, a versatile fibre laser was built incorporating a liquid crystal as a loss modulator. The primary goal was to employ the liquid crystal cell as an active mode-locking device. It was also demonstrated that the liquid crystal cell enables switching between mode-locked, Q-switched and continuous wave operation simply by changing the applied voltage waveform. To the best of our knowledge, this is the first time a liquid crystal has been used as the driving active mode-locking device. For mode-locked operation two methods were utilised, amplitude- and frequency-modulated mode-locking. Pulse durations as short as 55 ns were demonstrated with a pulse energy of 1.56 nJ at 907.9 kHz. However, the measured spectrum of 368 nm full width at half maximum should result in a theoretically transform-limited pulse of around 9 ps, and thus should be much smaller than that demonstrated here. The experiments showed that reducing the resonator length shortens the pulse duration towards the transform-limited value. However, there is a trade-off using the liquid crystal cell: the shorter the cavity length, the larger the axial mode spacing, the higher the repetition rate and, consequently, the faster the liquid crystal has to modulate the resonator losses. Unfortunately, at high repetition rates the modulation depth of the liquid crystal decreases, as shown in Chapter 3.4.4. Thus, it is impossible to achieve pulse durations as short as a few tens of picoseconds just by decreasing the resonator length. Beside the reduced modulation depth of the liquid crystal at high repetition rates itself there are several other possible reasons for a pulse with a time-bandwidth product that is 6200 times higher than the theoretical prediction.

In the literature, similar behaviour is reported when making use of passive mode-locking elements such as saturable absorbers or polarisation rotation. Noiselike pulses of 100 ps duration and 44 nm spectral width were reported [214]. Modelling suggested that dispersion within a 3 m fibre accompanied by a high birefringence was the reason for such long pulses. Kelleher *et al.* demonstrated a pulse width of 1.7 ns within a ring cavity of 1200 m length using a carbon nanotube sample as a mode-locking device [215]. The 1200 m long fibre had a dispersion parameter $D = -30\ \mathrm{ps{\cdot}(nm\ km)^{-1}}$. Similar to the setup presented in this chapter, solely the fibre dispersion can not be held responsible for the pulse broadening. Based on dispersion calculations the pulse broadening should have been only a few picoseconds instead of nanoseconds. In reference [215] the authors suggest that the dispersion does not explain

the extreme pulse broadening but an additional nonlinearity within the fiber is responsible for the giant pulses. Kelleher *et al.* also demonstrated that the pulse duration increases with the length of the cavity length, similar to the behaviour described earlier in this chapter and as predicted by the formulas presented. Further reports suggest that a balance of dispersion and nonlinearity within the additional fibre is responsible for long pulse durations [216–219]. Kobtsev *et al.* also demonstrated giant mode-locked pulses (3 ns) and made nonlinear polarisation evolution within a 2.6 km passive fiber responsible for it [219]. To summaries: all those publications make the (nonlinear) dispersion within the cavity responsible for such long pulses. In future experiments the dispersion of the active gain fiber and liquid crystal should be measured to narrow down the reasons for the anomalous long pulses.

For future applications there are three possible directions for optimising the mode-locked laser: (i) further shorten the pulse duration, (ii) focus on narrow bandwidth transform limited nanosecond pulses [220, 221], or (iii) use it as an initially chirped pulse for chirped pulse amplification applications [222].

(i): As mentioned above, to further decrease the pulse width in the cavity that was presented within this work, the cavity must be shortened. When reducing the cavity length the modulation depth has to be increased and thus it should be a focus of future work. The modulation depth could be increased by varying the liquid crystal composition.

(ii): Ultra-narrowband nanosecond laser sources are promising for some applications, e.g. in absorption spectroscopy [223]. Laser sources to generate transform-limited nanosecond pulses are available [223–225]; however, they usually involve complex and expensive setups. Recently, Kues *et al.* demonstrated a narrowband fibre laser setup ($\Delta\lambda \approx 0.84$ pm) that reduced the complexity of commonly available laser sources [221]. Utilising a liquid crystal within a fibre laser cavity could further simplify these systems. Thus, it is promising to focus in the next steps on narrowband (transform-limited) nanosecond pulses. As first approach, an ultra-narrowband fibre Bragg grating could be used as an output-coupling filter.

(iii): The third approach is using the mode-locked laser for seeding applications within a chirped-pulse amplification (CPA) scheme. Giant chirped nanosecond pulses were demonstrated and suggested for CPA applications [215–217, 226]. The next step is to validate (for the current laser) that the pulse is (linearly) chirped. If that is the case, it may be worthwhile to amplify the pulse within a fibre and later compress it (e.g. within a volume Bragg grating or externally by other means). In the normal dispersion regime, a compression factor of

approximately 100 has been recently reported. Woodward *et al.* demonstrated that within a 846 m long fibre cavity, 0.99 ns pulses were generated and compressed in a chirped-fibre Bragg grating to 11 ps [222].

6

Compact Q-switched waveguide laser – an application

In this chapter, the aim is to use the compact Q-switched Thulium waveguide laser described in Section 4.3.2 for nonlinear spectral broadening in a chalcogenide fibre. Most Q-switched waveguide lasers of similar size achieve peak powers well below 1 W as a result of high repetition rates, as shown earlier in Chapter 4 (Table 4.1). However, when using an active Q-switched laser, one can easily reduce the repetition rate and thereby increase the peak power. The downside is that actively Q-switched lasers are normally rather bulky because of the intracavity Q-switch. As demonstrated in Chapter 4, using a novel liquid crystal cell as an active Q-switch enables the realisation of a laser with cavity dimensions similar to a passively Q-switched laser while maintaining control over the repetition rate. Peak power levels well above 1 W were demonstrated within the present work. Such high peak powers open up the possibility of using those laser sources for nonlinear applications [227, 228], including supercontinuum generation, high-harmonic generation or nonlinear absorption for

material processing. In most publications on Q-switched lasers, the pulse peak power is calculated from measured values like the average output power, the repetition rate and the pulse duration. However, a small continuous-wave offset can lead to a high uncertainty when estimating the peak power, and it can be challenging to detect such an offset with commonly available photodiodes. Being able to measure a CW offset requires a high dynamic range. Alternatively, when using the laser for nonlinear spectral broadening, it provides a method for confirming the calculated peak power. This can be done experimentally, by comparing the broadening achieved with different laser sources with theoretically similar output characteristics. Consequently, the spectral broadening behaviour of the integrated Q-switched Thulium waveguide laser is also compared to a laser utilising a bulk AOM as an active Q-switch with similar peak power to validate its performance.

6.1 Background – nonlinear spectral broadening

Nonlinear spectral broadening using nanosecond pulses has not been as thoroughly investigated as spectral broadening utilising sub-nanosecond pulses. The benefit of the former lies in the simplicity of generating nanosecond pulses compared to pico/femtosecond pulses.

When utilising femtosecond pulses, the mature driving mechanism in the anomalous dispersion region that leads to spectral broadening is initiated by soliton fission [229]. A soliton is split into several soliton pulses as a result of higher order dispersion and stimulated Raman scattering. Each pulse will travel through the fibre at a different speed, and thus the pulses will break up (temporally split) [230, 231]. Continuous propagation through the fibre gives rise to additional spectral components from the generation of dispersive wave radiation and continuous spectral and temporal shifts as a result of the Raman self-frequency shift [232, 233]. In the normal dispersion region, spectral broadening using femtosecond pulses is initiated by self-phase modulation (SPM). Near the zero dispersion wavelength, SPM can shift spectral components into the anomalous region in which soliton dynamics can, as described above, further contribute to the generation of additional spectral components [233].

At longer pulse durations, soliton dynamics, such as higher-order soliton evolution and soliton fission, become less dominant. Instead, near the zero dispersion wavelength (ZDW), the broadening in the anomalous dispersion region is initiated by spontaneous mode instabilities and four-wave mixing (FWM). Mode instabilities lead to a pump pulse breaking up into

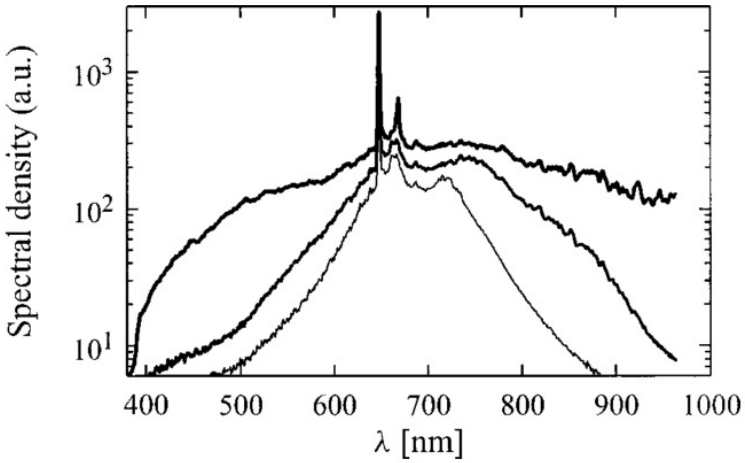

Figure 6.1: Typical output spectrum measured after a 10 m long photonic crystal fibre for varying input peak powers of P=120, 225, 675 W from bottom, smallest peak power, to top, highest peak power [241].

a large number of sub-pulses [233]. Those sub-pulses give rise, to soliton dynamics such as dispersive wave generation and Raman self-frequency shift. In the normal dispersion region near the ZDW, the initial spectral broadening is typically governed by four-wave mixing and stimulated Raman scattering (SRS). Usually, self-phase modulation is less dominant when utilising nanosecond pulses for spectral broadening [234, 235]. Due to the dominance of four-wave mixing and Raman scattering, the spectrum shows distinctive features. As demonstrated by Serebryannikov and Zheltikov [236], when utilising picosecond pulses FWM results in pronounced sidebands and SRS causes intense long-wavelength wings to appear. Furthermore, in the absence of SPM, the residual pump light in the spectrum stays almost unchanged in shape [235, 237–242]; see Fig. 6.1. However, at wavelengths that are further away from the ZDW the phase matching requirement for FWM is not fulfilled and thus FWM is less dominant or not apparent at all. In addition, below a certain threshold (<< 100 W), SRS does not contribute to spectral broadening. Note that this threshold for SRS depends on material parameters and the geometry of the waveguide. Serebryannikov and Zheltikov presented a study in which the spectrum was recorded for different lengths of the same nonlinear fiber (photonic crystal fiber) [236]. Away from the ZDW they demonstrated that the initial spectral broadening was solely governed by SPM. Once the spectral components were shifted towards the ZDW the phase matching condition for FWM was met and thus FWM contributed to the further spectral broadening.

The work presented in this thesis utilises peak powers of approximately 10 W (coupled

into the fibre), compared to peak powers of greater than 100 W typically found in the literature. Furthermore, the here used fiber was tailored to exhibit the ZDW near 3 µm and thus the phase matching condition in order to support efficient FWM was not met. Consequently, the results in this study were highly symmetric and did not exhibit signs of stimulated Raman scattering or four-wave mixing. The spectral features could be best reproduced by a model that uses self-phase modulation exclusively as a driving mechanism. Thus, in the following section a numerical model focusing on self-phase modulation is presented.

6.2 Self-phase modulation

Self-phase modulation is a result of the nonlinear Kerr effect, which itself describes an intensity-dependent refractive index change. The approach used here follows the theoretical analysis of Agrawal [243]. Assuming a pulse longer than a few picoseconds, it is possible to retrieve the pulse propagation equation from the wave equations in a simplified form:

$$i\frac{\partial A}{\partial z} + \frac{i\alpha}{2}A - \frac{\beta_2}{2}\frac{\partial^2 A}{\partial T^2} + \gamma|A|^2 A = 0. \tag{6.1}$$

Where T is the time in a reference frame that travels with the pulse's group velocity v_g ($T = t - z/v_g$). The fibre losses are represented in the coefficient α, while β_2 is the dispersion coefficient and γ is the nonlinearity coefficient. The slowly varying amplitude of the pulse envelope A is defined as follows:

$$A(z,\tau) = \sqrt{P_0}e^{-\frac{\alpha z}{2}}U(z,\tau), \tag{6.2}$$

where U is the normalised amplitude and P_0 is the launched peak power of the pulse. By substituting Eq. (6.2) into Eq. (6.1), the propagation equation can be rewritten in terms of the normalised amplitude U:

$$i\frac{\partial U}{\partial z} = \frac{sgn(\beta_2)}{2L_D}\frac{\partial^2 U}{\partial \tau^2} - \frac{e^{-\alpha z}}{L_{NL}}|U|^2 U. \tag{6.3}$$

On the right-hand side of the equation, the first term accounts for dispersion effects within the fibre and the second term accounts for fibre losses and nonlinear effects as a result of the pulse amplitude. It is the initial pulse width, the spectral width and peak power that determine

the effects that must be taken into account in Eq. (6.3). In the simplest case, there are either dispersive or nonlinear effects apparent. However, a combination of those two effects is also possible. Two length scales can be introduced to estimate which effect is dominant. The dispersion length L_D governs the distance over which dispersive effects take place and the nonlinear length L_{NL} describes the length required for the onset of nonlinear effects. The dispersion length L_D equals:

$$L_D = \frac{T_0^2}{|\beta_2|}, \tag{6.4}$$

where T_0 is the initial pulse duration when launched into the fibre and β_2 is the group velocity dispersion. The length over which nonlinear effects become important is:

$$L_{NL} = \frac{1}{\gamma P_0}. \tag{6.5}$$

By using the peak powers and pulse durations presented in Section 4.3.2, it is possible to estimate both values. The step-index chalcogenide fibre used was provided by the company IRFLEX (IRFS-5: As_2S_3 fibre, $d_{core} = 5\,\mu m$, $d_{cladding} = 100\,\mu m$, $n_{core} = 2.4$, $NA = 0.28–0.30$, propagation loss $\alpha = 0.25$ dB/m, 1.3 m length). The group velocity dispersion was computed to be $\beta_2 = 0.37$ ps^2/m based on using a vector eigenmode analysis [244] for the 5 µm cylindrical step index fiber. The nonlinear coefficient was estimated to be $\gamma = 0.45$ Wm^{-1} utilising $n_2 = 170 \times 10^{20}$ m^2/W [245]. The pulse duration T_0 was measured at 64 ns and the peak power launched into the fibre when taking into account reflection and insertion losses was estimated to be 9.6 W. Thus, in our case ($L_D = 10 \times 10^9$ m $>>$ L $>$ $L_{NL} = 0.222$ m) it is unlikely any dispersive effects will be seen; however, nonlinear effects should be apparent. Because of the pulses in the nanosecond regime and the relatively short fibre, group delay dispersion can be neglected in Eq. (6.3) ($\beta_2 = 0$). As a result, Eq. (6.3) can be simplified to only include nonlinear effects:

$$\frac{\partial U}{\partial z} = \frac{ie^{-\alpha z}}{L_{NL}}|U|^2\,U. \tag{6.6}$$

Substituting $U = Ve^{(i\phi_{NL})}$ into Eq. (6.6), one can solve the equation for the real and imaginary part:

$$\frac{\partial V}{\partial z} = 0, \qquad \frac{\partial \phi_{NL}}{\partial z} = \frac{ie^{-\alpha z}}{L_{NL}}|V|^2\,. \tag{6.7}$$

As can be seen from the real part, the amplitude does not change over the fibre length L. The imaginary part describes a phase change depending on the pulse amplitude. When integrating

the imaginary part over the propagation length, one retrieves a change in complex amplitude over the distance travelled depending on the nonlinear phase shift:

$$U(L,T) = U(0,T)e^{i\phi_{NL}(L,T)}. \tag{6.8}$$

The field amplitude at $z = 0$ equals $U(0,T)$. In Eq. (6.8), the nonlinear phase depends on the amplitude and distance travelled in the fibre as well as the nonlinear length:

$$\phi_{NL}(L,T) = |U(0,T)|^2 \frac{L_{eff}}{L_{NL}}. \tag{6.9}$$

Here, L_{eff} is the effective length of the fibre, which accounts for propagation losses α within the fibre. In the absence of any propagation losses, $L_{eff} = L$. However, in reality propagation losses are apparent and the length travelled within the fibre must be rewritten to an effective length:

$$L_{eff} = \frac{1 - e^{-\alpha L}}{\alpha}. \tag{6.10}$$

It becomes clear from Eq. (6.9) that a phase shift is introduced depending on the amplitude of the pulse. Otherwise, the pulse shape is unaffected. The maximum phase shift is introduced in the centre of the pulse at $T = 0$. When normalising the amplitude ($U = 1$), the maximum phase change is given by:

$$\phi_{max} = \frac{L_{eff}}{L_{NL}} = \gamma P_0 L_{eff}, \tag{6.11}$$

where ϕ_{max} is the maximum phase change in rad. Once the maximum phase change is known, the spectral broadening factor for a Gaussian pulse can be calculated [246]:

$$\frac{\Delta\omega_{RMS}}{\Delta\omega_0} = \left(1 + \frac{4}{3\sqrt{3}}\phi_{max}\right). \tag{6.12}$$

The initial spectral width $\Delta\omega_0$ for a unchirped pulse is determined by the root mean square (RMS) and $\Delta\omega_{RMS}$ is the RMS spectral width of the resulting pulse.

6.3 Split-step Fourier method

Equation (6.12) provides an estimate for the nonlinear spectral broadening. In the general case, more accurate results can be obtained by directly solving the partial differential equation

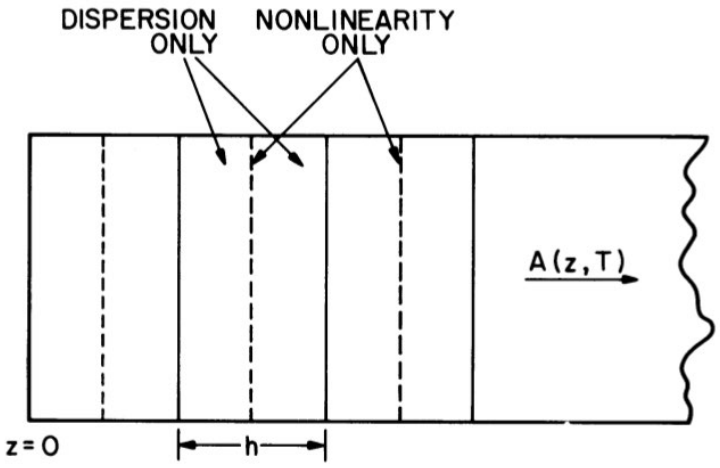

Figure 6.2: Schematic of the concept underpinning the split-step Fourier method. The interaction material is subdivided into a number of segments of length h. Dispersion and nonlinear effects are considered in a successive fashion, step by step. The nonlinearity is included in the middle of each segment [243].

(Eq. (6.1)). The idea behind the split-step Fourier method is that dispersive and nonlinear effects act independently over the whole propagation distance. For that, the overall fibre length is subdivided into small, equally spaced distances, h, as illustrated in Fig. 6.2. Each slice is solved in two successive steps. In the first step, the nonlinearity acts alone and dispersive effects are neglected. In a second step, nonlinearity is neglected, and only dispersive effects act. For that purpose, Eq. (6.1) can be simplified and rewritten to introduce two operators $\hat{D}$ and $\hat{N}$:

$$\frac{\partial A}{z} = (\hat{D} + \hat{N})A. \tag{6.13}$$

The differential operator $\hat{D}$ accounts for absorption and dispersion, and $\hat{N}$ applies to nonlinear effects. The operators themselves are defined as follows:

$$\hat{D} = -i\frac{\beta_2}{2}\frac{\partial^2}{\partial T^2} - \frac{\alpha}{2} \tag{6.14}$$

and

$$\hat{N} = -i\gamma\left(|A|^2 + i\frac{1}{w_0 A}\frac{\partial}{\partial T}(|A|^2 A) - T_R\frac{\partial |A|^2}{\partial T}\right). \tag{6.15}$$

The effect of those operators on the travelling pulse amplitude can be described as follows:

$$A(z+h,T) \approx e^{h\hat{D}}e^{h\hat{N}}A(z,T). \tag{6.16}$$

Table 6.1: Using the split-step Fourier method, six mathematical steps must be followed. Dispersive effects are handled in the frequency domain, whereas temporal effects are treated in the time domain.

Step Nb.:	Operation
Step 1	$A(z,T) = \sqrt{P_0}\mathrm{sech}(\tau/t_0)$
Step 2	$A(z,\omega) = \mathrm{fft}[A(z,T)]$
Step 3	$A(z+h,\omega) = A(z+h,\omega)e^{h\hat{D}}$
Step 4	$A(z+h/2,T) = \mathrm{fft}^{-1}[A(z+h,\omega)]$
Step 5	$A(z+1.5h,T) = A(z+h/2,T)e^{h\hat{N}}$
Step 6	$A(z,T) = A(z+1.5h,T)$

As mentioned before, over the distance h operators $\hat{D}$ and $\hat{N}$ both act independently. The dispersive operator is applied in the frequency domain rather than the time domain. In the frequency domain, $\hat{D}$ is just a number, and thus a straightforward operation. The differential operator $\partial/\partial T$ in Eq. (6.14) is replaced by $i\omega$. To ensure the accuracy of the numerical simulations, the timeframe T must be wide enough to include the temporal pulse shape within its window. Commonly, a timeframe 10–20 times the pulse width is chosen in order to achieve accurate results.

Table 6.1 outlines the sequence of steps used to simulate the pulse propagation along the fibre. During the first step, the initial pulse shape and its temporal amplitude are calculated. Once calculated, it is Fourier-transformed to the frequency domain. In the next step, the dispersive operator $\hat{D}$ is multiplied over the distance h, which accounts for dispersive effects and propagation losses. Then the signal is transformed back from the frequency domain to the time domain. In step five, the nonlinear effects are taken into account via its nonlinear operator $\hat{N}$ over the propagation distance h. Note that the position at which the nonlinear operator is considered is shifted forward in space by $h/2$, as shown in Fig. 6.2. Applying those steps across the whole fibre length will result in an altered initial temporal and spectral amplitude.

6.4 Experimental methods and results

In the following sections, the results of nonlinear spectral broadening using a chalcogenide fibre and the previously described Q-switched Thulium-doped chip laser are presented. First, handling of the fragile fibre is discussed. Second, the laser setup is presented. Finally, the

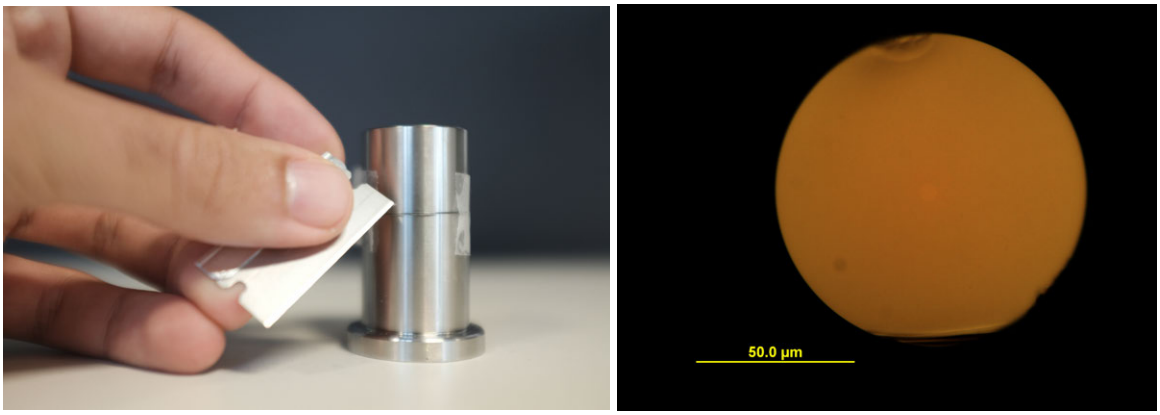

(a) (b)

Figure 6.3: The chalcogenide fibre is too fragile to be cleaved with a commonly used cleaver. Therefore, in (a) the fibre was cleaved by hand with a razor blade. Bending the fibre around a 1-inch post applies the tension needed for a clean cleave. In (b) the cleaved end facet is shown. The fibre used here was provided by the company IRFLEX (IRFS-5: As_2S_3 step-index fibre, d_{core} = 5 µm, $d_{cladding}$ = 100 µm, n_{core} = 2.4, NA = 0.28–0.30, propagation loss α = 0.25 dB/m, 1.3 m length).

results are presented and interpreted.

6.4.1 Fibre handling

Chalcogenide fibres are fragile and need special handling precautions. The main problem was to cleave the fibre to maximise the in-coupling efficiency. Unfortunately, commercially available automated cleavers could not be used because the minimum tension applied resulted in a damaged fibre facet. Prior to the cleave, the polymer coating had to be removed using a paste made from dichloromethane. Before the coating could be removed, the fibre had to rest for approximately one minute in the dichloromethane solution; the coating then peels away from the fibre and is easy to strip.

A razor blade was used for cleaving the fibre. To apply tension, the fibre was wrapped around a one-inch diameter post (see Fig. 6.3a). The induced tension was sufficient to create a clean cleave when the fibre was touched with the edge of a razor blade. Once cleaved, the end facet was inspected with an optical microscope; a microscopic image is shown in Fig. 6.3b. On average, every fifth cleave resulted in a good surface quality. However, the cleave angle is hard to control using this method, which can result additional coupling losses.

Employing an infrared camera (FJW Optical Systems: FIND-R-SCOPE Mode 85345A),

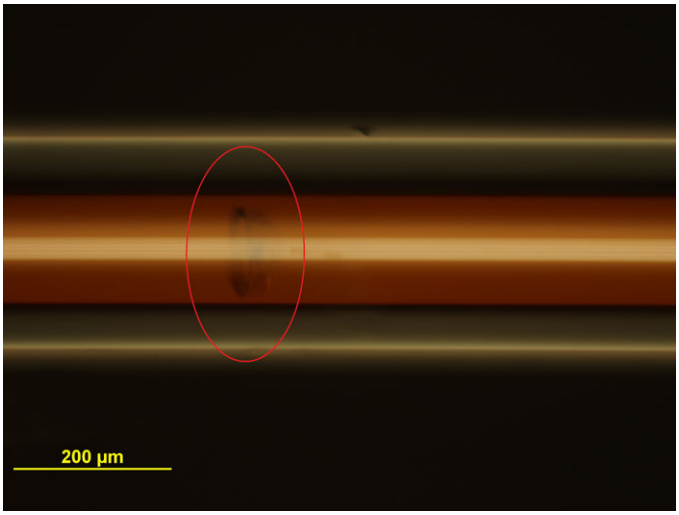

Figure 6.4: Illustration of fibre deflects. The dark area around the fibre core accounted for a small scattering centre that could be imaged with an infrared camera.

there were a couple of scattering centres visualised along the fibre. When further investigating the fibre with a microscope, a couple of dark spots were evident where the scattering centres were situated (see Fig. 6.4). In addition to an imperfect beam quality, as mentioned earlier, those little defects are responsible for increased propagation losses — and thus less efficient spectral broadening.

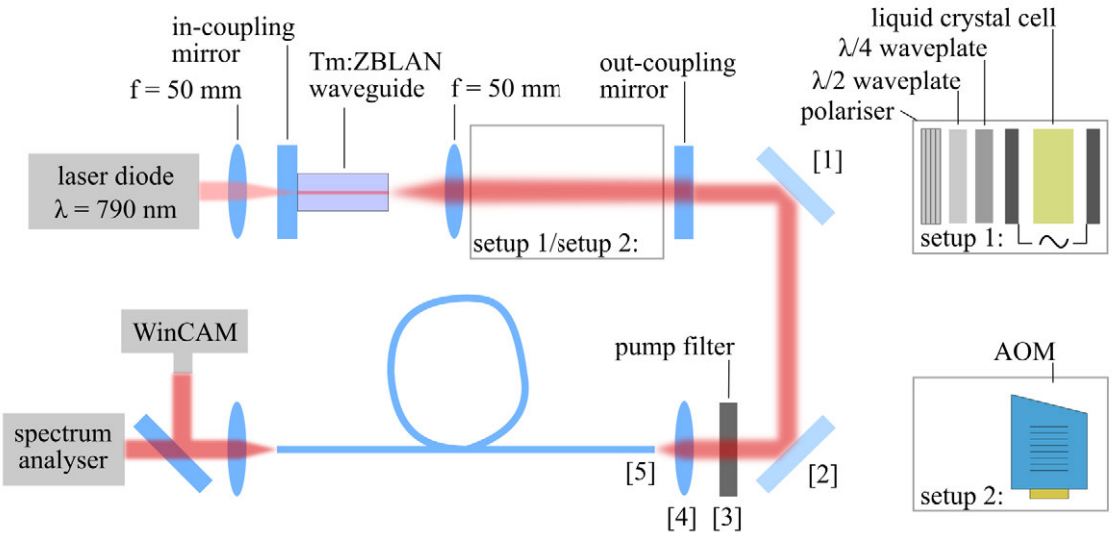

Figure 6.5: Schematic of the setup used for nonlinear spectral broadening. The Thulium-doped ZBLAN laser (see chapter 4.3.2), was coupled into a nonlinear chalcogenide fibre (IRFLEX - IRFS-5: As_2S_3 step-index fibre, d_{core} = 5 µm, $d_{cladding}$ = 100 µm, n_{core} = 2.4, NA = 0.28–0.30, propagation loss α = 0.25 dB/m, 1.3 m length). The coupling lens had a focal length of 6 mm and the chalcogenide fibre was 1.3 m in length. The relevant transmission losses on each component at approximately 1880 nm were: (1,2) 2 %, (3) 16.5 %, (4) 20 % and (5) 17 %. Note that, for comparison purposes, the polariser and liquid crystal cell were replaced in a later setup with a bulk acousto-optic modulator (AOM).

6.4.2 Experimental setup

The laser setup used was the same as that discussed in Section 4.3.2. A Thulium-doped ZBLAN glass chip with a femtosecond laser-inscribed waveguide was utilised as an active gain medium. Pulse durations of 64 ns and peak powers up to 27.4 W were achieved with a liquid crystal cell used as an active Q-switch. The laser beam was coupled into the chalcogenide fibre using an aspheric lens with a focal length of 6 mm (Innovative Photonics: LFO-5-6-3.75). To allow the best possible alignment, the fibre end-facet was constantly monitored using an imaging lens and a WinCAM infrared camera. Therefore, a small fraction of the beam was reflected via a wedge plate located between the spectrum analyser and the lens. The transmission losses for each component are summarised in the caption of Fig. 6.5. Accounting for all transmission losses from the optics leading towards the fibre, the optical power is attenuated by 35.8 % just before the fibre facet. The high refractive index difference between air and the As_2S_3 fibre core resulted in an additional 17 % Fresnel loss. In theory, it should be possible to inject 14.6 W from the total 27.4 W pulse peak power into the fibre. In this study, 9.6 W was coupled into the fibre, which corresponds

to a coupling efficiency of approximately 65.5 %. There are several potential causes for a degenerated coupling efficiency, with the most likely being a mode-field diameter mismatch at the in-coupling surface. The beam diameter at the position of the lens was measured at 2ω = 2.7 mm, which results in a calculated focal diameter behind the lens of 6 µm. The corresponding mode-field radius is ω_{focus} = 3.0 µm. The mode-field radius of the fibre is calculated to be ω_{fibre} = 2.0 µm. The corresponding coupling efficiency can be calculated as follows:

$$\eta = \frac{4\omega_{focus}^2 \omega_{fibre}^2}{(\omega_{focus}^2 + \omega_{fibre}^2)^2}. \tag{6.17}$$

In theory, one should be able to achieve a coupling efficiency of 85.4 %. As mentioned earlier, the fibre cleave may have resulted in an angled end surface. Furthermore, the fibre was mounted with its end suspended in free space. As a result, the fibre deviated slightly from the optical axes of the system. The input coupling is very sensitive to the relative angle and the wavefront of the focused beam. A slight relative angular mismatch of 3° degrees may have resulted in a further reduction of the coupling efficiency by approximately 16 %.

6.4.3 Experimental results

In the following subsections, the spectral broadening capabilities of the previously developed Q-switched Tm:ZBLAN laser are tested. To confirm the previously calculated peak power, the following experiment was conducted with two different laser setups. The first setup used a liquid crystal as an active Q-switch, while the second employed an acousto-optic modulator (AOM – NEOS Technologies - Model Number: 33024-50-50-HGM-(W)); see Fig. 6.2. Note that to implement the bulky AOM, the cavity had to be extended.

Setup 1 – Liquid crystal

The output beam was launched into the chalcogenide fibre through an aspheric lens. The peak power was varied by altering the repetition rate of the cavity internal modulator. The highest peak power, calculated at 27.4 W, was reached at 0.8 kHz. Behind the lens and just before coupling into the fibre, the remaining optical power measured 14.6 W. Taking into account 17 % Fresnel losses at the fibre facet and a coupling efficiency of 65.5 % resulted in a launched peak power of 9.6 W. The spectrum was recorded before and after the chalcogenide fibre.

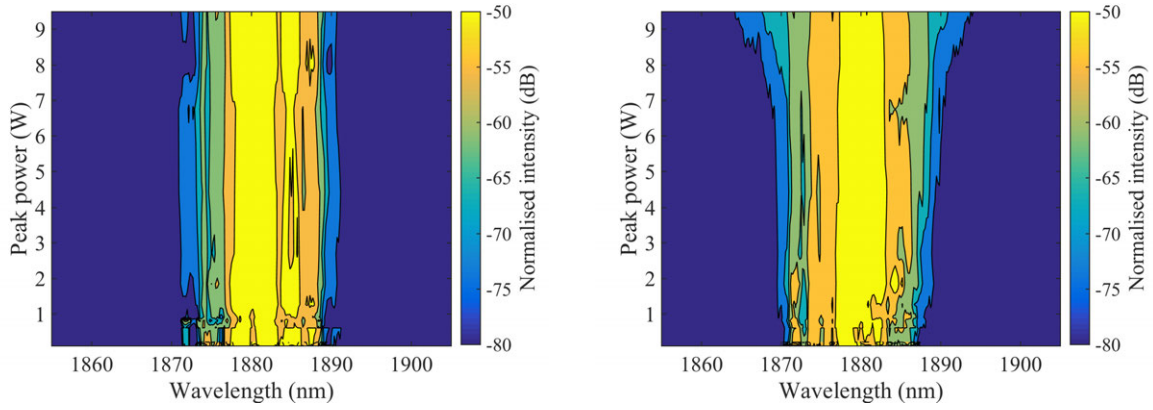

(a) (b)

Figure 6.6: Recorded spectra for different pulse peak powers utilising the liquid crystal as a Q-switch. The spectrum was measured before (a) and (b) after coupling into the chalcogenide fibre.

The spectrum before coupling into the chalcogenide fibre exhibited a spectral width of approximately 16.2 nm at -30 dB. Changing the repetition rate did not affect the spectral width (see Fig. 6.6a). Spectral broadening was observed for launched peak powers exceeding ~7 W, as illustrated in Fig. 6.6b. At 9.6 W of coupled peak power, the spectral width increased to 24.4 nm at -30 dB (see Fig. 6.7a). In the recorded spectrum there were no spectral features that originate from stimulated Raman scattering. Signs of SRS would show in the spectrum as peaks that are shifted by roughly $\Delta\lambda = 100\,\text{nm}$ [247] to either side of the pump peak.

The experimentally measured spectral width at -30 dB from the peak was compared to the simulation results. In Fig. 6.7b, the broadening ratio $\Delta\omega_{out}/\Delta\omega_{in}$ is plotted against the launched peak power. According to the numerical model, at 9.6 W peak power the spectrum should have broadened by a factor of 4.6, yet experimentally the spectrum broadened by a factor of 1.51. This can be attributed to several factors, including the nonlinear coefficient being and/or increased propagation losses. The nonlinear coefficient (γ) was calculated from the nonlinear refractive index (n_2), which was published for As_2S_3 [245, 248–253]. The published nonlinear refractive index ranges from $n_2 = 170\text{–}600\times10^{-20}$ m^2/W, which results in γ (for the fibre used in this study) between 0.45 and 1.6 W/m. It must be mentioned that throughout the published data the values for n_2 are recorded with probing wavelengths below 1550 nm. However, n_2 decreases for longer wavelengths away from the resonance frequency of the host material, and thus even smaller values for n_2 can be assumed [254, 255]. Utilising $n_2 = 49\times10^{-20}$ m^2/W) would yield a match between theory and the experimental data

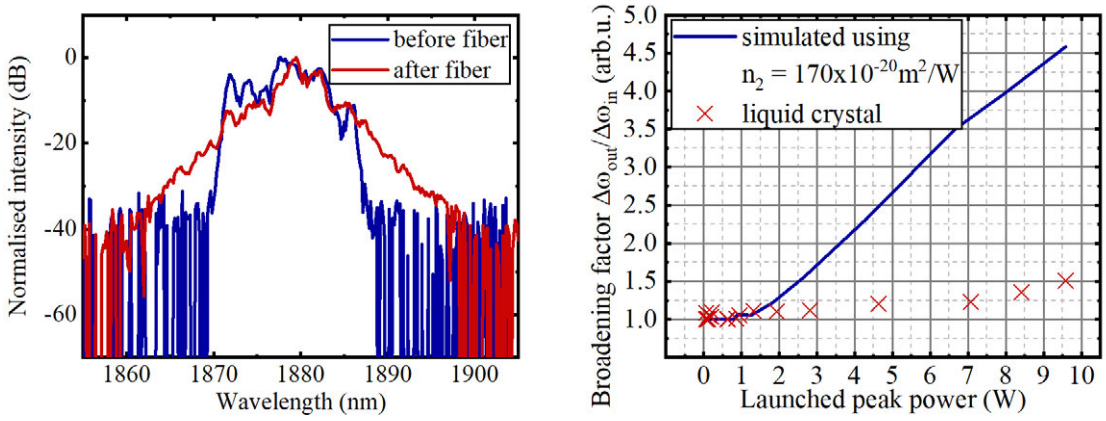

(a) (b)

Figure 6.7: Q-switched pulses were coupled into a chalcogenide fibre in order to broaden the spectrum. In (a) a direct comparison at 9.6 W launched peak power between the initial spectrum (blue trace) and the nonlinear broadened spectrum after propagation through the fibre (red line) is shown. In (b) the broadening factor was simulated (blue trace) and compared to the experimentally recorded data (red dots).

presented here.

Setup 2 – AOM

The Q-switched laser that incorporated an AOM was characterised for the peak power and pulse duration beforehand (see Fig. 6.8). At repetition rates below 2 kHz, peak powers well above 500 W were achieved. To compare the spectral broadening performance of Setup 1 to Setup 2, only repetition rates that resulted in similar peak powers were used. At a repetition rate of 6 kHz, the peak power was calculated to be 26.9 W. Taking into account the reflection and transmission losses within the optical setup (see Fig. 6.5), 17.3 W of peak power remained before launching the beam into the chalcogenide fibre. Fresnel losses of 17 %, and a degenerated coupling efficiency of 65.5 % resulted in 9.4 W of peak power launched into the fibre.

Figure 6.9b shows the recorded spectrum as a function of launched peak power. For comparison, the results achieved using the liquid crystal Q-switched laser are depicted in Fig. 6.9a. It is evident that both setups resulted in similar spectral broadening. This proves that the reduced broadening factor relative to the numerical modelling is not a result of CW-breakthrough between the Q-switched pulses. When further increasing the launched peak power up to 20 W (in Fig. 6.9c), the broadening increases in an expected fashion. However, the fibre was damaged at one of the aforementioned scattering centres near a launched peak

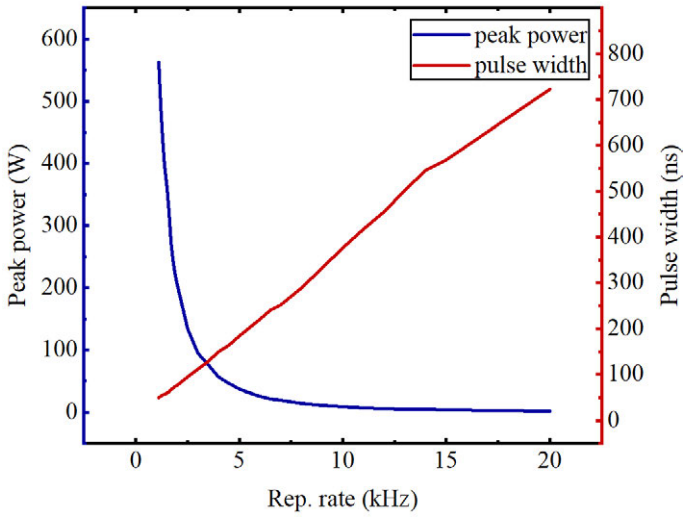

Figure 6.8: Laser performance of the AOM Q-switched laser. At repetition rates below 2 kHz, the peak power exceeded 500 W.

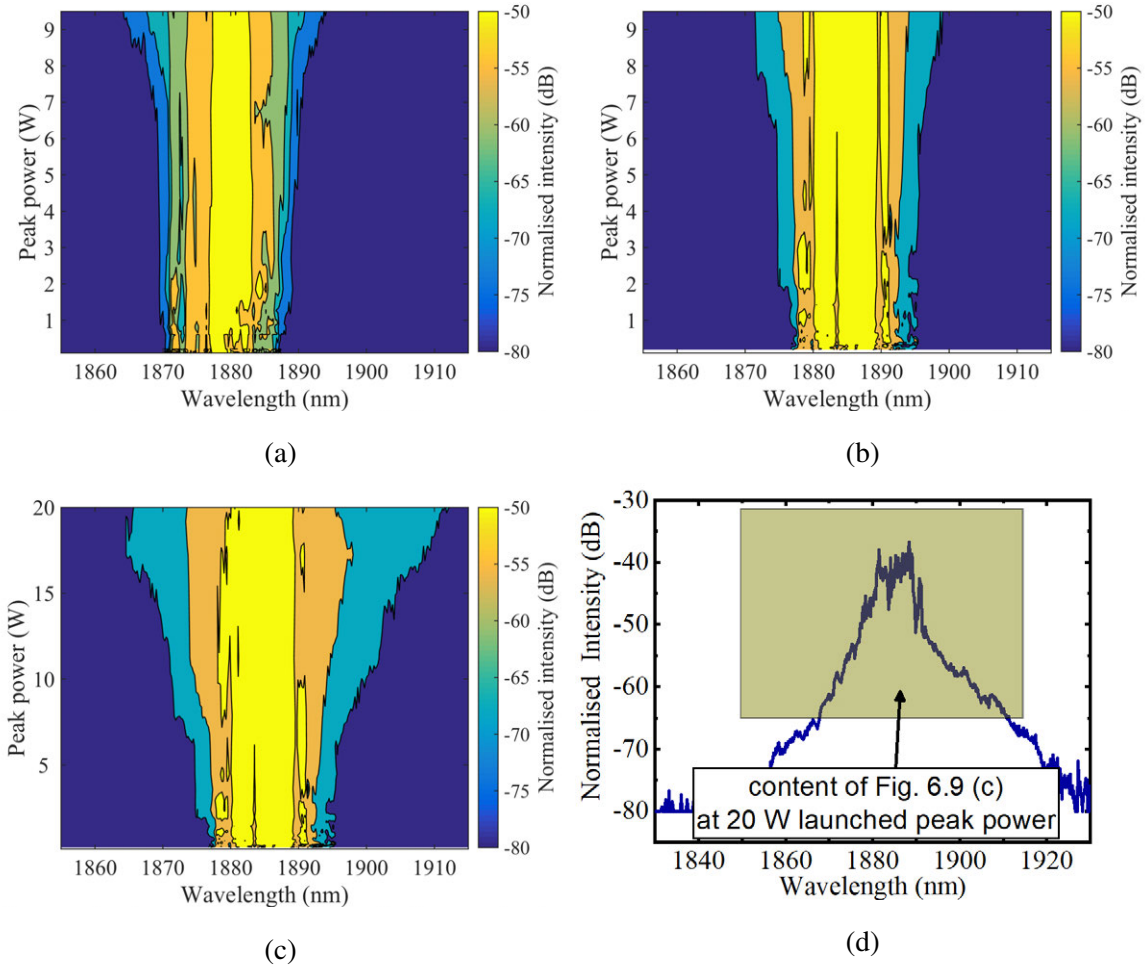

Figure 6.9: Experimentally recorded spectra at the output of the fibre as a function of peak power. (a) LC Q-switched laser, (b) AOM Q-switched laser, (c) AOM Q-switched laser using larger peak powers, (d) AOM Q-switched spectrum recorded at 20 W launched peak power.

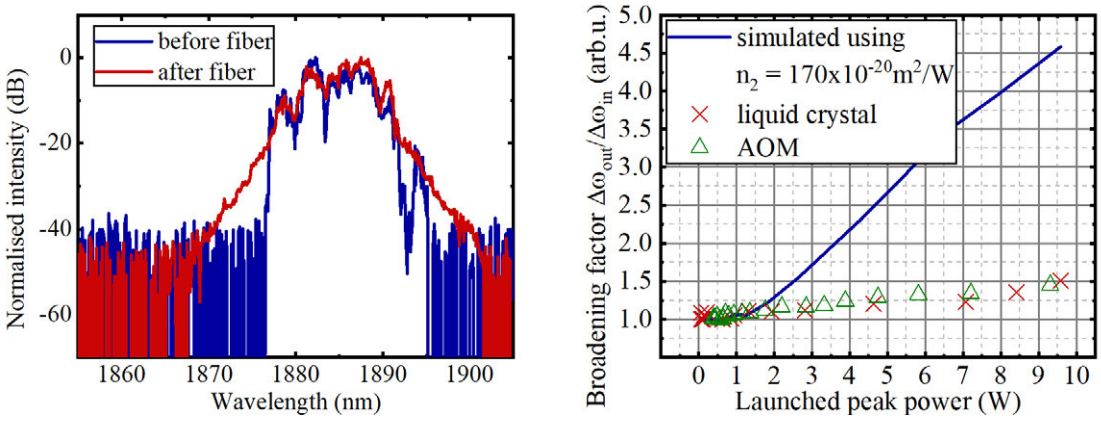

(a) (b)

Figure 6.10: (a) Comparison between the input and output spectrum at 9.4 W launched peak power using the AOM Q-switched laser. The spectrum is broadened by a factor of 1.45 at the -30 dB points. (b) Broadening factor predicted by the numerical model and experimentally measured broadening factor using the AOM Q-switched as well as LC Q-switched laser.

power of 20 W.

In Fig. 6.10a, a comparison of the spectrum before and after launching 9.4 W of peak power into the fibre is shown. The spectral width of the incident pulse is 16 nm at -30 dB. After the fibre, the spectrum was broadened to roughly 21.5 nm. To further compare the results between the two setups the broadening factor $\Delta\omega_{out}/\Delta\omega_{in}$ was measured for each recorded point. In Fig. 6.10b, the results are compared to the simulated value. At 9.4 W launched peak power, the spectrum of the AOM Q-switched laser was broadened by a factor of 1.45. In comparison with the simulated data using $n_2 = 170 \times 10^{-20}$ m^2/W, this value should be approximately 4.48.

6.5 Conclusion

The main aim of this study was to investigate the potential for nonlinear applications of the Q-switched waveguide laser, specifically to spectral broadening. A laser this small with the capability of producing a broad spectrum would be a promising device for laser spectroscopy applications [256–258], telecommunication [259], optical metrology [260] or as a seed source for lab-on-a-chip applications [28], especially as the liquid crystal can be used as a Q-switch for various wavelengths from the visible to the mid-infrared. An additional aim was to confirm that the Q-switched pulses are free of any CW-background signal. Simulations predict that the input spectrum should be broadened by a factor of 4.6 for a launched peak power of 9.6 W. The experimentally retrieved spectral data indicated no signs of stimulated Raman scattering or parametric processes, e.g., four-wave mixing. Note that, the involvement of parametric processes, such as four-wave mixing, requires a special dispersion-tailored fibre or operation near the zero-dispersion wavelength, which was not the case with the fibre used here. Thus, the model used here is based on spectral broadening through self-phase modulation only. In the conducted experiments, the input spectrum was broadened by a factor of 1.51, which is substantially less than anticipated. The base of the modelling presented here is the nonlinear refractive index, n_2. The simulation outcome strongly depends on n_2. The values found in the literature are diverse, and there are no measurements found for the wavelength used in this research. The lowest value mentioned in literature was $n_2 = 90{\times}10^{-20}$ m^2/W [261, 262], measured at a wavelength of 1550 nm. However, even though it is a chalcogenide fibre the composition of the fibre in this publication is not quite clear, and thus the next highest published nonlinear refractive index $n_2 = 170{\times}10^{-20}$ m^2/W was used as a base for the modelling in this research. Note that the nonlinear refractive index decreases for longer wavelengths [254, 255]. In Fig. 6.11, simulations conducted for different values of n_2 are presented. The upper limit is set by utilising $n_2 = 170{\times}10^{-20}$ m^2/W and the lower limit is defined by using $n_2 = 37{\times}10^{-20}$ m^2/W. Utilising $n_2 = 49{\times}10^{-20}$ m^2/W resulted in a good match to the experimentally retrieved data (green trace). It must be mentioned that the chalcogenide fibre used throughout the experiments showed scattering defects along the fibre, which can be seen as an indicator for increased propagation losses. A lower nonlinear refractive index n_2 in combination with increased propagation losses could be responsible for a decrease in spectral broadening. Ideally, in future experiments, a cut-back method would be conducted (with the remainder of the damaged fibre) to ascertain the influence of those

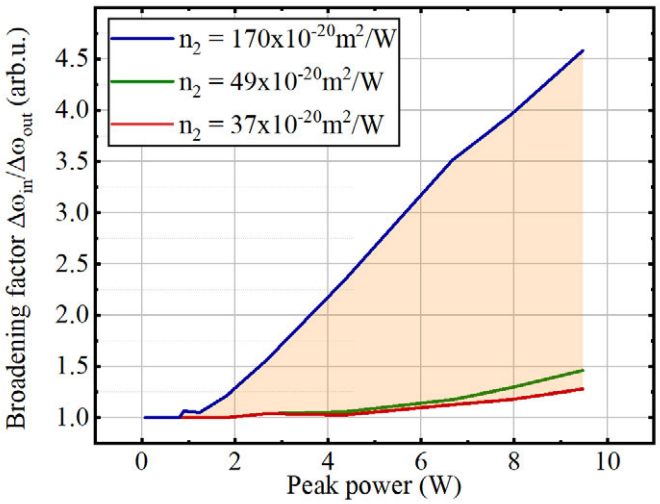

Figure 6.11: Broadening factor predicted by the numerical model for different nonlinear refractive indices n_2. The upper limit ($n_2 = 170\times10^{-20}$ m^2/W) utilises a nonlinear refractive index measured at a wavelength of 1550 nm [245]. $n_2 = 49\times10^{-20}$ m^2/W yields a good fit with the experimental data presented here.

defects on the propagation losses.

It was also shown that both laser setups (setup 1: liquid crystal, setup 2: AOM) achieved similar broadening factors, and thus it is reasonable to assume that they have similar peak powers. It supports the assumption that the output signal is free of any CW-background offset and, therefore, the previously estimated peak power seems legitimate. Furthermore, the outcome of the simulations and experimental results shows that the Q-switch waveguide laser has sufficient peak power to initiate nonlinear experiments. For this purpose, tailored nonlinear fibres with single-mode propagation and an optimised zero-dispersion wavelength around 1880 nm could be used in the future to further improve the broadening capabilities. There is promise also in investigating the broadening capabilities using a highly nonlinear tapered fibre. Al-kadry *et al.* demonstrated supercontinuum generation with femtosecond pulses with a pulse peak power of 18.8 W [263]. Such tapers are more compact and well suited for use with an integrated waveguide chip.

7

Summary and future work

The aim of this thesis was to develop a compact, actively Q-switched laser source that gives the user control over laser parameters such as repetition rate, pulse duration and pulse peak power. A second goal was to develop a versatile fibre laser that could be seamlessly switched between mode-locked, Q-switched and continuous-wave operation (CW). For these challenges, a suitable intracavity optical switch had to be found that supported a monolithic design.

The main findings of this study are summarised below and an outlook for future research, as well as a pathway to transfer the research to industrial applications, is given. A more detailed conclusion that includes links to the broader field of research is provided in the last four chapters.

7.1 Summary

The first step in this project was to find a suitable optical loss modulator that was fast enough for Q-switching/mode-locking and could be integrated to enable a monolithic setup. A collaboration was established with Zedelef Pty. Ltd., who recently developed and patented a novel liquid crystal-based transducer for sensing applications. The transducer is build utilising a ferroelectric smectic-C phase liquid crystal and was used for low voltages (< 2 V) to provide hysteresis-free linear responses. This transducer was adopted for loss modulations on a microsecond- to submicrosecond-timescale. Cells incorporating layer thicknesses between 3.3 µm and 9.0 µm were tested. The layer thickness showed a major influence on the switching speed. Thicker layers are faster and are thus preferable for intracavity loss modulation. It was possible to reach a switching speed of 36 % μs^{-1}. The switching speed of typically used active loss-modulators – for example, an accousto-optical modulator (AOM) – is approximately 3600 % μs^{-1}, on average a hundred times faster. The frequency response of the liquid crystal cell was also tested. The cell can be driven up to 50 kHz while maintaining its switching performance. Above this critical value, the switching speed decreases significantly. However, when applying a modified waveform it is possible to flatten the slope of this effect. Thus, a switching speed of 10.7 % μs^{-1} at a repetition rate of approximately 900 kHz was demonstrated. Depending on the probing wavelength, the double-pass transmission losses exceeded 60 %. The losses were observed to fluctuate from cell to cell by up to ±10 %, an effect attributed to fabrication variability. Overall, the characterisation showed that the cell is very promising for the purpose of intracavity loss modulation.

In a next step, several femtosecond laser-inscribed waveguide samples were employed as an active gain medium in a laser cavity. Each sample was doped with different active laser ions to realise laser transitions at wavelengths ranging from the visible to the mid-infrared (644 nm, 1016 nm, 1030 nm, 1878 nm). The liquid crystal cell, in conjunction with a polariser, was introduced into the cavity as a Q-switch. It was demonstrated that the Q-switch was sufficient to achieve single pulses with pulse durations as short as 21.4 ns (at 1030 nm). Furthermore, pulse peak powers of up to 49 W (at 1016 nm) were achieved. The repetition rate was tuneable by changing the frequency of the applied waveform from a few hertz up to hundreds of kilohertz. It is this tuneability that makes it possible to achieve much higher pulse peak powers than other setups of similar size. Typically, femtosecond inscribed waveguide

lasers incorporating a saturable absorber as a passive Q-switch achieve peak powers of up to 1 W at repetition rates of a few tens of kilohertz. Furthermore, it was possible to simplify the overall setup by using polarisation selective waveguides instead of an external polariser. A theoretical model was also developed to gain a deeper insight into the behaviour of the actively Q-switched laser source, which is required for optimisation purposes.

The liquid crystal cell was then used for active mode-locking. Within this study, frequency- and amplitude-modulated mode-locking were demonstrated. The shortest pulse duration achieved measured 55 ns, too long to be used as indicator for mode-locking. Instead, the radio-frequency spectrum was analysed; this exhibited a stable peak train at the frequency of the axial mode spacing and a multiples thereof. In addition, it was shown that, by changing the repetition rate of the applied voltage waveform, the laser could be operated in mode-locked, Q-switched and continuous-wave operation. Hence, using a liquid crystal cell it was possible to build a versatile fibre laser.

In a last step, a nonlinear chalcogenide step index fibre was employed to investigate the spectral broadening capabilities of the Q-switched chip laser source. For that, the Thulium-doped waveguide laser (1878 nm) was used. A peak power of 9.6 W was launched into the chalcogenide fibre. The spectrum was broadened by a factor of 1.51, from 16.2 nm to 24.4 nm, measured at -30 dB. Simulations based on published data for the nonlinear refractive index n_2 predict a broadening factor of 4.6. The cause for the relatively weak broadening factor is unclear; however, the simulations are sensitive to the pulse peak power and n_2. The pulse peak power was calculated from the average output power, pulse duration and repetition rate. This method is sensitive to parasitic oscillations, as it significantly overestimates the retrieved peak power. A CW background is difficult to detect with commonly available photodiodes. To rule out an overestimated peak power, a second setup was established that employed an intracavity AOM. It was demonstrated that at comparable pulse peak powers the broadening factor was similar, and thus the calculated peak power should be valid. However, several distinct scattering spots within the fibre were detected utilising an infrared camera, which indicates increased propagation losses. Furthermore, n_2 varies throughout published data and strongly depends on the wavelength at which it is measured. There was no publication that provided a n_2 for wavelengths used in this experiment. Thus, it was assumed that the decreased broadening factor is due at least in part to a combination of an increased propagation

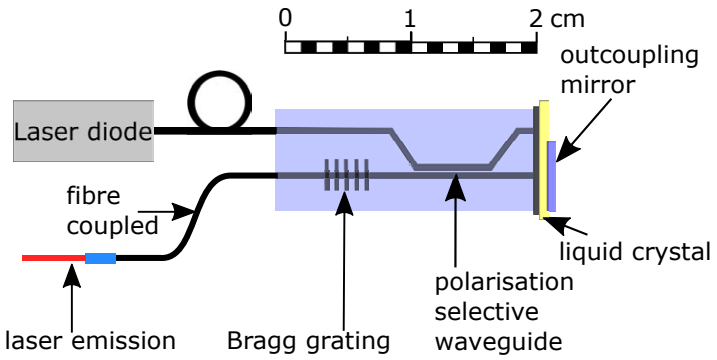

Figure 7.1: Schematic of a monolithic actively Q-switched waveguide laser. This future setup combines: polarisation-selective stressed waveguides [79], wavelength-selective beam combiner as a pump coupler [20], Bragg grating [21].

loss and overestimated value for n_2.

7.2 Future work

This section is grouped into two parts. In the first part, concepts are presented for future research and engineering opportunities. In the second part, the steps needed for transferring the Q-switched waveguide laser technology from the laboratory to practical applications are discussed.

Future outlook for engineering and research. The main goal is to achieve an overall improved laser performance for the versatile fibre laser and for the Q-switched waveguide laser. Therefore, enhancing the performance of the liquid crystal cell itself is the priority. Future work should focus on increasing (i) the switching speed and (ii) the liquid crystal quality. Throughout this work, the same liquid crystal composition was used for different laser wavelengths. The switching speed and the quality, e.g. the transmission, could be increased by finding different liquid crystal compositions for each setup. In addition, this study revealed that a thicker liquid crystal layer exhibited faster switching speeds. In future work, the liquid crystal layer thickness could be further scaled. These changes would benefit the laser performance and thus increase the pulse peak power. This is also advantageous for nonlinear spectral broadening. Within this study, problems with the quality of the nonlinear chalcogenide fibre were encountered. It would be useful to test a variety of nonlinear fibres or nonlinear tapers to explore the full potential of their spectral broadening capabilities. In working towards a fully monolithic waveguide laser setup, it would be useful to unite

several achievements within the femtosecond laser beam-writing community. This includes inscribing pump couplers into the gain material and butt-coupling a fibre-coupled laser diode directly to it. As demonstrated in this work, stressed waveguides can greatly simplify the setup, as no additional polariser is needed. Furthermore, dielectric coatings could be directly deposited onto the active gain material. Alternatively, Bragg gratings could be directly inscribed into the waveguide chip. Figure 7.1 shows a schematic incorporating all those technologies.

Transfer from the laboratory to applications. Transferring the technology for compact Q-switched laser sources to practical applications is another promising aspect. For that purpose, a laser model was developed that can be conveniently used to improve the laser performance in theory before implementation. The modelling emphasises two key parameters for increasing the laser efficiency, which are consistent with the abovementioned goals of increasing the switching speed (i) and the liquid crystal quality (ii). In addition, practical aims should be defined to enable (iii) production scalability and (iv) environmental stability. In this study, the liquid crystal cells were all of different quality and thus exhibited different transmission losses. For practical purposes, a method must be found of increasing the reproducibility of the cells. Overall, the study provides an approach that enables a monolithic actively Q-switched laser setup compatible with a compact packaging. The idea of using a liquid crystal cell in combination with a waveguide laser source was patented within the scope of this work. An industry partner (Lastek Pty Ltd) sees high potential in the current Q-switching approach and is working with us on commercialising this pulsed waveguide laser. A laboratory prototype was built and transferred to Lastek Pty Ltd. A photograph of this laboratory prototype is shown at Fig. 7.2. As a next step, a packaged prototype will be tested under a range of environmental conditions and its long-term stability will be monitored.

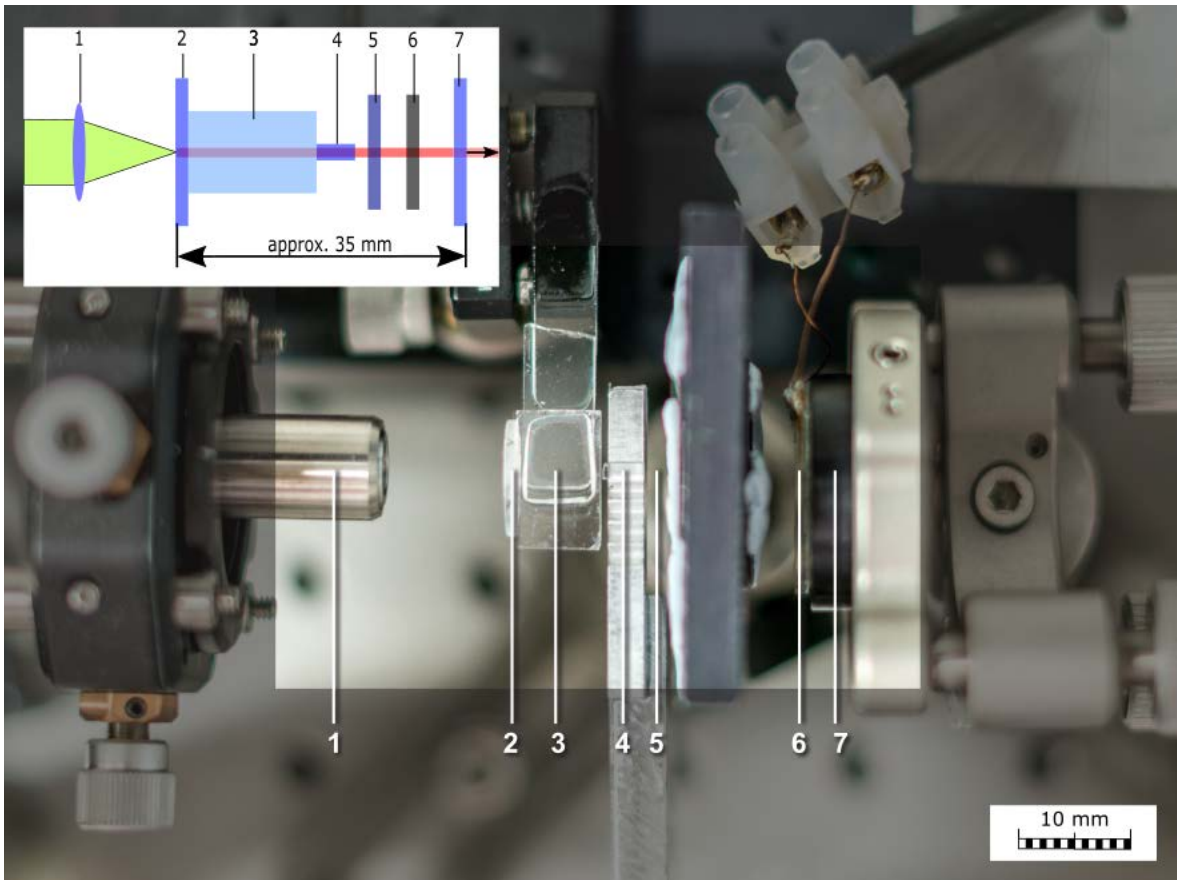

Figure 7.2: Image of laboratory prototype Q-switched waveguide laser with a cavity length of approximately 35 mm. The components are as follows: (1) focusing lens of the pump beam, (2) input-coupling mirror, (3) Yb:ZBLAN waveguide sample, (4) GRIN lens, (5) thin film polariser, (6) liquid crystal cell, (7) output-coupling mirror. In the schematic drawing, the pump beam at 976 nm is indicated by a green beam and the laser beam at 1016 nm is indicated by a red beam.

List of Publications

Journal papers

- **C. Wieschendorf**, J. Firth, L. Silvestri, S. Gross, F. Ladouceur, M. Withford, D. Spence, A. Fuerbach *Compact integrated actively Q-switched waveguide laser*. Optics Express **25**, 1692 – 1701 (2017)

International patent

- **C. Wieschendorf**, L. Silvestri, F. Ladouceur, A. Fuerbach *Voltage-controllable laser output coupler for integrated photonic devices*. (KLG Ref: 7410534.00003)

Conference papers

- **C. Wieschendorf**, J. Firth, S. Gross, M. Withford, D. Spence, F. Ladouceur, A. Fuerbach *Mid-infrared monolithic pulsed waveguide laser that is actively Q-switched by a liquid crystal cell*. (ICO The 24th congress of the international commission for optics 2017, Japan)

- **C. Wieschendorf**, J. Firth, L. Silvestri, S. Gross, F. Ladouceur, M. Withford, D. Spence, A. Fuerbach *Novel liquid crystal cells for short-pulsed monolithic guided-wave laser sources*. (CLEO/Europe-EQEC 2017, Germany)

- **C. Wieschendorf**, J. Firth, S. Gross, L. Silvestri, F. Ladouceur, D. Spence, A. Fuerbach *Actively Q-Switched integrated waveguide lasers*. (International Conference on Fibre Optics and Photonics 2016, Australia)

- X. Jiang, Simon Gross, **C. Wieschendorf**, H. Zhang, z. Guo, F. Rotermund, D.

Yeom, M.. Withford, and A. Fuerbach *Novel Saturable Absorbers for Short-pulsed Tm:ZBLAN Waveguide Lasers*. (Photonics and Fiber Technology 2016, Australia)

- **C. Wieschendorf**, S. Gross, L. Silvestri, F. Ladouceur, D. Spence, A. Fuerbach *Compact integrated actively Q-switched waveguide laser source on a chip scale.*. (The 7th International Conference on Optical, Optoelectronic and Photonic Materials and Applications 2016, Canada)

References

[1] K. M. Davis, K. Miura, N. Sugimoto, and K. Hirao. *Writing waveguides in glass with a femtosecond laser*. Optics Letters **21**(21), 1729 (1996).

[2] C. Florea, K. Winick, Y. Sikorski, A. Said, and P. Bado. *Optical waveguide amplifier in Nd-doped glass written with near-IR femtosecond laser pulses*. In *Conference on Lasers and Electro-Optics (CLEO 2000)*, vol. 36 (2000).

[3] K. Hirao and K. Miura. *Writing waveguides and gratings in silica and related materials by a femtosecond laser*. Journal of Non-Crystalline Solids **239**(1-3), 91 (1998).

[4] D. Homoelle, S. Wielandy, a. L. Gaeta, N. F. Borrelli, and C. Smith. *Infrared photosensitivity in silica glasses exposed to femtosecond laser pulses.* Optics Letters **24**(18), 1311 (1999).

[5] C. B. Schaffer, A. Brodeur, J. F. García, and E. Mazur. *Micromachining bulk glass using femtosecond laser pulses with nanojoule energy*. Optics Letters **26**(2), 93 (2001).

[6] A. M. Streltsov and N. F. Borrelli. *Fabrication and analysis of a directional coupler written in glass by nanojoule femtosecond laser pulses*. Optics Letters **26**(1), 42 (2001).

[7] M. Will, S. Nolte, B. N. Chichkov, and A. Tünnermann. *Optical properties of waveguides fabricated in fused silica by femtosecond laser pulses.* Applied Optics **41**(21), 4360 (2002).

[8] A. M. Streltsov. *Femtosecond-laser writing of tracks with depressed refractive index in crystals*. In *Proc. of SPIE, Laser Micromachining for Optoelectronic Device Fabrication*, vol. 4941, pp. 51–57 (2003).

[9] S. Nolte, M. Will, J. Burghoff, and a. Tuennermann. *Femtosecond waveguide writing: A new avenue to three-dimensional integrated optics*. Applied Physics A: Materials Science and Processing **77**(1), 109 (2003).

[10] G. D. Marshall, P. Dekker, M. Ams, J. a. Piper, and M. J. Withford. *Directly written monolithic waveguide laser incorporating a distributed feedback waveguide-Bragg grating*. Optics Letters **33**(9), 956 (2008).

[11] A. G. Okhrimchuk, A. V. Shestakov, I. Khrushchev, and J. Mitchell. *Depressed cladding, buried waveguide laser formed in a YAG:Nd^{3+} crystal by femtosecond laser writing*. Optics Letters **30**(17), 2248 (2005).

[12] G. Della Valle, S. Taccheo, R. Osellame, A. Festa, G. Cerullo, and P. Laporta. *1.5 um single longitudinal mode waveguide laser fabricated by femtosecond laser writing*. Optics Express **15**(6), 3190 (2007).

[13] R. Mary, S. J. Beecher, G. Brown, R. R. Thomson, D. Jaque, S. Ohara, and A. K. Kar. *Compact, highly efficient ytterbium doped bismuthate glass waveguide laser*. Optics Letters **37**(10), 1691 (2012).

[14] S. Taccheo, G. D. Valle, R. Osellame, G. Cerullo, N. Chiodo, P. Laporta, O. Svelto, A. Killi, U. Morgner, M. Lederer, and D. Kopf. *Er:Yb-doped waveguide laser fabricated by femtosecond laser pulses.* Optics Letters **29**(22), 2626 (2004).

[15] D. G. Lancaster, S. Gross, A. Fuerbach, H. E. Heidepriem, T. M. Monro, and M. J. Withford. *Versatile large-mode-area femtosecond laser-written Tm:ZBLAN glass chip lasers*. Optics Express **20**(25), 27503 (2012).

[16] R. Mary, G. Brown, S. J. Beecher, F. Torrisi, S. Milana, D. Popa, T. Hasan, Z. Sun, E. Lidorikis, S. Ohara, A. C. Ferrari, and A. K. Kar. *1.5 GHz picosecond pulse generation from a monolithic waveguide laser with a graphene-film saturable output coupler*. In *Pacific Rim Conference on Lasers and Electro-Optics, CLEO - Technical Digest*, vol. 21, pp. 7943–7950 (2013).

[17] A. G. Okhrimchuk and P. A. Obraztsov. *11-GHz waveguide Nd:YAG laser CW mode-locked with single-layer graphene*. Scientific Reports **5**, 11172 (2015).

[18] X. Jiang, S. Gross, H. Zhang, Z. Guo, M. J. Withford, and A. Fuerbach. *Bismuth telluride topological insulator nanosheet saturable absorbers for q-switched mode-locked Tm:ZBLAN waveguide lasers*. Annalen der Physik **528**(7-8), 543 (2016).

[19] S. Gross, N. Jovanovic, A. Sharp, M. Ireland, J. Lawrence, and M. J. Withford. *Low loss mid-infrared ZBLAN waveguides for future astronomical applications*. Optics Express **23**(6), 7946 (2015).

[20] M. Ams, R. J. Williams, and M. J. Withford. *Direct laser written waveguide coupler with an optically-tunable splitting ratio*. Frontiers in Ultrafast Optics: Biomedical, Scientific, and Industrial Applications Xi **7925**, 12 (2011).

[21] P. Dekker, M. Ams, T. Calmano, S. Gross, C. Kränkel, G. Huber, and M. J. Withford. *Spectral narrowing of Yb:YAG waveguide lasers through hybrid integration with ultrafast laser written Bragg gratings*. Optics Express **23**(15), 20195 (2015).

[22] J. L. Lovell, D. L. Jupp, D. S. Culvenor, and N. C. Coops. *Using airborne and ground-based ranging lidar to measure canopy structure in Australian forests*. Canadian Journal of Remote Sensing **29**(5), 607 (2003).

[23] A. H. Strahler, D. L. Jupp, C. E. Woodcock, C. B. Schaaf, T. Yao, F. Zhao, X. Yang, J. Lovell, D. Culvenor, G. Newnham, W. Ni-Miester, and W. Boykin-Morris. *Retrieval of forest structural parameters using a ground-based lidar instrument (Echidna®)*. Canadian Journal of Remote Sensing **34**, S426 (2008).

[24] F. Zhao, X. Yang, A. H. Strahler, C. L. Schaaf, T. Yao, Z. Wang, M. O. Román, C. E. Woodcock, W. Ni-Meister, D. L. Jupp, J. L. Lovell, D. S. Culvenor, G. J. Newnham, H. Tang, and R. O. Dubayah. *A comparison of foliage profiles in the Sierra National Forest obtained with a full-waveform under-canopy EVI lidar system with the foliage profiles obtained with an airborne full-waveform LVIS lidar system*. Remote Sensing of Environment **136**, 330 (2013).

[25] E. S. Douglas, J. Martel, Z. Li, G. Howe, K. Hewawasam, R. A. Marshall, C. L. Schaaf, T. A. Cook, G. J. Newnham, A. Strahler, and S. Chakrabarti. *Finding leaves in the forest: The dual-wavelength Echidna lidar*. IEEE Geoscience and Remote Sensing Letters **12**(4), 776 (2015).

[26] B. Hickernell, B. A. Kiberly, D. F. Plusquellic, and G. Wagner. *Differential absorption LIDAR for the detection and quantification of greenhouse gases* (2010).

[27] S. Kameyama, T. Ando, K. Asaka, Y. Hirano, and S. Wadaka. *Compact all-fiber pulsed coherent Doppler lidar system for wind sensing*. Applied Optics **46**(11), 1953 (2007).

[28] M. Merklein, B. Stiller, K. Vu, S. J. Madden, and B. J. Eggleton. *A chip-integrated coherent photonic-phononic memory*. Nature Communications **8**(1), 1 (2017).

[29] D. Grebe, R. Macdonald, and H. J. Eichler. *Cholesteric Liquid Crystal Mirrors for Pulsed Solid- State Lasers*. Molecular Crystals and Liquid Crystals Science and Technology. Section A. **282**(1), 309 (1996).

[30] S. V. Serak, H. J. Eichler, A. A. Kovalev, and T. A. Davidovich. *Passive laser Q-switching using a dye-doped liquid-crystalline layer near total internal reflection*. Optics Communications **196**, 269 (2001).

[31] I. Iryanto, H. J. Eichler, D. Grebe, and R. Macdonald. *Transient nematic liquid crystal modulator as an active Q-switch for solid state lasers*. In *Proc. of SPIE, Liquid Crystals VI*, vol. 4107, pp. 160–166 (2000).

[32] H. J. Eichler, D. Grebe, I. Iryanto, and R. Macdonald. *Active Q-Switching of a Solid State Laser Using Nematic Liquid Crystal Modulators*. Molecular Crystals and Liquid Crystals Science and Technology. Section A. **320**(1), 89 (1998).

[33] O. L. Antipov, D. V. Chausov, A. S. Kuzhelev, and A. P. Zinov. *Self-starting laser oscillator with a nonlinear nematic liquid-crystal mirror*. Journal of the Optical Society of America B **18**(1), 13 (2001).

[34] R. N. Brown, B. Bendow, G. Martin, C. T. Moynihan, M. Engineering, and N. Y. Bernard. *Ultraviolet absorption edge studies of fluorozirconate and fluorohafnate glass*. Applied Optics **21**(3), 361 (1982).

[35] S. Gross. *Direct-write Mid-IR Waveguide Lasers*. Ph.D. thesis (2012).

[36] C. B. Schaffer, A. Brodeur, and E. Mazur. *Laser-induced breakdown and damage in bulk transparent materials induced by tightly focused femtosecond laser pulses*. Measurement Science and Technology **12**(11), 1784 (2001).

[37] C. B. Schaffer, A. Brodeur, and E. Mazur. *Laser-induced breakdown and damage in bulk transparent materials induced by tightly focused femtosecond laser pulses*. Measurement Science and Technology **12**(11), 1784 (2001).

[38] L. V. Keldysh. *Ionization in the field of a string electromagnetic wave*. Journal of Experimental and Theoretical Physics **20**(5), 1307 (1965).

[39] R. A. Fox, R. M. Kogan, and E. J. Robinson. *Laser triple-quantum photoionization of cesium*. Physical Review Letters **26**(23), 1416 (1971).

[40] H. R. Reiss. *Polarization effects in high-order multiphoton ionization*. Physical Review Letters **29**(17), 1129 (1972).

[41] V. V. Temnov, K. Sokolowski-Tinten, P. Zhou, A. El-Khamhawy, and D. Von Der Linde. *Multiphoton ionization in dielectrics: Comparison of circular and linear polarization*. Physical Review Letters **97**(23), 1 (2006).

[42] X. Jing, Y. Tian, J. Zhang, S. Chen, Y. Jin, J. Shao, and Z. Fan. *Modeling validity of femtosecond laser breakdown in wide bandgap dielectrics*. Applied Surface Science **258**(10), 4741 (2012).

[43] K. K. Thornber. *Applications of scaling to problems in high field electronic transport*. Journal of Applied Physics **52**(1981), 279 (1981).

[44] M. Sparks, D. L. Mills, R. Warren, T. Holstein, A. A. Maradudin, L. J. Sham, E. Loh, and D. F. King. *Theory of electron-avalanche breakdown in solids*. Physical Review B **24**(6), 3519 (1981).

[45] B. C. Stuart, M. D. Feit, S. Herman, A. M. Rubenchik, B. W. Shore, and M. D. Perry. *Nanosecond-to-femtosecond laser-induced breakdown in dielectrics*. Physical Review B **53**(4), 1749 (1996).

[46] K. Itoh, W. Watanabe, S. Nolte, and C. B. Schaffer. *Ultrafast Processes for Bulk Modification of Transparent Materials*. MRS Bulletin **31**(8), 620 (2006).

[47] K. I. Kawamura, N. Sarukura, M. Hirano, and H. Hosono. *Holographic encoding of fine-pitched micrograting structures in amorphous SiO_2 thin films on silicon by a single femtosecond laser pulse*. Applied Physics Letters **78**(8), 1038 (2001).

[48] S. Nolte, M. Will, J. Burghoff, and A. Tuennermann. *Femtosecond waveguide writing: a new avenue to three-dimensional integrated optics*. Applied Physics A **77**(1), 109 (2003).

[49] J. W. Chan, T. Huser, S. Risbud, and D. M. Krol. *Structural changes in fused silica after exposure to focused femtosecond laser pulses*. Optics Letters **26**(21), 1726 (2001).

[50] K. M. Davis, K. Miura, N. Sugimoto, and K. Hirao. *Writing waveguides in glass with a femtosecond laser*. Optics Letters **21**(21), 1729 (1996).

[51] M. Efimov, L. B. Glebov, S. H. Park, K. a. Richardson, E. V. Stryland, C. Florida, T. Cardinal, M. Couzi, J. L. Brunéel, and U. B. I. *Waveguides in chalcogenide glasses produced by a train of femtosecond laser pulses*. Optical Materials **17**, 379 (2001).

[52] J. Chan, T. Huser, S. Risbud, and D. Krol. *Modification of the fused silica glass network associated with waveguide fabrication using femtosecond laser pulses*. Applied Physics A: Materials Science & Processing **76**(3), 367 (2003).

[53] J. W. Chan, T. R. Huser, S. H. Risbud, J. S. Hayden, and D. M. Krol. *Waveguide fabrication in phosphate glasses using femtosecond laser pulses*. Applied Physics Letters **82**(15), 2371 (2003).

[54] K. Hirao and K. Miura. *Writing waveguides in silica-related glasses with femtosecond laser*. Japanese Journal of Applied Physics **37**, 49 (1998).

[55] A. M. Streltsov and N. F. Borrelli. *Study of femtosecond-laser-written waveguides in glasses*. Journal of the Optical Society of America B **19**(10), 2496 (2002).

[56] W. J. Reichman, J. W. Chan, C. W. Smelser, S. J. Mihailov, and D. M. Krol. *Spectroscopic characterization of different femtosecond laser modification regimes in fused silica*. Journal of the Optical Society of America B **24**(7), 1627 (2007).

[57] D. J. Little, M. Ams, S. Gross, P. Dekker, C. T. Miese, A. Fuerbach, and M. J. Withford. *Structural changes in BK7 glass upon exposure to femtosecond laser pulses*. Journal of Raman Spectroscopy **42**(4), 715 (2011).

[58] Y. Shimotsuma, P. G. Kazansky, J. Qiu, and K. Hirao. *Self-Organized Nanogratings in Glass Irradiated by Ultrashort Light Pulses*. Physical Review Letters **91**(24), 247405 (2003).

[59] C. Hnatovsky, R. Taylor, E. Simova, P. Rajeev, D. Rayner, V. Bhardwaj, and P. Corkum. *Fabrication of microchannels in glass using focused femtosecond laser radiation and selective chemical etching*. Applied Physics A **84**(1-2), 47 (2006).

[60] B. Poumellec, L. Sudrie, M. Franco, B. Prade, and A. Mysyrowicz. *Femtosecond laser irradiation stress induced in pure silica*. Optics Express **11**(9), 1070 (2003).

[61] R. S. Taylor, C. Hnatovsky, E. Simova, P. P. Rajeev, D. M. Rayner, and P. B. Corkum. *Femtosecond laser erasing and rewriting of self-organized planar nanocracks in fused silica glass.* Optics Letters **32**(19), 2888 (2007).

[62] L. Sudrie, M. Franco, B. Prade, and A. Mysyrowicz. *Writing of permanent birefringent microlayers in bulk fused silica with femtosecond laser pulses*. Optics Communications **171**(4), 279 (1999).

[63] L. Sudrie, M. Franco, B. Prade, and A. Mysyrowicz. *Study of damage in fused silica induced by ultra-short IR laser pulses*. Optics Communications **191**(3-6), 333 (2001).

[64] S. S. Fedotov, R. Drevinskas, S. V. Lotarev, A. S. Lipatiev, M. Beresna, A. Čerkauskaite, V. N. Sigaev, and P. G. Kazansky. *Direct writing of birefringent elements by ultrafast laser nanostructuring in multicomponent glass*. Applied Physics Letters **108**(7) (2016).

[65] E. N. Glezer, M. Milosavljevic, L. Huang, R. J. Finlay, T.-H. Her, J. P. Callan, and E. Mazur. *Three-dimensional optical storage inside transparent materials*. Optics Letters **21**(24), 2023 (1996).

[66] E. N. Glezer and E. Mazur. *Ultrafast-laser driven micro-explosions in transparent materials*. Applied Physics Letters **71**, 882 (1997).

[67] D. Ashkenasi, G. Müller, A. Rosenfeld, R. Stoian, I. V. Hertel, N. M. Bulgakova, and E. E. B. Campbell. *Fundamentals and advantages of ultrafast micro-structuring of transparent materials*. Applied Physics A: Materials Science & Processing **77**(2003), 223 (2003).

[68] J. Qiu, K. Miura, and K. Hirao. *Three-Dimensional Optical Memory Using Glasses as a Recording Medium through a Multi-Photon Absorption Process*. Jpn. J. Appl. Phys. **37**, 2263 (1998).

[69] A. Horn, E. Kreutz, and R. Poprawe. *Ultrafast time-resolved photography of femtosecond laser induced modifications in BK7 glass and fused silica*. Applied Physics A **79**, 923 (2004).

[70] M. Sakakura, M. Terazima, Y. Shimotsuma, K. Miura, and K. Hirao. *Observation of pressure wave generated by focusing a femtosecond laser pulse inside a glass*. Optics Express **15**(9), 5674 (2007).

[71] H. Sun, J. Song, C. Li, J. Xu, X. Wang, Y. Cheng, Z. Xu, J. Qiu, and T. Jia. *Standing electron plasma wave mechanism of void array formation inside glass by femtosecond laser irradiation*. Applied Physics A: Materials Science and Processing **88**(2), 285 (2007).

[72] P. S. Salter and M. J. Booth. *Focussing over the edge: adaptive subsurface laser fabrication up to the sample face*. Optics Express **20**(18), 19978 (2012).

[73] M. Ams, G. D. Marshall, P. Dekker, M. Dubov, V. K. Mezentsev, I. Bennion, and M. J. Withford. *Investigation of ultrafast laser-photonic material interactions: Challenges for directly written glass photonics*. IEEE Journal on Selected Topics in Quantum Electronics **14**(5), 1370 (2008).

[74] D. J. Little, M. Ams, P. Dekker, G. D. Marshall, J. M. Dawes, and M. J. Withford. *Femtosecond laser modification of fused silica: the effect of writing polarization on Si-O ring structure*. Optics Express **16**(24), 20029 (2008).

[75] S. Gross, M. Dubov, and M. J. Withford. *On the use of the Type I and II scheme for classifying ultrafast laser direct-write photonics*. Optics Express **23**(6), 7767 (2015).

[76] V. Apostolopoulos, L. Laversenne, T. Colomb, C. Depeursinge, R. P. Salathé, M. Pollnau, R. Osellame, G. Cerullo, and P. Laporta. *Femtosecond-irradiation-induced refractive-index changes and channel waveguiding in bulk Ti^{3+}:Sapphire*. Applied Physics Letters **85**(7), 1122 (2004).

[77] S. Gross, M. J. Withford, and A. Fuerbach. *Direct femtosecond laser written waveguides in bulk Ti^{3+}:Sapphire*. In *Proceedings of SPIE 7589, Frontiers in Ultrafast Optics: Biomedical, Scientific, and Industrial Applications X*, vol. 7589, pp. 1–8 (2010).

[78] J. Siebenmorgen, K. Petermann, G. Huber, K. Rademaker, S. Nolte, and A. Tünnermann. *Femtosecond laser written stress-induced Nd:$Y_3Al_5O_{12}$ (Nd:YAG) channel waveguide laser*. Applied Physics B **97**(2), 251 (2009).

[79] T. Calmano, J. Siebenmorgen, O. Hellmig, K. Petermann, and G. Huber. *Highly efficient Yb:YAG channel waveguide laser written with a femtosecond-laser*. Applied Physics B: Lasers and Optics **100**(1), 131 (2010).

[80] C. N. Borca, V. Apostolopoulos, F. Gardillou, H. G. Limberger, M. Pollnau, and R.-P. Salathé. *Buried channel waveguides in Yb-doped KY(WO_4)$_2$ crystals fabricated by femtosecond laser irradiation*. Applied Surface Science **253**(19), 8300 (2007).

[81] R. Osellame, S. Taccheo, M. Marangoni, R. Ramponi, P. Laporta, D. Polli, S. De Silvestri, and G. Cerullo. *Femtosecond writing of active optical waveguides with astigmatically shaped beams*. Journal of the Optical Society of America B **20**(7), 1559 (2003).

[82] M. Ams, G. Marshall, D. Spence, and M. Withford. *Slit beam shaping method for femtosecond laser direct-write fabrication of symmetric waveguides in bulk glasses.* Optics Express **13**(15), 5676 (2005).

[83] T. Calmano, J. Siebenmorgen, F. Reichert, M. Fechner, A.-g. Paschke, N.-o. Hansen, K. Petermann, and G. Huber. *Crystalline Pr:$SrAl_{12}O_{19}$ waveguide laser in the visible spectral region*. Optics Letters **36**(23), 4620 (2011).

[84] R. Göring and M. Rothhardt. *Application of the refracted near-field technique to multimode planar and channel waveguides in glass*. Journal of Optical Communications **7**(3), 82 (1986).

[85] N. Gisin, J. P. Pellaux, P. Stamp, N. Hori, and M. Masuyama. *Alternative configuration for refracted near-field measurements of refractive index on glass-integrated-optics waveguides*. Applied Optics **31**(33), 7108 (1992).

[86] N. Gisin, R. Passy, P. Stamp, N. Hod, and S. Nagano. *New optical configuration for nondestructive measurements of refractive index profiles of LiNbO*. Applied Optics **33**(9), 1726 (1994).

[87] P. Oberson, B. Gisin, B. Huttner, and N. Gisin. *Refracted Near-Field Measurements of Refractive Index and Geometry of Silica-on-Silicon Integrated Optical Waveguides.* Applied Optics **37**, 7268 (1998).

[88] D. Findlay and R. A. Clay. *The measurement of internal losses in 4-level lasers*. Physics Letters **20**(3), 2 (1966).

[89] E. Collett. *Polarization* (SPIE - The International Society for Optical Engineering, 2005), 1 ed.

[90] F. Reinitzer. *Beiträge zur Kenntniss des Cholesterins*. Monatshefte für Chemie **9**(1), 421 (1888).

[91] O. Lehmann. *Über fließende Krystalle*. Zeitschrift für Physikalische Chemie **4**(1), 467 (1889).

[92] T. Bunning. *Cholesteric liquid crystals: properties and applications*. Liquid Crystals Today **23**(1), 23 (2014).

[93] G. H. Brown. *Structure, properties, and some applications of liquid crystals*. Optical Society of America **63**(12), 1505 (1973).

[94] T. T. Alkeskjold, L. Scolari, D. Noordegraaf, J. Lægsgaard, J. Weirich, L. Wei, G. Tartarini, P. Bassi, S. Gauza, S. T. Wu, and A. Bjarklev. *Integrating liquid crystal based optical devices in photonic crystal fibers*. Optical and Quantum Electronics **39**(12-13), 1009 (2007).

[95] B. Bahadur, D. Makow, S. Friberg, D. Chapman, C. Khetrapal, R. Weiss, A. Kunwar, Z. Witkiewicz, and W. Leigh. *Liquid Crystals, Applications and uses* (World Scientific, 1991), 2 ed.

[96] J. A. Castellano. *Liquid Gold* (2005).

[97] S. Singh. *Phase Transitions in Liquid Crystals*. Physics Reports **324**(2-4), 107 (2000).

[98] P. Raynes. *Liquid Crystals*. Liquid Crystals Today **3**(3), 7 (1993).

[99] P. G. Gennes and J. Prost. *The Physics of Liquid Crystals*, vol. 270 (1993), 2 ed.

[100] D. Coates and G. W. Gray. *Optical studies of the amorphous liquid-cholesteric liquid crystal transition: The "blue phase"*. Physics Letters A **45**(2), 115 (1973).

[101] S. R. Restaino and S. W. Teare. *Introduction to Liquid Crystals for Optical Design and Engineering* (2015).

[102] B. Christian. *Smectic Liquid Crystals : Ferroelectric Properties and Electroclinic Effect* (2001), 1 ed.

[103] Z. Brodzeli, L. Silvestri, A. Michie, Q. Guo, E. Pozhidaev, V. Chigrinov, and F. Ladouceur. *Reflective mode of deformed-helix ferroelectric liquid crystal cells for sensing applications*. Liquid Crystals **40**(10), 1427 (2013).

[104] E. Pozhidaev, V. Chigrinov, A. Murauski, V. Molkin, D. Tao, and H.-S. Kwok. *V-shaped electro-optical mode based on deformed-helix ferroelectric liquid crystal with subwavelength pitch*. Journal of the Society for Information Display **20**(5), 273 (2012).

[105] L. A. Beresnev, V. G. Chigrinov, D. I. Dergachev, E. P. Poshidaev, J. Fünfschilling, and M. Schadt. *Deformed helix ferroelectric liquid crystal display: A new electrooptic mode in ferroelectric chiral smectic C liquid crystals*. Liquid Crystals **5**(4), 1171 (1989).

[106] Z. Brodzeli, A. Michie, Q. Guo, E. P. Pozhidaev, V. Chirgrinov, F. Ladouceur, and L. Silvestri. *Sensors at Your Fibre Tips: A Novel Liquid Crystal- Based Photonic Transducer for Sensing Systems*. Lightwave Technology **31**, 7 (2013).

[107] A. D. Kiselev, E. P. Pozhidaev, V. G. Chigrinov, and H. S. Kwok. *Polarization-gratings approach to deformed-helix ferroelectric liquid crystals with subwavelength pitch*. Physical Review E - Statistical, Nonlinear, and Soft Matter Physics **83**(3), 1 (2011).

[108] A. D. Kiselev, E. P. Pozhidaev, V. G. Chigrinov, and H. S. Kwok. *Polarization-gratings approach to deformed-helix ferroelectric liquid crystals with subwavelength*

pitch. Physical Review E - Statistical, Nonlinear, and Soft Matter Physics **83**(3), 1 (2011).

[109] I. C. Khoo. *Extreme nonlinear optics of nematic liquid crystals*. J. Opt. Soc. Am. B **28**(12), A45 (2011).

[110] U. A. Hrozhyk, S. V. Serak, N. V. Tabiryan, L. Hoke, D. M. Steeves, and B. R. Kimball. *Azobenzene liquid crystalline materials for efficient optical switching with pulsed and or continuous wave laser beams* **18**(8), 8697 (2010).

[111] I. C. Khoo, R. G. Lindquist, R. R. Michael, R. J. Mansfield, and P. Lopresti. *Dynamics of picosecond laser induced density, temperature and flow-reorientation effects in the mesophases of liquid crystals*. J. Appl. Phys. **69**, 3853 (1991).

[112] H. J. Eichler and R. Macdonald. *Flow alignment and inertial effects in picoseconds laser-induced reorientation phenomena of nematic liquid crystals*. Physical Review Letters **67**, 2666 (1991).

[113] I. C. Khoo, J. D. Liou, and M. V. Stinger. *Microseconds to nanoseconds all-optical switching of visible-near infrared (0.5 um-1.55 um) lasers with dye-doped nematic liquid crystals*. Molecular Crystals and Liquid Crystals **527**, 109 (2010).

[114] A. Shishido, O. Tsutsumi, A. Kanazawa, T. Shiono, T. Ikeda, and N. Tamai. *Rapid optical switching by means of photoinduced change in refractive index of azobenzene liquid crystals detected by reflection-mode analysis*. J. Am. Chem. Soc. **119**, 7791 (1997).

[115] I. C. Khoo, J. H. Park, and J. D. Liou. *Theory and experimental studies of all-optical transmission switching in a twist-alignment dye-doped nematic liquid crystal*. J. Opt. Soc. Am. B **25**, 1931 (2008).

[116] R. Manohar. *An apparatus of increased precision for the measurement of electro-optical parameters of liquid crystals*. Materials Engineering **20**, 40 (2013).

[117] V. A. Baikalov, L. A. Beresnev, and L. M. Blinov. *Measures of the Molecular Tilt Angle and Optical Anisotropy n Ferroelectric Liquid Crystals*. Molecular Crystals and Liquid Crystals **127**(1), 397 (1985).

[118] M. Gu, S. V. Shiyanovskii, and O. D. Lavrentovich. *Electrically Accelerated Turn-off Process in the Nematic Liquid Crystals*. Symposium Digest of Technical Papers **39**(1), 44 (2008).

[119] Z. Zhang, Z. You, and D. Chu. *Fundamentals of phase-only liquid crystal on silicon (LCOS) devices*. Light: Science and Applications **3**(10), 1 (2014).

[120] N. A. Clark and S. T. Lagerwall. *Submicrosecond bistable electro-optic switching in liquid crystals*. Appl. Phys. Lett. **36**(11), 899 (1980).

[121] J. S. Patel. *Ferroelectric liquid crystal modulator using twisted smectic structure*. Applied Physics Letters **60**(3), 280 (1992).

[122] N. A. Clark and S. T. Lagerwall. *Submicrosecond bistable electro-optic switching in liquid crystals*. Appl. Phys. Lett. **36**(11), 899 (1980).

[123] I.-K. Huh and Y.-B. Kim. *Electro-optical Properties of Liquid Crystal Mixtures Containing Fluoroisothiocyanated Compounds*. Japanese Journal of Applied Physics **41**(11A), 6484 (2002).

[124] V. Borshch, S. V. Shiyanovskii, and O. D. Lavrentovich. *Nanosecond electro-optic switching of a liquid crystal*. Physical Review Letters **111**(10), 1 (2013).

[125] M. W. Geis, R. J. Molnar, G. W. Turner, T. M. Lyszczarz, R. M. Osgood, and B. R. Kimball. *30 To 50 Ns Liquid-Crystal Optical Switches*. Optics Express **18**(18), 18886 (2010).

[126] M. Gu, Y. Yin, S. V. Shiyanovskii, and O. D. Lavrentovich. *Effects of dielectric relaxation on the director dynamics of uniaxial nematic liquid crystals*. Physical Review E - Statistical, Nonlinear, and Soft Matter Physics **76**(6), 1 (2007).

[127] H. Takanashi, J. E. Maclennan, and N. A. Clark. *Sub 100 nanosecond pretilted planar-to-homeotropic reorientation of nematic liquid crystals under high electric field*. Japanese Journal of Applied Physics, Part 1: Regular Papers and Short Notes and Review Papers **37**(5 A), 2587 (1998).

[128] B.-X. Li, S. V. Shiyanovskii, and O. D. Lavrentovich. *Nanosecond switching of micrometer optical retardance by an electrically controlled nematic liquid crystal cell*. Optics Express **24**(26), 29477 (2016).

[129] R. A. Becker, R. H. Rediker, and T. A. Lind. *Wide-bandwidth guided-wave electro-optic intensity modulator at λ=3.39 μm*. Applied Physics Letters **46**(9), 809 (1985).

[130] C. M. Liebig, J. T. Goldstein, S. A. McDaniel, D. M. Krein, and G. Cook. *Femtosecond laser writing of electro-optic crystalline structures in glass*. Photonic Fiber and Crystal Devices: Advances in Materials and Innovations in Device Applications XI **1038207**, 6 (2017).

[131] G. R. Castillo, J. R. V. D. Aldana, F. Chen, R. He, Q. An, Y. Jia, G. R. Castillo-vega, J. R. V. De, and F. Chen. *Femtosecond laser micromachining of lithium niobate depressed cladding waveguides*. Optical Materials Express **3**(9), 1378 (2013).

[132] H. T. Bookey, R. R. Thomson, N. D. Psaila, A. K. Kar, N. Chiodo, R. Osellame, and G. Cerullo. *Femtosecond Laser Inscription of Low Insertion Loss Waveguides in Z-Cut Lithium Niobate*. IEEE Photonics Technology Letters **19**(12), 892 (2007).

[133] J. Thomas, M. Heinrich, J. Burghoff, S. Nolte, A. Ancona, and A. Tünnermann. *Femtosecond laser-written quasi-phase-matched waveguides in lithium niobate*. Applied Physics Letters **91**(15), 89 (2007).

[134] R. Osellame, M. Lobino, N. Chiodo, M. Marangoni, G. Cerullo, R. Ramponi, H. T. Bookey, R. R. Thomson, N. D. Psaila, and A. K. Kar. *Femtosecond laser writing of waveguides in periodically poled lithium niobate preserving the nonlinear coefficient*. Applied Physics Letters **90**(24) (2007).

[135] J. Chiles and S. Fathpour. *Mid-infrared integrated waveguide modulators based on silicon-on-lithium-niobate photonics*. Optica **1**(5), 350 (2014).

[136] Y. Jiang, W. Jiang, L. Gu, X. Chen, and R. T. Chen. *80-Micron Interaction Length Silicon Photonic Crystal Waveguide Modulator*. Applied Physics Letters **87**(22), 1 (2005).

[137] J.-M. Brosi, C. Koos, L. C. Andreani, J. Leuthold, and W. Freude. *Modulator with a polymer-infiltrated silicon photonic crystal waveguide*. Optics Express **16**(6), 4177 (2008).

[138] P. Rabiei and W. H. Steier. *Lithium niobate ridge waveguides and modulators fabricated using smart guide*. Applied Physics Letters **86**(16), 1 (2005).

[139] W. Koechner. *Solid-State Laser Engineering* (Springer-Verlag, 2006), 6 ed.

[140] A. E. Siegman. *Lasers* (University Science Books, 1986).

[141] T. H. Maiman. *Stimulated Optical Radiation in Ruby*. Nature **187**, 493 (1960).

[142] R. W. Hellwarth. *Theory of the pulsation of fluorescent light from ruby*. Physical Review Letters **6**(1), 9 (1961).

[143] F. J. McClung and R. W. Hellwarth. *Giant optical pulsations from ruby*. Journal of Applied Physics **33**(3), 828 (1962).

[144] M. Rose. *A History of the Laser: A Trip Through the Light Fantastic*.

[145] Y. Tan, Y. Yao, J. R. Macdonald, A. K. Kar, H. Yu, H. Zhang, and F. Chen. *Self-Q-switched waveguide laser based on femtosecond laser inscribed Nd:Cr:YVO_4 crystal*. Optics Letters **39**(18), 5289 (2014).

[146] Y. Tan, C. Cheng, S. Akhmadaliev, S. Zhou, and F. Chen. *Nd:YAG waveguide laser Q-switched by evanescent-field interaction with graphene*. Optics Express **22**(8), 9101 (2014).

[147] Y. Tan, R. He, J. Macdonald, A. K. Kar, and F. Chen. *Q-switched Nd:YAG channel waveguide laser through evanescent field interaction with surface coated graphene*. Applied Physics Letters **105**(10), 2014 (2014).

[148] A. Choudhary, S. Dhingra, B. D'Urso, T. L. Parsonage, K. A. Sloyan, R. W. Eason, and D. P. Shepherd. *Q-switched operation of a pulsed-laser-deposited Yb:Y_2O_2 waveguide using graphene as a saturable absorber.* Optics Letters **39**(15), 4325 (2014).

[149] W. Bolanos, J. J. Carvajal, X. Mateos, E. Cantelar, G. Lifante, U. Griebner, V. Petrov, V. L. Panyutin, G. S. Murugan, J. S. Wilkinson, M. Aguilo, and F. Diaz. *Continuous-wave and Q-switched Tm-doped $KY(WO_4)_2$ planar waveguide laser at 1.84 μm*. Optics Express **19**(2), 1449 (2010).

[150] L. Ma, Y. Tan, S. Wang, S. Akhmadaliev, S. Zhou, H. Yu, H. Zhang, and F. Chen. *Continuous-wave and Q-switched Yb:YSGG waveguide laser*. Journal of Lightwave Technology **35**(13), 2642 (2017).

[151] Y. Tan, S. Akhmadaliev, S. Zhou, S. Sun, and F. Chen. *Guided continuous-wave and graphene-based Q-switched lasers in carbon ion irradiated Nd:YAG ceramic channel waveguide.* Optics Express **22**(3), 3572 (2014).

[152] H. Liu, Y. Tan, J. R. Vázquez de Aldana, and F. Chen. *Efficient laser emission from cladding waveguide inscribed in Nd:$GdVO_4$ crystal by direct femtosecond laser writing*. Optics Letters **39**(15), 4553 (2014).

[153] Y. Cheng, J. Peng, B. Xu, H. Xu, Z. Cai, and J. Weng. *Passive Q-switching of 604 nm Pr:$LiYF_4$ visible laser using topological insulators Bi_2Se_3 as saturable absorber*. Optics and Laser Technology **88**(March 2016), 1 (2017).

[154] N. A. Kalanda, I. M. Kolesova, N. V. Kuleshov, and W. Sibbett. *Continuous-wave and Q-switched operation of a waveguide laser*. Optics Express **17**(3), 1666 (2009).

[155] Y. Jia, Y. Tan, C. Cheng, J. R. Vázquez de Aldana, and F. Chen. *Efficient lasing in continuous wave and graphene Q-switched regimes from Nd:YAG ridge waveguides produced by combination of swift heavy ion irradiation and femtosecond laser ablation.* Optics Express **22**(11), 12900 (2014).

[156] J. W. Kim, S. Y. Choi, D.-I. Yeom, S. Aravazhi, M. Pollnau, U. Griebner, V. Petrov, and F. Rotermund. *Yb:KYW planar waveguide laser Q-switched by evanescent-field interaction with carbon nanotubes.* Optics Letters **38**(23), 5090 (2013).

[157] R. He, J. R. Vázquez de Aldana, and F. Chen. *Passively Q-switched Nd:YVO_4 waveguide laser using graphene as a saturable absorber*. Optical Materials **46**, 414 (2015).

[158] C. Cheng, H. Liu, Z. Shang, W. Nie, Y. Tan, B. d. R. Rabes, J. R. Vázquez de Aldana, D. Jaque, and F. Chen. *Femtosecond laser written waveguides with MoS_2 as saturable absorber for passively Q-switched lasing*. Opt. Mater. Express **6**(2), 367 (2016).

[159] S. Y. Choi, T. Calmano, M. H. Kim, D.-I. Yeom, C. Kränkel, G. Huber, and F. Rotermund. *Q-switched operation of a femtosecond-laser-inscribed Yb:YAG channel waveguide laser using carbon nanotubes.* Optics express **23**(6), 7999 (2015).

[160] C. Cheng, H. Liu, Y. Tan, J. R. Vázquez de Aldana, and F. Chen. *Passively Q-switched waveguide lasers based on two-dimensional transition metal diselenide*. Optics Express **24**(10), 10385 (2016).

[161] Y. Tan, Q. Luan, F. Liu, F. Chen, and J. R. Vázquez de Aldana. *Q-switched pulse laser generation from double-cladding Nd:YAG ceramics waveguides.* Optics Express **21**(16), 18963 (2013).

[162] H. Liu, C. Cheng, C. Romero, J. R. Vázquez de Aldana, and F. Chen. *Graphene-based Y-branch laser in femtosecond laser written Nd:YAG waveguides*. Optics Express **23**(8), 9730 (2015).

[163] M. H. Kim, T. Calmano, S. Y. Choi, B. J. Lee, I. H. Baek, K. J. Ahn, D.-I. Yeom, C. Kränkel, and F. Rotermund. *Monolayer graphene coated Yb:YAG channel waveguides for Q-switched laser operation*. Optical Materials Express **6**(8), 2468 (2016).

[164] S. A. McDaniel, P. A. Berry, G. Cook, D. Zelmon, S. Meissner, H. Meissner, and X. Mu. *CW and passively Q-Switched operation of a Ho:YAG waveguide laser*. Optics and Laser Technology **91**(June 2016), 1 (2017).

[165] H. Lin, F. Tang, W. Chen, W. Guo, Q. Huang, N. Wang, L. Guan, Y. Cao, and G. Zhang. *Diode-pumped tape casting planar waveguide YAG/Nd:YAG/YAG ceramic laser*. Optics Express **23**(6), 8104 (2015).

[166] A. Choudhary, S. J. Beecher, S. Dhingra, B. D. Urso, T. L. Parsonage, J. A. Grantjacob, P. Hua, J. I. Mackenzie, R. W. Eason, and D. P. Shepherd. *456-mW graphene Q-switched Yb:yttria waveguide laser by evanescent-field interaction*. Optics Letters **40**(9), 1912 (2015).

[167] H. Suche and W. Sohler. *Q-switched Ti:Er:$LiNbO_3$ waveguide laser*. Optical and Quantum Electronics **31**, 29 (1999).

[168] E. Lallier, J. P. Pocholle, M. Papuchon, Q. He, M. de Micheli, and D. B. Ostrowsky. *Integrated Q-switched Nd:MgO:$LiNbO_3$ waveguide laser*. Electronics Letters **28**(15), 1428 (1992).

[169] H. Ouslimani, L. Bastard, and J. E. Broquin. *Narrow-linewidth Q-switched DBR laser on Ytterbium-doped glass*. Ceramics International **41**(7), 8650 (2015).

[170] J. A. Aust, K. J. Malone, D. L. Veasey, and N. A. Sanford. *Passively Q-switched Nd-doped waveguide laser*. Optics Letters **19**(22), 1849 (1994).

[171] A. Yeniay, J. Delavaux, J. Toulouse, and W. J. Minford. *Duty cycle ratio dependence on the performance of a Q-switched laser with an Er^{3+}-Yb^{3+} codoped glass waveguide.* Applied Optics **39**(9), 1430 (2000).

[172] A. Yeniay, J. P. Delavaux, J. Toulouse, D. Barbier, T. Strasser, and J. Pedrazanni. *High power Er^{3+}-Yb^{3+} co-doped glass waveguide Q-switched laser*. Electronics Letters **33**(21), 1792 (1997).

[173] E. Lallier, D. Papillon, J. P. Pocholle, M. Papuchon, M. de Micheli, and D. B. Ostrowsky. *Short pulse, high power Q-switched Nd:MgO:$LiNbO_3$ waveguide laser*. Electronics Letters **29**(2), 12 (1993).

[174] D. G. Lancaster, S. Gross, A. Fuerbach, H. E. Heidepriem, T. M. Monro, and M. J. Withford. *Versatile large-mode-area femtosecond laser-written Tm:ZBLAN glass chip lasers*. Optics Express **20**(25), 27503 (2012).

[175] T. Calmano, A.-G. Paschke, S. Müller, C. Kränkel, and G. Huber. *Q-Switched Operation of a fs-Laser Written Nd:YAG / Cr^{4+}:YAG monolithic waveguide laser*. In *Lasers, Sources, and Related Photonic Devices Technical Digest* (2012).

[176] H. Suche, T. Oesselke, J. Pandavenes, R. Ricken, K. Rochhausen, W. Sohler, S. Balsamo, I. Montrosset, and K. K. Wong. *Efficient Q-switched Ti:Er:$LiNbO_3$ waveguide laser*. Electronics Letters **34**(12), 1228 (1998).

[177] C. Becker, T. Oesselke, J. Pandavenes, R. Ricken, K. Rochhausen, G. Schreiber, W. Sohler, A. Member, H. Suche, R. Wessel, S. Balsamo, I. Montrosset, and D. Sciancalepore. *Advanced Ti:Er:LiNbO$_3$ Waveguide Lasers*. IEEE Journal of selected topics in Quantum electronicsl **6**(1), 101 (2000).

[178] G. Salamu, F. Jipa, M. Zamfirescu, and N. Pavel. *Watt-level output power operation from diode-laser pumped circular buried depressed-cladding waveguides inscribed in Nd:YAG by direct femtosecond-laser writing*. IEEE Photonics Journal **8**(1) (2016).

[179] J. I. Mackenzie and D. P. Shepherd. *End-pumped, passively Q-switched Yb:YAG doubleclad waveguide laser*. Optics Letters **27**(24), 2161 (2002).

[180] R. J. Beach, S. C. Mitchell, H. E. Meissner, O. R. Meissner, W. F. Krupke, J. M. McMahon, W. J. Bennett, and D. P. Shepherd. *Continuous-wave and passively Q-switched cladding-pumped planar waveguide lasers.* Optics Letters **26**(12), 881 (2001).

[181] J. Xu, I. J. Thomson, J. D. R. Valera, H. J. Baker, A. B. Russell, and D. R. Hall. *A Planar Waveguide Nd:YAG Laser Using Active Q-Switching of a Hybrid Unstable Resonator*. IEEE Journal on Selected Topics in Quantum Electronics **13**(3), 638 (2007).

[182] X. Zou and H. Toratani. *Evaluation of spectroscopic properties of Yb^{3+}-doped glasses*. Physical Review B **52**(22), 15889 (1995).

[183] G. Palmer, S. Gross, A. Fuerbach, D. G. Lancaster, and M. J. Withford. *High slope efficiency and high refractive index change in direct-written Yb-doped waveguide lasers with depressed claddings*. Optics Express **21**(14), 17413 (2013).

[184] D. G. Lancaster, S. Gross, H. Ebendorff-Heidepriem, K. Kuan, T. M. Monro, M. Ams, A. Fuerbach, and M. J. Withford. *Fifty percent internal slope efficiency femtosecond direct-written Tm^{3+}:ZBLAN waveguide laser*. Optics Letters **36**(9), 1587 (2011).

[185] B. M. Walsh and N. P. Barnes. *Comparison of Tm: ZBLAN and Tm: Silica fiber lasers; Spectroscopy and tunable pulsed laser operation around 1.9 μm*. Applied Physics B: Lasers and Optics **78**(3-4), 325 (2004).

[186] J. L. Doualan, S. Girard, H. Haquin, J. L. Adam, and J. Montagne. *Spectroscopic properties and laser emission of Tm doped ZBLAN glass at 1.8 μm*. Optical Materials **24**(3), 563 (2003).

[187] T. Calmano, J. Siebenmorgen, A.-G. Paschke, C. Fiebig, K. Paschke, G. Erbert, K. Petermann, and G. Huber. *Diode pumped high power operation of a femtosecond laser inscribed Yb:YAG waveguide laser [Invited]*. Optical Materials Express **1**(3), 428 (2011).

[188] T. Calmano, J. Siebenmorgen, O. Hellmig, K. Petermann, and G. Huber. *Nd:YAG waveguide laser with 1.3 W output power, fabricated by direct femtosecond laser writing*. Applied Physics B: Lasers and Optics **100**(1), 131 (2010).

[189] J. Bai, G. Cheng, X. Long, Y. Wang, W. Zhao, G. Chen, R. Stoian, and R. Hui. *Polarization behavior of femtosecond laser written optical waveguides in Ti:Sapphire*. Optics Express **20**(14), 15035 (2012).

[190] R. Paschotta. *YAG Lasers*.

[191] F. Reichert, D. Marzahl, P. Metz, M. Fechner, N. Hansen, and G. Huber. *Efficient visible laser operation of Pr,Mg:$SrAl_{12}O_{19}$ channel waveguides*. Optics Letters **38**(15), 2698 (2013).

[192] F. Reichert, D. Marzahl, P. Metz, M. Fechner, N. Hansen, and G. Huber. *Efficient laser operation of Pr^{3+},Mg^{2+}:$SrAl_{12}O_{19}$*. Optics Letters **37**(23), 4889 (2012).

[193] M. Fechner, F. Reichert, N. O. Hansen, K. Petermann, and G. Huber. *Crystal growth, spectroscopy, and diode pumped laser performance of Pr, Mg:$SrAl_{12}O_{19}$*. Applied Physics B: Lasers and Optics **102**(4), 731 (2011).

[194] K. Gürs and R. Müller. *Breitband-modulation durch steuerung der emission eines optischen masers (Auskoppelmodulation)*. Physics Letters **5**(3), 179 (1963).

[195] H. Statz and C. L. Tang. *Zeeman effect and nonlinear interactions between oscillating laser modes*. Quantum Electronics III pp. 469 – 498 (1964).

[196] L. E. Hargrove, R. L. Fork, and M. A. Pollack. *Locking of He-Ne laser modes ninduced by synchronous intracavity modulatio*. Appl. Phys. Lett. **5**(1), 4 (1964).

[197] DiDomenico M. *Small-signal analysis of internal (coupling type) modulation of lasers*. Journal of Applied Physics **35**(10), 2870 (1964).

[198] A. Yariv. *Internal modulation in multimode laser oscillators*. Journal of Applied Physics **36**(2), 388 (1965).

[199] M. H. Crowell. *Characteristics of Mode-Coupled Lasers*. IEEE J. Quantum Electronics **1**, 12 (1965).

[200] S. E. Harris and O. P. McDuff. *FM laser oscillation-theory*. Applied Physics Letters **5**(10), 205 (1964).

[201] S. E. Harris and R. Targ. *FM oscillation of the He-Ne laser*. Applied Physics Letters **5**(10), 202 (1964).

[202] A. J. DeMaria and D. A. Stetser. *Laser pulse-shaping and mode-locking with acoustic waves*. Applied Physics Letters **7**(3), 5 (1965).

[203] T. Deutsch. *Mode-locking effects in an internally modulated ruby laser*. Applied Physics Letters **7**(4), 80 (1965).

[204] H. W. Mocker and R. J. Collins. *Mode Competition and Self-Locking Effects in a Q-Switched Ruby Laser*. Appl. Phys. Lett. **7**(270), 1 (1965).

[205] A. J. DeMaria, C. M. Ferrar, and G. E. Danielson. *Mode locking of a Nd^{3+} doped glass laser*. Appl. Phys. Lett. **8**(1), 22 (1966).

[206] M. DiDomenico Jr., J. E. Geusic, H. M. Marcos, and R. G. Smith. *Generation of ultrashort optical pulses by mode locking the YAG:Nd laser*. Appl. Phys. Lett. **8**(7), 180 (1966).

[207] A. J. DeMaria, D. A. Stetser, and H. Heynau. *Self Mode-Locking of Lasers With Saturable Absorbers*. Appl. Phys. Lett. **8**(174), 10 (1966).

[208] R. L. Kohn and R. H. Pantell. *Second-harmonic enhancement with an internally-modulated ruby laser*. Appl. Phys. Lett. **8**(9), 231 (1966).

[209] M. Maier, W. Kaiser, and J. A. Giordmaine. *Intense light bursts in the stimulated Raman effect*. Physical Review Letters **17**(26), 1275 (1966).

[210] J. A. Armstrong. *Measurement of picosecond laser pulse widths*. Applied Physics Letters **10**(1), 16 (1967).

[211] H. P. Weber. *Method for Pulsewidth Measurement of Ultrashort Light Pulses Generated by Phase-Locked Lasers Using Nonlinear Optics*. J. Appl. Phys. **38**(5), 2231 (1967).

[212] D. Radnatarov, S. Khripunov, S. Kobtsev, A. Ivanenko, and S. Kukarin. *Automatic electronic-controlled mode locking self-start in fibre lasers with non-linear polarisation evolution*. Optics Express **21**(18), 20626 (2013).

[213] S. Antipov, M. Ams, R. J. Williams, E. Magi, M. J. Withford, and A. Fuerbach. *Direct infrared femtosecond laser inscription of chirped fiber Bragg gratings*. Optics Express **24**(1), 30 (2016).

[214] M. Horowitz, Y. Barad, and Y. Silberberg. *Noiselike pulses with a broadband spectrum generated from an erbium-doped fiber laser*. Optics Letters **22**(11), 799 (1997).

[215] E. J. R. Kelleher, J. C. Travers, Z. Sun, A. G. Rozhin, A. C. Ferrari, S. V. Popov, and J. R. Taylor. *Nanosecond-pulse fiber lasers mode-locked with nanotubes*. Applied Physics Letters **95**(11), 1 (2009).

[216] H. Xia, H. Li, Z. Wang, Y. Chen, X. Zhang, X. Tang, and Y. Liu. *Nanosecond pulse generation in a graphene mode-locked erbium-doped fiber laser*. Optics Communications **330**, 147 (2014).

[217] J. Xu, S. Wu, J. Liu, Q. Wang, Q. H. Yang, and P. Wang. *Nanosecond-pulsed erbium-doped fiber lasers with graphene saturable absorber*. Optics Communications **285**(21-22), 4466 (2012).

[218] D. Mao, X. Liu, L. Wang, H. Lu, and H. Feng. *Generation and amplification of high-energy nanosecond pulses in a compact all-fiber laser*. Optics Express **18**(22), 23024 (2010).

[219] S. Kobtsev, S. Kukarin, and Y. Fedotov. *Ultra-low repetition rate mode-locked fiber laser with high-energy pulses*. Optics Express **16**(26), 21936 (2008).

[220] M. E. Likhachev, S. S. Aleshkina, and M. M. Bubnov. *Narrow-linewidth mode-lock figure-eight nanosecond pulse fiber laser*. Laser Physics Letters **11**(12), 125104 (2014).

[221] M. Kues, C. Reimer, B. Wetzel, P. Roztocki, B. E. Little, S. T. Chu, T. Hansson, E. A. Viktorov, D. J. Moss, and R. Morandotti. *Passively mode-locked laser with an ultra-narrow spectral width*. Nature Photonics **11**(3), 159 (2017).

[222] R. I. Woodward, E. J. R. Kelleher, T. H. Runcorn, S. Loranger, D. Popa, V. J. Wittwer, A. C. Ferrari, S. V. Popov, R. Kashyap, and J. R. Taylor. *Fiber grating compression of giant-chirped nanosecond pulses from an ultra-long nanotube mode-locked fiber laser*. Optics Letters **40**(3), 387 (2015).

[223] W. Shi, M. A. Leigh, J. Zong, Z. Yao, D. T. Nguyen, A. Chavez-Pirson, and N. Peyghambarian. *High-Power all-fiber-based narrow-linewidth single-mode fiber laser pulses in the C-band and frequency conversion to THz generation*. IEEE Journal on Selected Topics in Quantum Electronics **15**(2), 377 (2009).

[224] B. Bolger and L. Baede. *Production of 300 W, nanosecond, transformlimited optical pulses*. Optics Communications **19**(3), 346 (1976).

[225] R. Nicolaescu, E. S. Fry, and T. Walther. *Generation of near-Fourier-transform-limited high-energy pulses in a chain of fiber-bulk amplifiers.* Optics Letters **26**(1), 13 (2001).

[226] M. Zhang, E. J. R. Kelleher, E. D. Obraztsova, S. V. Popov, and J. R. Taylor. *Nanosecond pulse generation in lumped normally dispersive all-fiber mode-locked laser*. IEEE Photonics Technology Letters **23**(19), 1379 (2011).

[227] E. Garmire. *Nonlinear optics in daily life*. Optics Express **21**(25), 30532 (2013).

[228] E. Garmire. *Overview of Nonlinear Optics*. Nonlinear Optics pp. 3–52 (2012).

[229] Y. Kodama and K. Nozaki. *Soliton interaction in optical fibers.* Optics Letters **12**(12), 1038 (1987).

[230] X. Jiang, N. Y. Joly, M. A. Finger, F. Babic, R. Sopalla, M. H. Frosz, and S. Poulain. *Supercontinuum generation in microstructured ZBLAN fibre with six nanobore cores*. In *Conference on Lasers and Electro-Optics (CLEO 2016)* (2016).

[231] E. A. Golovchenko, E. M. Dianov, A. M. Prokhorov, and V. N. Serkin. *Decay of optical solitons* (1985).

[232] G. Genty, M. Lehtonen, J. Broeng, M. Kaivola, and H. Ludvigsen. *Spectral broadening of femtosecond pulses into continuum radiation in microstructured fibers*. Optics Express **10**(20), 1083 (2002).

[233] J. Dudley and T. Roy. *Supercontinum Generation in Optical Fibers* (Cambridge University Press, 2010), 1 ed.

[234] J. M. Dudley, L. Provino, N. Grossard, H. Maillotte, R. S. Windeler, B. J. Eggleton, and S. Coen. *Supercontinuum generation in air-silica microstructured fibers with nanosecond and femtosecond pulse pumping*. Journal of the Optical Society of America B **19**(4), 765 (2002).

[235] L. Provino, J. M. Dudley, H. Maillotte, N. Grossard, R. S. Windeler, and B. J. Eggleton. *Compact broadband continuum source based on microchip laser pumped microstructured fibre*. Electronics Letters **37**(9), 558 (2001).

[236] E. E. Serebryannikov and A. M. Zheltikov. *Supercontinuum generation through cascaded four-wave mixing in photonic-crystal fibers: When picoseconds do it better*. Optics Communications **274**(2), 433 (2007).

[237] G. E. Town, T. Funaba, T. Ryan, and K. Lyytikainen. *Optical supercontinuum generation from nanosecond pump pulses in an irregularly microstructured air-silica optical fiber*. Applied Physics B: Lasers and Optics **77**(2-3), 235 (2003).

[238] N. Korneev, E. A. Kuzin, B. Ibarra-Escamilla, M. Bello-Jiménez, A. Flores-Rosas, and O. Pottiez. *Initial development of supercontinuum in fibers with anomalous dispersion pumped by nanosecond-long pulses*. Optics Express **16**(4), 2636 (2008).

[239] Y. Yu, Y. Zhang, B. Zhang, and Z. Wang. *Supercontinuum generation in polarization maintaining photonic crystal fibers using nanosecond pulses*. In *Proc. of SPIE-OSA-IEEE Asia Cimmunications and Photonics*, vol. 8307 (2011).

[240] R. Song, J. Hou, Z.-F. Wang, R. Xiao, and Q.-S. Lu. *Effect of initial chirp on near-infrared supercontinuum generation by a nanosecond pulse in a nonlinear fiber amplifier*. Chinese Physics B **22**(8), 084206 (2013).

[241] S. Coen, A. H. L. Chau, R. Leonhardt, J. D. Harvey, J. C. Knight, W. J. Wadsworth, and P. S. J. Russell. *Supercontinuum generation by stimulated Raman scattering and*

parametric four-wave mixing in photonic crystal fibers. Journal of the Optical Society of America B **19**(4), 753 (2002).

[242] A. Wang, B. Zhang, J. Hou, H. Wei, W. Tong, J. Luo, and Z. Zhang. *Visible supercontinuum generation with sub-nanosecond 532-nm pulses in all-solid photonic bandgap fiber*. IEEE Photonics Technology Letters **24**(2), 143 (2012).

[243] G. P. Agrawal. *Nonlinear Fiber Optics* (Academic Press, 2012).

[244] A. W. Snyder and J. Love. *Optical Waveguide Theory* (Chapman and Hall, 1983).

[245] M. Asobe, K. Suzuki, T. Kanamori, and K. Kubodera. *Nonlinear refractive index measurement in chalcogenideglass fibers by self phase modulation Nonlinear refractive index measurement by self-phase modulation*. Appl. Phys. Lett. **60**(10), 1153 (1992).

[246] S. C. Pinault and M. J. Potasek. *Frequency broadening by self-phase modulation in optical fibers*. J. Opt. Soc. Am. B **2**(8), 1318 (1985).

[247] W. Gao, T. Cheng, X. Xue, L. Liu, L. Zhang, M. Liao, T. Suzuki, and Y. Ohishi. *Stimulated Raman scattering in $AsSe_2$-As_2S_5 chalcogenide microstructured optical fiber with all-solid core*. Optics Express **24**(4), 3278 (2016).

[248] R. Rangel-Rojo, T. Kosa, E. Hajto, P. J. Ewen, A. E. Owen, A. K. Kar, and B. S. Wherrett. *Near-infrared optical nonlinearities in amorphous chalcogenides*. Optics Communications **109**(1), 145 (1994).

[249] K. S. Bindra, H. T. Bookey, A. K. Kar, B. S. Wherrett, X. Liu, and A. Jha. *Nonlinear optical properties of chalcogenide glasses: Observation of multiphoton absorption*. Applied Physics Letters **79**(13), 1939 (2001).

[250] G. I. Stegeman and E. M. Wright. *All-optical waveguide switching*. Optical and Quantum Electronics **22**(2), 95 (1990).

[251] M. R. E. Lamont, C. M. Sterke, and B. J. Eggleton. *Dispersion engineering of highly nonlinear As_2S_3 waveguides for parametric gain and wavelength conversion*. Optics Express **15**(15), 9458 (2007).

[252] F. Smektala, C. Quemard, V. Couderc, and A. Barthelemy. *Non-linear optical properties of chalcogenide glasses measured by Z-scan*. Journal of Non-Crystalline Solids **274**(1), 232 (2000).

[253] J. M. Laniel, N. Ho, C. Gk, and A. Villeneuve. *Nonlinear-refractive-index measurement in As_2S_3 channel waveguides by asymmetric self-phase modulation*. J. Opt. Soc. Am. B **22**(2), 437 (2005).

[254] M. Sheik-Bahae, D. C. Hutchings, D. J. Hagan, and E. W. Van Stryland. *Dispersion of Bound Electronic Nonlinear Refraction in Solids*. IEEE Journal of Quantum Electronics **27**(6), 1296 (1991).

[255] J. S. Sanghera, C. M. Florea, L. B. Shaw, P. Pureza, V. Q. Nguyen, M. Bashkansky, Z. Dutton, and I. D. Aggarwal. *Non-linear properties of chalcogenide glasses and fibers*. Journal of Non-Crystalline Solids **354**(2-9), 462 (2008).

[256] M. N. Fiddler, I. Begashaw, M. A. Mickens, M. S. Collingwood, Z. Assefa, and S. Bililign. *Laser spectroscopy for atmospheric and environmental sensing*. Sensors **9**(12), 10447 (2009).

[257] S. Liakat. *Development of a Noninvasive in Vivo Glucose Sensor Based on Mid-Infrared Quantum Cascade Laser Spectroscopy*. Ph.D. thesis (2015).

[258] T. v. Lerber, A. Bohren, and M. W. Sigrist. *Multicomponent trace gas analysis with broadly tunable mid-infrared laser spectrometer based on an optical parametric oscillator*. In *Conference on Lasers and Electro-Optics Europe*, p. 1 (2000).

[259] S. V. Smirnov, J. D. Ania-Castanon, T. J. Ellingham, S. M. Kobtsev, S. Kukarin, and S. K. Turitsyn. *Optical spectral broadening and supercontinuum generation in telecom applications*. Optical Fiber Technology **12**(2), 122 (2006).

[260] J. Hult, R. S. Watt, and C. F. Kaminski. *Dispersion measurement in optical fibers using supercontinuum pulses*. Journal of Lightwave Technology **25**(3), 820 (2007).

[261] F. Smektala, C. Quemard, L. Leneindre, J. Lucas, a. Barthélémy, and C. De Angelis. *Chalcogenide glasses with large non-linear refractive indices*. Journal of Non-Crystalline Solids **239**(1-3), 139 (1998).

[262] A. Zakery and S. R. Elliott. *Optical properties and applications of chalcogenide glasses: A review*. Journal of Non-Crystalline Solids **330**(1-3), 1 (2003).

[263] A. Al-kadry, C. Baker, M. El Amraoui, Y. Messaddeq, and M. Rochette. *Broadband supercontinuum generation in As_2Se_3 chalcogenide wires by avoiding the two-photon absorption effects*. Optics Letters **38**(7), 1185 (2013).